ALBERT-LUDWIGS UNIVERSITÄT FREIBURG

Master Thesis

OBSERVATION OF $\gamma\gamma \to \tau\tau$ PRODUCTION AND SENSITIVITY TO THE ANOMALOUS MAGNETIC MOMENT OF THE τ-LEPTON WITH THE ATLAS DETECTOR

Submitted for the Degree of

Master of Science in Physics

by

Leonie Hermann

Supervision: Prof. Dr. Markus Schumacher

Faculty of Mathematics and Physics
University of Freiburg, Germany
March 2022

ABSTRACT

The anomalous magnetic moment a_ℓ is an important property of leptons in the Standard Model of particle physics and is highly sensitive to the physics that cannot be explained by the Standard Model. For electrons and muons, the anomalous magnetic moment is among the most precisely measured quantities in the Standard Model. The short lifetime of the τ-lepton presents significant challenges to the corresponding measurement for the τ-lepton. In ultra-peripheral Pb+Pb collisions at the LHC, the τ-lepton production process $\gamma\gamma \to \tau\tau$ can be measured by taking advantage of the large photon flux. The value of the anomalous magnetic moment of the τ-lepton a_τ changes the total cross section of $\gamma\gamma \to \tau\tau$ production as well as the shapes of differential cross-sections in various kinematic observables.

In the analysis performed within this thesis, a first estimate of the accuracy of a the measurement of a_τ is performed based on Pb+Pb collision data with a center-of-mass energy of $\sqrt{s} = 5.02\,\text{TeV}$ collected by the ATLAS experiment in 2018, corresponding to an integrated luminosity of $1.44\,\text{nb}^{-1}$. Events with one leptonically decaying τ-lepton, i.e. an electron or muon in the final state, and the other τ-lepton decaying hadronically or leptonically to the other lepton flavor are exploited. $\gamma\gamma \to \tau\tau$ production is observed at the ATLAS experiment for the first time in Pb+Pb collisions in this analysis. The expected sensitivity of the measurement to a_τ is determined by a maximum likelihood fit to the number of selected events, the shape of kinematic distributions and a combination of both in five signal regions corresponding to different final states. The kinematic observables are compared regarding their sensitivity. The p_T distribution of the leading lepton of the final state is expected to be most sensitive with an expected confidence interval for a_τ of $-0.036 < a_\tau < 0.023$ at 95 % confidence level corresponding to an interval length of $l = 0.059$. The derived sensitivity is compatible with the currently most precise measurement of a_τ by the DELPHI collaboration of $-0.052 < a_\tau < 0.013$ at 95 % confidence level.

ZUSAMMENFASSUNG

Das anormale magnetische Moment a_ℓ ist eine wichtige Größe von Leptonen im Standardmodell der Teilchenphysik und ist sensitiv auf Physik, die über das Standardmodell hinaus geht. Die anomalen magnetischen Momente von Elektron und Myon gehören zu den am präzisesten gemessenen Größen im Standardmodell. Im Falle des τ-Leptons stellt seine kurze Lebensdauer eine Herausforderung für die Messung dar. In ultraperiphären Pb-Pb-Kollisionen am LHC kann die τ-Lepton-Produktion $\gamma\gamma \to \tau\tau$ aufgrund des hohen Flusses an Photonen gemessen werden. Der Wert des anomalen magnetischen Moments des τ-Leptons a_τ verändert den Gesamtwirkungsquerschnitt der $\gamma\gamma \to \tau\tau$-Produktion sowie die differentiellen Wirkungsquerschnitte in verschiedenen kinematischen Verteilungen.

In der vorgestellten Analyse wird eine erste Abschätzung für die Genauigkeit der Messung von a_τ auf Basis von Pb-Pb-Kollisionsdaten bei einer Schwerpunktsenergie von $\sqrt{s} = 5{,}02\,\text{TeV}$ durchgeführt, die mit dem ATLAS-Experiment im Jahr 2018 aufgenommen wurden und einer integrierten Luminosität von $1{,}44\,\text{nb}^{-1}$ entsprechen. Dafür werden Ereignisse mit einem leptonisch zerfallenden τ-Lepton, also einem Elektron oder einem Myon im Endzustand, und einem hadronisch oder ein in die andere Leptonenart zerfallenden τ-Lepton verwendet. Die $\gamma\gamma \to \tau\tau$-Produktion in Pb-Pb-Kollisionen wird mit dem ATLAS-Detektor in dieser Analyse zum ersten Mal beobachtet. Die erwartete Empfindlichkeit der Messung von a_τ wird durch eine Maximum-Likelihood-Anpassung an die Anzahl selektierter Ereignisse, die Form kinematischer Verteilungen und einer Kombination aus beiden in fünf verschiedenen Signal-Regionen, die unterschiedlichen Endzuständen entsprechen, bestimmt. Die kinematischen Verteilungen werden hinsichtlich ihrer Empfindlichkeit verglichen. Die p_T-Verteilung des führenden Leptons im Endzustand zeigt die höchste Sensitivität auf a_τ. Das erwartete Konfidenzintervall für a_τ wird auf $-0{,}036 < a_\tau < 0{,}023$ bei 95 % Konfidenzniveau mit einer Intervalllänge von $l = 0{,}059$ bestimmt. Diese Sensitivität ist kompatibel mit der derzeit genauesten Messung von a_τ durch die DELPHI-Kollaboration von $-0{,}052 < a_\tau < 0{,}013$ bei einem Konfidenzniveau von 95 %.

CONTENTS

1 INTRODUCTION

What does the universe consist of? How does it function and why? These are fundamental question that we are trying to understand. In particle physics, the Standard Model (SM) currently provides the best answer to these questions and gives a description of the elementary particles and their fundamental interactions in the universe. It describes three of the four fundamental interactions: the electromagnetic, the weak and the strong force as well as the known elementary particles. The existence of the last missing piece of the SM theory, the Higgs boson, was experimentally confirmed in 2012 by the ATLAS and CMS experiments at the Large Hadron Collider (LHC) [1, 2]. The SM, however, fails to describe some phenomena observed in nature such as the existence of dark matter or the matter-antimatter asymmetry.

The challenge today is to probe the SM and search for signs of any physics beyond the Standard Model (BSM) where the SM falls short.

The anomalous magnetic moment a_ℓ of charged leptons ℓ, i.e. electrons, muons and τ-leptons, is an important property of leptons that is sensitive to higher order corrections in SM calculations as well as BSM contributions [3]. Precision measurements of a_ℓ have been performed for electrons and muons resulting in $a_e = 1\,159\,652\,180.73(28) \times 10^{-12}$ for electrons [4] and $a_\mu = 1\,159\,652\,180.252(95) \times 10^{-12}$ for muons [5]. For muons a 4.2σ tension with the SM is reported [5] - a possible sign of BSM physics.

The anomalous magnetic moment of the τ-lepton a_τ, however, has not been measured with a sufficient precision to test the SM prediction of $a_\tau^{\text{th}} = 0.001\,177\,21(5)$ [6, 7]. A measurement following similar experimental setups as for the electron or muon are extremely challenging for the τ-lepton due to its high mass and its subsequent short lifetime. The most precise experimental constraints of the anomalous magnetic moment of the τ-lepton, a_τ, were obtained by the DELPHI collaboration [8] with the process $e^+e^- \to e^+e^-\tau^+\tau^+$ at the LEP2 collider as $-0.052 < a_\tau < 0.013$ (at 95 % confidence level) [9], which is significantly less precise than the currently available theoretical predictions.

In this thesis, the $\gamma\gamma \to \tau\tau$ process in ultra-peripheral lead-lead (Pb+Pb) collisions (UPC) at $\sqrt{s_{\text{NN}}} = 5.02\,\text{TeV}$ at the LHC, is measured by the ATLAS detector and simulated events of it, which are validated with the measured data, are used to extract first expected estimations of a_τ. The data set corresponds to an integrated luminosity of $1.44\,\text{nb}^{-1}$. In UPC, the heavy ion nuclei pass each other with an impact parameter larger than twice the radius of the nuclei, resulting in an interaction of their electromagnetic fields and thus in γ-induced processes, such as $\gamma\gamma \to \ell\ell$ production. These γ-induced processes exhibit an enhanced cross section which scales with Z^4 in comparison to pp collisions, where Z denotes the number of protons in the lead nucleus ($Z = 82$). The presence of the vertex $\gamma\tau\tau$ in the di-τ-lepton production $\gamma\gamma \to \tau\tau$ is sensitive to the anomalous magnetic moment a_τ of the τ-lepton.

In this thesis, the expected confidence intervals for a_τ are determined through a maximum likelihood fit to selected $\gamma\gamma \to \tau\tau$ events, using also the shape of different

kinematic distributions of the selected $\gamma\gamma \to \tau\tau$ events. Due to the short lifetime of the τ-leptons, the $\gamma\gamma \to \tau\tau$ events are reconstructed through the decay products of the τ-leptons. This analysis focuses on the final states where one τ-lepton decays into a muon or an electron and neutrinos and the other τ-lepton decays hadronically into pions or kaons and a neutrino or leptonically into a different flavor as well.
The signal selection for the discussed final states is optimized as part of this thesis. Various kinematic observables in the selected phase space regions are investigated regarding their sensitivity to a_τ and, if found to be sensitive, are used in fits to extract expected confidence intervals (CIs) on a_τ. Combinations of the signal regions are tested to increase the expected sensitivity to a_τ. Basic systematic and statistical uncertainties are included in the fit model.

The structure of this thesis, is the following: Chapter 2 introduces the theoretical concepts used in this thesis, including the motivation for the measurement of the $\gamma\gamma \to \tau\tau$ production in ultra-peripheral Pb+Pb collisions. In Chapter 3, the experimental setup is described which consists of the LHC and the ATLAS detector. Chapter 4 describes signal and background processes relevant for this thesis and their simulation. Chapter 5 focuses on the reconstruction and identification of particles and detector signatures which are used to construct physics objects based on the individual detector signals. Chapter 6 introduces to the concepts of statistical data analysis, including the definition of figures of merit and the description of the method of likelihood fits. Chapter 7 presents the general measurement strategy, the trigger used in this analysis and gives the definition and optimization for the signal selection and the background control regions. Chapter 8 contains the validation of the background estimation and the observation of the signal process $\gamma\gamma \to \tau\tau$ through comparison of the predictions with the data recorded in 2018. In Chapter 9, the procedure to obtain the expected 95 % confidence intervals (CIs) for a_τ using maximum likelihood fits is described. Studies are performed to investigate the most sensitive observables in a maximum likelihood fit which is used to extract the best fit value of a_τ and the expected CIs on a_τ. The impact of backgrounds, systematics and the combination of signal regions on the results are studied. In addition, the comparison with the currently best measurement results for a_τ from DELPHI are discussed. In Chapter 10, the results of this thesis are summarized.

2

τ-LEPTONS IN THE STANDARD MODEL AND AT THE LHC

The Standard Model (SM) [10] of particle physics describes the elementary particles and their interactions in a quantum field theoretical approach. An overview about the spectrum of elementary particles of the SM is given in Figure 2.1.

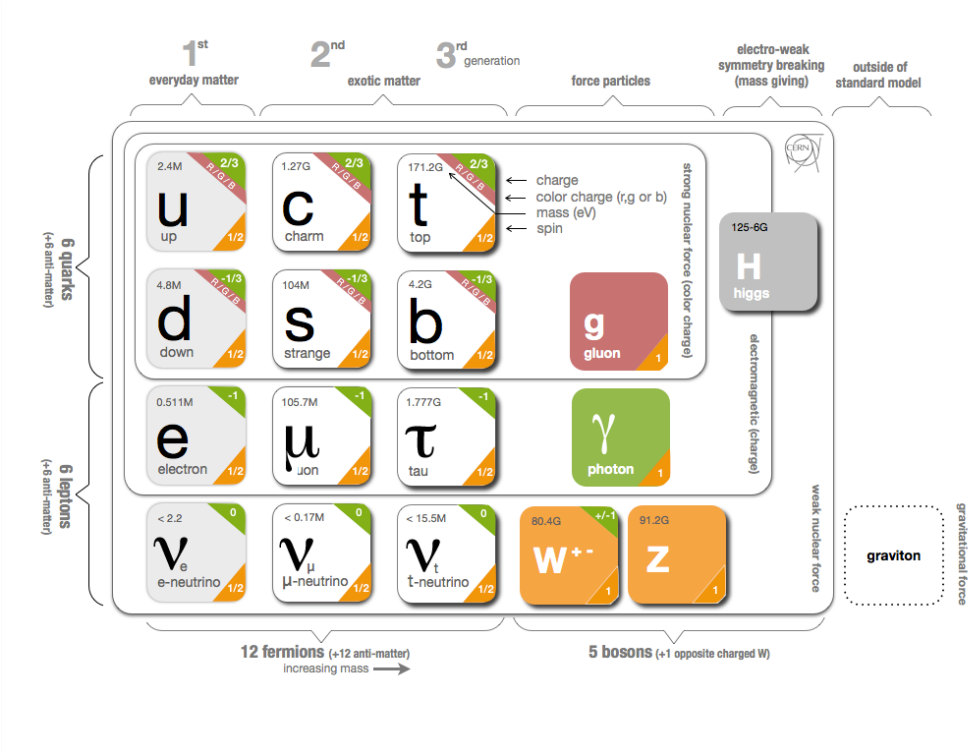

Figure 2.1: Elementary particles of the Standard Model in particle physics and their interaction mediators [11].

The elementary particles are divided into two classes. The particles in the first class are called fermions and have half-integer spin. Matter is built up from these particles. The interactions between the fermions are described by so-called exchange particles that belong to the second class of particles, bosons. These have an integer spin of 1 for vector bosons and of 0 for scalar bosons.
The fermions are further divided into quarks and leptons and into three generations with increasing mass. The quarks, up quark u, charm quark c and top quark t carry an electric charge of $+2/3$, while down quark d, strange quark s and bottom quark b have an electric charge Q of $-1/3$. Additionally, all quarks carry a color charge C red, blue or green. Quarks are building blocks for mesons (consisting of a quark and an antiquark) and baryons (3 quarks) which are colorless. Protons, for instance, are baryons and are

composed of two up quarks and one down quark. The leptons are the electron e^-, the muon μ^- and the tau τ^- with charge -1 and their corresponding neutrinos ν_e, ν_μ and ν_τ with charge 0. The charge of weak interactions is called weak-isospin $\mathbf{I}_W$ and is for all fermions $I_W = 1/2$, for the W- and Z-bosons $I_W = 1$ and for the photon γ and the gluon g $I_W = 0$. The hypercharge Y is connected to the electrical charge Q by the *Gell-Mann-Nishijima* formula [12, 13] as $Q = I_{W_3} + Y/2$ with the third component of the weak-isospin $\mathbf{I}_W$.
The SM underlies the $\mathrm{SU}(3)_C \times \mathrm{SU}(2)_{I_W} \times \mathrm{U}(1)_Y$ symmetry group and describes three out of the four fundamental forces: the electromagnetic [14–16] underlying the $\mathrm{U}(1)_Q$, weak [17–19] underlying the $\mathrm{U}(1)_Y \times \mathrm{SU}(2)_{I_W}$ and strong interaction [20–22] underlying the $\mathrm{SU}(3)_C$ symmetry group. The corresponding exchange particles are the photon γ, the $W^\pm$ and Z boson and the gluon g, which are all vector bosons. The only fundamental scalar boson is the Higgs boson that has been discovered in 2012 at the LHC [1], which is produced by the quantum excitation of the Higgs field. Particles acquire mass by interacting with the Higgs field, described through the Brout-Englert-Higgs mechanism [23, 24] with breaks spontaneously the $\mathrm{U}(1)_Y \times \mathrm{SU}(2)_{I_W}$ symmetry. The Higgs boson mass was measured to be $M_{H,\mathrm{lit}} = 125.18(16)\,\mathrm{GeV}$ [25]. The Higgs boson carries neither electric charge nor color charge but the weak isospin $I_W = -1/2$ and the hypercharge $Y = 1$.

2.1 ANOMALOUS MAGNETIC MOMENTS OF LEPTONS

The interactions of charged particles and photons is described by the theory of quantum electrodynamics (QED). It is a relativistic quantum field theory with a $\mathrm{U}(1)_Q$ symmetry describing the interaction with the massless mediator particle γ coupled to electric charge [26]. The theory is renormalizable and hence allows to compute finite physical quantities to high precision using perturbation theory. One of these quantities is the anomalous magnetic moment of a lepton a_ℓ.
The magnetic moment of a lepton is an intrinsic particle property that is proportional to the spin $\vec{s}$ of leptons as

$$\vec{\mu}_\ell = g\frac{e}{2m_\ell}\vec{s} \tag{2.1}$$

with the charge e, the mass m_ℓ of the lepton and the gyro-magnetic factor g. For a lepton inside an electromagnetic field, the magnetic moment can be deduced from the non-relativistic Dirac equation [26] as

$$\vec{\mu} = \frac{e}{2m_\ell}\vec{\sigma} = \frac{e}{m_\ell}\vec{s} \tag{2.2}$$

where spin angular momentum operator $\vec{s}$ can be expressed by the Pauli matrices $\vec{\sigma}$ as $\vec{s} = 1/2\,\vec{\sigma}$. Comparing the magnetic moment in Equation (2.1) with the non-relativistic result in Equation (2.2), the gyro-magnetic factor is predicted to be $g = 2$ at leading order in QED. The corresponding leading order QED diagram is shown for τ-leptons in Figure 2.2.

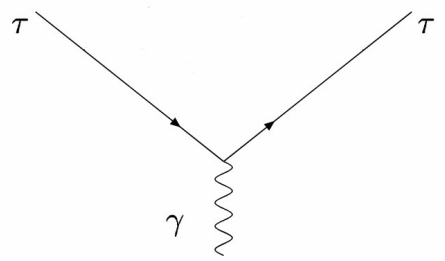

Figure 2.2: Leading order α QED diagram for τ-lepton predicting $g = 2$.

Radiative effects need to be accounted at higher orders of QED. The QED diagrams for the second order are shown in Figure 2.3. Including the corrections for higher order effects, the gyro-magnetic factor g can be written as

$$g = 2(F_1(0) + F_2(0)) = 2(1 + F_2(0)) \tag{2.3}$$

with the Dirac form factor $F_1(0) = 1$ from Equations (2.1) and (2.2) and the so-called Pauli form factor $F_2(0)$ being the anomalous magnetic moment of the lepton ℓ

$$a_\ell = \frac{g-2}{2}. \tag{2.4}$$

The anomalous magnetic moment of a lepton a_ℓ can be divided into three terms describing the SM contributions and one term from potential contributions of BSM effects:

$$a_\ell = a_\ell(\text{QED}) + a_\ell(\text{weak}) + a_\ell(\text{hadron}) + a_\ell(\text{BSM}). \tag{2.5}$$

The first term, $a_\ell(\text{QED})$, involves the QED contribution from leptons and photons, the second term, $a_\ell(\text{weak})$, the weak interaction with the $W^\pm$ and Z^0 bosons and the third term, $a_\ell(\text{hadron})$, comes from quarks and hadrons. Out of those three SM contributions, the QED term $a_\ell(\text{QED})$, also called Schwinger term [16], dominates a_ℓ. The Schwinger term $a_\ell(\text{QED})$ can be further divided according to its lepton-mass dependence. For the τ-lepton [7], it can be rewritten as

$$a_\tau(\text{QED}) = A_1 + A_2\left(\frac{m_\tau}{m_e}\right) + A_2\left(\frac{m_\tau}{m_\mu}\right) + A_3\left(\frac{m_\tau}{m_e}, \frac{m_\tau}{m_\mu}\right)$$

with the masses m_e, m_μ and m_τ of the electron, muon and τ-lepton, respectively. The first term A_1 is mass and flavour independent and therefore the same for all lepton types. The residual terms, A_2 and A_3, are functions depending on the mass ratios of the τ-lepton with either the electron or the muon. The three functions A_i $(i = 1, 2, 3)$ can be written as a power series expansion

$$A_i = A_i^{(2)}\left(\frac{\alpha}{\pi}\right) + A_i^{(4)}\left(\frac{\alpha}{\pi}\right)^2 + A_i^{(6)}\left(\frac{\alpha}{\pi}\right)^3 + A_i^{(8)}\left(\frac{\alpha}{\pi}\right)^4 + \cdots \tag{2.6}$$

expressed in terms of the fine structure constant

$$\alpha = \frac{e^2}{4\pi\epsilon_0\hbar c} \approx \frac{1}{137.035} \tag{2.7}$$

and π. The fine structure constant α is proportional to the elementary charge e of leptons squared. It depends further on the electric constant ϵ_0, the constant $\hbar = {}^{h}/_{2\pi}$ with the Planck constant h and the speed of light c. The higher order coefficients $A_i^{(2n)}$ can be calculated using Feynman rules [16] i.e. the leading order is calculated to be $A_i^{(2)} = \frac{1}{2}$ using the QED diagram shown in Figure 2.2 and the second order of α^2 is calculated to be $A_i^{(4)} = -0.32847896557919378\ldots$ using the QED diagrams shown in Figure 2.3 [7].

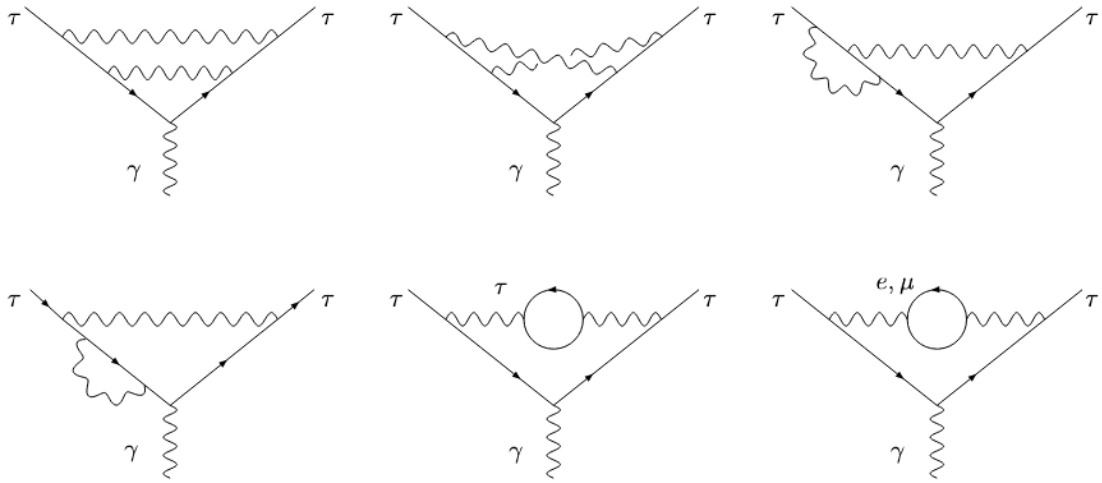

Figure 2.3: QED diagrams contributing at order α^2 to $(g-2)$ for the τ-lepton. Mirror reflections of the third and fourth diagram are not shown but need to be accounted in the calculation of Equation (2.6) [7].

The electroweak contribution $a_\ell(\text{weak})$ in Equation (2.5) is suppressed by the ratio $(m_\ell/M_W)^2$ of the lepton mass m_ℓ and the W boson mass M_W. The contribution is of the same order of magnitude as the three-loop QED term.
The last SM contribution to a_ℓ are the hadronic effects: $a_\ell(\text{hadron})$. While the hadronic effects in the two loop electroweak coupling are already included in the $a_\ell(\text{weak})$ term as explained in Ref. [7], only higher orders are accounted via $a_\ell(\text{hadron})$. Those are thus much smaller than the contribution coming from the Schwinger term $a_\ell(\text{QED})$.
The anomalous magnetic moment of a lepton a_ℓ can also be affected by BSM effects which is expressed in Equation (2.5) by the term $a_\ell(\text{BSM})$. It is expected that $a_\ell(\text{BSM})$ couples to the mass of the lepton m_ℓ [3] as

$$a_\ell(\text{BSM}) \propto \frac{m_\ell^2}{\Lambda^2} \tag{2.8}$$

with Λ being the energy scale of the new physics contributions. Given the large mass of the τ-lepton, the strongest effects of the BSM contributions could thus be seen in the anomalous magnetic moment of the τ-lepton.

Theoretical calculations and experimental measurements have been performed to determine the anomalous magnetic moments of leptons. The anomalous magnetic moment of the electron a_e [4] is measured to be

$$(a_e)_{\text{exp}} = 1\,159\,652\,180.73(28) \times 10^{-12}$$

with the SM prediction of

$$(a_e)_{\text{SM}} = 1\,159\,652\,181.88(78) \times 10^{-12}.$$

The precision of both, the measurement and the SM prediction, is 10^{-10} where a 2σ discrepancy between both is observed. A high precision measurement for the anomalous magnetic moment of the muon a_μ has been recently performed at the Fermilab National Accelerator Laboratory [27], resulting in a new world average value using several $g-2$ measurements of

$$(a_\mu)_{\text{exp}} = 116\,592\,061(41) \times 10^{-11}$$

which has a 4.2σ discrepancy from the SM prediction [28] of

$$(a_\mu)_{\text{SM}} = 116\,591\,810(43) \times 10^{-11}$$

where the precision of the measurement is on the level of the SM prediction at 10^{-7}. The precision for the prediction of the anomalous magnetic moment of the τ-lepton [7] of

$$(a_\tau)_{\text{SM}} = 117\,721(5) \times 10^{-8}.$$

is with 10^{-5} significantly lower than for those of the electron and muon. The experimental bound, however, has a even less precision. The most precise single-experiment measurement for the anomalous magnetic moment of the τ-lepton has been performed at the Large Electron Positron Collider (LEP) by the DELPHI Collaboration in 2004 [8] constraining a_τ to

$$-0.052 < a_\tau < 0.013$$

at 95 % CL with the process $e^+e^- \to e^+e^-\tau^+\tau^+$. The experimental mean value [8], using additionally the results from L3 and OPAL collaborations [29, 30] where the process $Z \to \tau\tau\gamma$ is studied, is determined to be

$$(a_\tau)_{\text{exp}} = -0.018(17)$$

which has not yet sufficient precision to test the SM prediction.

2.2 PRODUCTION OF τ-LEPTON PAIRS IN UPC HEAVY ION COLLISIONS AT THE LHC

The collisions of ions heavier than single protons [31] are called heavy ion collisions. Depending on the impact parameter b, the minimal distance between the mass center of two ions in a collision, heavy ion collisions can be classified as central, less central or peripheral. If the impact parameter is $b \approx 0$, the events are called central. For an impact parameter $b \approx 2R_A$ of twice the nuclear radius R_A, events are denoted as peripheral. In ultra-peripheral collisions (UPC), the heavy ions pass each other at $b > 2R_A$. In this case, no hadronic interactions occur due to the spatial separation between the two ions. Instead, the strong electromagnetic fields of the highly charged colliding ions generate quasi-real photons, equivalent to a large photon flux. The flux is proportional to the charge of the ions to the power four Z^2 if the photons are emitted coherently by the entire nucleus. For lead ions with $Z = 82$, the production cross section is therefore enhanced by a factor of $82^4 = 4 \times 10^7$ compared to proton collisions. Any contribution from the strong interaction is subdominant in UPCs and therefore negligible [32].
The Pb+Pb UPC collisions at the LHC can be used for to study dilepton production via the process

$$\mathrm{Pb} + \mathrm{Pb} \rightarrow \mathrm{Pb}(\gamma\gamma \rightarrow \ell\ell)\mathrm{Pb}. \tag{2.9}$$

The Feynman diagram of exclusive dilepton production (here τ-leptons) in Pb+Pb UPC collisions is shown in Figure 2.4. The lead ions stay intact, emitting quasi real photons that are interacting and generating the dilepton pair. The final state consists of two leptons, here τ-leptons with a clean experimental signature and without significant presence of additional particles from ion break-up or simultaneous additional collisions.

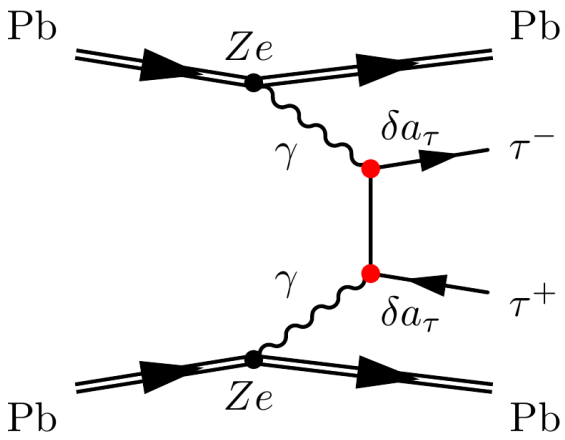

Figure 2.4: Leading order Feynman diagram for the process Pb+Pb→Pb+Pb+$\tau\tau$ in ultra relativistic heavy ion collisions. The vertices $\gamma\tau\tau$ marked by the red points are sensitive to the anomalous magnetic moment of the τ-lepton a_τ.

The production cross section of $\mathrm{Pb}+\mathrm{Pb}\to\mathrm{Pb}(\gamma\gamma\to\ell\ell)\mathrm{Pb}$ is given by

$$\begin{aligned}\sigma\left(\mathrm{Pb}+\mathrm{Pb}\to\mathrm{Pb}(\gamma\gamma\to\ell\ell)\mathrm{Pb};\sqrt{s_{\mathrm{NN}}}\right)=\int\sigma\left(\gamma\gamma\to\ell^+\ell^-;W_{\gamma\gamma}\right)\\ \times N\left(\omega_1,b_1\right)N\left(\omega_2,b_2\right)S^2_{abs}(\boldsymbol{b})\\ \times\frac{W_{\gamma\gamma}}{2}dW_{\gamma\gamma}dy_{\ell\ell}d\bar{b}_x d\bar{b}_y d^2b\end{aligned}\tag{2.10}$$

depending on the impact parameter b, the invariant mass of the diphoton system $W_{\gamma\gamma}=\sqrt{4\omega_1\omega_2}$ with the energy $\omega_i\,(i=1,2)$ emitted from the first or second nucleus, respectively and the rapidity of the dilepton system $y_{\ell\ell}$. The distances from the first and second nucleus are accounted by $\bar{b}_x=\left(b_{1x}+b_{2x}\right)/2, \bar{b}_y=\left(b_{1y}+b_{2y}\right)/2$ with the vectors b_1 and b_2 pointing to the position of the collision of the photons. The photon flux $N\left(\omega_i,\boldsymbol{b}_i\right)$ and the absorption factor $S^2_{abs}(\boldsymbol{b})=\theta\left(\boldsymbol{b}-2R_{Pb}\right)$ which ensures that only peripheral collisions are considered, are included in the calculation of the production cross section as well.
The partonic differential cross section of the dilepton production $\gamma\gamma\to\ell\ell$ is given by

$$\frac{\mathrm{d}\sigma(\gamma\gamma\to\ell\ell)}{\mathrm{d}\cos\theta}=\frac{2\pi}{64\pi^2 s}\frac{|\boldsymbol{p}_{\mathrm{out}}|}{|\boldsymbol{p}_{\mathrm{in}}|}\frac{1}{4}\sum_{\mathrm{spin}}|\mathcal{M}|^2\tag{2.11}$$

with θ being the angle between the outgoing leptons and the beam direction in the $\gamma\gamma$ center-of-mass frame, the squared invariant mass s of the $\gamma\gamma$ system and the 3-momenta of the incoming photon p_{in} and the outgoing lepton p_{out} [33]. The amplitude for this process $\mathcal{M}$ in the spacelike t- and u-channel with the photon p_1 and p_2, and the positive p_3 and negative charged p_4 lepton momenta [34] is given by

$$\begin{aligned}\mathcal{M}=&(-i)\epsilon_{1\mu}\epsilon_{2\nu}\bar{u}\left(p_3\right)\left(i\Gamma^{(\gamma\ell\ell)\mu}\left(p_3,p_t\right)\frac{i\left(\not{p}_t+m_\ell\right)}{t-m_\ell^2+i\epsilon}i\Gamma^{(\gamma\ell\ell)\nu}\left(p_{t'}-p_4\right)\right.\\ &\left.+i\Gamma^{(\gamma\ell\ell)\nu}\left(p_3,p_u\right)\frac{i\left(\not{p}_u+m_\ell\right)}{u-m_\ell^2+i\epsilon}i\Gamma^{(\gamma\ell\ell)\mu}\left(p_{u'}-p_4\right)\right)\nu\left(p_4\right)\end{aligned}\tag{2.12}$$

where the relations $p_{t^{(\prime)}}=p_2-p_4=p_3-p_1$ and $p_{u^{(\prime)}}=p_1-p_4=p_3-p_2$ are used. The incoming lepton is denoted by p' and the outgoing lepton by p. The photon vertex function $i\Gamma^{(r\ell\ell)}_\mu\left(p',p\right)$ with the momentum transfer $q=p'-p$ can be written as

$$i\Gamma^{(r\ell\ell)}_\mu\left(p',p\right)=-ie\left[\gamma_\mu F_1\left(q^2\right)+\frac{i}{2m_\ell}\sigma_{\mu\nu}q^\nu F_2\left(q^2\right)+\frac{1}{2m_\ell}\gamma^5\sigma_{\mu\nu}q^\nu F_3\left(q^2\right)\right]\tag{2.13}$$

with the spin tensor $\sigma_{\mu\nu}=\frac{i}{2}\left[\gamma_\mu,\gamma_\nu\right]$ and the Dirac $F_1(q^2)$, the Pauli $F_2(q^2)$ and the electric dipole form factor $F_3(q^2)$.
In UPC Pb+Pb collisions at LHC, the momentum transfer is typically small with $q^2_{1,2}<0.001\,\mathrm{GeV}^2$ for both photons [33] so that the asymptotic limit of $q^2\to 0$ can be used in Equation (2.13). The Dirac form factor becomes $F_1(0)=1$, the Pauli form factor $F_2(0)=a_\ell$ and electric dipole form factor $F_3(0)=d_\ell\frac{2m_t}{t}$. The Form factors describe the electromagnetic properties of the lepton such as the anomalous magnetic moment of the lepton and the electric dipole moment.
The τ-lepton pair production $\gamma\gamma\to\tau\tau$ in UPC heavy ion collisions contains the vertex

$\gamma\tau\tau$ which is sensitive to the anomalous magnetic moment of the τ-lepton a_τ as deduced from the Pauli form factor in Equation (2.12) and Equation (2.13). Since the vertex exists twice in the $\gamma\gamma \to \tau\tau$ production process as illustrated by the vertices marked in red in Figure 2.4, the sensitivity to a_τ is enhanced.

2.3 DECAY OF THE τ-LEPTON

The τ-lepton is the heaviest lepton in the SM. The charged spin 1/2 particle has a mass of $1776.86(12)\,\mathrm{MeV}/c^2$ [35] which is almost 3500 times heavier than the mass of an electron. The high mass results in a short lifetime for the τ-lepton of only $\tau_\tau = 290.3(5) \times 10^{-15}\,\mathrm{s}$ [35]. The decay length of a τ-lepton $c\tau_\tau = 87.03\,\mu\mathrm{m}$ [35] is therefore too short to reach the detector material and to interact with it, before it decays. In the detector, τ-leptons are identified by the reconstruction of its decay products, using the different decay modes of the τ-leptons. The τ-lepton decays into lighter particles via the weak interaction. There are two classes of decay channels: The τ-lepton decays into lighter leptons i.e., electrons e or muons μ and two neutrinos, denoted as the leptonic decay channel. Alternatively, the τ-lepton decays into hadrons, mainly pions π or kaons K and one neutrino, referred to as hadronic decay channel.
An overview of the most common decay channels is given in Table 2.1. Around 2/3 of the τ-leptons decay hadronically with either one charged pion $\pi^\pm$ or three charged pions $\pi^\pm + \pi^\pm + \pi^\mp$, a number of neutral pions π^0 and a τ-neutrino ν_τ. The residual 1/3 of the τ-leptons decay leptonically. The decay modes can be classified by the number of charged particles in the final state as 1-prong with one charged particle and 3-prong with three charged particles in the final state. For τ-leptons, around 80 % of the decays are 1-prong and 20 % are 3-prong.

Type of Decay		Decay Modes of τ^-	BR [%]
leptonic	1-prong	$\tau^- \to e^- + \bar{\nu}_e + \nu_\tau$	17.82(4) %
		$\tau^- \to \mu^- + \bar{\nu}_\mu + \nu_\tau$	17.39(4) %
hadronic	1-prong	$\tau^- \to \pi^- + \nu_\tau$	10.82(5) %
		$\tau^- \to \pi^- + \pi^0 + \nu_\tau$	25.49(9) %
		$\tau^- \to \pi^- + 2\pi^0 + \nu_\tau$	9.26(10) %
		$\tau^- \to \pi^- + 3\pi^0 + \nu_\tau$	1.04(7) %
	3-prong	$\tau^- \to 2\pi^- + \pi^+ + \nu_\tau$	8.99(5) %
		$\tau^- \to 2\pi^- + \pi^+ + \pi^0 + \nu_\tau$	2.74(7) %

Table 2.1: Most common decay modes of the τ^-lepton and their BRs [35]. The final state for the decay modes of the τ^+-lepton are charged conjugated. The decay modes of a τ-lepton decay are classified into leptonic or hadronic and into 1- or 3-prong decay mode, depending on the decay products.

3 EXPERIMENTAL SETUP

The experimental setup for data taking of heavy ion collisions is located at the largest particle physics laboratory in the world - the European Organization for Nuclear Research (CERN) [36]. The experimental setup consists of a complex accelerator system including the Large Hadron Collider (LHC) [37] which is the largest and most powerful human-made particle accelerator in the world and the ATLAS detector [38], which is a multipurpose detector designed to measure the collisions at the LHC. The LHC is described in Section 3.1, with details on the Pb+Pb data taking in Section 3.2. The ATLAS detector and its components are described in Section 3.3.

3.1 THE LARGE HADRON COLLIDER AT CERN

The particle accelerator complex of the LHC [39] is located at CERN at the border of France and Switzerland near Geneva. It is designed to accelerate and collide beams of protons or heavy ions in a 26.7 km long circular tunnel up to 170 m below ground level. The tunnel complex was formerly used for the Large Electron-Positron Collider (LEP) until the year 2000 and now hosts the LHC, with the start of operations in 2008.
Particle beams circulate clockwise and anticlockwise inside two separate beam pipes in the LHC. They are accelerated by superconducting radiofrequency cavities that are operating at 400 MHz. In the circular sections of the accelerator, dipole magnets with a magnetic field strength up to 8.33 T are used to keep the beams on their path. The beams are focused by quadrupole magnets, where strong quadrupole magnets are placed directly before the four intersection points. At an intersection point, the two beams pipes are joined and the beams are brought into collision. After the collisions, the beams are separated again by further magnets and guided back into the separate beam pipes.
The LHC is designed to accelerate and collide protons and heavy ions. A maximum center of mass energy of $\sqrt{s} = 13\,\text{TeV}$ for protons and $\sqrt{s_{\text{NN}}} = 5.02\,\text{TeV}$ for heavy ions has been reached in the years, 2015-2018, denoted also as Run-2 of the LHC. The particles are traveling with a speed near the speed of light in so-called bunches. In the case of proton collisions, a maximum of 2808bunches with 1.15×10^{11} protons per bunch can be filled in the LHC, with a spacing of 25 ns between bunches. This results in a nominal crossing rate of 40 MHz, or an average crossing rate of 31.6 MHz, factoring in that the 2808 bunches do not fill the entire LHC circumference, but some gaps need to left for steering magnets to fill and remove the beams from the accelerator. Given around 20 collisions in the same crossing, this would correspond to around 600×10^6 collisions per second. In heavy ion collisions [40], the maximum number of ions in each bunch is 2.2×10^8 and the number of bunches is - with 733 - lower than for pp collisions, resulting in an overall lower average crossing rate of 8.2 MHz. The bunches are spaced with a gap of 75 ns instead of 25 ns which gives a nominal crossing rate of 13.3 MHz.

The ion beams enter the LHC after they have been preaccelerated by the accelerator chain illustrated in Figure 3.1. The acceleration chain towards the LHC differs for protons and heavy ions. In the following description, the maximum energy reached in each acceleration step is denoted in brackets for protons and per nucleon n, respectively. Protons coming from LINAC 2 (50 MeV) are injected into the Proton Synchrotron Booster (PSB) (1.4 GeV) and then transferred to the Proton Synchrotron (PS) (25 GeV), while heavy ions are injected from LINAC 3 (4.2 MeV/n) and the Low Energy Ion Ring (LEIR) (72 MeV/n) to the PS (6 GeV/n). At this step, the acceleration chain for protons and heavy ions becomes the same up to and including the LHC. The ions are transferred from the PS to the Super Proton Synchrotron (SPS) (450 GeV/ 177 GeV/n) which is the last preaccelerator before the LHC (7 TeV/2.5 TeV/n).
At each interaction point of the LHC, particle-physics detectors are placed [41]. The largest experiments are ATLAS and CMS which are general purpose detectors designed for new discoveries and precision measurements of the SM of particle physics. These are accompanied by the ALICE experiment studying quark-gluon plasma produced in Pb+Pb collisions and the LHCb experiment investigating b-hadron physics.

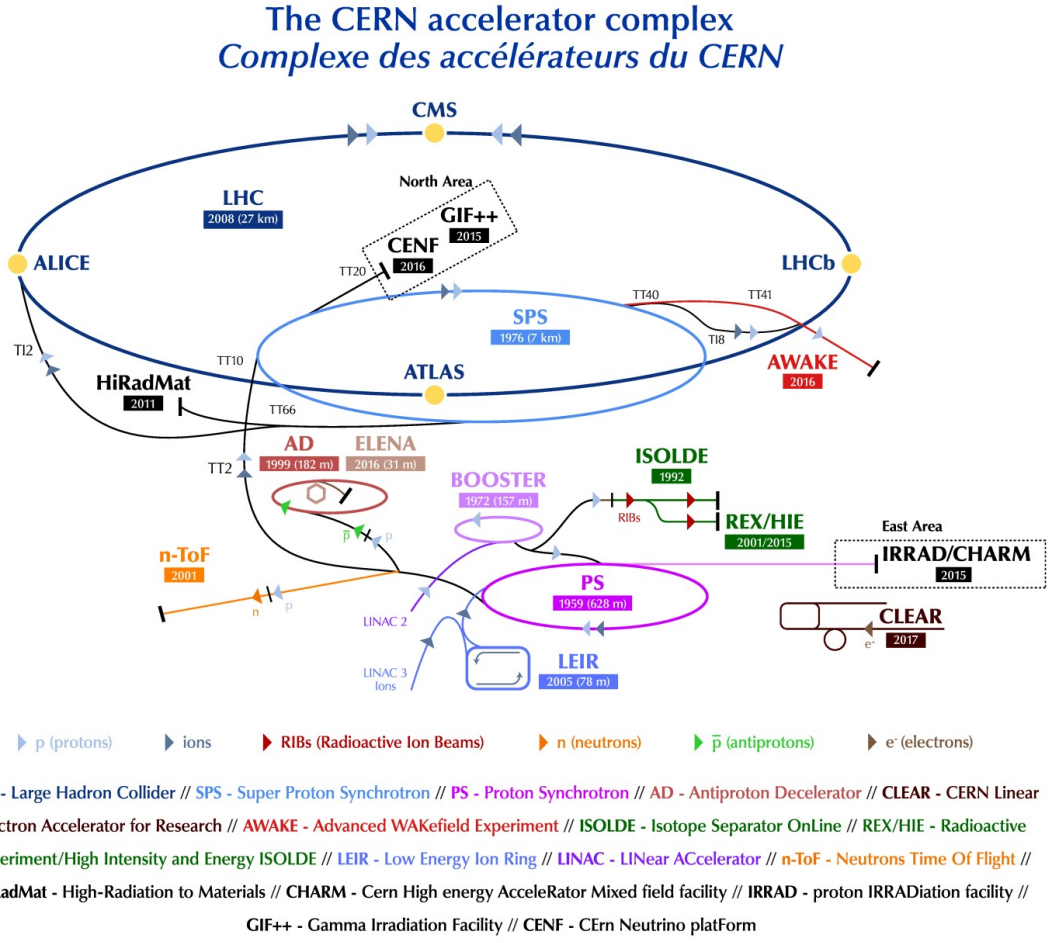

Figure 3.1: Accelerator chain for the LHC denoted by the largest blue ring [42]. The collision points, indicated with yellow dots, host the large experiments CMS, LHCb, ATLAS and ALICE.

3.2 HEAVY ION COLLISIONS IN 2018 AT THE LHC

A heavy ion program [31] was established at CERN to collide Pb+Pb, Xe-Xe and p+Pb at multiple energies with the LHC until now. Several weeks per year, the LHC operates as a heavy ion collider.
Starting in November 2018, for 3.5 weeks, data taking was performed with Pb+Pb collisions. The single beam energy of $E = 2.51\,\text{TeV}$ per nucleon leads to a collision energy of $\sqrt{s_{\text{NN}}} = 5.02\,\text{TeV}$. An instantaneous luminosity[1] of $L = 6.1 \times 10^{27}\,\text{cm}^{-2}\text{s}^{-1}$ was reached with 733 bunches and a bunch intensity of $N = 2.2 \times 10^{8}$ [40].
The integrated luminosity, defined as $\mathcal{L} = \int L\,\text{d}t$, delivered by the LHC for the Pb+Pb run in 2018 is shown in Figure 3.2. A data set from 2018 corresponding to an integrated luminosity of $1.76\,\text{nb}^{-1}$ was recorded, of which $1.44\,\text{nb}^{-1}$ pass data quality criteria and is used in this analysis. The uncertainty in the integrated luminosity is 1.9 % [43].

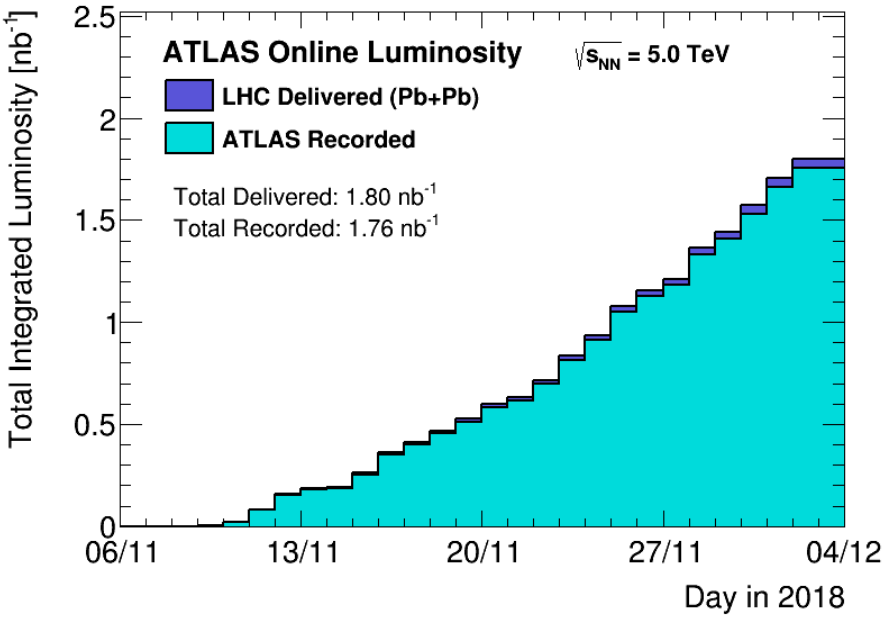

Figure 3.2: Delivered and recorded integrated luminosity of the LHC for Pb+Pb collisions in 2018 [44].

1 One of the most important quantities determining the performance of an accelerator is the number of collisions produced per time, denoted as the instantaneous luminosity L. The instantaneous luminosity L depends on the number of bunches n, the number of ions per bunch N_1 and N_2, the crossing rate of the bunches f, the beam width of the colliding bunches in $x-$ and $y-$direction σ_x and σ_y expressed simplified as $L = fn\frac{N_1 N_2}{4\pi\sigma_x\sigma_y}$.

3.3 THE ATLAS EXPERIMENT

The outcome of the particle collisions at the LHC at one of the interaction points is measured by the multi-purpose detector: ATLAS [38] . The ATLAS detector is located 100 m below the surface and has a cylindrical shape with a diameter of 25 m, 44 m length and a weight of 7000 t. The ATLAS detector is made of concentric layers, measuring directions, momenta, type and energy of the particles created in the interaction. From inside out, the ATLAS detector consists of: The inner detector (ID), followed by the electromagnetic calorimeter (ECAL) and the hadronic calorimeter (HCAL), as well as the muon spectrometer (MS). An additional calorimeter, the Zero Degree calorimeter (ZDC), is located at a distance of 140 m from the interaction point on either side of the ATLAS detector along the beam pipe, to measure neutrons emitted in the very forward direction. The coordinate system of the ATLAS detector and the individual detector components are described in more detail in Section 3.3.1 and Section 3.3.2, respectively. A sketch of the ATLAS detector without the ZDC is given in Figure 3.3.

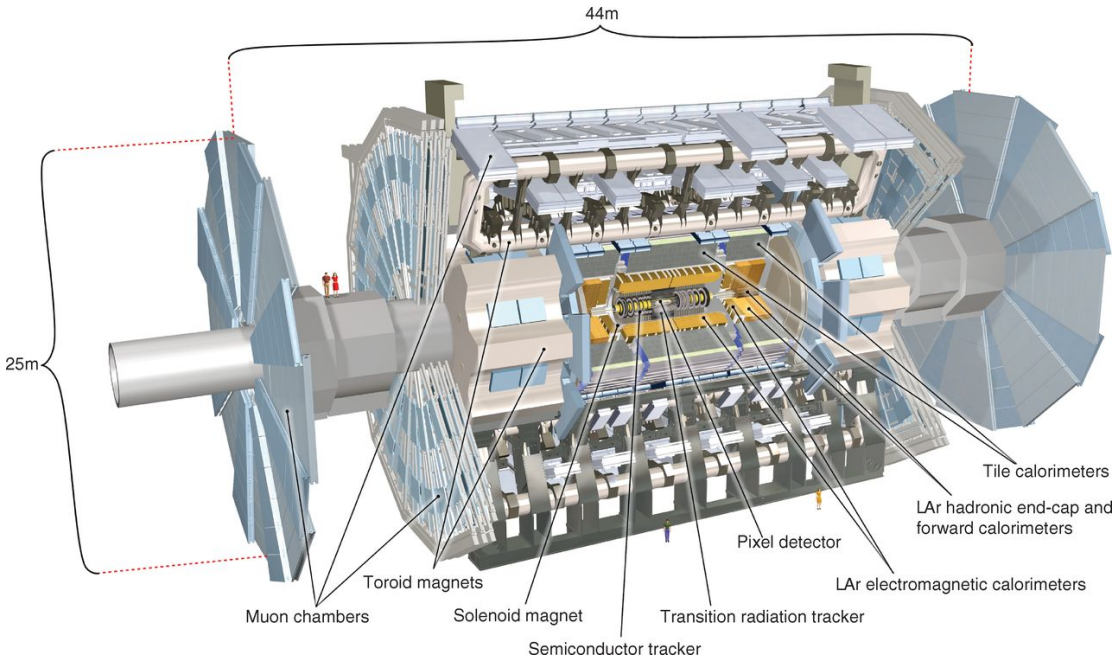

Figure 3.3: Sketch of the ATLAS detector and its components [45].

3.3.1 *Coordinate System*

The righthanded coordinate system of the ATLAS detector is shown in Figure 3.4. The collision point at the center of the detector is defined as the origin of the coordinate system. The detector is described both in terms of a polar and a cartesian coordinate system. The cartesian x-axis points towards the center of the LHC, the y-axis upwards and the z-axis in the direction of the particle beam that circulating counterclockwise. The x-y-plane is called transverse plane.
In polar coordinates, the angle around the z-axis in the transverse plane is denoted as

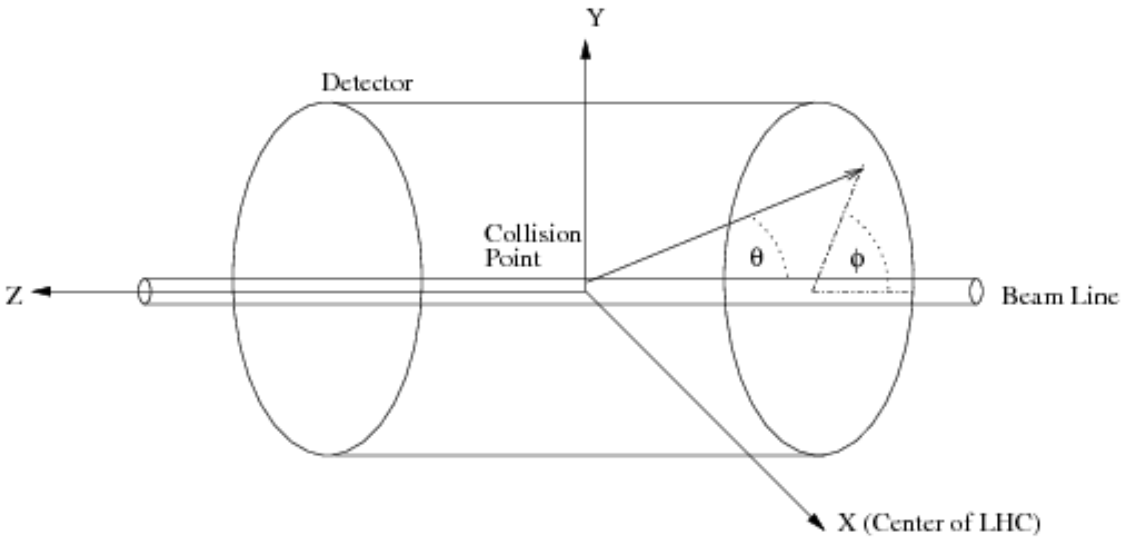

Figure 3.4: Sketch showing the coordinate system of the ATLAS detector [46].

azimuthal angle ϕ and the angle with respect to the z-axis as the polar angle θ. The pseudorapidity η is defined as

$$\eta = -\ln\left(\tan(\theta/2)\right) \tag{3.1}$$

and corresponds to a particle's rapidity y given by

$$y = \frac{1}{2}\ln\left(\frac{E + p_z}{E - p_z}\right) \tag{3.2}$$

in the case of $E \gg m$ or $m \to 0$ where E is the energy , m the mass and p_z the z-components of the momentum of the particle. The angular distance between two measured objects is given by

$$\Delta R = \sqrt{(\Delta\eta)^2 + (\Delta\phi)^2}. \tag{3.3}$$

The transverse momentum p_T and the transverse energy E_T are calculated by

$$p_T = \sqrt{p_x^2 + p_y^2} = p\sin\theta \tag{3.4}$$

$$E_T = \sqrt{E_x^2 + E_y^2} = E\sin\theta, \tag{3.5}$$

respectively, where p denotes the absolute value of the momentum and E the energy of the particle. The momentum components of the momentum vector become

$$p_x = p_T\cos\phi \tag{3.6}$$

$$p_y = p_T\sin\phi \tag{3.7}$$

$$p_z = p_T\sinh\eta. \tag{3.8}$$

3.3.2 *Detector Components*

Inner Detector

The ID [47] is responsible for charged particle tracking and measuring the transverse momenta of charged particles. It is placed in the 2 T strong magnetic field of a superconducting solenoid magnet which bends the tracks of charged particles in the transverse plane. The 6.2 m long ID has a diameter of 2.1 m and consists of three parts from inside out: the pixel detector (PD), the semiconductor tracker (SCT) and the transition radiation tracker (TRT).
The high resolution PD is positioned right around the beam pipe covering the region up to $|\eta| < 2.5$. In three cylindrical layers in the barrel region and three disks in the endcap region, approximately 80 million pixels with a size of $R\text{-}\phi \times z = 50 \times 200\,\mu\text{m}$ in the most parts of the PD are arranged in 1744 modules. In the barrel region, an additional fourth layer, the insertable b-layer (IBL), is added as innermost layer with 12 million pixels with a size of $R\text{-}\phi \times z = 25 \times 200\,\mu\text{m}$. The tracks of charged particles typically leave hits in at least three PD layers and are reconstructed with an accuracy of 10 µm in $R\text{-}\phi$ plane and 115 µm in z- and R-direction for a single module.
The SCT surround the PD and consists of silicon micro-strip detectors arranged in four layers in the barrel region and nine disks in the endcap regions, covering $|\eta| < 2.5$. The strips with a length of 6.4 cm and a pitch of 80 µm are aligned parallel to the beamline in the barrel regions and perpendicular in the endcap regions providing in each of the eight layers a position measurement of the tracks. The momentum, the impact parameters and the vertex positions of the tracks can be obtained through the track reconstruction. The accuracy of the 6.3 million readout channels in the SCT is 17 µm in $R\text{-}\phi$ plane and 580 µm in z-direction in the barrel and in R-direction in the endcap regions.
The outermost sub-detector of the inner detector is the TRT consisting of about 50,000 straw tubes in the barrel and 250,000 straw tubes in the endcap region and covers $|\eta| < 2.0$. The straw tubes have a diameter of 4 mm and a length of either 144 cm in the barrel or 37 cm in the endcap regions and are filled with two gas mixtures, either Xenon-based or Argon-based, amounting to a total volume of 12 m^2. During the LHC run 1, severe gas leaks were found in some modules of the TRT which are now filled with the Argon-based gas. The TRT has a limited resolution of 130 µm in $R\text{-}\phi$ but contributes to the tracking accuracy through its high number of expected hits of 36 per track, as well as to the particle identification through transition radiation signals for electrons. The p_T resolution for charged particles in the ID is

$$\sigma_{p_\text{T}} / p_\text{T} = 0.05\,\% p_\text{T} \oplus 1\%$$

where the notation $x \oplus y = \sqrt{x^2 + y^2}$ is used.

Calorimeter System

The main calorimeter system [47] consists of the electromagnetic (ECAL) and hadronic (HCAL) calorimeter, located concentrically around the ID. An additional zero degree (ZDC) calorimeter is installed in the very forward directions along the beam pipe, and is specifically employed in the ATLAS heavy ion program. The calorimeters are made

of active and absorber material layers, covering the full angle in ϕ and the η range $|\eta| \leq 4.9$ and $|\eta| > 8.3$ for ECAL/HCAL and ZDC, respectively. The calorimeters are used for energy measurements of the generated particles and in combination with other sub-detectors, for particle identification.

ELECTROMAGNETIC CALORIMETER The ECAL [48] surrounds the ID, and consists of a 5.6 m long EM barrel, covering $|\eta| < 1.475$, two 2.6 m long EM endcap calorimeters, covering $1.375 < |\eta| < 3.2$, and the forward calorimeter (FCal) covering $3.1 < |\eta| < 4.9$. The endcap calorimeter is divided into a central and a forward region, covering $1.375 < |\eta| < 2.5$ and covering $2.5 < |\eta| < 3.2$, respectively.
The ECAL consists of liquid argon as active and lead as absorber material in the barrel and endcap regions while copper is used in the FCal. The granularity of the different components differ: The highest granularity of $\Delta\eta \times \Delta\phi = 0.050 \times 0.025$ is achieved in the central region of the endcap calorimeter. The forward region and the other components of the ECAL have a coarser granularity.
The ECAL measures electromagnetically interacting particles by producing electromagnetic showers [49] which are measured by the different layers of the ECAL. The first layer in the ECAL is designed to identify $\pi^0 \to \gamma\gamma$ processes, the second layer collects the bulk of electromagnetic showers and the third layer the tails of the electromagnetic showers. In total, the ECAL has over 170,000 readout channels. The energy resolution for electrons and photons in the ECAL is

$$\sigma_E / E = 10\,\% / \sqrt{E} \oplus 0.7\,\%.$$

HADRONIC CALORIMETER The HCAL is located outside the ECAL and consists of a central, covering the pseudorapidity range of $|\eta| < 1.0$, and two extended barrels - one in either direction, covering $0.8 < |\eta| < 1.7$, a hadronic endcap, covering $1.5 < |\eta| < 3.2$, and a forward tile calorimeter, covering $3.1 < |\eta| < 4.9$.
Plastic scintillator tiles are used as active and steel plates as absorber material in the tile calorimeter. For the endcap calorimeter, liquid argon is used as active and copper plates as absorber material. The FCal is located between the beamline and the hadronic endcap calorimeter has three layers. The two layers in the hadronic part of the FCal uses tungsten as absorber material and liquid argon as active material.
The highest granularity in the HCAL of $\Delta\eta \times \Delta\phi = 0.1 \times 0.1$ is achieved in the first two layer of the extended barrels and for the hadronic endcap calorimeter for $|\eta| < 2.5$.
The HCAL is designed to measure the energy of jets and the missing transverse energy. The FCal measures particles close to the beam pipe. Outside the HCAL, shielding is installed to prevent non-stopped showers to reach the MS. The energy and position of the showers are measured by over 9000 readout channels in the HCAL. The jet energy resolution in the barrel and endcap regions of the HCAL is

$$\sigma_E / E = 50\,\% / \sqrt{E} \oplus 3\,\%$$

and for the FCal combined with the electromagnetic part

$$\sigma_E / E = 100\,\% / \sqrt{E} \oplus 10\,\%.$$

ZERO DEGREE CALORIMETER The ZDC consists of two detectors [50], denoted as ZDC+ and ZCD- which are installed at a distance of $\pm 140\,\mathrm{m}$ from the interaction point along the beam axis. Each detector side covers $|\eta| > 8.3$ and provides energy and position measurements of forward neutrons. The ZDC consists of four modules on either side with vertical quartz rods as active and 11 tungsten plates as absorber material. The energy resolution of the ZDC is

$$\sigma_E / E = 16\,\%.$$

Muon spectrometer

Muons generated in particle collisions are minimally ionizing particles and thus deposit only small amounts of energy in the calorimeters. Hence, the MS is installed as the outermost part of the ATLAS detector [47]. The MS is made of precision tracking chambers, the Monitored Drift Tubes and the Cathode Strip Chambers, covering $|\eta| < 2.7$, and trigger chambers, the Thin Gap Chambers and the Resistive Plate Chambers, covering $|\eta| < 2.4$. The gas-filled chambers are placed inside an air-core toroid magnet system consisting of a large barrel and two endcap toroids creating a magnetic field to bend the muon tracks parallel to the beamline. The momentum of the muons is determined from the curvature of the muon tracks using approximately 800,000 readout channels. The resolution of the MS is given by

$$\sigma_{p_\mathrm{T}} / p_\mathrm{T} = 10\,\%$$

for muons at $p_\mathrm{T} = 1\,\mathrm{TeV}$.

3.3.3 *Trigger System*

The LHC delivers particle collisions with a particle crossing rate of 40 MHz [51]. A multi-level trigger system [52] is implemented to select events relevant for further analysis directly during data taking (online). This significantly reduces readout bandwidths as well as required data storage capacities. The trigger is designed to filter events based on kinematics and multiplicities of physical objects such as muons, electrons, photons or jets as well as total energy sums, missing transverse energy, or topological criteria. The trigger ensures that only the most interesting events are saved for detailed offline analysis.
The first trigger level is hardware based and is called Level 1 (L1) trigger. It reduces the event rate from 40 MHz to 100 kHz within 2.5 µs using mainly information from muon trigger chambers and the calorimeters. The second trigger level runs on a computing farm consisting of largely commercially available components and is denoted as: the High Level Trigger (HLT). The HLT is software-based and reduces the event rate to maximally about 1.2 kHz within 200 ms on average. The data is stored at the CERN Tier 0 computing center.

4

SIGNAL AND BACKGROUND PROCESSES AND THEIR SIMULATION

For the analysis of the $\gamma\gamma \to \tau\tau$ process in Pb+Pb heavy ion collisions, the theoretical prediction for the signal and contributing background processes is obtained through Monte Carlo (MC) simulations. This includes the modeling of both, the properties of the signal and background as well as detector response on the simulated particles.
In this chapter, the simulation of the signal prediction for $\gamma\gamma \to \tau\tau$ with and without the effect of different anomalous magnetic moments a_τ and of the contributing background processes is described. The MC simulation is corrected through dedicated reweighting to the detector performance as seen in data.

4.1 SIGNAL PROCESS

The signal process of this analysis is $\gamma\gamma \to \tau\tau$ in ultaperipheral Pb+Pb collisions. It is simulated for the SM prediction as described in Section 4.1.1 and event weights are used to predict the di-τ-lepton production under the influence of BSM physics, quantified by different values of a_τ, as described in Section 4.1.2.
The Feynman diagram for the di-τ-lepton production is shown in Figure 4.1. The $\gamma\tau\tau$ vertex which is contained twice in the $\gamma\gamma \to \tau\tau$ process provides the sensitivity to the non-SM component δa_τ of the anomalous magnetic moment a_τ of the τ-lepton. For the SM, $a_\tau = 0$ is assumed in this analysis. This is a appropriate assumption given the theoretical prediction $a_\tau^{\text{th}} = 0.001\,177\,21(5)$ [6, 7] at the order of 10^{-3}, while the experimental precision so far only reaches the level of 10^{-2}. For the BSM prediction, a_τ values between -0.10 and 0.10 are used.

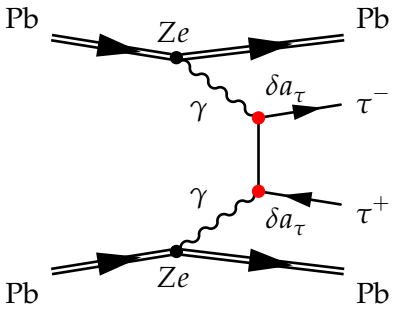

Figure 4.1: Feynman diagram for the signal process $\gamma\gamma \to \tau\tau$ in ultraperipheral Pb+Pb collisions. The $\gamma\tau\tau$ vertex is present twice in this process.

4.1.1 *Signal Process in the SM*

The STARLIGHT 2.0 [53] MC generator is used to simulate $\gamma\gamma \to \ell\ell$ production together with PYTHIA 8.245 [54, 55] for τ-lepton decay and EM final state radiation modeling. Effects related to FSR from charged decay products of τ-leptons are modeled with PHOTOS++ 3.61 [56–58]. The photon flux modeling of STARLIGHT 2.0 is reweighted to the SUPERCHIC 3.05 [59] photon flux modeling. Studies within the ATLAS collaboration [60] showed that it is advantageous to correct the photon flux from the STARLIGHT 2.0 generator to the SUPERCHIC 3.0 generator since its description for the shapes of the kinematic distributions is better in accordance with data measured in Pb+Pb collisions from 2018 for a muon-dominated selection. The cross section of the signal sample is blinded within $\pm 10\,\%$ of the actual cross section. Statistics in the kinematically interesting region for the measurement is enhanced through requirements on the generated true particles. The invariant mass of the two τ-leptons is required to be $m_{\tau\tau} > 4\,\text{GeV}$ and the transverse momentum of the leading τ-lepton to be $p_{\text{T}} > 2\,\text{GeV}$. A filter on the leading charged particle in the final state is applied within $|\eta| < 2.6$ accepting events with at least one leading charged particles with $p_{\text{T}} > 3\,\text{GeV}$. The name of the sample, the used cross section, 263.23 µb, the efficiency of the charged particle filter, 0.079817, and the number of produced events are listed in Table 4.1.
An alternative signal sample without FSR effects is produced using the STARLIGHT 2.0 generator only. The same true particle selections are applied as above in the generation of the events. Details on the sample are again listed in Table 4.1.

4.1.2 *Signal Simulation for anomalous a_τ*

BSM predictions, affecting both the overall cross section as well as the kinematic distributions, for $\gamma\gamma \to \tau\tau$ production have been provided by the authors of Ref. [61]. The BSM predictions are parameterized as function of $m_{\tau\tau}$, $|y_{\tau\tau}|$ and $|\Delta\eta_{\tau\tau}|$ and are provided as event weights for the a_τ values: -0.1, -0.06, -0.05, -0.04, -0.03, -0.02, -0.01, 0.01, 0.02, 0.03, 0.04, 0.05, 0.06, 0.1. The 3D weights are applied to the SM signal sample, which was discussed above, on an per-event basis. The effect of intermediate a_τ values is calculated through a quadratic or linear interpolation procedure, discussed in more detail in Chapter 6.

4.2 BACKGROUND PROCESSES

The detector measures not only the signal process $\gamma\gamma \to \tau\tau$ but also background processes with a similar signature in the detector. A precise estimate of the contributions of these backgrounds to the selected events in data requires an accurate modeling of these processes in MC simulation. Background events can come from different background processes. The main sources for the background are di-muon $\gamma\gamma \to \mu\mu$ (Section 4.2.1) and di-electron $\gamma\gamma \to ee$ (Section 4.2.2) production. A minor background process considered is the jet production $\gamma\gamma \to q\bar{q}$ (Section 4.2.3). The photonuclear production $\gamma A \to \gamma A X$ (Section 4.2.4) requires a data-driven estimate, but has overall only a minor impact on this analysis and is therefore neglected [60]. All considered background samples are summarized in Table 4.1.

4.2.1 $\gamma\gamma \to \mu\mu$

The main contributing background in the signal regions (SRs) requiring a muon, namely SR-1M1T, SR-1M3T and SR-1M1E introduced in Section 7.3, is the production of two muons in ultraperipheral Pb+Pb collision created in a two-photon induced process: $\gamma\gamma \to \mu\mu$. The Feynman diagram for this exclusive di-muon production is shown in Figure 4.2 (left). An additional hard FSR photon is emitted in the process $\gamma\gamma \to \mu\mu + \gamma$ in Figure 4.2 (right). The extra FSR photon can create, also together with a muon, an e^+e^- pair and is then measured e.g. as two extra tracks or as an electron. This contributes then especially to the background in the SRs where a muon and three tracks or a muon and an electron in required.

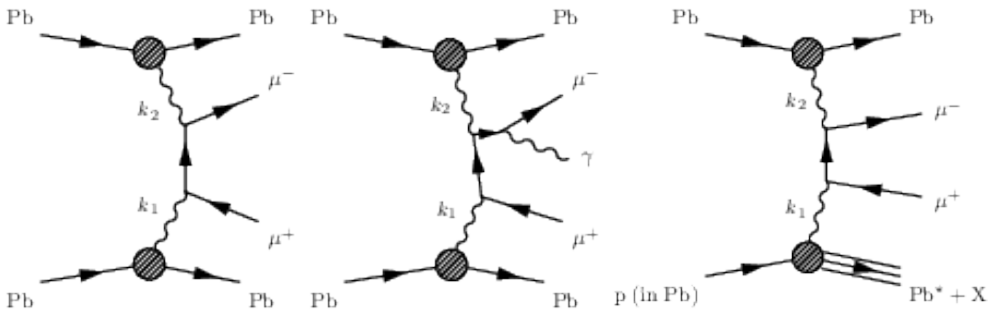

Figure 4.2: Feynman diagrams for the contributing background process $\gamma\gamma \to \mu\mu$ (left), $\gamma\gamma \to \mu\mu + \gamma$ with a hard photon γ emitted as final state radiation (middle) and dissociative photon emission from the Pb constituents (right) in ultraperipheral Pb+Pb collisions [60].

The di-muon $\gamma\gamma \to \mu\mu$ pair production is modeled with the STARLIGHT 2.0 generator interfaced to PYTHIA 8.245 for the modeling of final state radiation and hadronisation effects. The process is split into two ranges of the invariant mass of the muon pair: $7 < m_{\mu\mu} < 20\,\text{GeV}$ and $m_{\mu\mu} > 20\,\text{GeV}$ with a total cross section of 83.75 µb. The sample names, cross section and simulated numbers of events are listed in Table 4.1. The photon flux from the STARLIGHT 2.0 generator is corrected to the modeling of the SUPERCHIC 3.0 generator with the same motivation as for the signal sample. The $\gamma\gamma \to \mu\mu + \gamma$ process is simulated with the MADGRAPH5_AMC@NLO [62] generator, interfaced to PYTHIA 8.245 for the modeling of FSR photons modifying di-muon kinematics that mimic τ-lepton decays. This sample has a kinematic overlap with $\gamma\gamma \to \mu\mu$ production with FSR effects, which needs to be removed if both samples are meant to be used together. The contribution of $\gamma\gamma \to \mu\mu + \gamma$ is small as studied in Appendix A.1, however, so in this thesis, it is not considered, and final state photon emission is solely simulated through FSR in the $\gamma\gamma \to \mu\mu$ samples.

4.2.2 $\gamma\gamma \to ee$

The dominating background in the SRs requiring an electron, namely SR-1E1T, SR-1E3T and SR-1M1E introduced in Section 7.3, is the production of two electrons in ultraperipheral Pb+Pb collisions in a two-photon induced process: $\gamma\gamma \to ee$. The Feynman diagram for this process is shown in Figure 4.3.

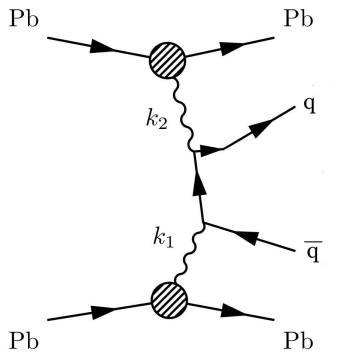

Figure 4.4: Feynman diagram for the background process $\gamma\gamma \to q\bar{q}$. Adapted from Ref. [60].

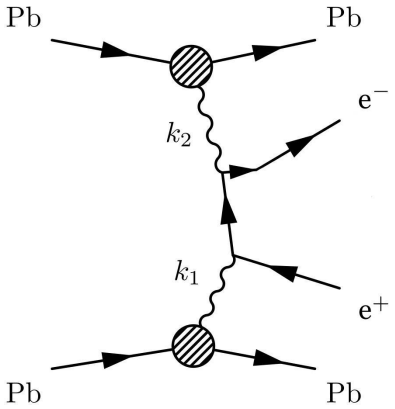

Figure 4.3: Feynman diagram for the background process $\gamma\gamma \to ee$ in ultraperipheral Pb+Pb collisions. Adapted from Ref. [60].

The di-electron $\gamma\gamma \to ee$ pair production is modeled with the STARLIGHT 2.0 generator interfaced to PYTHIA 8.245 for FSR and hadronisation effects, similarly to $\gamma\gamma \to \mu\mu$ production. The process is simulated in three slices of in the invariant di-electron mass: $4.5 < m_{ee} < 7\,\text{GeV}$, $7 < m_{ee} < 15\,\text{GeV}$ and $m_{ee} > 15\,\text{GeV}$ with a total cross section of 296.15 µb. The sample names, the individual cross sections and number of events are listed in Table 4.1.

4.2.3 $\gamma\gamma \to q\bar{q}$

Instead of leptons, a quark anti-quark pair can be produced in a two-photon induced process leading to jets inside the detector. The respective Feynman diagram of $\gamma\gamma \to q\bar{q}$, equivalently to $\gamma\gamma \to$ jets can be found in Figure 4.4.
The background from $\gamma\gamma \to$ jets or $\gamma\gamma \to q\bar{q}$ production is estimated using MC simulation based on PYTHIA 8. Four different samples with 2 million events each are generated and used. Direct D and resolved R photons are distinguished in the samples. A direct photon interacts directly to a quark inside the target photon while for a resolved photon, only a virtual excitation of the target photon interacts with the photon. This virtual excitation is at least one $q\bar{q}$ pair and possibly gluons [63]. The resulting samples are labeled as *DD*, *DR*, *RD* and *RR* with a total cross section of 71.12 µb and are listed together with their individual cross section and simulated number of events in Table 4.1.

4.2.4 *Photonuclear Background*

A non-UPC process that contributes as background is the photonuclear process $\gamma A \rightarrow \gamma AX$. In this case, a colourless object called pomeron P is exchanged instead of one photon γ. The pomeron as QCD object has the same quantum number as the vacuum $J^{PC} = 0^{++}$ [64] and can then produce low-activity photonuclear particles as shown in the Feynman diagram in Figure 4.5. Often it is also accompanied by ion dissociation. Events can be categorized according to the configuration of neutron emissions in forward direction as 0n0n, Xn0n and XnXn, where the number of neutrons measured in the Zero Degree Calorimeter (c.f. Section 3.3.2) at either side of the interaction point is counted and "0n" stands for no neutrons, while "Xn" stands for any non-zero number of neutrons measured. In this thesis, only events with 0n0n topology are considered to suppress the photonuclear background.
Studies in Ref. [60] have been performed in order to investigate the impact of the photonuclear processes. The inclusive photonuclear background is simulated using STARLIGHT interfaced with DPMJETIII [65] and is further estimated using a fully data-driven method. The MC-based investigations showed no contribution to the signal selections, the data-driven estimate resulted in very low contributions as discussed in Appendix A.2. For the context of this thesis, the background is thus not included.

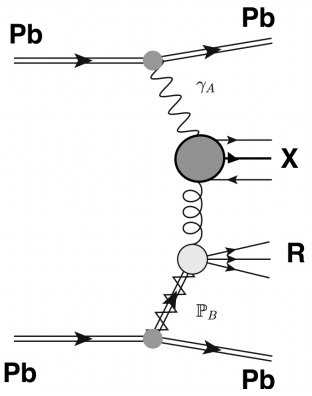

Figure 4.5: Feynman diagram for the photonuclear background process $\gamma A \rightarrow \gamma AX$ where low-activity photonuclear particles are produced in ultraperipheral Pb+Pb collisions. Taken from Ref. [60].

4.3 CORRECTION WEIGHTS APPLIED TO SIMULATED EVENTS

Two characteristics in the simulated event samples of the discussed signal and background processes are addressed using a reweighting technique: the restriction to the 0n0n topology, and the modeling of the photon flux.
The ZDC calorimeter is used in data to veto events with without neutrons in either direction along the beam pipe of the interaction point, in order to suppress the photonuclear background. This 0n0n topology leads to a 30-40 % reduction of the signal and the dominant dilepton backgrounds, where neutrons can be emitted from the Pb constituent as well due to extra soft Coulomb exchanges. The simulated event samples are simulated taking into account the $\gamma\gamma \rightarrow \ell\ell$ production through dissociative - photon emission from the nucleon constituents and thus, all neutron topologies, so the restriction to 0n0n

Process	MC sample name	Cross-section	Number of Events
Signal			
$\gamma\gamma \to \tau\tau$	mc16_5TeV.860059.StarlightPy8_gammagamma2tautau_4M.recon.AOD.e8201_s3469_r11509	263.23 µb	2 M
	mc16_5TeV.420256.Starlight_gammagamma2tautau_breakupMode5_4M.recon. AOD.e7256_s3469_r11509	263.23 µb	1 M
Backgroud			
$\gamma\gamma \to \mu\mu$	mc16_5TeV.860055.StarlightPy8_gammagamma2mumu_breakupMode5_7M20.recon.AOD.e8201_s3469_r11509	76.64 µb	4.1 M
	mc16_5TeV.860054.StarlightPy8_gammagamma2mumu_breakupMode5_20M.recon.AOD.e8201_s3469_r11509	7.12 µb	1.1 M
$\gamma\gamma \to ee$	mc16_5TeV.860057.StarlightPy8_gammagamma2ee_4p5M7.recon.AOD.e8201_s3469_r11509	156.55 µb	4 M
	mc16_5TeV.860058.StarlightPy8_gammagamma2ee_7M15.recon.AOD.e8201_s3469_r11509	121.77 µb	4 M
	mc16_5TeV.860056.StarlightPy8_gammagamma2ee_15Mv1.recon.AOD.e8201_s3469_r11509	17.83 µb	1 M
$\gamma\gamma \to q\bar{q}$	mc16_5TeV.800806.Py8EG_A14_gamgam2jets_DD.recon.AOD.e8312_s3469_r11509	40.2 µb	2 M
	mc16_5TeV.800807.Py8EG_A14_gamgam2jets_DR.recon.AOD.e8312_s3469_r11509	8.41 µb	2 M
	mc16_5TeV.800808.Py8EG_A14_gamgam2jets_RD.recon.AOD.e8312_s3469_r11509	8.41 µb	2 M
	mc16_5TeV.800809.Py8EG_A14_gamgam2jets_RR.recon.AOD.e8312_s3469_r11509	14.1 µb	1.999 M

Table 4.1: List of simulated event samples for the signal and background processes used in the analysis with the respective cross-section, number of events and filter efficiencies.

is implemented as an event weight in the simulation. The photon-photon interaction depends on the invariant mass and the rapidity of the dilepton system. The probability for 0n0n events is extracted from data in terms of invariant mass and the rapidity of the dilepton system and is fitted by an exponential function to smooth statistical fluctuations. This function parametrizes the reduction in signal and dilepton production in the weight denoted as *data_0n0n_flux_weight*. More details on the procedure can be found in Ref. [60] and Ref. [50].
The modeling of the photon flux for the main signal and dilepton background with the MC generator: STARLIGHT 2.0, has been found to not fully describe the production of di-muon events in ATLAS [50]. A better prediction was obtained by the SUPERCHIC 3.0 generator. The main difference between the generators is the respective modeling approach for the photon flux: The STARLIGHT 2.0 generator treats the nucleus as a point-like charge where the photon pair production is ignored within the geometrical radius of the nucleus while SUPERCHIC 3.0 includes the whole geometric radius of the nucleus by taking charge form factor derived from the Woods–Saxon distribution. To improve the photon flux modeling in the STARLIGHT samples, a two-dimensional reweighting procedure is applied. Per-event weights denoted as *sl_to_sc3_flux_weight* parametrize the photon flux modeling effect as a function of the true dilepton invariant mass and absolute rapidity of the dilepton system, and are applied to the STARLIGHT simulated signal and dilepton background samples. More details on the procedure can be found in Ref [60].
The electron and muon trigger, reconstruction, identification efficiencies can be accounted by the introduction of scale factors (SFs). A SF is the ratio $SF = \epsilon_{\text{data}}/\epsilon_{\text{MC}}$ scaling the MC efficiency ϵ_{MC} to correct it to data ϵ_{data}. The SFs are found to have a small impact on the signal and background prediction as discussed in Appendix C and therefore not yet implemented.

5

RECONSTRUCTION AND IDENTIFICATION OF PHYSICS OBJECTS

The reconstruction and identification techniques of physics objects from the ATLAS detector signals are an essential part for the analysis and are described in this chapter. For the analysis of $\gamma\gamma \to \tau\tau$ production, tracks, calorimeter clusters, τ-leptons, electrons, muons and photons are the most important objects. The reconstructed objects are typically required to pass a number of identification criteria together labeled as *working point*, with different efficiency and background rejection levels. Isolation criteria can be applied to reconstructed objects if they are expected to be produced isolated . In Monte Carlo simulation, trigger, reconstruction, identification or isolation efficiencies need to be corrected to data, which is implemented through the application of SFs, measured as efficiency ratios in data over simulation in dedicated pure environments.
In UPC heavy ion collisions, the $\gamma\gamma$-interactions occur in an extremely clean environment. The standard recommendations from the ATLAS collaboration for reconstruction, identification and isolation [66–70] which are reliable requirements for the objects in proton-proton analyses, are not always useful to be applied and can even harm the signal to background ratio. Thus, if necessary, looser requirements than detailed in these standard recommendations are sufficient and applied.
Details on the reconstruction and identification of physics objects measured by the ATLAS experiment are discussed in the following for this analysis, with an overview given at the end of the section.

5.1 TRACK RECONSTRUCTION

Tracks are measured in the ID, specially the PD, the SCT and the TRT and are used to determine the trajectory, the charge and the momentum of charged particles as described in Section 3.3.
Charged particles traversing the ID result in recorded hits on the sensors of the ID [71]. Hits nearby on pixel or strip sensors are grouped into clusters. A preliminary trajectory is then defined by three clusters in different layers of the silicon detector. The *inside-out* iterative tracking algorithm is used to extrapolate the track to the outer silicon detector layer and creates a track candidate. The combinatorial *Kalman filter* [72] adds then successively hits from additional clusters towards the initial interaction point matching the clusters to the track candidate.
Ambiguities of track candidates can emerge as a result of different combinations of the preliminary trajectories and track extensions. These are resolved by rejecting track candidates which fail additional quality criteria such as transverse momentum, pseudorapidity and associated clusters in the pixel detector and SCT.

Hits from the drift-circles around the wires in the TRT are tested for compatibility with the remaining track candidates. For tracks occurring with an insufficient number of hits in the PD, the *inside-out* chain is flipped around to the *ouside-in* chain. In the *outside-in* procedure starting at the TRT, track hits are extrapolated to the inner layers of the ID, and matched if they were not used in the *inside-out* procedure.
Reconstructed tracks are required to pass a set of selection criteria for use in an analysis. For the presented $\gamma\gamma \to \tau\tau$ analysis, the *Loose Primary* track selection [60, 73] is chosen. This requires either more than six silicon hits in the PD and SCT, a maximum of one shared pixel hit or two shared SCT hits and maximally two holes in the SCT and PD together with maximum of on hole in the pixel detector and a χ^2/ndof cut as described in Ref. [74]. Only tracks which have a transverse momentum of $p_\text{T} > 100\,\text{MeV}$, a pseudorapidity of $|\eta| < 2.5$ and a transverse impact parameter of $|d_0| < 1.5\,\text{mm}$ are considered. Tracks with $100\,\text{MeV} > p_\text{T} > 200\,\text{MeV}$ have a reconstruction efficiency between 24 % and 40 %, with $200\,\text{MeV} > p_\text{T} > 500\,\text{MeV}$ between 60 % and 85 % and $p_\text{T} > 500\,\text{MeV}$ up to 93 % [60]. The track reconstruction efficiencies are shown in Appendix B.

5.2 CLUSTER RECONSTRUCTION

Calorimeter clusters are energy deposits in the electromagnetic and hadronic calorimeters and are used in the reconstruction of electrons, photons and jets [75]. The reconstruction of the clusters is described in detail in Ref. [76].
There are two methods for reconstruction of clusters: In the first method, the calorimeters cells are grouped into clusters by the sliding window algorithm for electrons and photons. The second method is preferred used for hadronically decaying τ-leptons and jets and is called topological clustering.
In the sliding window algorithm, towers of the size $\Delta\eta \times \Delta\varphi = 0.025 \times 0.025$ are defined, adding up the longitudinal layers in the ECal in this region. The deposited energy in a tower is summed up. As sliding window, a window with different tower sizes $N_\eta \times N_\phi$, typically 3×5, in $\eta - \phi$ space are defined depending on the hypothesized particle type and the cluster's location in the calorimeter. Due to the magnetic field that curves the trajectory of charged particles, the ϕ direction is typically enlarged for the barrel region. The magnetic field in the endcap region is smaller so that the sizes in η and ϕ are the same. The tower window scans the tower map for local maxima with a minimum transverse energy of $E_\text{T} > 2.5\,\text{GeV}$. The found local maxima are used to reconstruct electrons, photons and jets. The reconstruction efficiency of the clusters is between 65 % and 99 % [77].
The topological clustering is applied in the ECal and HCal. A signal significance of $\zeta_\text{cell} = E_\text{cell}/\sigma_\text{noise}$ is defined for each cell energy using the electronic noise levels of the calorimeters σ_noise. If the signal is four times higher than the noise level $\zeta_\text{cell} > 4$, a seed cell is defined. By adding neighboring cells iteratively, it becomes a proto-cluster where a neighbored cell is added if its signal significance is $\zeta_\text{cell} > 2$ [75]. In order to consider the structure inside a proto-cluster that is caused by the detection of multiple particles, the cells are split by taking the local signal maximum as new seed cell, It must have $E_\text{cell} > 500\,\text{MeV}$ and be surrounded by four neighboring cells with a lower absolute signal significance. After splitting up the proto-clusters as described above, they become topoclusters. Cells that are included in two proto-clusters are called shared cells. These

are weighted according to the energy deposited in the cell compared to the total energy of the cluster and the distance from the cell to the center of the proto-cluster. A four momentum vector is then assigned to each cluster using the cluster direction as the weighted average of the η_{cluster} and ϕ_{cluster}-coordinates of the contributing cells.
For the $\gamma\gamma \to \tau\tau$ analysis, topoclusters are used to suppress background processes within the range of $|\eta| < 4.9$. The topoclusters are required to have a transverse momentum of $p_{\text{T}} > 1.0\,\text{GeV}$ for $|\eta| < 2.5$ and $p_{\text{T}} > 0.1\,\text{GeV}$ for $2.5 < |\eta| < 4.9$. Furthermore, the object quality requirement *TopoSigCut* defined in Ref. [67] needs to be fulfilled. Topoclusters from hotspot regions are removed using the so called *Hotspot Cleaning* described in Ref. [60]. The topocluster object definition is summarized in Table 5.1.

5.3 τ-LEPTON RECONSTRUCTION AND IDENTIFICATION

Approximately 35 % of the τ-leptons decay leptonically into an electron or a muon and two neutrinos. These τ-leptons are reconstructed by using the electron and muon objects as described in Section 5.4 and Section 5.5. The residual 65 % τ-leptons decay hadronically into pions and kaons and a neutrino. The τ-leptons in this analysis have typically a $p_{\text{T}} < 10\,\text{GeV}$ and therefore are low energetic, where the standard ATLAS hadronic τ-lepton reconstruction can not be used. Further details on that and the reconstruction efficiencies are discussed in Appendix B. Instead, hadronically decaying τ-leptons are reconstructed through the number of charged tracks, either one or three, in the event. For the discussion of the track reconstructions, see Section 5.1.

5.4 ELECTRON RECONSTRUCTION AND IDENTIFICATION

Electrons are reconstructed from tracks in the ID, matched to energy deposits in the ECal [77]. The reconstructed clusters in the ECal use the sliding window algorithm (cf. Section 5.2). The effect of the energy loss of electrons through bremsstrahlung is considered by refitting tracks with at least four hits in the silicon detector layer and matched to deposits in the ECal with the Gaussian-sum filter [78]. The energy of the electrons is obtained from the energy deposited in the calorimeter cluster after calibration through a combination of MC-based and data-driven techniques. Energy losses are caused by geometric effects of the detector, the different energy response in the calorimeter layers or energy losses of the electron before interaction with the calorimeter material.
Two categories of electron objects are defined. *Signal* electrons are a subset of the looser *baseline* electrons. Signal electrons are used to select the $\gamma\gamma \to \tau\tau$ signal and the *baseline* electrons to suppress the $\gamma\gamma \to ee$ background.
Baseline electrons are required to have $p_{\text{T}} > 2\,\text{GeV}$ and lie within the pseudorapidity range $|\eta| < 2.47$ excluding the calorimeter transition region $1.37 < |\eta| < 1.52$. Signal electrons have a tighter requirement on p_{T} with $p_{\text{T}} > 4\,\text{GeV}$ within the same pseudorapidity range. Signal electrons are furthermore required to pass additional identification criteria. The working points *Loose*, *Medium* and *Tight* [79] with exhibit decreasing signal efficiency, but increasing purity are defined. In this analysis, the low detector occupancy allows to use the best signal efficiency and thus, the *Loose* working point is chosen. A *Good* object quality [79] is required. The transverse impact parameter d_0 of the electron track is defined as the point of closest approach to the beam spot position in the r-ϕ

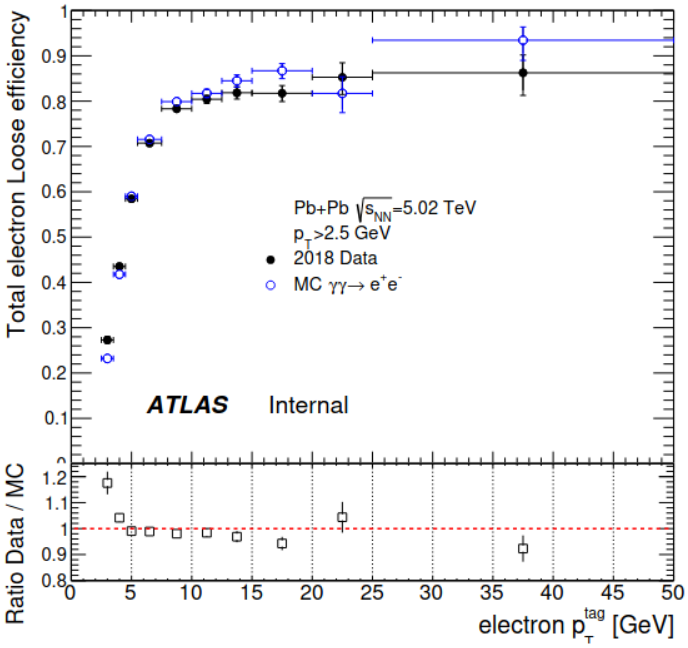

Figure 5.1: Total electron efficiency for the *Loose* working point as a function of electron p_T in $-2.4 < |\eta| < 2.4$. Taken from Ref. [80].

plane. Its significance $|d_0/\sigma(d_0)|$ with $\sigma(d_0)$ being the uncertainty in the measurement of d_0, is required to be smaller than 5. The total electron efficiency has been derived in Ref. [80] and is shown in Figure 5.1. It is calculated to be between 88 % and 98 % for electrons with a p_T between $p_T > 4\,\text{GeV}$ and $p_T < 50\,\text{GeV}$, respectively. The electron object definition is summarized in Table 5.1. The definition of baseline electrons was studied and optimized as part of this thesis (see Section 7.4.1).

5.5 MUON RECONSTRUCTION AND IDENTIFICATION

Muons have a unique experimental signature in the detector since they are the only particles detected by the MS. Muon tracks are visible in the ID, but muons leave only minimal energy deposits in the calorimeter, which in combination allows to distinguish them from jets, electrons and photons. So-called *Combined muons* are obtained by matching the tracks reconstructed in the muons system with the respective ID tracks [81] (cf. Section 5.1).
Hit patterns within muon chambers are used to build track segments that are combined through a fit with input from different layers in the muon system. The fits are first seeded by track segments in the middle layers of the MS, and later extended to also use seeds from the inner and outer layers. The used muon segments must fulfill quality conditions on the number of hits and the fit quality. In the barrel-endcap transition region $1.0 < |\eta| < 1.3$, one track segment with high quality is sufficient to build a track, in other MS regions at least two track segments are needed. An overlap removal algorithm is applied in case a track segment is used in several tracks. Hits related to a MS track candidate are refit using a global χ^2 fit, to obtain the MS muons where the χ^2 satisfies specific selection criteria. For combined muons, the MS muon tracks are

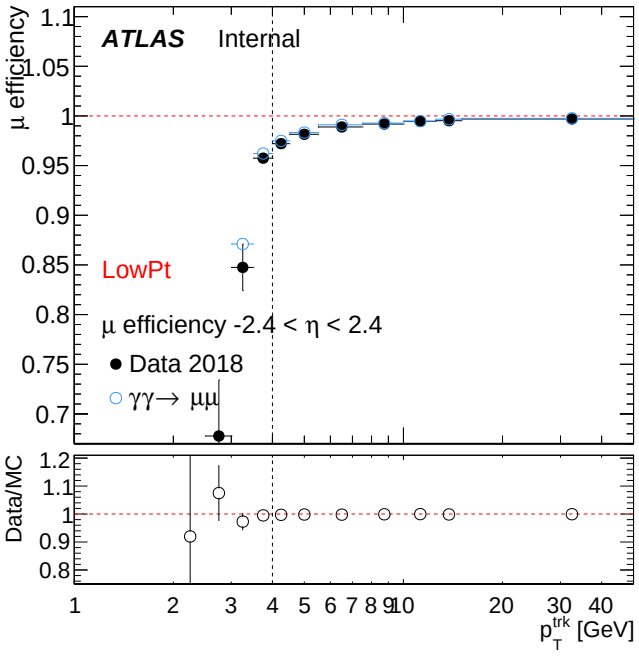

Figure 5.2: Total muon efficiency for the *LowPt* working point as a function of p_T in $-2.4 < |\eta| < 2.4$. The muon efficiency is calculated as the product of the ID and the MS efficiency. Taken from Ref. [60]

extrapolated to the ID (first in an outside-in and then in an inside-out approach) and a global refit with hits from both detectors is performed.
In this thesis, two categories of muons are defined: *Baseline* and *signal* muons, where *signal* muons are a subset of the looser *baseline* muons. The baseline muons are used to suppress the $\gamma\gamma \to \mu\mu$ background and the signal muons to identify events with τ-leptons. Signal muons are required to have $p_T > 4\,\text{GeV}$ and lie within $|\eta| < 2.4$ while the baseline muons only need to fulfill $p_T > 2\,\text{GeV}$ with the same pseudorapidity range requirement. Signal muons are furthermore required to pass additional identification criteria. The working points *Loose*, *Medium* and *Tight* with exhibit decreasing signal efficiency, but increasing purity and *LowPt* and *HighPt* with increasing signal efficiency for muons with the respective p_T [82] are defined. In this analysis, the *LowPt* working point is chosen due to the low p_T of the τ-leptons decaying into muons. The transverse impact parameter significance $|d_0/\sigma(d_0)|$ is required to be smaller than 3. The muon object definition is summarized in Table 5.1. The total efficiency for the muons is measured in Ref. [60] to be $> 97\,\%$ for a muon $p_T > 4\,\text{GeV}$ at the *LowPt* working point as shown in Figure 5.2. The definition of baseline muons was studied and optimized as part of this thesis (see Section 7.4.1).

5.6 PHOTON RECONSTRUCTION AND IDENTIFICATION

Photons [83] are reconstructed similar to the electrons as discussed in Section 5.4. Due to the charge neutrality of photons, they do not leave a track in the ID, but only energy in the calorimeter cells. Therefore, the energy deposits in the ECal that cannot be matched to a track in the ID are identified as a photon.

The photons in this analysis need to have a transverse momentum of $p_T > 1.5\,\text{GeV}$ within the pseudorapidity range of $|\eta| < 2.37$ excluding the calorimeter transition region $1.37 < |\eta| < 1.52$. The identification criteria, object quality and cleaning requirements are taken from the Light-by-Light scattering measurement [80] using neural networks and the information of shower shapes. The reconstructed photons are only used to reduce the $\gamma\gamma \to \mu\mu$ and $\gamma\gamma \to ee$ background using a requirement on the p_T of lepton, track and observed photons in the event. The photon object definition is summarized in Table 5.1.

Property	Signal	Baseline
Muons		
Kinematic	$p_T > 4$ GeV, $\|\eta\| < 2.4$	$p_T > 2$ GeV, $\|\eta\| < 2.5$
Identification	LowPt	—
Impact parameter	$\|d_0/\sigma(d_0)\| < 3$	—
Electrons		
Kinematic	$p_T > 4$ GeV, $\|\eta\| < 2.47$ (excluding $1.37 < \|\eta\| < 1.52$)	$p_T > 2$ GeV, $\|\eta\| < 2.47$ (excluding $1.37 < \|\eta\| < 1.52$)
Identification	Loose	—
Object Quality (OQ)	Good	—
Impact parameter	$\|d_0/\sigma(d_0)\| < 5$	—
Tracks		
Kinematic	$p_T > 100$ MeV, $\|\eta\| < 2.5$	—
Reconstruction	Loose Primary	—
Impact parameter	$\|d_0\| < 1.5$ mm	—
Photons		
Kinematic	$p_T > 1.5$ GeV, $\|\eta\| < 2.37$	—
	(excluding $1.37 < \|\eta\| < 1.52$)	—
Identification	Author, NN_PID	—
Object Quality (OQ) and Cleaning	Good	—
Cleaning	pass OQ quality	—
TopoClusters		
Kinematic	$p_T > 1$ GeV for $\|\eta\| < 2.5$	—
	$p_T > 0.1$ GeV for $2.5 < \|\eta\| < 4.9$	—
Quality	pass TopoSigCut	—
	and pass HotspotCleaning	—

Table 5.1: Summary of reconstruction and identification requirements for different physics objects.

6 STATISTICAL DATA ANALYSIS

This chapter describes the statistical formalism used in this analysis to optimize selections and to determine the expected sensitivity of the anomalous magnetic moment a_τ from $\gamma\gamma \to \tau\tau$ production.
The first part gives an introduction to the figures of merit which are used as a metric for the optimization of the signal selection. In the second part, the likelihood function is introduced which is used for a Log-Likelihood (LL) fit. Two fit options are presented: the normal LL fit and the extended LL fit. In the last part, the inclusion of systematic uncertainties in the LL fits is described.

6.1 FIGURES OF MERIT

Figures of merit are numerical quantities that are used to compare the relative performance of different methods based on statistical measures [84]. Here, figures of merit are used to optimize the selection criteria for the signal selection and the background rejection in different SRs. For that purpose, different figures of merit are studied to consider different aspects of the signal selection such as signal purity and the influence of statistical and systematic uncertainties. The number of selected signal events s, the number of selected background events b and the total number of selected events $n = s + b$ are used to derive the following figures of merit: *Signal-to-noise ratio* (SNR), *Signal purity* and *Signal Significance* with and without systematic uncertainties, respectively.
The SNR gives the level of the signal strength to the level of the background noise and is defined as the ratio of expected signal events s over the expected background events b

$$\text{SNR} = s/b. \tag{6.1}$$

A SNR > 1 corresponds to a dominating signal yield over expected backgrounds in the SR whereas for SNR < 1 the background contribution dominates. Thus, a SNR > 1 is preferred in order to obtain reasonable information about the signal.
The *Signal purity* p gives a measure how clean the SR is. It is calculated as the ratio of the number of selected signal events s and the total number of selected events n

$$p = \frac{s}{n} = \frac{s}{s+b}. \tag{6.2}$$

In the limit of a clean SR, i.e. only signal contribution and no background, it is given as

$$p_{\text{clean}} = \lim_{s \to n} \frac{s}{n} = 1. \tag{6.3}$$

The total number of observed events n in a measurement consists of signal and background events $n = s + b$. The Standard deviation for n is $\sqrt{n}$ for a process following Poisson statistics. In the limit of large n, the Poisson-distributed process can be approxi-

mated by a Gaussian distribution so that $\sqrt{n}$ gives the CI at the 68 % confidence level (CL). The *Signal Significance* Σ is the size of the signal with respect to the uncertainty of the observed events and defined as

$$\Sigma = \frac{s}{\Delta n} = \frac{s}{\sqrt{s+b}}. \tag{6.4}$$

To include also systematic uncertainties into the Signal Significance definition in Equation (6.4) can be extended to

$$\Sigma_{\text{sys}} = s/\sqrt{s+b+(\zeta s)^2+(\zeta b)^2} \tag{6.5}$$

with an arbitrary relative systematic uncertainty ζ. In this thesis, $\zeta = 0.1$ is chosen. Depending on the choice of the requirements for the signal selection, the values of each figure of merit will change. In order to define the best selection criteria, the figures of merit should be maximized.

6.2 THE LIKELIHOOD FUNCTION

The likelihood defines the probability of a certain outcome of an experiment as a function of one or more parameters which the outcome depends on. A likelihood function $L(\boldsymbol{\mu}|n)$ is used to estimate the values of parameters $\boldsymbol{\mu} = (\mu_1, \dots \mu_N)$ given a measured outcome n. The maximum likelihood fit extracts the most probable values for the parameters of interests $\boldsymbol{\mu}$ by maximizing the likelihood function with respect to $\boldsymbol{\mu}$. The statistical background of the likelihood function is described in detail in Ref. [85]. This section gives a brief overview about the likelihood function and its application [86] to the $\gamma\gamma \to \tau\tau$ measurement with the anomalous magnetic moment of the τ-lepton being the parameter of interest $\mu = a_\tau$. The terms defining the likelihood function are introduced including those that consider statistical and systematic uncertainties. The calculation of two different likelihood types: the normal and the extended version, are described. The concept of a negative LL fit to obtain the most probable values for the parameter of interest a_τ and their CI at 68 % and 95 % CL are discussed.

6.2.1 *Likelihood Function for Binned Data*

For a data set in the form of a histogram with N bins, the number of entries in each bin i is given by $\mathbf{n} = (n_1, \dots n_N)$, composed of the signal and background events. The number of expected events $\boldsymbol{\nu} = (\nu_1, \dots \nu_N)$ in bin i can be expressed as

$$\nu_i(a_\tau) = s_i(a_\tau) + b_i \tag{6.6}$$

where the signal events s_i depend on the parameter a_τ and the background events b_i are independent of a_τ. The total number of observed events in data is given by $n_{\text{tot}} = \sum_i^N n_i$ with the number of observed events n_i in the bin i. The expected value in a single bin $\nu_i(a_\tau)$ is given as

$$\nu_i(a_\tau) = n_{\text{tot}} \int_{x_{i,\min}}^{x_{i,\max}} g(x; a_\tau) \mathrm{d}x \tag{6.7}$$

for the observable x with the probability density function $g(x; a_\tau)$. $x_{i,\text{min}}$ and $x_{i,\text{max}}$ are the upper and the lower bin edges, respectively.
The probability to observe n_i events in bin i is given by the Poisson probability

$$P_{\text{Poisson}}(n_i|a_\tau) = \frac{\nu_i(a_\tau)^{n_i}}{n_i!} e^{-\nu_i(a_\tau)}. \tag{6.8}$$

With this, the likelihood function is constructed as

$$L(a_\tau|\mathbf{n}) = \prod_i \frac{\nu_i(a_\tau)^{n_i}}{n_i!} e^{-\nu_i(a_\tau)} \tag{6.9}$$

with n_i, number of observed events in each bin i.
To consider statistical and systematic uncertainties in the maximum likelihood fit, the likelihood function from Equation (6.9) is extended. Systematic uncertainties are accounted for by introducing a Gaussian probability density function for a set of nuisance parameters (NPs) $\boldsymbol{\theta}$ as

$$P_{\text{Gaussian}}(\theta|\hat{\theta}, \sigma_\theta) = \frac{1}{\sqrt{2\pi}\sigma_\theta} \exp\left(-\frac{(\theta - \hat{\theta})^2}{2\sigma_\theta^2}\right) \tag{6.10}$$

with $\hat{\theta}$ being the best estimate for a nuisance parameter θ and σ_θ its standard deviation. The term in Equation (6.10) in the likelihood function penalizes if the fit tries to move the NPs, the source of systematic uncertainties described by θ, too far away from the original estimate. The set of NPs $\boldsymbol{\theta}$ impacts the signal $s_i(a_\tau, \boldsymbol{\theta})$ and the background $b_i(\boldsymbol{\theta})$ contribution in Equation (6.6), i.e., it modifies the number of expected events. The Poisson probability for the likelihood function in Equation (6.9) is thus affected by $\boldsymbol{\theta}$ as

$$P_{\text{Poisson}}(n_i|a_\tau, \boldsymbol{\theta}) = \frac{\nu_i(a_\tau, \boldsymbol{\theta})^{n_i}}{n_i!} e^{-\nu_i(a_\tau, \boldsymbol{\theta})}. \tag{6.11}$$

The systematic uncertainties from the limited statistics in the prediction of the background processes need to be considered differently. This is done by introducing so-called gamma factors γ_i for each bin i:
The number of MC-based background events b_i is the sum of the weighted evens in bin i, $b_i = \sum_{j=1}^{N} w_j$, where w_i are the weights of the events. The statistical uncertainty of b_i is given by the squared sum of the weighted events w_j as $\sigma_i = \sqrt{\sum_{j=1}^{N} w_j^2}$. The relative uncertainty of σ_i is typically larger than one would obtain from Poisson statistics [87]. The expected number of background events in each bin i, b_i, can be redefined as $B_i = (b_i/\sigma_i)^2$ where B_i has the same relative uncertainty as b_i and follows Poisson statistics with the uncertainty $\sqrt{B_i}$. The gamma factor γ_i is the parameter that is estimated to obtain the observed true yield in bin i: $\gamma_i B_i$. This is accounted in the likelihood function by

$$P_\Gamma(B_i|\gamma_i) = \frac{(\gamma_i B_i)^{(B_i)}}{\Gamma(B_i)} e^{-(\gamma_i B_i)} \tag{6.12}$$

with the gamma function $\Gamma(x)$ and the unweighted B_i as the Poisson distribution needs to be generalized since B_i is not cogent an integer [86].

The full likelihood function includes the probability from terms Equation (6.8), Equation (6.12) to include statistical uncertainties on the background simulation and Equation (6.10) to include systematic uncertainties. This results in

$$L(a_\tau, \boldsymbol{\gamma}, \boldsymbol{\theta}, \sigma_\theta | \boldsymbol{n}) = \prod_i P_{\text{Poisson}}(n_i | a_\tau, \boldsymbol{\theta}) \prod_\theta P_{\text{Gaussian}}(\theta | \hat{\theta}, \sigma_\theta) \prod_i P_\Gamma(B_i | \gamma_i). \tag{6.13}$$

The likelihood function can be obtained for different (kinematic) observables x in different signal selections. The information from these different signal selections (SR_1, SR_2, SR_3, etc.) can be joined in a combined likelihood function under the assumption that the signal selections are exclusive so that the likelihood dependencies $\boldsymbol{\gamma}_{\text{SR}_j}$, $\boldsymbol{\theta}_{\text{SR}_j}$, $\sigma_{\theta_{\text{SR}_j}}$ and $\boldsymbol{n}_{\text{SR}_j}$ are signal selection specific where the same systematic uncertainty can be shared by different signal selections. The combined likelihood is given by the product of the single likelihood functions in each signal selection SR_j and can be written as

$$L_{\text{comb}}(a_\tau, \boldsymbol{\gamma}, \boldsymbol{\theta}, \sigma_\theta | \boldsymbol{n}) = \prod_j L_{\text{SR}_j}(a_\tau, \boldsymbol{\gamma}_{\text{SR}_j}, \boldsymbol{\theta}_{\text{SR}_j}, \sigma_{\theta_{\text{SR}_j}} | \boldsymbol{n}_{\text{SR}_j}). \tag{6.14}$$

6.2.2 *Normal Log-Likelihood Function*

The first term in Equation (6.13) considers the number of expected events $\nu_i(a_\tau)$ in each bin which depends on the parameter of interest a_τ. In the normal (log-) likelihood function, $\nu_i(a_\tau)$ encapsulates the information of the shape of a distribution for an observable x for a given value of a_τ. The total number of expected events $\nu_{\text{tot}} = \sum_i \nu_i$ is normalized to data such that

$$n_{\text{tot}} = \nu_{\text{tot}} = \sum_i \nu_i(a_\tau) = n_{\text{tot}} \sum_i f_i(a_\tau) \tag{6.15}$$

with $f_i(a_\tau) = \frac{s_i(a_\tau)+b_i}{\nu_{\text{tot}}}$ and $\sum_i f_i(a_\tau) = 1$. Equation (6.7) becomes

$$\nu_i(a_\tau) = n_{\text{tot}} \cdot f_i(a_\tau) = n_{\text{tot}} \cdot \left(\frac{s_i(a_\tau) + b_i}{\nu_{\text{tot}}} \right). \tag{6.16}$$

The parametrization of the signal prediction $s_i(a_\tau)$ is discussed in detail in Section 9.2. The normal Log-Likelihood (nLL) function is given as the logarithm of Equation (6.9):

$$\log L(a_\tau) = \sum_{i=1}^{N} n_i \log \left(\nu_i(a_\tau) \right) \tag{6.17}$$

which corresponds to the logarithm of a multinomial distribution of a single measurement of a binned histogram. Additive terms of the multinomial distribution independent of a_τ are dropped in the LL function as they only shift $\log L(a_\tau)$ but do not influence the position of the maximum of the function.

6.2.3 *Extended Log-Likelihood Function*

In the extended (log-)likelihood function, the total expected number of events, or the cross section, is considered as a free parameter in the fit, in addition to the shape information as a function of the observable x. As the likelihood function L is a product of independent Poisson factors, Equation (6.17) becomes for the extended likelihood

$$\log L(a_\tau) = \nu_{\text{tot}} + \sum_{i=1}^{N} n_i \log(\nu_i(a_\tau)) \tag{6.18}$$

where total expected number of events $\nu_{\text{tot}}\ (a_\tau) = \sum \nu_i(a_\tau)$ is added as a free parameter. The expected number of events is given in Equation (6.7), whereas the parametrization of the signal is explained in in Section 9.2.

6.2.4 *Negative Log-Likelihood Fits*

The maximum likelihood method [85] uses the likelihood function from Equation (6.13), either the normal or the extended version, to extract the parameter of interest: here a_τ. The best fit value $\hat{a}_\tau$ is obtained by maximizing the likelihood function with respect to a_τ and the NPs γ_i and θ_i. For practical purposes, it is simpler to minimize the negative log-likelihood than to maximize the likelihood, while the results remain identical due to the monotonic behavior of the logarithm.
The uncertainty of the best fit value $\hat{a}_\tau$ is determined with the so-called graphical method as described in Ref. [85]. The Taylor expansion of the logarithmic likelihood as function of a_τ with its best fit value $\hat{a}_\tau$ can be written as:

$$\begin{aligned}\log L\left(a_\tau\right) = \log L\left(\hat{a}_\tau\right) + \left[\frac{\partial \log L\left(a_\tau\right)}{\partial a_\tau}\right]_{a_\tau=\hat{a}_\tau} \left(a_\tau - \hat{a}_\tau\right) \\ + \frac{1}{2}\left[\frac{\partial^2 \log L\left(a_\tau\right)}{\partial^2 a_\tau}\right]_{a_\tau=\hat{a}_\tau} \left(a_\tau - \hat{a}_\tau\right)^2 + \ldots\end{aligned} \tag{6.19}$$

Since the best fit value $\hat{a}_\tau$ maximizes the likelihood function, the second term vanishes in Equation (6.19). Using the variance $\hat{\sigma}^2_{\hat{a}_\tau}$ of $\hat{a}_\tau$ as

$$\hat{\sigma}^2_{\hat{a}_\tau} = -\left[\frac{\partial^2 \log L\left(a_\tau\right)}{\partial^2 a_\tau}\right]^{-1}_{a_\tau=\hat{a}_\tau}, \tag{6.20}$$

Equation (6.19) simplifies to

$$\log L\left(a_\tau\right) = \log L\left(\hat{a}_\tau\right) - \frac{1}{2}\frac{\left(a_\tau - \hat{a}_\tau\right)^2}{\hat{\sigma}^2_{\hat{a}_\tau}}, \tag{6.21}$$

when ignoring higher terms.
For the CIs at 68 % and 95 % CL, Equation (6.21) needs to be evaluated at $a_\tau = \hat{a}_\tau \pm N\hat{\sigma}^{\pm}_{\hat{a}_\tau}$ with $N = 1$ and $N = 1.96$ [85], respectively where the probability function $\Pr(\hat{a}_\tau - N\sigma \leq a_\tau \leq \hat{a}_\tau + N\sigma) = 95\,\%$ is approximated for $N = 1.96 \approx 2$. The CI at 68 % CL is estimated

as the intersection of the negative LL function $-\log L(a_\tau)$ with a straight line at 0.5 above the minimum:

$$-\log L(\hat{a}_\tau \pm 1\sigma) = \log L(\hat{a}_\tau) + 0.5. \tag{6.22}$$

For the determination of the CI at 95 % CL for $\hat{a}_\tau$, the intersection of $\log L(a_\tau)$ with a straight line at $1/2 \cdot (1.96)^2 = 1.92$ above the minimum:

$$-\log L(\hat{a}_\tau \pm 2\sigma) = \log L(\hat{a}_\tau) + 1.92 \tag{6.23}$$

is calculated.

6.3 EXTENDED LIKELIHOOD FITS WITH TREXFITTER

Extended likelihood fits, with and without the inclusion of systematic uncertainties in Equation (6.13), can be performed with the tool TRExFitter [86, 88] including the `ROOSTATS` [89] and the `ROOFIT` [90] packages with `Minuit` [91].
In TRExFitter, the impact of the NPs can be studied with an approach which is called *NP Ranking*. The effect of one single NP on the central value of $\hat{a}_\tau$ is estimated and ranked by the size of the impact on the best-fit value of $\hat{a}_\tau$:
For that, two further fits are performed per NP in addition to the nominal fit: one where the input samples affected by this NP are varied to the $+1\sigma$ prediction and subsequently fixed in the fit, and one where they are varied to the -1σ prediction and refit in the same way. The impact $\Delta a_{\tau\pm\sigma}$ is defined as the difference between $\hat{a}_\tau$ and $\hat{a}_{\tau_{\pm\sigma}}$ of the respective up and down variation $\pm\sigma$:

$$\Delta a_{\tau\pm\sigma} = \hat{a}_{\tau_{\pm\sigma}} - \hat{a}_\tau \tag{6.24}$$

A large $\Delta a_{\tau\pm\sigma}$ for a NP is considered as a large impact on a_τ. This can be evaluated *pre-fit*, i.e. for the $\pm1\sigma$ variations using the size of the variation as determined directly in the analysis, or *post-fit*, using the size of the variation which as been constrained in the nominal fit by the data. A constraint c of a NP θ is defined as

$$c = \frac{\hat{\theta} - \theta_0}{\Delta\theta} \tag{6.25}$$

with the best-fit value $\hat{\theta}$, the nominal input value θ_0 and the input uncertainty $\Delta\theta$, i.e., the $\pm1\sigma$ pre-fit variation of the measurement for the respective NP.

7 MEASUREMENT STRATEGY AND SELECTION OF SIGNAL EVENTS

The full data set recorded with the ATLAS detector consists of many different types of events where according to the production probabilities different particles are produced and according to the ATLAS trigger configuration, different signatures are recorded. In order to filter out the interesting events for an analysis, it is essential to apply an appropriate trigger and event selection. The process of interest in this analysis is the $\gamma\gamma \to \tau\tau$ production in ultaperipheral Pb+Pb collisions with two τ-leptons. The τ-lepton cannot be detected directly so that it needs to be reconstructed by its decay products. Background processes with the same final state particles need to be removed in the selection. The final state signatures of two decaying τ-leptons contain one electron or one muon and tracks(s) or another electron or muon. These can be mimicked by the processes of $\gamma\gamma \to ee$ and $\gamma\gamma \to \mu\mu$.
In this chapter, the measurement strategy is described in Section 7.1. The trigger requirements and the selections used in the $\gamma\gamma \to \tau\tau$ analysis are motivated in Section 7.2. Several signal regions with different leptonic and hadronic τ-lepton decays are considered and defined in Section 7.3. Section 7.4 discusses the various optimizations of the signal selections for five final states. Background control regions are introduced in Section 7.5 for the major backgrounds.

7.1 MEASUREMENT STRATEGY

The analysis is performed with a data set of Pb+Pb collisions at a center-of-mass energy $\sqrt{s} = 5.02\,\text{TeV}$ corresponding to an integrated luminosity of $1.44\,\text{nb}^{-1}$ recorded by the ATLAS detector in Run 2 in 2018. Monte Carlo simulation, described in Chapter 4, is used to model the SM as well as the prediction for different anomalous moments of a_τ for the signal process $\gamma\gamma \to \tau\tau$ and the main contribution background processes: $\gamma\gamma \to \mu\mu$, $\gamma\gamma \to ee$ and $\gamma\gamma \to q\bar{q}$ or rather $\gamma\gamma \to$ jets. The cross-section of the signal process $\gamma\gamma \to \tau\tau$ is blinded within $\pm 10\,\%$[1].
High quality candidate events for $\gamma\gamma \to \tau\tau$ are selected by applying selection criteria to improve the signal significance for SM $\gamma\gamma \to \tau\tau$ production and the signal-to-background ratio. The production cross section of $\gamma\gamma \to \tau\tau$ is sensitive to the value for a_τ, so a good significance for $\gamma\gamma \to \tau\tau$ also enhances the sensitivity to a_τ which is the focus of this analysis. Signal candidates are divided into five groups called *Signal Regions (SRs)* based on the possible τ-lepton decay products. A trigger is set on at least one electron or one muon. Additionally, either one or three tracks or another light, different flavor lepton is required in order to supress contributions from $\gamma\gamma \to ee$ and $\gamma\gamma \to \mu\mu$ background suppression. The number of tracks represent the hadronically

1 The production cross section of $\gamma\gamma \to \tau\tau$ is given by 263.234 17 µb which is blinded and within $\pm 10\,\%$ of the true production cross section.

decaying τ-leptons in a 1- or 3-prong decay, respectively. The fifth *Signal Region (SR)* is based on only two leptons with different flavor: one signal muon and one signal electron. Events, where both τ-leptons decay hadronically are are not considered due to the lack of an appropriate trigger and high expected background contribution. The five SRs have the following final states and names:

- one muon and one track (SR-1M1T) for $\tau\tau \to \tau_\mu \tau_{\text{had,1-prong}}$
- one muon and three tracks (SR-1M3T) for $\tau\tau \to \tau_\mu \tau_{\text{had,3-prong}}$
- one electron and one track (SR-1E1T) for $\tau\tau \to \tau_e \tau_{\text{had,1-prong}}$
- one electron and three tracks (SR-1E3T) for $\tau\tau \to \tau_e \tau_{\text{had,3-prong}}$
- one muon and one electron (SR-1M1E) for $\tau\tau \to \tau_\mu \tau_e$.

The SRs are optimized based on the metrics s/b, $s/\sqrt{b}$ and $s/\sqrt{s+b}$ as well as $s/\sqrt{s+b+(\zeta s)^2+(\zeta b)^2}$ with an included uncertainty on signal s and background b event yields of $\zeta = 10\%$ by maximizing those as described in Section 6.1.
The value of a_τ effects the cross-section of $\gamma\gamma \to \tau\tau$ production and the shape of several kinematic observables. The sensitivity of different observables is investigated, using a_τ values within -0.1 and 0.1.
Binned maximum likelihood fits to several kinematic distributions as well as for the overall number of events in each SR are performed to extract the expected best fit value for a_τ and its CI on 68 % and 95 % CL. Instead of real data, an Pseudo data set is used for the fit. It is constructed by simulated events for the SM signal and the contributing background prediction. An extended (eLL) and a normal loglikelihood (nLL) fit (cf. Section 6.2.2 and Section 6.2.3) are performed. In the eLL fit, the cross-section and the shape information is used where the nLL applies only the changes in the shape. Therefore, a higher sensitivity for the eLL fit is expected. The expected length of the CI is additionally used as a figure of merit in the procedure of the SR optimization.
Two tools are used to compute the confidence intervals for a_τ using both fit methods: a `Python-based` self-written software the TRExFitter software [88]. Different studies are performed with the two software setups, and agreement for the overlapping configurations has been carefully checked. The `Python-based` software is used to study the effect of the inclusion of the background prediction to fit and statistical uncertainties. The TRExFitter software is used to study the impact of systematic uncertainties, including statistical uncertainties in the background predictions obtained from simulation. Combined fits of the different SRs are performed with either setup. A combined fit, including the control region for the $\gamma\gamma \to \mu\mu$ background allows to constrain systematic uncertainties and is performed with the TRExFitter setup only.
The aim of this thesis is to define an optimized definition of exclusive SRs and an optimized fit strategy to obtain the best expected sensitivity to the anomalous magnetic moment a_τ of the τ-lepton.

7.2 TRIGGER REQUIREMENTS

Heavy ion bunches cross inside the ATLAS detector at a rate of up to 40 MHz [51]. The ATLAS trigger system is used to reduce to the large amount of data in real time (online) to filter for the most relevant and interesting events. The triggers used in this analysis rely on the presence of a low p_T muon or a low p_T τ-lepton object which leaves energy in the electromagnetic calorimeter, similar to an electron. The triggers furthermore set a limit on the presence of large overall transverse energies, considering that UPC events are typically very clean events with little activity except the hard process from diphoton interaction. The exact triggers used in this analysis are as follows:

- `HLT_mu4_hi_upc_FgapAC3_L1MU4_VTE50`
  At L1 stage, the trigger is passed if a muon with $p_T > 4\,\text{GeV}$ (`L1MU4`) is detected. A veto on large transverse energies E_T is applied, i.e. $E_T < 50\,\text{GeV}$ (`VTE50`) is required. With the HLT, an additional requirement is set for ultraperipheral heavy ion `hi_upc` collisions on the missing transverse energy in the FCal to be consistent with the noise [52]. The sum of the missing transverse energy in the FCal on both A and C sides individually needs to be $\sum E_T^{\text{FCal(A,C)}} < 3\,\text{GeV}$ (`FgapAC3`). This trigger is used for all muon based SRs listed in Section 7.3.

- `HLT_hi_upc_FgapAC3_hi_gg_upc_L1TAU1_TE4_VTE200`
  In L1 stage, the trigger is passed if a hadronic τ-lepton [92] with $p_T > 1\,\text{GeV}$ (`L1TAU1`) is detected and $E_T > 4\,\text{GeV}$ (`TE4`). A veto on large transverse energies E_T is applied, i.e. $E_T < 200\,\text{GeV}$ (`VTE200`) is required. The HLT was originally designed to target $\gamma\gamma \to \gamma\gamma$ production (`gg`). An additional requirement is set for ultraperipheral heavy ion (`hi_upc`) collisions on the missing transverse energy in the FCal to be consistent with then noise. The sum of the missing transverse energy in the FCal on both A and C sides individually needs to be $\sum E_T^{\text{FCal(A,C)}} < 3\,\text{GeV}$ (`FgapAC3`). This trigger is used for electron based SRs with one additional track required listed in Section 7.3.

- `HLT_hi_upc_FgapAC3_mb_sptrk_exclusiveloose2_L12TAU1_VTE50` In L1 stage, the trigger is passed if two hadronic τ-leptons [92] with $p_T > 1\,\text{GeV}$ (`L12TAU1`) are measured. A veto on large transverse energies E_T is applied, i.e. $E_T < 50\,\text{GeV}$ (`VTE50`) is required. This trigger is designed to target $\gamma\gamma \to ee$ production - see e.g. here where this is listed in the excel file for Run 3 under https://its.cern.ch/jira/browse/ATR-22067. Additional requirements are set in the HLT for ultraperipheral heavy ion (`hi_upc`) collisions on the missing transverse energy in the FCal to be consistent with then noise. The sum of the missing transverse energy in the FCal on both A and C sides individually needs to be $\sum E_T^{\text{FCal(A,C)}} < 3\,\text{GeV}$ (`FgapAC3`). The minimum bias (`mb`) trigger requires a space point and at least one track (`sptrk`) with $p_T \leq 200\,\text{MeV}$ and $|z_0| < 400\,\text{mm}$. Furthermore, more than two tracks with $p_T > 1\,\text{GeV}$ are required (`exclusiveloose2`) [93]. This trigger is used for the electron SRs requiring three additional tracks listed in Section 7.3.

7.3 SIGNAL SELECTION

The aim of the signal selection is to reject as many background events as possible while keeping the interesting signal events. A preselection of events is performed in order to ensure data quality. The data are split into five signal regions targeting different final states of the decayed τ-leptons. Kinematic requirements that distinguish properties of signal and background events are optimized to improve the signal purity. A number of these kinematic requirements have been studied in the context of this thesis and will be discussed in more detail in Section 7.4.

Events in data are required to pass the so-called *Good Run List (GRL)* that ensures that only events from data taking periods where the ATLAS detector was fully operational are included. To suppress events where the lead ions are broken up in the interaction and forward neutrons might be emitted, such as photo-nuclear background events, the allowed deposited energy in the ZDC calorimeter on the A and C side of the ATLAS detector is limited to $E_{\mathrm{ZDC}}^{A/C} < 1\,\mathrm{TeV}$. Since the ZDC is not simulated in MC, the affect of the ZDC requirement on signal and background simulation is considered through weights obtained in a data-driven way from $\gamma\gamma \to \mu\mu$ events [60] which is further explained in Section 4.3.

The five SRs introduced in Section 7.1 are chosen to be orthogonal. For that, requirements are set on the number of signal muons, signal electrons, baseline muons and the number of tracks outside a cone with $\Delta R = 0.1$ around the respective signal lepton. The object definition for signal and baseline leptons and the tracks used is given in Table 5.1. The choice of the number of leptons and tracks depends on the categorization in the SRs and is summarized in Table 7.1. For the SR-1M1E, SR-1E1T and SR-1E3T, no requirement is set on the baseline muons which denoted by $-$. The baseline electrons are currently not used at all but could be, if necessary, introduced for improvement of the background suppression in the electron based SRs. Studies on this are discussed in Section 7.4.1.

The signal selection is described in following for the five categories. The additionl kinematic requirements on the signal selection applied for further background suppression are listed for each SR individually and then summarized in Table 7.8. The motivation for the respective requirement is described in Section 7.4. Finally, the SRs are compared based on the resulting event yields for data, signal and background prediction and the signal significance summarized in Table 7.7.

Number of	1M1T	1M1E	1E1T	1M3T	1E3T
Signal muons	1	1	0	1	0
Signal electrons	0	1	1	0	1
Baseline muons	1	–	–	1	–
Baseline electrons	–	–	–	–	–
N_{trks} ($\Delta R > 0.1$ from signal μ/e)	1	0	1	3	3

Table 7.1: Exclusive definition of the SRs using the number of signal leptons, number of baseline muons and the number of tracks not matched to the signal leptons. If no requirement is set on the number of the physical objects, it is denoted by $-$.

SR-1M1T-excl

In the SR-1M1T-excl, one of the two τ-leptons from the $\gamma\gamma \to \tau\tau$ interaction decays leptonically into one muon and two neutrinos and the other τ-lepton via the 1-prong hadronic decay mode into one charged pion, one neutrino and a number of neutral pions, which is observed as a single track. The presence of another baseline muon is vetoed. For further background reduction of $\gamma\gamma \to \mu\mu$ production, the looser baseline muon definition is used in the additional muon veto. The $\gamma\gamma \to ee$ background is suppressed by requiring the number of signal electrons to be zero. Furthermore, events with clusters that are not matched to any of the reconstructed particles are rejected. Since one τ-lepton is positively and the other one negatively charged, the sum of the charge of the decay products needs to be zero, or in other words, the charge of the track Q_{trks} needs to be the opposite charge of the muon Q_μ as $Q_{\text{trk}} = -Q_\mu$ due to charge conservation. For further $\gamma\gamma \to \mu\mu$ background suppression, the p_{T} requirement on the muon and track system of $p_{\text{T}}^{\mu,\text{trk}} = |\vec{p}_{\text{T}}^{\,\mu} + \vec{p}_{\text{T}}^{\,\text{trk}}| > 1\,\text{GeV}$ is applied. If additional photons or matched topoclusters are present in the event, the leading photon, and respectively the leading topocluster are included to the muon and track system, and the p_{T} requirement is extended to the system to $p_{\text{T}}^{\text{system}} = |\vec{p}_{\text{T}}^{\,\mu} + \vec{p}_{\text{T}}^{\,\text{trk}} + \vec{p}_{\text{T}}^{\,\gamma/\text{cluster}}| > 1\,\text{GeV}$. The photonuclear background is suppresses by an acoplanarity requirement of $A_\phi^{\ell,\text{trk(s)}} < 0.4$.
Table 7.2 shows the event yield of the data and MC samples after applying each requirement subsequently. The signal significance given in the last column increases from 5.1 after the preselection requirement to 20.1. This SR is characterized by its high statistics for the signal yield of 455.5 events with a high signal purity of 88.7 %. The agreement between signal and background prediction of 513.4 and the observed data events 485.0 is good considering the blinded cross-section of the $\gamma\gamma \to \tau\tau$ process by ± 10 %.

Requirement	Data 18	$\gamma\gamma \to \tau\tau$ 4M	$\gamma\gamma \to \mu\mu$ 7M20	$\gamma\gamma \to \mu\mu$ 20M	$\gamma\gamma \to ee$ 4p5M7	$\gamma\gamma \to ee$ 7M15	$\gamma\gamma \to ee$ 15Mv1	$\gamma\gamma \to$ jets DD	$\gamma\gamma \to$ jets DR	$\gamma\gamma \to$ jets RD	$\gamma\gamma \to$ jets RR	$\text{sig}/\sqrt{\text{sig+bkg}}$
pass GRL	4335070.0	23615.5	89052.9	7554.2	177294.7	135156.7	19274.8	35981.6	7677.2	7677.2	12524.5	32.9
$E_{\text{ZDC}}^{A,C} < 1$ TeV	1435464.0	23615.5	89052.9	7554.2	177294.7	135156.7	19274.8	35981.6	7677.2	7677.2	12524.5	32.9
HLT mu4 trigger	60313.0	1214.5	48651.8	6142.1	0.0	0.1	0.3	36.0	5.7	6.1	9.5	5.1
$N_\mu^{\text{baseline}} = 1$	13806.0	1113.8	5976.3	1263.1	0.0	0.1	0.2	34.1	5.5	5.8	9.1	12.1
$N_\mu^{\text{sig}} = 1$	10641.0	906.1	4729.3	1177.2	0.0	0.1	0.2	21.8	3.3	3.6	5.7	10.9
$N_e^{\text{sig}} = 0$	10575.0	874.2	4726.6	1176.1	0.0	0.0	0.0	21.6	3.2	3.6	5.7	10.6
$N_{\text{trk}}(\Delta R > 0.1 \text{ from } \mu) = 1$	1790.0	569.7	761.6	39.8	0.0	0.0	0.0	0.5	0.0	0.0	0.0	15.4
Veto unmatched clusters	1320.0	560.9	714.4	33.2	0.0	0.0	0.0	0.3	0.0	0.0	0.0	15.5
$\sum$ charge $= 0$	1304.0	553.8	712.0	32.0	0.0	0.0	0.0	0.2	0.0	0.0	0.0	15.4
$p_{\text{T}}^{(\mu,\text{trk})} > 1$ GeV	688.0	518.4	204.6	15.7	0.0	0.0	0.0	0.2	0.0	0.0	0.0	19.1
$p_{\text{T}}^{(\mu,\text{trk},\gamma)} > 1$ GeV	577.0	496.0	100.4	7.0	0.0	0.0	0.0	0.2	0.0	0.0	0.0	20.2
$p_{\text{T}}^{(\mu,\text{trk,cluster})} > 1$ GeV	501.0	457.3	54.8	4.5	0.0	0.0	0.0	0.1	0.0	0.0	0.0	20.1
$A_\phi^{\mu,\text{trk}} < 0.4$	485.0	455.5	54.0	3.8	0.0	0.0	0.0	0.1	0.0	0.0	0.0	20.1

Table 7.2: Overview of the event counts after the selection requirements for SR-1M1T-excl applied sequentially. Simulated samples are normalized to $\mathcal{L} = 1.44\ \text{fb}^{-1}$.

SR-1M3T-excl

The SR-1M13-excl covers the τ decays from $\gamma\gamma \to \tau\tau$ production where one τ-lepton decays leptonically into a muon and two neutrinos and the other τ-lepton via the 3-prong hadronic decay mode into three charged pions, one neutrino and a number of neutral

pions, which is observed by three tracks in the detector. The presence of additional baseline muons or signal electrons is vetoed, similar as in SR-1M1T. Furthermore, events with topoclusters that are not matched to any of the reconstructed particles, the muon and the three tracks, are rejected. The sum of the charge of three tracks Q_{trks} needs to be the opposite charge of the muon Q_μ as $Q_{\text{trks}} = -Q_\mu$ due to charge conservation. The hadronic background from $\gamma\gamma \to$ jets production is suppressed by requiring the limit on the invariant mass of the three tracks to be $m_{\text{trks}} < 1.7\,\text{GeV}$ and the acoplanarity between the muon and the track system $A_\phi^{\mu,\text{trks}} < 0.4$.
Table 7.3 shows the event yield of the data and MC samples after applying each requirement subsequently. The SR-1M3T is very clean with only 5.7 expected background events but 92.7 signal events. The total number of expected events 98.4 is higher by around 20 % than the 78 observed events. The statistical uncertainties in the data for the measured events is around 10 %. The numbers of data and expected events could be in reasonable agreement including after unblinding of the cross section of $\gamma\gamma \to \tau\tau$ production. Despite the high signal purity of 94.2 %, the signal significance is smaller with 9.3 smaller than for the SR-1M1T-excl due to the lower expected statistics.

Requirement	Data 18	$\gamma\gamma \to \tau\tau$ 4M	$\gamma\gamma \to \mu\mu$ 7M20	$\gamma\gamma \to \mu\mu$ 20M	$\gamma\gamma \to ee$ 4p5M7	$\gamma\gamma \to ee$ 7M15	$\gamma\gamma \to ee$ 15Mv1	$\gamma\gamma \to$ jets DD	$\gamma\gamma \to$ jets DR	$\gamma\gamma \to$ jets RD	$\gamma\gamma \to$ jets RR	$\text{sig}/\sqrt{\text{sig+bkg}}$
pass GRL	4335070.0	23615.5	89052.9	7554.2	177294.7	135156.7	19274.8	35981.6	7677.2	7677.2	12524.5	32.9
$E_{\text{ZDC}}^{A,C} < 1$ TeV	1435464.0	23615.5	89052.9	7554.2	177294.7	135156.7	19274.8	35981.6	7677.2	7677.2	12524.5	32.9
HLT mu4 trigger	60313.0	1214.5	48651.8	6142.1	0.0	0.1	0.3	36.0	5.7	6.1	9.5	5.1
$N_\mu^{\text{baseline}} = 1$	13806.0	1113.8	5976.3	1263.1	0.0	0.1	0.2	34.1	5.5	5.8	9.1	12.1
$N_\mu^{\text{sig}} = 1$	10641.0	906.1	4729.3	1177.2	0.0	0.1	0.2	21.8	3.3	3.6	5.7	10.9
$N_e^{\text{sig}} = 0$	10575.0	874.2	4726.6	1176.1	0.0	0.0	0.0	21.6	3.2	3.6	5.7	10.6
$N_{\text{trk}}(\Delta R > 0.1 \text{ from } \mu) = 3$	310.0	95.8	7.1	0.7	0.0	0.0	0.0	1.8	0.1	0.1	0.2	9.3
Veto unmatched clusters	135.0	94.7	7.1	0.7	0.0	0.0	0.0	1.5	0.1	0.1	0.1	9.3
$\sum$ charge $= 0$	121.0	93.4	7.0	0.7	0.0	0.0	0.0	1.2	0.0	0.1	0.0	9.2
$m_{\text{trks}} < 1.7$ GeV	78.0	92.8	5.0	0.4	0.0	0.0	0.0	0.4	0.0	0.0	0.0	9.3
$A_\phi^{\mu,\text{trks}} < 0.4$	78.0	92.7	5.0	0.4	0.0	0.0	0.0	0.3	0.0	0.0	0.0	9.3

Table 7.3: Overview of the event counts after the selection requirements for SR-1M3T-excl applied sequentially. Simulated samples are normalized to $\mathcal{L} = 1.44\,\text{fb}^{-1}$.

SR-1E1T-excl

The electron based SR-1E1T contains the events where one τ-lepton decays leptonically into an electron, neutrinos and the other τ-lepton via the 1-prong hadronic decay mode into one charged pions, one neutrino and a number of neutral pions, which is observed as single track. The presence of another signal electron is vetoed. The $\gamma\gamma \to \mu\mu$ background is suppressed by requiring the number of signal muons to be zero. Furthermore, events with clusters that are not matched to any of the reconstructed particles, i.e. to the electron or the track, are rejected. The charge of the track Q_{trk} needs to be the opposite charge of the muon Q_e as $Q_{\text{trk}} = -Q_e$ due to charge conservation. Additional background suppression of $\gamma\gamma \to ee$ production is achieved through the p_{T} requirement on the electron and track system where $p_{\text{T}}^{e,\text{trk}} = |\vec{p}_{\text{T}}^{\,e} + \vec{p}_{\text{T}}^{\,\text{trk}}| > 1\,\text{GeV}$ is applied. If additional photons or matched topoclusters are present in the event, the leading photon, and respectively the leading topocluster are included to the electron and track system, and the p_{T} requirement is extended to the system to $p_{\text{T}}^{\text{system}} = |\vec{p}_{\text{T}}^{\,e} + \vec{p}_{\text{T}}^{\,\text{trk}} + \vec{p}_{\text{T}}^{\,\gamma/\text{cluster}}| > 1\,\text{GeV}$.
Table 7.4 shows the event yield of the observed data and the yield predicted from

simulated event samples after applying each requirement subsequently. The SR-1E1T is more dominated by background events - 321.4 events from background predictions vs. 293.9 events from signal predictions. The total number of expected events, 615.3, is higher than for any other signal region, partially compensating for the large background contribution in terms of signal sensitivity. The signal significance is with 11.8 still better than for SRs, SR-1M3T-excl and SR-1M1E-excl, where the signal purity is significantly better, at the cost of lower statistics. The difference between data and prediction is about 11 % resulting in a reasonable agreement considering the blinded cross-section of the $\gamma\gamma \to \tau\tau$ process by ± 10 %.

Requirement	Data 18	$\gamma\gamma \to \tau\tau$ 4M	$\gamma\gamma \to \mu\mu$ 7M20	$\gamma\gamma \to \mu\mu$ 20M	$\gamma\gamma \to ee$ 4p5M7	$\gamma\gamma \to ee$ 7M15	$\gamma\gamma \to ee$ 15Mv1	$\gamma\gamma \to$ jets DD	$\gamma\gamma \to$ jets DR	$\gamma\gamma \to$ jets RD	$\gamma\gamma \to$ jets RR	sig/$\sqrt{\text{sig+bkg}}$
pass GRL	4335070.0	23615.5	89052.9	7554.2	177294.7	135156.7	19274.8	35981.6	7677.2	7677.2	12524.5	32.9
$E_{\text{ZDC}}^{A,C} < 1$ TeV	1435464.0	23615.5	89052.9	7554.2	177294.7	135156.7	19274.8	35981.6	7677.2	7677.2	12524.5	32.9
HLT hi gg L1TAU1	1094198.0	3294.2	11561.0	1154.7	25735.0	52791.1	12072.2	155.7	5.2	5.4	6.4	10.1
$N_e^{\text{sig}} = 1$	26007.0	589.0	2.9	2.8	321.6	16873.4	4656.3	0.8	0.0	0.1	0.0	3.9
$N_\mu^{\text{sig}} = 0$	25972.0	557.1	0.5	0.2	321.6	16873.4	4656.2	0.8	0.0	0.1	0.0	3.7
$N_{\text{trk}}(\Delta R > 0.1 \text{ from } e) = 1$	16476.0	428.0	0.2	0.1	284.5	12673.6	2806.5	0.2	0.0	0.0	0.0	3.4
Cluster veto	15774.0	421.0	0.2	0.1	284.3	12586.7	2743.3	0.1	0.0	0.0	0.0	3.3
$\sum$ charge $= 0$	15690.0	419.6	0.2	0.1	284.1	12544.6	2710.3	0.1	0.0	0.0	0.0	3.3
$p_{\text{T}}^{(e,\text{trk})} > 1$ GeV	10204.0	388.9	0.1	0.1	221.2	7998.9	2096.8	0.1	0.0	0.0	0.0	3.8
$p_{\text{T}}^{(e,\text{trk},\gamma)} > 1$ GeV	8349.0	370.6	0.1	0.1	200.4	6335.4	1685.1	0.1	0.0	0.0	0.0	4.0
$p_{\text{T}}^{(e,\text{trk,cluster})} > 1$ GeV	7056.0	339.3	0.1	0.1	172.4	5280.7	1366.9	0.1	0.0	0.0	0.0	4.0
$A_\phi^{e,\text{trk}} > 0.012$	548.0	293.9	0.1	0.0	3.2	235.1	82.9	0.1	0.0	0.0	0.0	11.8

Table 7.4: Overview of the event counts after the selection requirements for SR-1E1T-excl applied sequentially. Simulated samples are normalized to $\mathcal{L} = 1.44$ fb^{-1}.

SR-1E3T-excl

The electron based SR-1E3T contains the events where one τ-lepton decays leptonically into an electron and two neutrinos and the other τ-lepton via the 3-prong hadronic decay mode into three charged pions, one neutrino and a number of neutral pions, which is observed by three tracks. The presence of another electron is vetoed. The $\gamma\gamma \to \mu\mu$ background is suppressed by requiring the number of signal muons to be zero. Furthermore, events with clusters that are not matched to any of the reconstructed particles, i.e. the electron and the three tracks, are rejected. The sum of the charge of three tracks Q_{trks} needs to be the opposite charge of the electron Q_e as $Q_{\text{trks}} = -Q_e$ due to charge conservation. Additional background suppression of $\gamma\gamma \to ee$ is achieved by requirements on the invariant mass of the three track system as $0.5\,\text{GeV} < m_{\text{trks}} < 1.7\,\text{GeV}$ which is motivated by Figure 7.8 in Section 7.4.5.
Table 7.5 shows the event yield of the data and MC samples after applying each requirement subsequently. The SR-1E3T has a significant background contribution with 51.3 background events compared to the 94.4 expected signal events. The signal purity of 65.3 % is higher than for SR-1E1T. The total number of expected events is with 147.7 events almost three times higher than the number of observed events with 52 events. The prediction clearly overestimates the data. The reason remains to be further investigated. The signal significance results then into 7.9 as shown in the last column of the table.

Requirement	Data 18	$\gamma\gamma \to \tau\tau$ 4M	$\gamma\gamma \to \mu\mu$ 7M20	$\gamma\gamma \to \mu\mu$ 20M	$\gamma\gamma \to ee$ 4p5M7	$\gamma\gamma \to ee$ 7M15	$\gamma\gamma \to ee$ 15Mv1	$\gamma\gamma \to$ jets DD	$\gamma\gamma \to$ jets DR	$\gamma\gamma \to$ jets RD	$\gamma\gamma \to$ jets RR	sig/$\sqrt{\text{sig+bkg}}$
pass GRL	4335070.0	23615.5	88094.6	7380.6	177294.7	135156.7	19274.8	35981.6	7677.2	7677.2	12524.5	32.9
$E_{\text{ZDC}}^{A,C} < 1$ TeV	1435464.0	23615.5	88094.6	7380.6	177294.7	135156.7	19274.8	35981.6	7677.2	7677.2	12524.5	32.9
HLT hi upc L12TAU1	192906.0	10652.2	47378.8	3546.3	95296.6	88813.9	14651.0	19309.4	4031.1	4030.8	6143.0	19.7
$N_e^{\text{sig}} = 1$	23133.0	792.5	2.8	2.8	534.2	20455.3	4866.7	51.8	7.7	7.5	12.2	4.8
$N_\mu^{\text{sig}} = 0$	23130.0	753.8	0.5	0.2	534.2	20455.3	4866.5	51.6	7.7	7.5	12.2	4.6
$N_{\text{trk}}(\Delta R > 0.1 \text{ from } e) = 3$	302.0	103.0	0.0	0.0	0.3	64.9	42.2	4.7	0.4	0.3	0.4	7.0
Cluster veto	203.0	101.6	0.0	0.0	0.3	64.6	41.5	3.8	0.2	0.2	0.2	7.0
$\sum$ charge $= 0$	183.0	99.7	0.0	0.0	0.3	62.4	39.0	2.5	0.1	0.1	0.1	7.0
$m_{\text{trks}} < 1.7$ GeV	73.0	96.8	0.0	0.0	0.3	58.4	35.3	0.7	0.0	0.0	0.0	7.0
$m_{\text{trks}} > 0.5$ GeV	52.0	96.4	0.0	0.0	0.1	32.0	18.5	0.7	0.0	0.0	0.0	7.9

Table 7.5: Overview of the event counts after the selection requirements for SR-1E3T-excl applied sequentially. Simulated samples are normalized to $\mathcal{L} = 1.44$ fb^{-1}.

SR-1M1E-excl

The fully leptonic SR with one τ-lepton decaying into a muon and the other τ-lepton into an electron, together with two neutrinos in both cases, uses the same muon trigger as the muon-based regions. In accordance with the targeted decay mode, exactly one signal muon and one signal electron are required. No additional tracks, apart from those assigned to the leptons are allowed. The charge of the muon Q_μ needs to be the opposite charge of the electron Q_e as $Q_\mu = -Q_e$ due to charge conservation.
Table 7.6 shows the event yield of the data and MC samples after applying each requirement subsequently. The SR-1M1E is very clean with only 2.9 expected background events and 39.6 signal events. The total number of expected events 42.5 is in agreement to the 42 measured events. The signal significance is with 6.1 the lowest among the signal regions, despite of the clean signature, as a result of the low statistics in this region.

Requirement	Data 18	$\gamma\gamma \to \tau\tau$ 4M	$\gamma\gamma \to \mu\mu$ 7M20	$\gamma\gamma \to \mu\mu$ 20M	$\gamma\gamma \to ee$ 4p5M7	$\gamma\gamma \to ee$ 7M15	$\gamma\gamma \to ee$ 15Mv1	$\gamma\gamma \to$ jets DD	$\gamma\gamma \to$ jets DR	$\gamma\gamma \to$ jets RD	$\gamma\gamma \to$ jets RR	sig/$\sqrt{\text{sig+bkg}}$
pass GRL	4335070.0	23615.5	89052.9	7554.2	177294.7	135156.7	19274.8	35981.6	7677.2	7677.2	12524.5	32.9
$E_{\text{ZDC}}^{A,C} < 1$ TeV	1435464.0	23615.5	89052.9	7554.2	177294.7	135156.7	19274.8	35981.6	7677.2	7677.2	12524.5	32.9
HLT mu4 trigger HLT hi gg L1TAU1	1153927.0	4283.1	53253.4	6286.0	25735.0	52791.2	12072.4	191.5	10.9	11.4	15.9	10.9
$N_\mu^{\text{sig}} = 1$	19581.0	1043.3	13365.5	1964.5	0.0	0.1	0.3	22.7	3.4	3.8	5.9	8.1
$N_e^{\text{sig}} = 1$	75.0	40.9	4.1	2.5	0.0	0.0	0.2	0.1	0.0	0.0	0.0	5.9
N_{trk} ($\Delta R > 0.1$ from μ/e) $= 0$	45.0	39.7	2.2	1.2	0.0	0.0	0.0	0.0	0.0	0.0	0.0	6.0
$\sum$ charge $= 0$	42.0	39.6	1.9	1.0	0.0	0.0	0.0	0.0	0.0	0.0	0.0	6.1

Table 7.6: Overview of the event counts after the selection requirements for SR-1M1E-excl applied sequentially. Simulated samples are normalized to $\mathcal{L} = 1.44$ fb^{-1}.

Summary and Comparison of the Signal Regions

The event yields for data, signal and background predictions are presented in Table 7.7 together with the figure of merits: s/b, $s/\sqrt{b}$, $s/\sqrt{s+b}$ and $s/\sqrt{s+b+(\zeta s)^2+(\zeta b)^2}$ with a very conservative uncertainty assumption of $\zeta = 10\,\%$ to quantify the size of and the sensitivity to the signal. The requirements applied to obtain the yields are listed in Table 7.8.
The signal regions based on muons+track(s) and on a muon and an electron have a

	SR-1M1T	SR-1M3T	SR-1E1T	SR-1E3T	SR-1M1E
Data d	485.0	78.0	548.0	52.0	42.0
Expected Events $s+b$	513.4	98.4	615.3	147.7	42.5
Signal s	455.5	92.7	293.9	96.4	39.6
Total Background b	57.9	5.7	321.4	51.3	2.9
Background $\gamma\gamma \to \mu\mu$	57.8	5.4	0.1	0.0	2.9
Background $\gamma\gamma \to ee$	0.0	0.0	321.2	50.6	0.0
Background $\gamma\gamma \to q\bar{q}$	0.1	0.3	0.1	0.7	0.0
Signal purity in [%]	88.7	94.2	47.8	65.3	93.2
s/b	7.9	16.3	0.9	1.9	13.7
$s/\sqrt{b}$	59.9	38.8	16.4	13.5	23.3
$s/\sqrt{s+b}$	20.1	9.3	11.8	7.9	6.1
$s/\sqrt{s+b+(\zeta s)^2+(\zeta b)^2}$	20.0	9.3	11.8	7.9	6.0

Table 7.7: Event yields for data, signal and background predictions together with the signal purity and the figure of merits: s/b, $s/\sqrt{b}$, $s/\sqrt{s+b}$ and $s/\sqrt{s+b+(\zeta s)^2+(\zeta b)^2}$ with a very conservative uncertainty assumption of $\zeta = 10\,\%$ for the SR-*excl*.

high signal purity of $> 88.7\,\%$. The signal regions based on electrons+tracks have a higher expected background contribution resulting in a worse signal purity of $< 70\,\%$. The best signal significance, 20.1, is observed for the SR-1M1T-excl due to the high number of expected signal events and the low background contribution. Despite the large signal purity $> 90\,\%$ in SR-1M3T and SR-1M1E, the signal significance is lower than in SR-1E1T which is caused by the low signal statistics. The high background contribution in SR-1E1T can therefore be compensated by the high number of signal events. The muon based SRs show overall a slightly better performance than the electron based SRs. The agreement between expected and observed events differs for the several SRs. For the electron based SRs, SR-1E1T and SR-1E3T, the data is clearly undershot. For muon based SRs, SR-1M1T and SR-1M3T, the data is also undershot compared to the prediction, but shows a slightly better agreement than the electron based SRs. The fully leptonic SR-1M1E shows a very good agreement between data and prediction.

Requirement	SR-1M1T-excl	SR-1M3T-excl	SR-1E1T-excl	SR-1E3T-excl	SR-1M1E-excl
pass GRL			pass_GRL		
E^A_{ZDC} & E^C_{ZDC}			< 1 TeV		
Trigger	HLT mu4 trigger		HLT hi gg L1TAU1	HLT hi upc L12TAU1	HLT mu4 trigger OR HLT hi gg L1TAU1
N_μ^{sig}	1	1	0	0	1
N_e^{sig}	0	0	1	1	1
N_μ^{baseline}	1	1	-	-	-
$N_{\text{trk}}(\Delta R > 0.1 \text{ from } \ell)$	1	3	1	3	0
Cluster veto	0	0	0	0	-
$\sum$ charge	0	0	0	0	0
$p_{\text{T}}^{(\ell,\text{trk})}$	> 1.0 GeV	-	> 1.0 GeV	-	-
$p_{\text{T}}^{(\ell,\text{trk},\gamma)}$	> 1.0 GeV	-	> 1.0 GeV	-	-
$p_{\text{T}}^{(\ell,\text{trk,cluster})}$	> 1.0 GeV	-	> 1.0 GeV	-	-
m_{trks}	-	< 1.7 GeV	-	< 1.7 GeV	-
	-	-	-	> 0.5 GeV	-
$A_\phi^{\ell,\text{trk(s)}}$	< 0.4	< 0.4	> 0.012	-	-

Table 7.8: Selection criteria for the five SRs in this analysis. The "-excl" suffix is used to indicate the statistical exclusivity of the regions. If no requirement is set on a parameter, it is denoted by "-".

7.4 OPTIMIZATION OF SIGNAL SELECTIONS

The signal selection with the categorization into SRs, defined and discussed in Section 7.3, are an essential part of this analysis. Clean SRs with high statistics provide not only a clean signal for $\gamma\gamma \to \tau\tau$ production, but also increase the sensitivity to a_τ.
The signal selection for the five SRs as listed in Table 7.8 as well as the definition of the signal and baseline leptons, summarized in Table 5.1 are optimized within this work. In this section, various requirements of the signal region definitions are studied and the chosen values are motivated. The figures of merit described in Section 6.1 are maximized for the optimization. The figures in the following show mostly kinematic distributions with the simulation normalized to the integrated luminosity of data, and compared to data. The simulated processes are presented in stacked histograms with the signal estimation for $\gamma\gamma \to \mu\mu$, $\gamma\gamma \to ee$ and $\gamma\gamma \to q\bar{q}$ respectively. The data of 2018 are shown for comparison. In the lower panel, the ratio of data and prediction is shown to indicate the agreement between both. Note, that for the studies in this chapter, a different set of weights[2] for the MC samples has been used and therefore, especially the numbers for the background from $\gamma\gamma \to \mu\mu$ production might differ compared to the numbers in Section 7.3.

7.4.1 *Baseline Leptons*

In addition to requirements on the signal leptons (cf. Table 7.8), requirements on the number of additional looser leptons can be useful to further suppress in particular the same-flavor dilepton backgrounds ($\gamma\gamma \to \mu\mu$ and $\gamma\gamma \to ee$). For this purpose different

2 A weight to exclude double counting of events for the $\gamma\gamma \to \mu\mu$ STARLIGHT 2.0 interlaced with PYTHIA 8.245 MC samples and a MADGRAPH $\gamma\gamma \to \mu\mu + \gamma$ sample is applied even though the $\gamma\gamma \to \mu\mu + \gamma$ sample is not used in this thesis. The contribution of the $\gamma\gamma \to \mu\mu + \gamma$ sample is less than 3 % for the prediction of events. The impact of this additional weight is thus negligible, from which follows, that the conclusions remain the same with correct weights applied.

looser object definitions for muons and electrons are investigated and tested regarding their impact on the signal selection when applying a veto using these leptons, called *baseline* leptons. The baseline leptons are now introduced and defined based on their veto ability.
The kinematic properties, p_{T} and $|\eta|$, are studied to properly define the baseline leptons. Originally, no p_{T} requirement has been applied for these leptons, in the analysis. First, the p_{T} of the reconstructed leptons is investigated here for the 2018 data and the signal MC sample. The p_{T} distribution of reconstructed muons and the reconstructed electrons are shown in Figure 7.1 and Figure 7.2 without any selection, respectively. For both lepton flavors, a low p_{T} tail can be observed. These likely do not come from $\gamma\gamma \to \tau\tau$ leptons but are of hadronic origin such as π and K decays from the processes $\pi^+/K^+ \to \mu^+\nu_\mu$ and $\pi^+/K^+ \to e^+\nu_e$ or from other objects like jets faking the signature of the corresponding lepton type. In the muon distributions in Figure 7.1, a small step is observed at $p_{\mathrm{T}} = 2\,\mathrm{GeV}$. A $p_{\mathrm{T}} > 2\,\mathrm{GeV}$ requirement is introduced on veto muons such that they have a clean definition. The impact on the total number of selected veto muons compared to all reconstructed muons is negligible. The criterion on $|\eta|$ is chosen with $|\eta| < 2.5$ slightly looser than for the definition of signal muons with $|\eta| < 2.4$.
Similar to the case of baseline muons, a step is visible at $p_{\mathrm{T}} > 3\,\mathrm{GeV}$ for baseline electrons. Baseline electrons were tested [60] with the definitions $p_T > 1, 2$ and $3\,\mathrm{GeV}$. Differences were found to be small, hence the $p_T > 2\,\mathrm{GeV}$ requirement was chosen for consistency with the baseline muon definition. The pseudorapidity is chosen to be the same as the one for signal electrons with $|\eta| < 2.47$ excluding $1.37 < |\eta| < 1.52$. The final definitions used in this thesis have been summarized in Table 5.1.

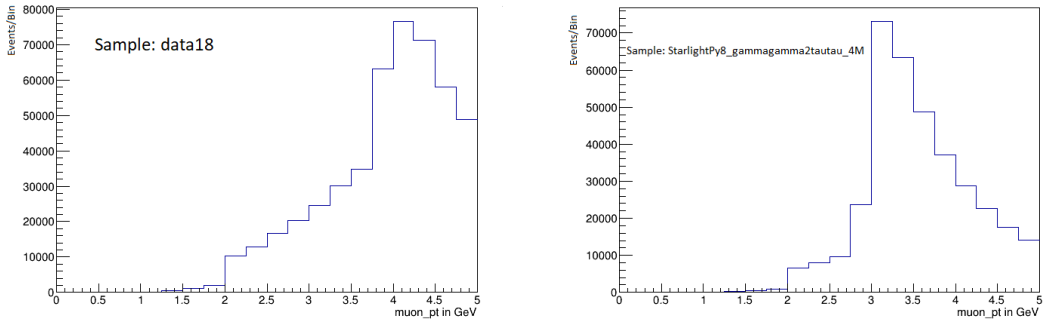

(a) **(b)**

Figure 7.1: p_{T}-distributions of all reconstructed muons, zoomed in on the very low p_{T} range for 2018 data (a) and the signal MC sample (b). Both distributions show no explicit lower limit on the reconstructed muon p_{T} when no selection criteria are applied.

The definitions of the SR-1M1T and of the SR-1M3T include the requirement of exactly one baseline muon, thus effectively vetoing the presence of any other baseline muon. The impact of this requirement is studied by dropping the veto on an additional baseline muon once and comparing to the situation with the baseline muon veto applied. The results of this study can be found in Table 7.9. There, the event yields for data, signal and background predictions together with the figure of merits s/b, $s/\sqrt{b}$ and $s/\sqrt{s+b}$ as well as $s/\sqrt{s+b+(\zeta s)^2+(\zeta b)^2}$ with a very conservative uncertainty assumption of $\zeta = 10\,\%$ are compared. Table D.1 and Table D.2 show the overview of the event counts

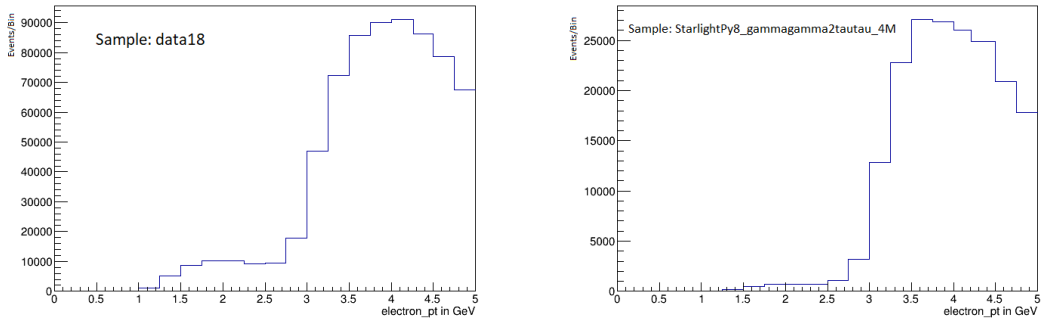

(a) **(b)**

Figure 7.2: p_{T}-distributions of all reconstructed electrons, zoomed in on the very low p_{T} range for 2018 data (a) and the signal MC sample (b). Both distributions show no explicit lower limit on the reconstructed electron p_{T} when no selection criteria are applied.

after applying the selection requirements for the selection without a baseline muon veto which can be found in Appendix D.
The expected value $s + b$ is the sum of the signal s and background b yield. The signal significances are calculated as indicated by the formulae in the table. The background events are significantly reduced with the baseline muon veto for both SRs, while the signal is only slightly affected. This gives an significant improvement in each statistical measure, e.g. for $s/\sqrt{s+b}$, where the signal significance is improved from 16.8 to 20.5 in SR-1M1T and from 9.3 to 9.5 for SR-1M3T. In SR-1M1T, the background reduction from 382.8 to 38.9 with the introduction of the additional baseline muon requirement is enormous leading to an increase of all figures of merits.
Thus, this optimization is used as further selection criteria. The baseline muon veto with the baseline muon definition studied above was introduced in the official ATLAS $\gamma\gamma \to \tau\tau$ analysis as a result of the studies discussed here.

	SR-1M1T w/ baseline μ	SR-1M1T w/o baseline μ	SR-1M3T w/ baseline μ	SR-1M3T w/o baseline μ
Data d	485.0	860.0	78.0	89.0
Expected $s+b$	494.4	881.1	96.2	104.4
Signal s	455.5	498.3	92.7	95.0
Background b	38.9	382.8	3.5	9.4
s/b	11.7	1.3	26.5	10.1
$s/\sqrt{b}$	73.0	25.5	49.6	31.0
$s/\sqrt{s+b}$	20.5	16.8	9.5	9.3
$s/\sqrt{s+b+(\zeta s)^2+(\zeta b)^2}$ $\zeta = 10\%$	20.4	16.7	9.4	9.3

Table 7.9: Comparison of the yields for data, signal, background predictions and the figure of merits s/b, $s/\sqrt{b}$ and $s/\sqrt{s+b}$ as well as $s/\sqrt{s+b+(\zeta s)^2+(\zeta b)^2}$ with a very conservative uncertainty assumption of $\zeta = 10\,\%$ for the muon signal regions SR-1M1T and SR-1M3T with and without a baseline muon veto.

The same study is performed for the electron based SRs, SR-1E1T-excl and SR-1E3T-excl, requiring exactly one baseline electron in addition to the requirements defined

in Table 7.1. The results for the comparison of the yield with and without a baseline electron are shown in Table 7.10. There, the event yields for data, signal and background predictions together with the figure of merits s/b, $s/\sqrt{b}$ and $s/\sqrt{s+b}$ as well as $s/\sqrt{s+b+(\zeta s)^2+(\zeta b)^2}$ with a very conservative uncertainty assumption of $\zeta = 10\,\%$ are compared. Table D.3 and Table D.4 show the overview of the event counts after applying the selection requirements for the selection without a baseline muon veto which can be found in Appendix D.
The expected value $s+b$ is the sum of the signal s and background b yield. The signal significances are calculated as indicated by the formulae in the table.
The number of background events are reduced with the baseline electron veto for both SRs by 74.1 from 321.4 to 247.1 for SR-1E1T and by 17.1 from 51.3 to 34.2 events for SR-1E3T, but much less significantly than in the case of the muon-based SRs and the baseline muon veto. The signal is also reduced a bit, by 15 % for SR-1E1T and 8 % for SR-1E3T. The baseline electron veto still leads to an improvement in background suppression in all four signal significance quantifiers, but to a much smaller extend than previously observed for the baseline muon veto. $s/\sqrt{s+b}$, for example, increases from 11.8 to 12.0 for SR-1E1T-excl and from 7.9 to 8.0 for SR-1E3T-excl. Hence the gain of applying the baseline electron veto is considered not sufficient and it was therefore not applied.
The decision on the possible inclusion of a baseline electron veto might be revisited in the future. The definition is chosen such, that it can easily be implemented in the future without the need of modifying the muon-based and muon-electron SRs or the risk of loosing the exclusiveness of the SRs.

	SR-1E1T w/ baseline e	SR-1E1T w/o baseline e	SR-1E3T w/ baseline e	SR-1E3T w/o baseline e
Data d	469.0	548.0	36.0	52.0
Expected $s+b$	523.5	615.3	123.3	147.7
Signal s	276.4	293.9	89.1	96.4
Background b	247.1	321.4	34.2	51.3
s/b	1.1	0.9	2.6	1.9
$s/\sqrt{b}$	17.6	16.4	15.2	13.5
$s/\sqrt{s+b}$	12.1	11.8	8.0	7.9
$s/\sqrt{s+b+(\zeta s)^2+(\zeta b)^2}$ $\zeta = 10\%$	12.0	11.8	8.0	7.9

Table 7.10: Comparison of the yields for data, signal, background predictions and the figure of merits s/b, $s/\sqrt{b}$ and $s/\sqrt{s+b}$ as well as $s/\sqrt{s+b+(\zeta s)^2+(\zeta b)^2}$ with a very conservative uncertainty assumption of $\zeta = 10\,\%$ for the electron signal regions SR-1E1T and SR-1E3T with and without a baseline electron veto.

7.4.2 *Cluster Veto*

Particles interacting electromagnetically and hadronically deposit their energy in the calorimeter systems of the ATLAS detector. Neighboring detector cells with signals from incoming particles are grouped into so-called clusters as described in Section 5.2. The clusters are matched with the tracks from the ID if the cluster position is in accordance with that of the track. Clusters with a distance $\Delta R(\ell, \text{cluster}) > 0.3$ to the lepton and

$\Delta R(\text{trk}, \text{cluster}) > 1.0$ to the selected track are called unmatched clusters. Such a cluster could be created by electrically neutral particles which do not leave a track in the ID or background decay products not being expected in the final state of $\gamma\gamma \to \tau\tau$ such as photonuclear background or calorimeter noise.
The numbers of unmatched clusters for the SRs, SR-1M1T, SR-1M3T, SR-1E1T and SR-1E3T are shown in Figure 7.3. Only the preselection requirements, see Section 7.3, and the lepton requirements from Table 7.8 are applied.
The majority of events in all four SRs have no unmatched cluster in data and prediction as expected. In MC simulation, mainly events from the hadronic $\gamma\gamma \to$ jets production leave a few unmatched clusters. The backgrounds $\gamma\gamma \to \mu\mu$ and $\gamma\gamma \to ee$ contribute also to events with mostly lower than two unmatched clusters. In data, a large tail with up to or more than ten unmatched clusters is observed, which is neither modeled by the MC-based background predictions nor by the data-driven estimate of the photonuclear background used here. The signal process is located mostly in the bin with zero unmatched clusters, making an unmatched cluster veto a powerful tool for background suppression.
Events are thus removed in the following by vetoing unmatched clusters $N_{\text{clusters}}(\Delta R > 1.0/0.3 \text{ from tracks}/\ell) = 0$.
The cluster veto is applied for the four SRs including tracks, but not for the fully leptonic SR-1M1E which has already a high purity of 91.3 % and is shown in Figure 7.4. The cluster veto increases the signal purity by around 1 % for the the four SRs including tracks.

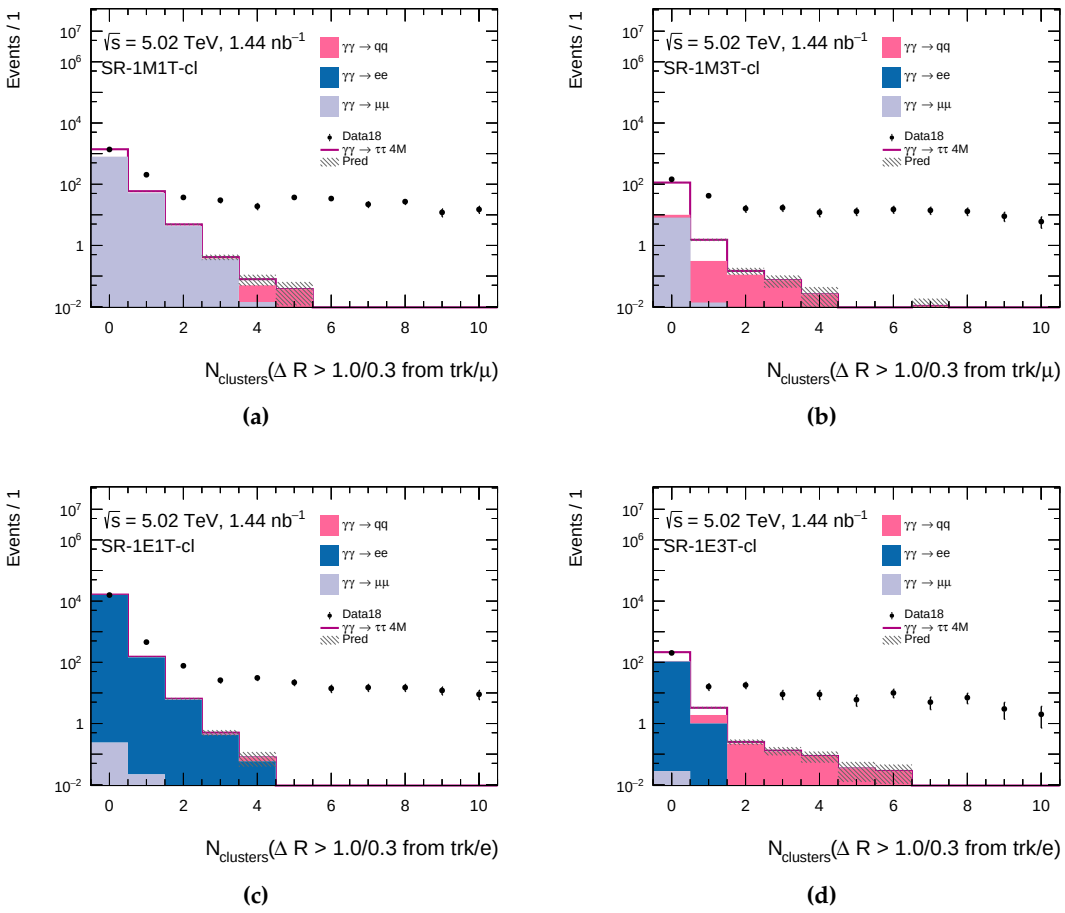

Figure 7.3: Distributions of the number of clusters not matched to a lepton or a track in the SRs (a) SR-1M1T, (b) SR-1M3T, (c) SR-1E1T and (d) SR-1E3T. The selection criteria applied are listed in Table 7.1 excluding all listed requirements from the *Cluster veto* downwards.

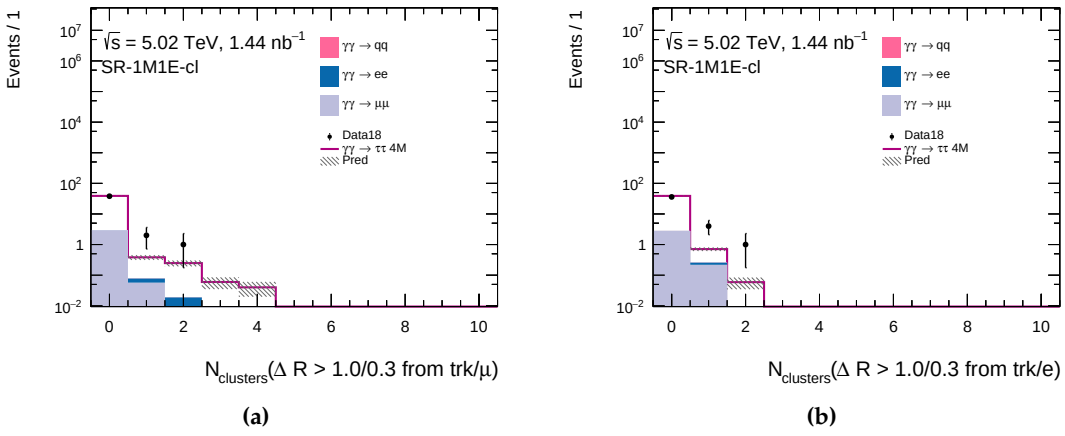

Figure 7.4: Distributions of the number of clusters not matched to the muon (a) and the electron (b) in SR-1M1E. The selection criteria applied are listed in Table 7.1 excluding all listed requirements from the *Cluster veto* downwards.

7.4.3 $\sum$ *Charge*

In the $\gamma\gamma \to \tau\tau$ process, two opposite charged τ-leptons, τ^+ and τ^-, are created. When the τ-leptons decay in the ATLAS detector, the main decay products are leptons and pions identified through a track need to have opposite charge. The resulting sum of the charge is then 0 - the same as the sum of charge of the two photons creating the ditau pair.
The sum of charge distributions in the five SRs are presented in Figure 7.5. A logarithmic scale in the y-axis is chosen to better show the contributing backgrounds. As expected, the signal process as well as the $\gamma\gamma \to ee$ and $\gamma\gamma \to \mu\mu$ backgrounds are located mostly at $\sum$charge $= 0$. A non-negligible contribution is observed at $\sum$charge $= \pm 2$, which is largely background dominated. In SR-1M3T, also $\gamma\gamma \to$ jets production shows a significant contribution at $\sum$charge $= \pm 2$. Furthermore, a mismatch between data and prediction is observed there which might come from the photonuclear background which is not considered in this thesis.
The measurement of $\sum$charge $= \pm 2$ from the decay products can have different origin: The charge of the second lepton in the $\gamma\gamma \to \mu\mu$ or $\gamma\gamma \to ee$ production might not measured correctly, such that the same charge is assigned to the leptons in the final state. Furthermore, in the hadronic decay of the τ-leptons from the $\gamma\gamma \to \tau\tau$ production into three charged pions, the tracks of the charged pions might be out of acceptance due to their too low p_T such that only one track is measured having opposite charge then the decayed τ-lepton. Then, the event could be categorized to the selection with one track and and have $\sum$charge $= \pm 2$.
To suppress these background contributions, the requirement $\sum$charge $= 0$ is introduced for all SRs. Since $\gamma\gamma \to \tau\tau$ production is also affected by this requirement, the figure of merits are kept nearly constant.

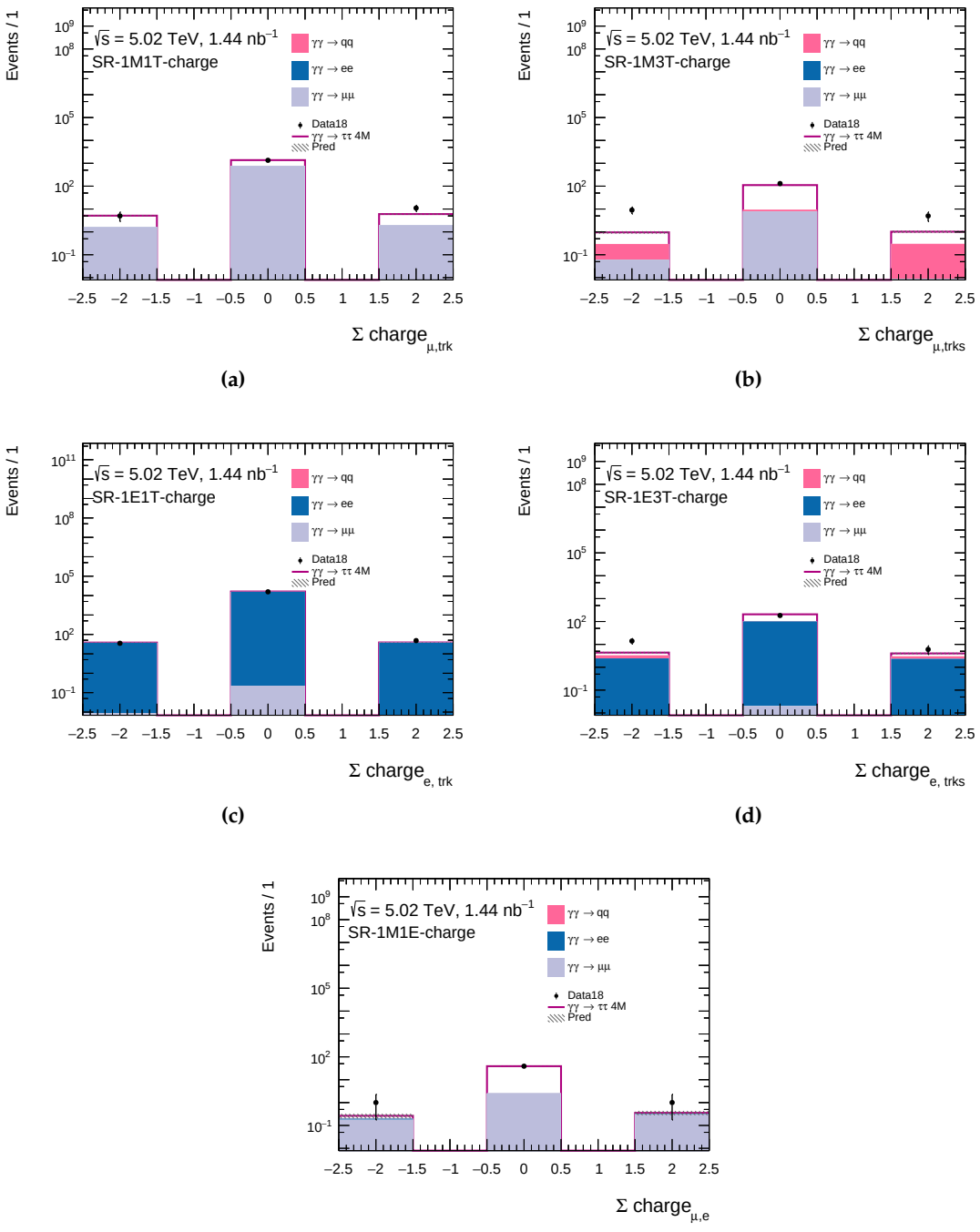

Figure 7.5: Distribution of the sum of the charges of the lepton(s) and track(s) in the five SRs (a) SR-1M1T, (b) SR-1M3T, (c) SR-1E1T, (d) SR-1E3T and (e) SR-1M1E. The sum of the charge is expected to be zero for the signal process $\gamma\gamma \to \tau\tau$. The selection criteria applied are listed in Table 7.1 excluding all listed requirements from the $\sum$charge downwards.

7.4.4 p_T Requirements

For further background reduction, different kinematic observables are investigated regarding their ability to discriminate signal and background in the SRs with one lepton and one track (1L1T). The SRs with one lepton and three tracks (1L3T) can be optimized more effectively with an requirement on $m(\ell, \text{trk(s)}/\ell')$ which is discussed in Section 7.4.5. For the fully leptonic SR-1M1E, no further background suppression is needed, due to its high purity.
The process $\gamma\gamma \to \mu\mu$ is still dominating in the muon based SRs and $\gamma\gamma \to ee$ in the electron based SRs. To suppress these dilepton backgrounds, p_T of the lepton and track system as well as the p_T of the three body system of lepton, track and one photon or one topological cluster are investigated. The photon needs to pass the object requirements in Table 5.1 and to be within a $\Delta R < 1.0$ from the track. The leading photon is used for the vectorial $p_T(\ell, \text{trk}, \gamma)$ calculation if several photons satisfy these requirements. Similarly, it is done for clusters passing the requirements from Table 5.1 and satisfying $\Delta R < 1.0$ with respect to the track. Additionally, the cluster needs to have a p_T greater than 2 GeV to be included in the calculation of the vectorial $p_T(\ell, \text{trk}, \text{cluster})$. These kinematic observables provide an approximate measure of the transverse momentum carried away by the decay neutrinos in $\gamma\gamma \to \tau\tau$ signal events, which does ideally not exist in $\gamma\gamma \to \mu\mu$ and $\gamma\gamma \to ee$ events.
The $p_T(\ell, \text{trk}) = |\vec{p}_T^{\,\ell} + \vec{p}_T^{\,\text{trk}}|$, $p_T(\ell, \text{trk}, \gamma) = |\vec{p}_T^{\,\ell} + \vec{p}_T^{\,\text{trk}} + \vec{p}_T^{\,\gamma}|$ and $p_T(\ell, \text{trk}, \text{cluster}) = |\vec{p}_T^{\,\ell} + \vec{p}_T^{\,\text{trk}} + \vec{p}_T^{\,\text{cluster}}|$ distributions for muons in SR-1M1T and for electrons in SR-1E1T are shown in Figure 7.6 and Figure 7.7 respectively. The distributions are displayed once with stacked predictions in comparison with data and once normalized (and non-stacked) compared to each other, in order to see the contributions of the signal and background processes in different p_T regions.. The p_T requirements are subsequently applied: the $p_T(\ell, \text{trk})$ requirement is used for the $p_T(\ell, \text{trk}, \gamma)$ and $p_T(\ell, \text{trk}, \text{cluster})$ distributions and the $p_T(\ell, \text{trk}, \gamma)$ requirement for the $p_T(\ell, \text{trk}, \text{cluster})$ distributions to better see shape differences between signal and the dominant background. The dilepton backgrounds, $\gamma\gamma \to \mu\mu$ and $\gamma\gamma \to ee$, lie mostly in the low p_T region (< 1 GeV) while the signal is distributed over a larger p_T range for all three p_T-distributions. Between 45 and 90 % of the $\gamma\gamma \to \mu\mu$ production has a $p_T^{\text{system}} < 1$ GeV while only between 20 and 50 % of the $\gamma\gamma \to ee$ production decay products have a low p_T^{system}. For $p_T > 1$ GeV, the signal production $\gamma\gamma \to \tau\tau$ is located to a larger extend. The p_T requirements: $p_T(\ell, \text{trk}) > 1$ GeV, $p_T(\ell, \text{trk}, \gamma) > 1$ GeV and $p_T(\ell, \text{trk}, \text{cluster}) > 1$ GeV, are introduced in the analysis to suppress the dilepton backgrounds by 92 % in SR-1M1T and by 56 % in SR-1E1T where the signal significance improves from 15.4 to 20.1 and from 3.3 to 4.0, respectively. As a result of the stronger discrimination of the three p_T-variables for $\gamma\gamma \to \mu\mu$ than for $\gamma\gamma \to ee$, the background suppression by these three requirements is significantly better in SR-1M1T than in SR-1E1T. In the latter, the $\gamma\gamma \to ee$ background contribution is reduced but still dominates the SR-1E1T.

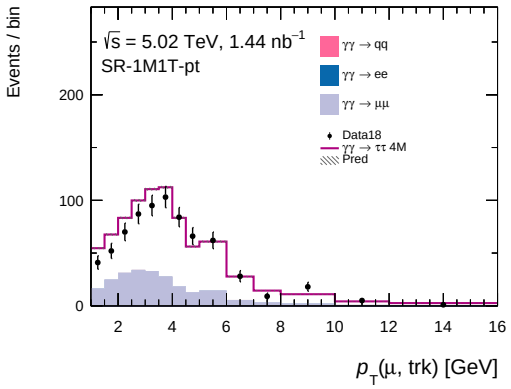

(a) No p_{T} cut applied.

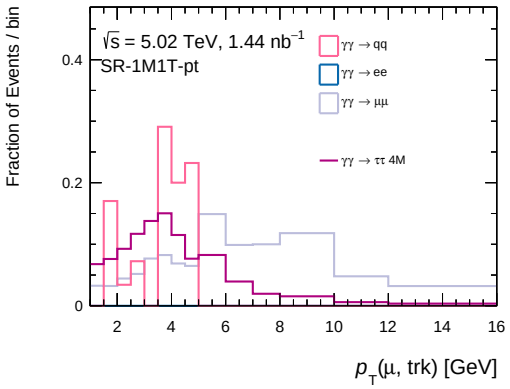

(b) No p_{T} cut applied.

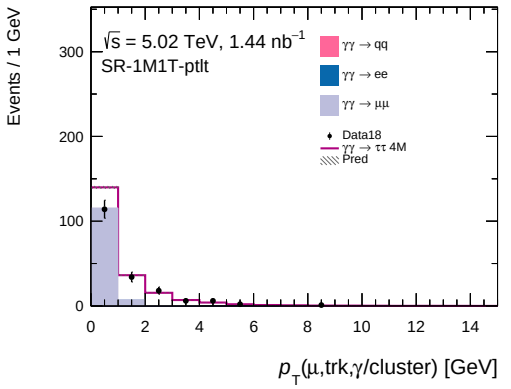

(c) $p_{\mathrm{T}}(\mu, \mathrm{trk}) > 1\,\mathrm{GeV}$ applied.

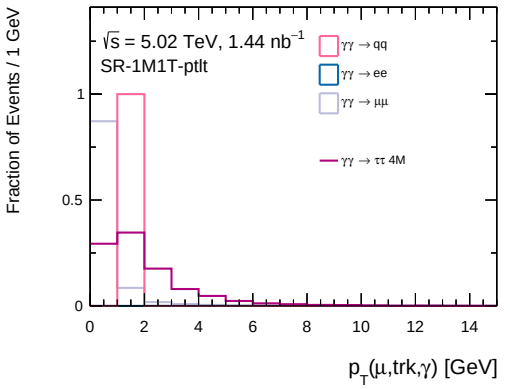

(d) $p_{\mathrm{T}}(\mu, \mathrm{trk}) > 1\,\mathrm{GeV}$ applied.

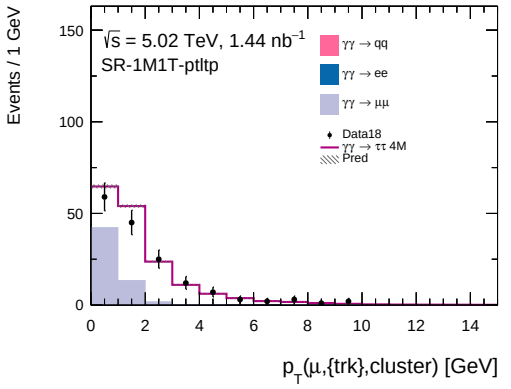

(e) $p_{\mathrm{T}}(\mu, \mathrm{trk}) > 1\,\mathrm{GeV}$ and $p_{\mathrm{T}}(\mu, \mathrm{trk}, \gamma) > 1\,\mathrm{GeV}$ applied.

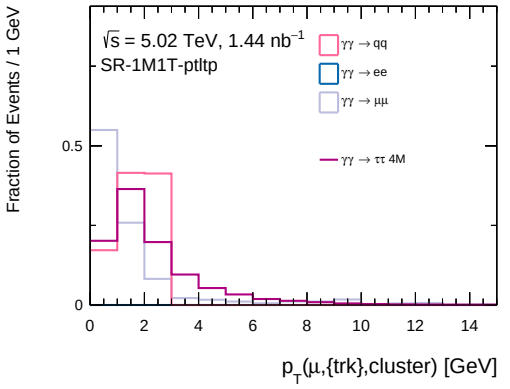

(f) $p_{\mathrm{T}}(\mu, \mathrm{trk}) > 1\,\mathrm{GeV}$ and $p_{\mathrm{T}}(\mu, \mathrm{trk}, \gamma) > 1\,\mathrm{GeV}$ applied.

Figure 7.6: $p_{\mathrm{T}}(\mu, \mathrm{trk})$ (a/b), $p_{\mathrm{T}}(\mu, \mathrm{trk}, \gamma)$ (c/d) and $p_{\mathrm{T}}(\mu, \mathrm{trk}, \mathrm{cluster})$ (e/f) distributions for the SR-1M1T in a stacked histogram (a/c/e) and with signal and background predictions individually normalized to unity (b/d/f). The selection criteria applied are listed in Table 7.1 excluding all listed requirements from the $m(\mathrm{trks})$ downwards. The p_{T} requirements, $p_{\mathrm{T}}(\mu, \mathrm{trk}) > 1\,\mathrm{GeV}$ and $p_{\mathrm{T}}(\mu, \mathrm{trk}, \gamma) > 1\,\mathrm{GeV}$ are subsequently applied. The spikes in the normalized $\gamma\gamma \to$ jets distributions are based on very few events that are scaled up by the normalization and can thus be ignored.

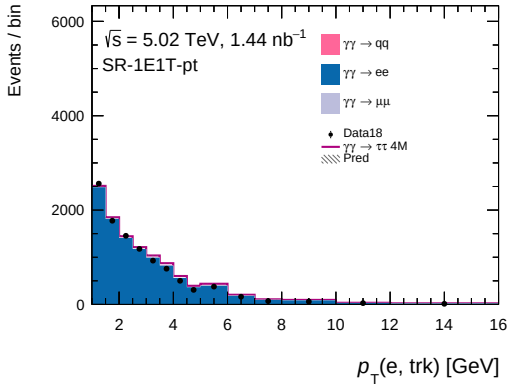

(a) No p_{T} cut applied.

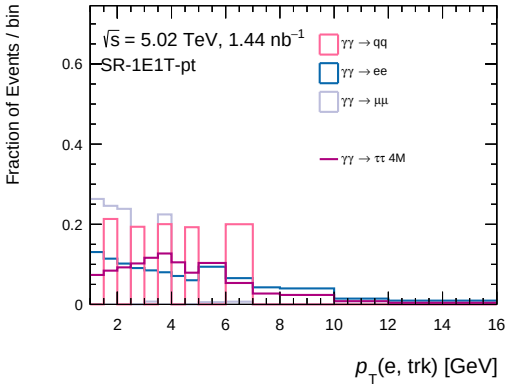

(b) No p_{T} cut applied.

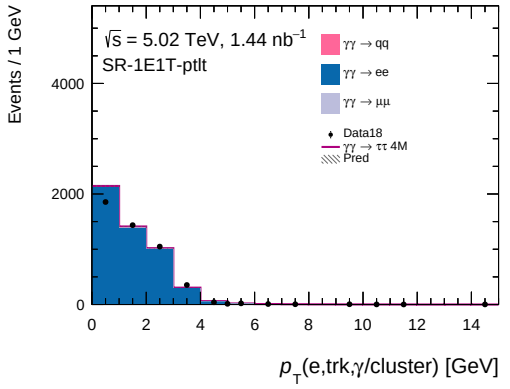

(c) $p_{\mathrm{T}}(e, \mathrm{trk}) > 1\,\mathrm{GeV}$ applied.

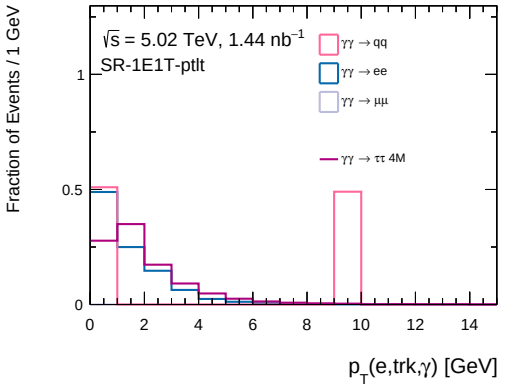

(d) $p_{\mathrm{T}}(e, \mathrm{trk}) > 1\,\mathrm{GeV}$ applied.

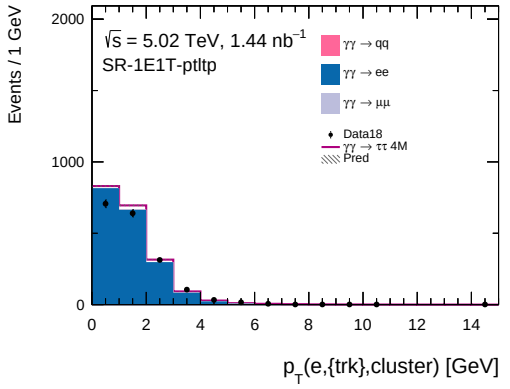

(e) $p_{\mathrm{T}}(e, \mathrm{trk}) > 1\,\mathrm{GeV}$ and $p_{\mathrm{T}}(e, \mathrm{trk}, \gamma) > 1\,\mathrm{GeV}$ applied.

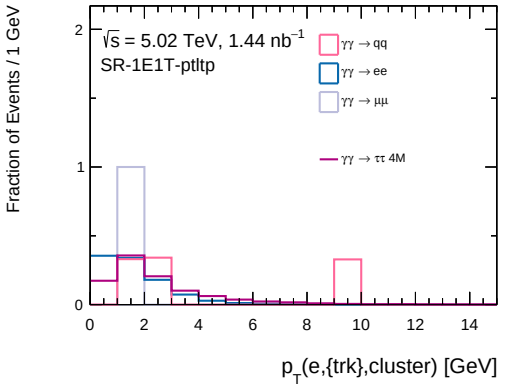

(f) $p_{\mathrm{T}}(e, \mathrm{trk}) > 1\,\mathrm{GeV}$ and $p_{\mathrm{T}}(e, \mathrm{trk}, \gamma) > 1\,\mathrm{GeV}$ applied.

Figure 7.7: $p_{\mathrm{T}}(e, \mathrm{trk})$ (a/b), $p_{\mathrm{T}}(e, \mathrm{trk}, \gamma)$ (c/d) and $p_{\mathrm{T}}(e, \mathrm{trk}, \mathrm{cluster})$ (e/f) distributions for SR-1E1T in a stacked histogram (a/c/e) and with signal and background predictions individually normalized to unity (b/d/f). The selection criteria applied are listed in Table 7.1 excluding all listed requirements from the $m(\mathrm{trks})$ downwards. The p_{T} requirements, $p_{\mathrm{T}}(e, \mathrm{trk}) > 1\,\mathrm{GeV}$ and $p_{\mathrm{T}}(e, \mathrm{trk}, \gamma) > 1\,\mathrm{GeV}$ are subsequently applied. The spikes in the normalized $\gamma\gamma \to$ jets distributions are based on very few events that are scaled up by the normalization and can thus be ignored.

7.4.5 *Invariant Mass of the Track System*

Similar to SR-1M1T and SR-1E1T, the signal regions based on a signal lepton and three tracks (SR-1M3T and SR-1E3T) are contaminated by a large background contribution, unless the background is kinematically suppressed. The background contributions $\gamma\gamma \to \mu\mu$ and $\gamma\gamma \to ee$ in the SRs with one track could be reduced by implementing p_{T} requirements. For the SRs with three tracks, the m_{trks} observable provides a good separation between the $\gamma\gamma \to \tau\tau$ signal and the $\gamma\gamma \to \mu\mu$ and $\gamma\gamma \to ee$ background.

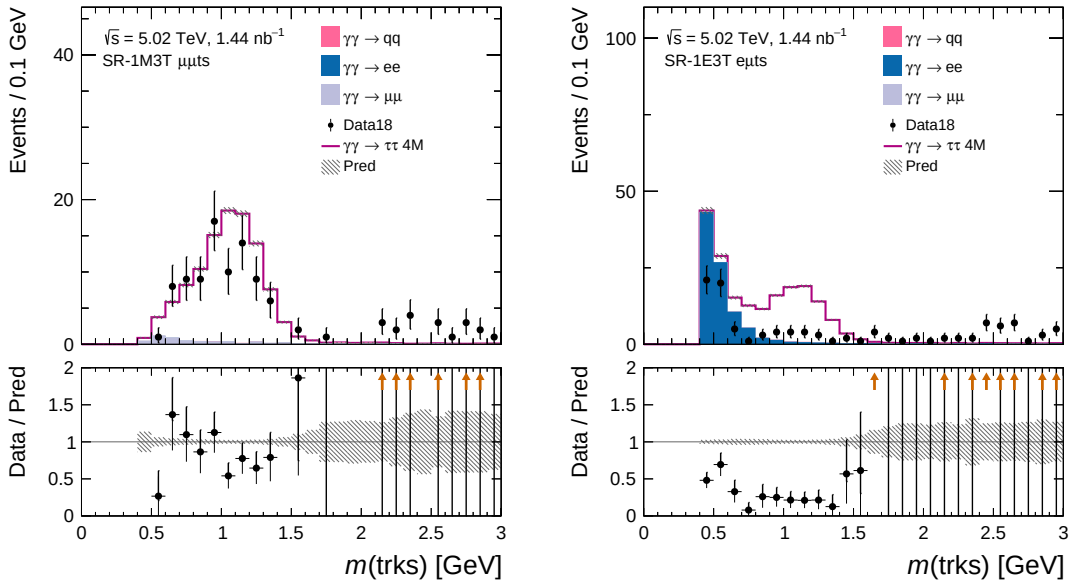

Figure 7.8: Signal and background prediction as well as the data for the observable m_{trks} in SR-1M3T (a) and SR-1E3T (b). The selection criteria applied are listed in Table 7.1 excluding all listed requirements from the $\sum$charge downwards.

The m_{trks} distributions before applying any requirement on m_{trks} for SR-1M3T and SR-1E3T are shown in Figure 7.8. The $\gamma\gamma \to \mu\mu$ and $\gamma\gamma \to ee$ backgrounds are located at small values of $m(\mathrm{trks})$ while the signal covers a range up to around 1.7 GeV, where also the statistics of the MC signal simulation is limited. At higher values of $m(\mathrm{trks})$, an almost flat contribution is still visible in the data, but in none of the used MC simulations. Here, likely an additional, not-considered background, such as the photonuclear process contributes. A requirement of $m_{\mathrm{trks}} < 1.7\,\mathrm{GeV}$ suppresses this contribution and is applied for both SRs.
The $\gamma\gamma \to ee$ background in Figure 7.8 (b) is clearly found in the low m_{trks} region. Requirements of $m_{\mathrm{trks}} > 0.0/0.5/0.6/0.7/0.8\,\mathrm{GeV}$ are tested, regarding their impact on the signal significance $s/\sqrt{s+b}$. The results are shown in Table 7.11. The signal significance is maximized for $m_{\mathrm{trks}} > 0.7\,\mathrm{GeV}$ rising from 7.0 to 8.9. Earlier studies on m_{trks} used a slightly different object selection and different events selection as shown in Table 7.12 and 7.13, respectively. Furthermore, the alternative signal sample[3] without

3 Earlier results are labeled through the input sample version, denoted as v09 ntuples, while the newer input samples are denoted as v17 ntuples.

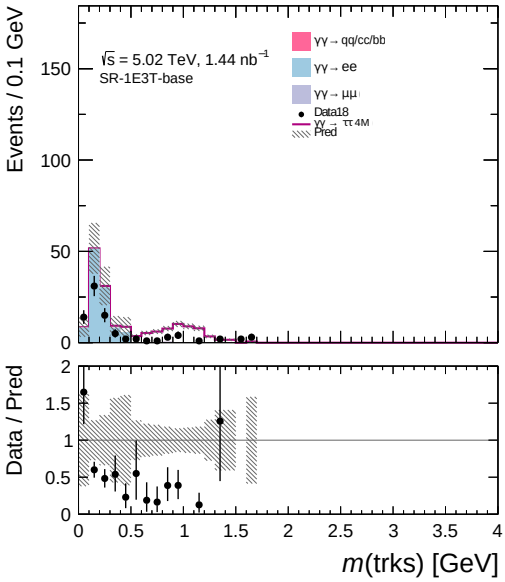

Figure 7.9: Signal and background prediction as well as the data for the observable m_{trks} in SR-1E3T-base. The earlier input samples of v09 are used together with the signal selection listed in Table 7.13 up to the signal selection criteria of $m_{trks} < 1.7\,\text{GeV}$.

FSR effects listed in Table 4.1 is used. The distribution of m_{trks} with these selections is presented in Figure 7.9. Requirements of $m_{\text{trks}} > 0.0/0.3/0.4/0.5\,\text{GeV}$ were tested at the time, regarding their impact on the signal significance $s/\sqrt{s+b}$. The results are shown in Table 7.13. The signal significance rises from 4.7 for $m_{\text{trks}} > 0\,\text{GeV}$ to 7.5 for $m_{\text{trks}} > 0.5\,\text{GeV}$.
Based on the earlier studies the best requirement had been chosen as $m(\text{trks}) > 0.5\,\text{GeV}$ which is used in this analysis. The newer studies indicate that $m(\text{trks}) > 0.7\,\text{GeV}$ provides an even better signal-background discrimination and could be used in future updates of this analysis.

Requirement	Data 18	$\gamma\gamma \to \tau\tau$ 4M	$\gamma\gamma \to \mu\mu$ 7M20	$\gamma\gamma \to \mu\mu$ 20M	$\gamma\gamma \to ee$ 4p5M7	$\gamma\gamma \to ee$ 7M15	$\gamma\gamma \to ee$ 15Mv1	$\gamma\gamma \to$ jets DD	$\gamma\gamma \to$ jets DR	$\gamma\gamma \to$ jets RD	$\gamma\gamma \to$ jets RR	sig/$\sqrt{\text{sig+bkg}}$
pass GRL	4335070.0	23615.5	88094.6	7380.6	177294.7	135156.7	19274.8	35981.6	7677.2	7677.2	12524.5	32.9
$E_{\mathrm{ZDC}}^{A,C} < 1\,\mathrm{TeV}$	1435464.0	23615.5	88094.6	7380.6	177294.7	135156.7	19274.8	35981.6	7677.2	7677.2	12524.5	32.9
HLT hi upc L12TAU1	192906.0	10652.2	47378.8	3546.3	95296.6	88813.9	14651.0	19309.4	4031.1	4030.8	6143.0	19.7
$N_e^{\mathrm{sig}} = 1$	23133.0	792.5	2.8	2.8	534.2	20455.3	4866.7	51.8	7.7	7.5	12.2	4.8
$N_\mu^{\mathrm{sig}} = 0$	23130.0	753.8	0.5	0.2	534.2	20455.3	4866.5	51.6	7.7	7.5	12.2	4.6
$N_{\mathrm{trk}}(\Delta R > 0.1 \text{ from } e) = 3$	302.0	103.0	0.0	0.0	0.3	64.9	42.2	4.7	0.4	0.3	0.4	7.0
Cluster veto	203.0	101.6	0.0	0.0	0.3	64.6	41.5	3.8	0.2	0.2	0.2	7.0
$\sum \text{charge} = 0$	183.0	99.7	0.0	0.0	0.3	62.4	39.0	2.5	0.1	0.1	0.1	7.0
$m_{\mathrm{trks}} < 1.7\,\mathrm{GeV}$	73.0	96.8	0.0	0.0	0.3	58.4	35.3	0.7	0.0	0.0	0.0	7.0
$m_{\mathrm{trks}} > 0.5\,\mathrm{GeV}$	52.0	96.4	0.0	0.0	0.1	32.0	18.5	0.7	0.0	0.0	0.0	7.9
$m_{\mathrm{trks}} > 0.6\,\mathrm{GeV}$	31.0	94.5	0.0	0.0	0.0	14.8	8.8	0.7	0.0	0.0	0.0	8.7
$m_{\mathrm{trks}} > 0.7\,\mathrm{GeV}$	26.0	90.1	0.0	0.0	0.0	8.1	4.7	0.6	0.0	0.0	0.0	8.9
$m_{\mathrm{trks}} > 0.8\,\mathrm{GeV}$	25.0	83.1	0.0	0.0	0.0	4.8	2.6	0.6	0.0	0.0	0.0	8.7

Table 7.11: Overview of the event counts after the selection requirements for SR-1E3T applied sequentially. The effect on background reduction is tested for $m_{\mathrm{trks}} > 0.5\,\mathrm{GeV}$ to $> 0.8\,\mathrm{GeV}$. MC samples are normalized to $\mathcal{L} = 1.44\ \mathrm{fb}^{-1}$.

Property	Signal	Veto
Muons		
Kinematic	$p_{\mathrm{T}} > 4$ GeV, $\lvert\eta\rvert < 2.4$	
Identification	LowPt	LowPt
Impact parameter	$\lvert d_0/\sigma(d_0)\rvert < 3$	—
Electrons		
Kinematic	$p_{\mathrm{T}} > 4$ GeV	
Identification	LHVeryLoose	LHVeryLoose
Object Quality (OQ)	Good	—
Impact parameter	$\lvert d_0/\sigma(d_0)\rvert < 3$	—
Tracks		
Kinematic	$p_{\mathrm{T}} > 100$ MeV, $\lvert\eta\rvert < 2.5$	—
Reconstruction	Loose Primary	—
Impact parameter	$\lvert d_0\rvert < 3$ mm	—

Table 7.12: Summary of former reconstructed object definitions for v09 ntuples.

Requirement	Data 18	$\gamma\gamma \to \tau\tau$ MC	$\gamma\gamma \to \mu\mu$ 7M20 MC	$\gamma\gamma \to \mu\mu$ 20M MC	$\gamma\gamma \to ee$ 3p6M15 MC	$\gamma\gamma \to ee$ 15M MC	$\gamma\gamma \to q\bar{q}$ MC	$\gamma\gamma \to c\bar{c}$ MC	$\gamma\gamma \to b\bar{b}$ MC	sig/$\sqrt{\text{sig+bkg}}$
pass GRL	3876916.0	265340.0	77253.1	7177.0	522446.4	18748.8	310464.0	214704.0	1340.6	222.9
$E^{A}_{\text{ZDC}} < 1$ TeV	2080972.0	265340.0	77253.1	7177.0	522446.4	18748.8	310464.0	214704.0	1340.6	222.9
$E^{C}_{\text{ZDC}} < 1$ TeV	1115488.0	265340.0	77253.1	7177.0	522446.4	18748.8	310464.0	214704.0	1340.6	222.9
HLT hi upc L12TAU1	191994.0	43465.1	43498.1	3639.0	263422.7	13895.1	62785.1	36161.5	529.2	63.6
$N_e^{sig} = 1$	18304.0	600.5	1.5	5.8	12747.7	4081.8	41.9	31.1	3.6	4.5
$N_\mu^{veto} = 0$	18289.0	543.4	0.0	0.1	12747.7	4081.8	41.9	31.1	3.4	4.1
N_{trk} (dR > 0.1 from e) $= 3$	337.0	77.5	0.0	0.0	130.6	68.4	4.7	2.1	0.2	4.6
Cluster veto	212.0	69.8	0.0	0.0	125.4	64.5	0.0	1.1	0.1	4.3
$\sum$ charge = 0	157.0	64.7	0.0	0.0	73.1	37.1	0.0	1.1	0.0	4.9
$m_{trks} < 1.7$ GeV	86.0	61.6	0.0	0.0	73.1	32.4	0.0	0.0	0.0	4.8
$m_{trks} > 0.3$ GeV	26.0	59.4	0.0	0.0	10.4	5.2	0.0	0.0	0.0	6.9
$m_{trks} > 0.4$ GeV	21.0	58.4	0.0	0.0	5.2	2.2	0.0	0.0	0.0	7.2
$m_{trks} > 0.5$ GeV	19.0	56.3	0.0	0.0	0.0	1.7	0.0	0.0	0.0	7.4

Table 7.13: Overview of the event counts after the selection requirements for SR-1E3T applied sequentially. The effect on background reduction is tested for $m_{\text{trks}} > 0.0\,\text{GeV}$ to $> 0.5\,\text{GeV}$ colored in red. MC samples are normalized to $\mathcal{L} = 1.44\,\text{fb}^{-1}$.

7.4.6 *Acoplanarity*

Four SRs are based on the signature of a lepton accompanied by one or three tracks: SR-1M1T/SR-1E1T and SR-1M3T/SR-1E3T as discussed in Section 7.3. These SRs differ in statistics and purity and therefore in sensitivity to a_τ. Higher purity as well as more statistics increase the sensitivity to a_τ. Especially, the electron based SR-1E1T shows a small purity of 5 % without an additional background suppression through a requirement on $A_\phi^{e,\text{trk}}$, as listed in Table 7.4. The acoplanarity $A_\phi^{\ell,\text{trk(s)}}$ is defined as

$$A_\phi^{\ell,\text{trk(s)}} = 1 - \frac{|\Delta\phi|}{\pi} \tag{7.1}$$

with $\Delta\phi$ denotes the azimuth angle difference between the lepton and the track(s) and provides a measure of the extend to which the lepton and the track(s) are emitted in a back-to-back configuration.
Figure 7.10 and Figure 7.11 show the acoplanarity $A_\phi^{\ell,\text{trk(s)}}$ distributions for the muon-based and electron-based SRs, respectively.
For the muon based SRs, the $\gamma\gamma \to \mu\mu$ background is observed to be located at very low acoplanarity, in line with the back-to-back configuration for the muons in this case, while at large acoplanarity, $A_\phi^{\mu,\text{trk(s)}} > 0.4$, an overshoot of data compared to the prediction is observed. The photonuclear background which is neglected in this thesis could create this data overshoot [94] and is located in this range. In the electron based SRs, similar observations are made, with $\gamma\gamma \to ee$ located at low acoplanarities and a data overshoot for $A_\phi^{e,\text{trk(s)}} > 0.4$, though with less statistics in this region compared to the muon-based SRs. The application of an upper threshold on the acoplanarity is possible and potentially interesting in the future, but in the following not applied, since the effect was considered to be small.
The electron based SR-1E1T suffers most in terms of low purity, and potential improvements are discussed in the following. Two kinematic distributions which can

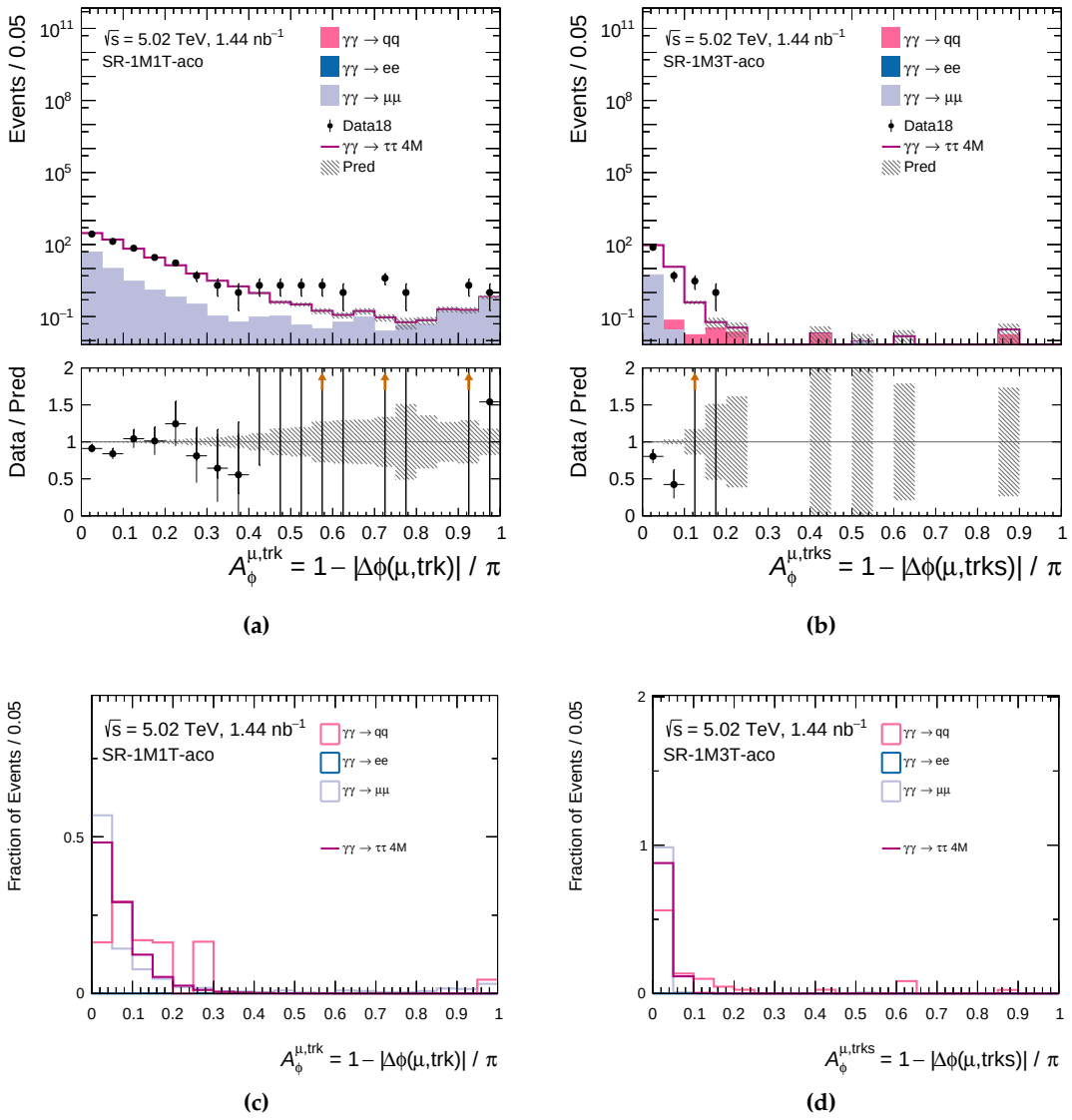

Figure 7.10: Acoplanarity $A_\phi^{\mu,\mathrm{trk}}$ (left) and $A_\phi^{\mu,\mathrm{trks}}$ (right) distributions in the SR-1M1T (left) and SR-1M3T (right) before applying a requirement on $A_\phi^{\ell,\mathrm{trk(s)}}$, comparing the signal and background prediction to data (top) and with signal and background predictions individually normalized to unity (bottom). The selection criteria applied are listed in Table 7.1 excluding all listed requirements from the $p_\mathrm{T}(\ell, \mathrm{trk}, \mathrm{cluster})$ requirement downwards.

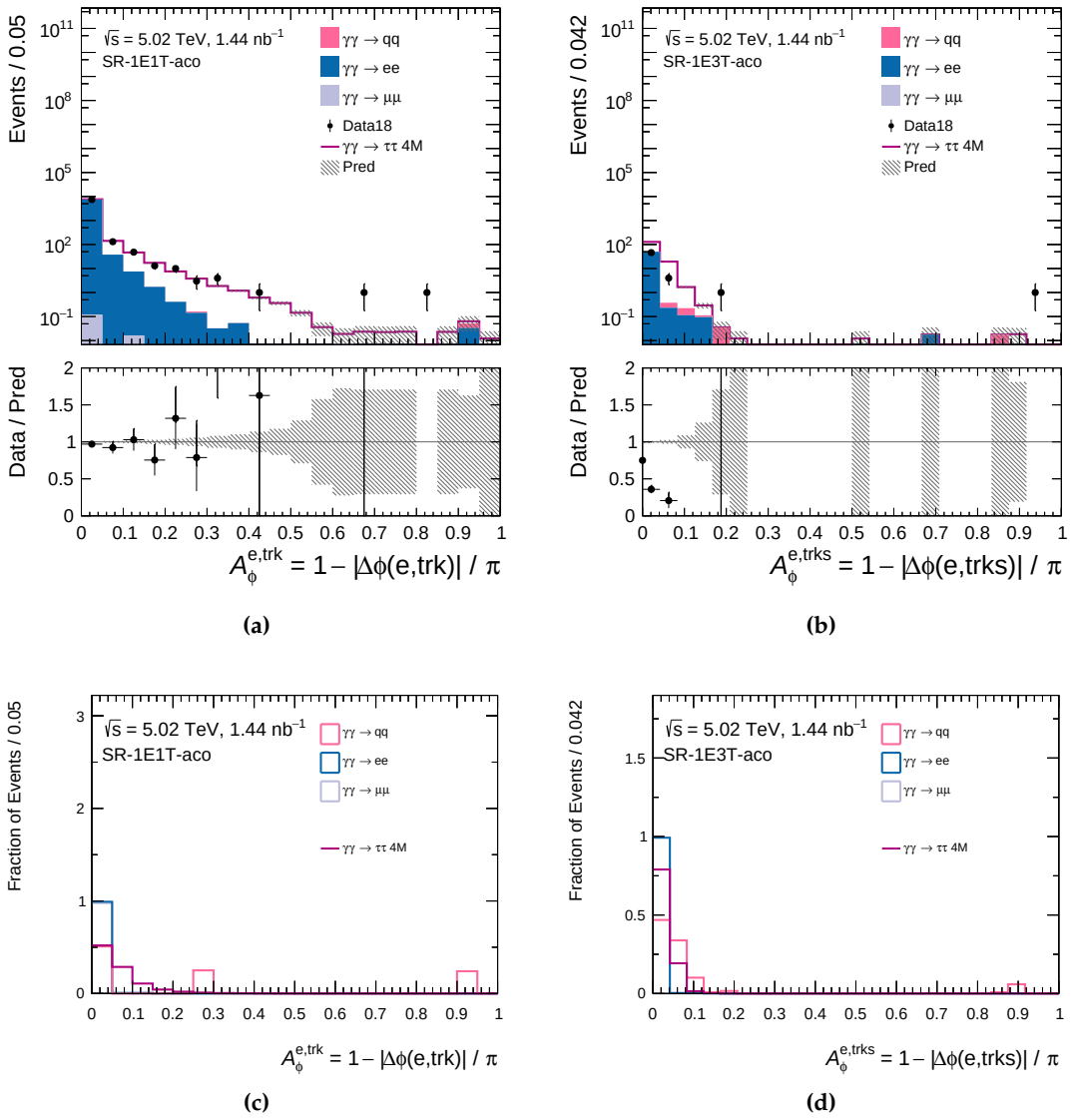

Figure 7.11: Acoplanarity $A_\phi^{e,\mathrm{trk}}$ (left) and $A_\phi^{e,\mathrm{trks}}$ (right) distributions in the SR-1E1T (left) and SR-1E3T (right) before applying a requirement on $A_\phi^{\ell,\mathrm{trk(s)}}$, comparing the signal and background prediction to data (top) and with signal and background predictions individually normalized to unity (bottom). The selection criteria applied are listed in Table 7.1 excluding all listed requirements from the $p_\mathrm{T}(\ell, \mathrm{trk}, \mathrm{cluster})$ requirement downwards.

discriminate between signal and background are: $p_{\mathrm{T}}(e,\mathrm{trk})$ and $A_{\phi}^{e,\mathrm{trk}}$ which are shown in Figure 7.12.
Both distributions demonstrate a clear shape difference between the $\gamma\gamma \to \tau\tau$ signal and the dominant $\gamma\gamma \to ee$ background and have therefore the potential to suppress the $\gamma\gamma \to ee$ background significantly.
The best selection requirement using the two variables $p_{\mathrm{T}}(e,\mathrm{trk})$ and $A_{\phi}^{e,\mathrm{trk}}$ was investigated using a 2D scan through varying the lower thresholds in these observables, within the following ranges and with the following stepsizes:

- $p_{\mathrm{T}}(e,\mathrm{trk})$: from 1.0 GeV to 4.0 GeV in steps of 0.5 GeV
- $A_{\phi}^{e,\mathrm{trk}}$: from 0 to 0.010 in steps of 0.002

At each step, the four statistical measures introduced in Section 6.1: s/b, $s/\sqrt{b}$, $s/\sqrt{s+s}$ and $s/\sqrt{s+b+(\zeta s)^2+(\zeta b)^2}$ with $\zeta = 10\,\%$ were evaluated. Higher values signify an improvement in the purity, but also often are accompanied with a loss in statistics that can reduce the performance in the final fit[4]. Figure 7.13 shows the results of the 2D scans in $p_{\mathrm{T}}(e,\mathrm{trk})$ and $A_{\phi}^{e,\mathrm{trk}}$. The values of all statistical figures of merit can be improved by including a $A_{\phi}^{e,\mathrm{trk}}$ requirement. They also profit from larger $p_{\mathrm{T}}(e,\mathrm{trk})$, but only up to $p_{\mathrm{T}}(e,\mathrm{trk}) > 2.5\,\mathrm{GeV}$. The maximum is different for each figure of merit. The maximum is given at $A_{\phi}^{e,\mathrm{trk}} > 0.01$ and for s/b and $s/\sqrt{s+b+(\zeta s)^2+(\zeta b)^2}$ at $p_{\mathrm{T}}(e,\mathrm{trk}) > 2.5\,\mathrm{GeV}$ and for $s/\sqrt{b}$ and $s/\sqrt{s+s}$ at $p_{\mathrm{T}}(e,\mathrm{trk}) > 1.0\,\mathrm{GeV}$. Figures 7.13 (c) and (d) show that for higher $p_{\mathrm{T}}(e,\mathrm{trk})$ thresholds, the figure of merits degrade due to the loss of statistics.
Based on this, the SR-1E1T selection in Table 7.8 and two working points with the additional requirements, based on the figure of merits in Figure 7.13 – denoted as *pure* and *highpure* selections – are tested with the TRExFitter setup discussed in more detail in Section 6.3:

- pure: $p_{\mathrm{T}}(e,\mathrm{trk}) > 2.0\,\mathrm{GeV}$ and $A_{\phi}^{e,\mathrm{trk}} > 0.004$
- highpure: $p_{\mathrm{T}}(e,\mathrm{trk}) > 1.0\,\mathrm{GeV}$ and $A_{\phi}^{e,\mathrm{trk}} > 0.008$

The event count tables for these two pure selections are given in Table 7.14 and Table 7.15, respectively. A $p_{\mathrm{T}}(e,\mathrm{trk}) > 1.0\,\mathrm{GeV}$ requirement combined with a tighter requirement for $A_{\phi}^{e,\mathrm{trk}}$ makes the SR more sensitive with respect to the signal significance than the stricter $p_{\mathrm{T}}(e,\mathrm{trk}) > 2.0\,\mathrm{GeV}$ requirement, combined with a looser requirement on $A_{\phi}^{e,\mathrm{trk}}$. For the highpure working point, the signal significance increases from 4.0 to 10.6 while the pure working point reaches only a signal significance of 7.7.
A scan up to higher requirements on $A_{\phi}^{e,\mathrm{trk}}$, $A_{\phi}^{e,\mathrm{trk}} > 0.015$, with steps of 0.001 in $A_{\phi}^{e,\mathrm{trk}}$ including $p_{\mathrm{T}}(e,\mathrm{trk}) > 1.0\,\mathrm{GeV}$ is performed with the TRExFitter setup. A very rough approximation of systematic uncertainties, considering a 5 % global systematic uncertainty for signal and background, independently is included in the likelihood fit. In Section 9.6, the global systematic uncertainty of 5 % is motivated for signal and background prediction.
The results of the extended maximum likelihood fits – the length of the 68 % CIs –

4 The statistical analysis is based on an extended negative loglikelihood fit. The procedure is further described in Chapter 9.

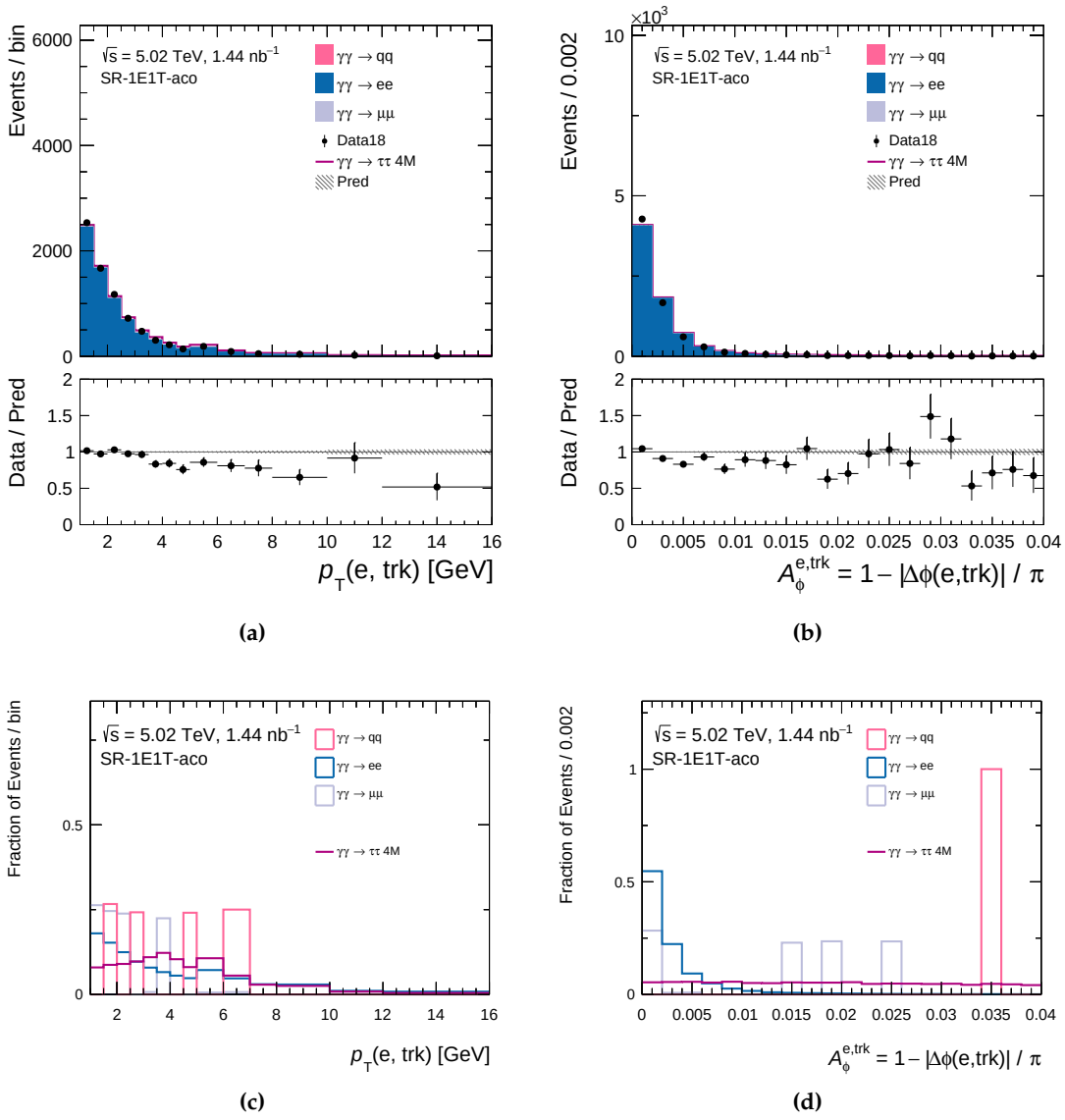

Figure 7.12: $p_{\mathrm{T}}(e, trk)$ (left) and acoplanarity (right) distributions in the SR-1E1T before applying tighter requirements on $A_{\phi}^{e,\mathrm{trk}}$, comparing the signal and background prediction to data (top) and with signal and background predictions individually normalized to unity (bottom). The selection criteria applied are listed in Table 7.1 excluding all listed requirements from the $p_{\mathrm{T}}(\ell, \mathrm{trk}, \mathrm{cluster})$ requirement downwards.

are presented in Table 7.16. The shortest CI of $l = 0.0594$, i.e. the best performance for the different acoplanarity requirements is obtained for $p_{\mathrm{T}}(e,\mathrm{trk}) > 1.0\,\mathrm{GeV}$ and $A_{\phi}^{e,\mathrm{trk}} > 0.014$ while previous studies [60] identified the best performance at

$$p_{\mathrm{T}}(e,\mathrm{trk}) > 1.0\,\mathrm{GeV} \text{ and } A_{\phi}^{e,\mathrm{trk}} > 0.012$$

with $l = 0.0599$. The performances of both working points are on the same order 10^{-3} and therefore, the previously suggested working point $p_{\mathrm{T}}(e,\mathrm{trk}) > 1.0\,\mathrm{GeV}$ and $A_{\phi}^{e,\mathrm{trk}} > 0.012$ is used. The purity of the signal increases from 4.7 % to 47.4 % and the signal significance from 4.0 to 11.8. The signal region 1E1T, presented in Section 7.3, therefore includes the requirement $A_{\phi}^{e,\mathrm{trk}} > 0.012$ as last step in the event selection - see e.g. Table 7.1.

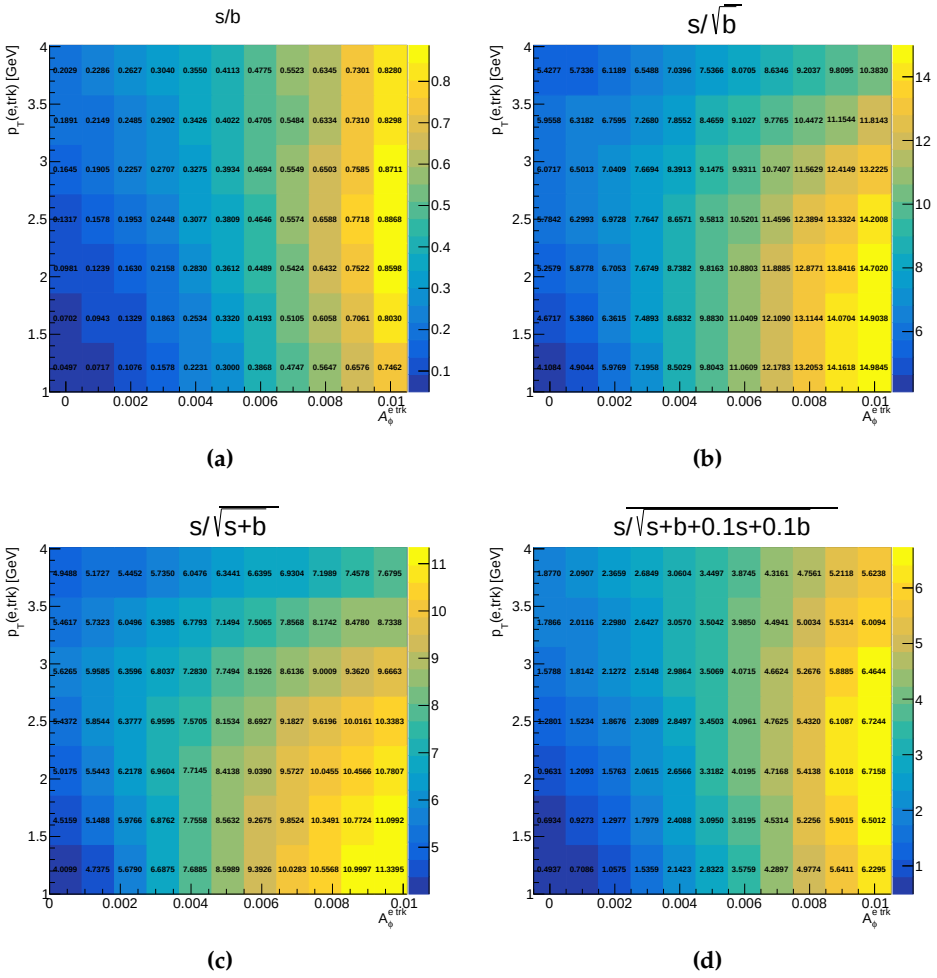

Figure 7.13: Statistical figures of merit: s/b (a), $s/\sqrt{b}$ (b), $s/\sqrt{s+b}$ (c), $s/\sqrt{s+b+(\zeta s)^2+(\zeta b)^2}$ (d) from a 2D scan of tightened requirements on $p_{\mathrm{T}}(e,\mathrm{trk})$ and $A_{\phi}^{e,\mathrm{trk}}$ for the SR-1E1T For (d), a systematic uncertainty of 10 % for signal and background is assumed.

Requirement	Data 18	$\gamma\gamma \to \tau\tau$ 4M	$\gamma\gamma \to \mu\mu$ 7M20	$\gamma\gamma \to \mu\mu$ 20M	$\gamma\gamma \to ee$ 4p5M7	$\gamma\gamma \to ee$ 7M15	$\gamma\gamma \to ee$ 15Mv1	$\gamma\gamma \to$ jets DD	$\gamma\gamma \to$ jets DR	$\gamma\gamma \to$ jets RD	$\gamma\gamma \to$ jets RR	sig/$\sqrt{\text{sig+bkg}}$
pass GRL	4335070.0	23615.5	88094.6	7380.6	177294.7	135156.7	19274.8	35981.6	7677.2	7677.2	12524.5	32.9
$E_{\text{ZDC}}^{A,C} < 1\,\text{TeV}$	1435464.0	23615.5	88094.6	7380.6	177294.7	135156.7	19274.8	35981.6	7677.2	7677.2	12524.5	32.9
HLT hi gg L1TAU1	1094198.0	3294.2	11228.2	1064.3	25735.0	52791.1	12072.2	155.7	5.2	5.4	6.4	10.1
$N_e^{\text{sig}} = 1$	26007.0	589.0	1.9	1.9	321.6	16873.4	4656.3	0.8	0.0	0.1	0.0	3.9
$N_\mu^{\text{sig}} = 0$	25972.0	557.1	0.3	0.1	321.6	16873.4	4656.2	0.8	0.0	0.1	0.0	3.7
$N_{\text{trk}}(\Delta R > 0.1 \text{ from } e) = 1$	16476.0	428.0	0.2	0.1	284.5	12673.6	2806.5	0.2	0.0	0.0	0.0	3.4
Cluster veto	15774.0	421.0	0.2	0.1	284.3	12586.7	2743.3	0.1	0.0	0.0	0.0	3.3
$\sum \text{charge} = 0$	15690.0	419.6	0.2	0.1	284.1	12544.6	2710.3	0.1	0.0	0.0	0.0	3.3
$p_{\text{T}}^{(e,\text{trk})} > 1\,\text{GeV}$	10204.0	388.9	0.1	0.1	221.2	7998.9	2096.8	0.1	0.0	0.0	0.0	3.8
$p_{\text{T}}^{(e,\text{trk},\gamma)} > 1\,\text{GeV}$	8349.0	370.6	0.1	0.1	200.4	6335.4	1685.1	0.1	0.0	0.0	0.0	4.0
$p_{\text{T}}^{(e,\text{trk,cluster})} > 1\,\text{GeV}$	7056.0	339.3	0.1	0.1	172.4	5280.7	1366.9	0.1	0.0	0.0	0.0	4.0
$p_{\text{T}}^{(e,\text{trk})} > 2.0\,\text{GeV}$	2973.0	281.7	0.0	0.0	26.3	1961.1	882.8	0.1	0.0	0.0	0.0	5.0
$A_\phi^{e,\text{trk}} > 0.004$	1062.0	269.8	0.0	0.0	10.2	662.8	280.0	0.1	0.0	0.0	0.0	7.7

Table 7.14: Overview of the event counts after the selection requirements for SR-1E1T-pure applied sequentially. MC samples are normalized to $\mathcal{L} = 1.44\,\text{fb}^{-1}$.

Requirement	Data 18	$\gamma\gamma \to \tau\tau$ 4M	$\gamma\gamma \to \mu\mu$ 7M20	$\gamma\gamma \to \mu\mu$ 20M	$\gamma\gamma \to ee$ 4p5M7	$\gamma\gamma \to ee$ 7M15	$\gamma\gamma \to ee$ 15Mv1	$\gamma\gamma \to$ jets DD	$\gamma\gamma \to$ jets DR	$\gamma\gamma \to$ jets RD	$\gamma\gamma \to$ jets RR	sig/$\sqrt{\text{sig+bkg}}$
pass GRL	4335070.0	23615.5	88094.6	7380.6	177294.7	135156.7	19274.8	35981.6	7677.2	7677.2	12524.5	32.9
$E_{\text{ZDC}}^{A,C} < 1\,\text{TeV}$	1435464.0	23615.5	88094.6	7380.6	177294.7	135156.7	19274.8	35981.6	7677.2	7677.2	12524.5	32.9
HLT hi gg L1TAU1	1094198.0	3294.2	11228.2	1064.3	25735.0	52791.1	12072.2	155.7	5.2	5.4	6.4	10.1
$N_e^{\text{sig}} = 1$	26007.0	589.0	1.9	1.9	321.6	16873.4	4656.3	0.8	0.0	0.1	0.0	3.9
$N_\mu^{\text{sig}} = 0$	25972.0	557.1	0.3	0.1	321.6	16873.4	4656.2	0.8	0.0	0.1	0.0	3.7
$N_{\text{trk}}(\Delta R > 0.1 \text{ from } e) = 1$	16476.0	428.0	0.2	0.1	284.5	12673.6	2806.5	0.2	0.0	0.0	0.0	3.4
Cluster veto	15774.0	421.0	0.2	0.1	284.3	12586.7	2743.3	0.1	0.0	0.0	0.0	3.3
$\sum \text{charge} = 0$	15690.0	419.6	0.2	0.1	284.1	12544.6	2710.3	0.1	0.0	0.0	0.0	3.3
$p_{\text{T}}^{(e,\text{trk})} > 1\,\text{GeV}$	10204.0	388.9	0.1	0.1	221.2	7998.9	2096.8	0.1	0.0	0.0	0.0	3.8
$p_{\text{T}}^{(e,\text{trk},\gamma)} > 1\,\text{GeV}$	8349.0	370.6	0.1	0.1	200.4	6335.4	1685.1	0.1	0.0	0.0	0.0	4.0
$p_{\text{T}}^{(e,\text{trk,cluster})} > 1\,\text{GeV}$	7056.0	339.3	0.1	0.1	172.4	5280.7	1366.9	0.1	0.0	0.0	0.0	4.0
$A_\phi^{e,\text{trk}} > 0.008$	741.0	308.8	0.1	0.0	6.7	399.8	140.0	0.1	0.0	0.0	0.0	10.6

Table 7.15: Overview of the event counts after the selection requirements for SR-1E1T-highpure applied sequentially. MC samples are normalized to $\mathcal{L} = 1.44\,\text{fb}^{-1}$.

$A_\phi^{e,\mathrm{trk}} >$	Confidence Interval	Interval length
0.008	$[-0.0396, 0.0230]$	0.0626
0.009	$[-0.0396, 0.0223]$	0.0619
0.010	$[-0.0391, 0.0217]$	0.0609
0.011	$[-0.0389, 0.0213]$	0.0602
0.012	$[-0.0389, 0.0210]$	0.0599
0.013	$[-0.0390, 0.0208]$	0.0597
0.014	$[-0.0389, 0.0206]$	0.0594
0.015	$[-0.0392, 0.0205]$	0.0597

Table 7.16: CI boundaries and lengths for the determination of a_τ from extended maximum likelihood fits to the electron p_T distribution in the SR-1E1T, with additional requirements on $A_\phi^{e,\mathrm{trk}}$, calculated using TRExFitter. The most sensitive requirement is marked in green color and corresponds to $A_\phi^{e,\mathrm{trk}} > 0.014$ and the used requirement is marked in blue color and corresponds to $A_\phi^{e,\mathrm{trk}} > 0.012$.

7.5 DEFINITION OF $\gamma\gamma \to \mu\mu$ AND $\gamma\gamma \to ee$ CONTROL REGIONS

A di-muon and a dielectron control region (CR) are defined to check the modelling of the $\gamma\gamma \to \mu\mu$ and $\gamma\gamma \to ee$ background.

CR-2M-excl

The control region for the $\gamma\gamma \to \mu\mu$ process is called CR-2M-excl. The same preselection is performed for the control region as for the signal regions: passing the GRL and $E_\mathrm{ZDC}^{A/C} < 1\,\mathrm{TeV}$. The muon-based trigger `HLT_mu4_hi_upc_FgapAC3_L1MU4_VTE50` is used. Two signal muons are required to select $\gamma\gamma \to \mu\mu$ events. Events with more than two baseline muons are rejected - using the looser muon definition for a strong suppression of background events with non-prompt muons or cosmic muons. Furthermore, only tracks inside the cones of $\Delta R < 0.1$ from the two muons are considered. Due to charge conservation, the muons need to be of opposite charge. Additionally, the invariant mass of the muon system is chosen to be $m_{\mu\mu} > 11\,\mathrm{GeV}$ which is required to suppress contamination from exclusive upsilon $\Upsilon(nS) \to \mu\mu$ background [60]. However, in the distribution of the invariant mass of lepton and track(s) systems in the SRs, the $\gamma\gamma \to \mu\mu$ background is located between 2 GeV and 17 GeV with its highest contribution at around 8 GeV. The selection is summarized in Table 7.17. The event counts after the different requirements are shown in Table 7.18.
In the CR-2M-excl, a very high $\gamma\gamma \to \mu\mu$ purity and large statistics is obtained with 21838.8 expected $\gamma\gamma \to \mu\mu$ events vs. a $\gamma\gamma \to \tau\tau$ signal contamination of 17.5 events and no $\gamma\gamma \to ee$ and $\gamma\gamma \to q\bar{q}$ events expected. The signal contamination is only around 0.1 % coming from muons pairs from the di-tau decay which are not explicitly removed by a further requirement. The total number of expected events is with 21856.3 events

Requirement	Data 18	$\gamma\gamma \to \tau\tau$ 4M	$\gamma\gamma \to \mu\mu$ 7M20	$\gamma\gamma \to \mu\mu$ 20M	$\gamma\gamma \to ee$ 4p5M7	$\gamma\gamma \to ee$ 7M15	$\gamma\gamma \to ee$ 15Mv1	$\gamma\gamma \to$ jets DD	$\gamma\gamma \to$ jets DR	$\gamma\gamma \to$ jets RD	$\gamma\gamma \to$ jets RR	sig/bkg in %
pass GRL	4335070.0	23615.5	89052.9	7554.2	177294.7	135156.7	19274.8	35981.6	7677.2	7677.2	12524.5	4.8
$E_{\mathrm{ZDC}}^{A,C} < 1$ TeV	1435464.0	23615.5	89052.9	7554.2	177294.7	135156.7	19274.8	35981.6	7677.2	7677.2	12524.5	4.8
HLT mu4 trigger	60313.0	1214.5	48651.8	6142.1	0.0	0.1	0.3	36.0	5.7	6.1	9.5	2.2
$N_{\mu}^{\mathrm{baseline}} = 2$	46189.0	100.0	42426.3	4857.4	0.0	0.0	0.1	1.7	0.2	0.3	0.4	0.2
$N_{\mu}^{\mathrm{sig}} = 2$	33259.0	24.4	30835.8	4047.8	0.0	0.0	0.0	0.2	0.0	0.0	0.0	0.1
$N_{\mathrm{trk}}(\Delta R > 0.1 \text{ from } \mu) = 0$	32623.0	24.2	30792.6	4028.9	0.0	0.0	0.0	0.0	0.0	0.0	0.0	0.1
$m_{\mu\mu} > 11$ GeV	20104.0	17.5	17811.5	4027.3	0.0	0.0	0.0	0.0	0.0	0.0	0.0	0.1
$\sum$ charge $= 0$	20104.0	17.5	17811.5	4027.3	0.0	0.0	0.0	0.0	0.0	0.0	0.0	0.1

Table 7.18: Overview of the event counts after the selection requirements for CR-2M-excl applied sequentially. Simulated samples are normalized to $\mathcal{L} = 1.44$ fb^{-1}.

about 8 % higher than the number of observed events with 20104.0 events which needs to be investigated in further studies.

Requirement	CR-2M-excl	CR-2E-excl
pass GRL	`pass_GRL`	
E_{ZDC}^{A} & E_{ZDC}^{C}	< 1 TeV	
Trigger	HLT mu4 trigger	HLT hi gg L1TAU1
$N_{\ell}^{\mathrm{baseline}}$	μ: 2	e: 2
N_{ℓ}^{sig}	μ:2	e:2
$N_{\mathrm{trk}}(\Delta R > 0.1 \text{ from } \ell)$	`0`	
$\sum$ charge	`0`	
$m_{\ell\ell}$	> 11 GeV	

Table 7.17: Selection criteria for the di-muon (CR-2M-excl) and dielectron (CR-2E-excl) control regions. The "-excl" suffix indicates the statistical exclusivity to the CRs.

CR-2E-excl

The control region for the $\gamma\gamma \to ee$ process is called CR-2E-excl. The same preselection is performed for the control region as for the signal regions: passing the GRL and $E_{\mathrm{ZDC}}^{A/C} < 1$ TeV. The single τ-lepton trigger `HLT_hi_upc_FgapAC3_hi_gg_upc_L1TAU1_TE4_VTE200` is used. Two signal electrons are required to select $\gamma\gamma \to ee$ events. Events with more than two baseline electrons are rejected - using the looser electron definition for a strong suppression of background events with non-prompt electrons. Furthermore, only tracks inside the cones of $\Delta R < 0.1$ from the two electrons are considered. Due to charge conservation, the electrons need to be of opposite charge. Additionally, the invariant mass of the electron system is chosen to be $m_{ee} > 11$ GeV which is required to suppress contamination from exclusive upsilon $\Upsilon(nS) \to ee$ background. The selection is summarized in Table 7.17. The event counts after the different requirements are shown in Table 7.19.
In the CR-2E-excl, a very high $\gamma\gamma \to ee$ purity and large statistics is obtained with 11663.6 expected $\gamma\gamma \to ee$ events vs. a $\gamma\gamma \to \tau\tau$ signal contamination of 11.4 events

and no $\gamma\gamma \to \mu\mu$ and $\gamma\gamma \to q\bar{q}$ events expected. The signal contamination is $< 0.1\,\%$ coming from electron pairs from the di-tau decay which are not explicitly removed by a further requirement. The total number of expected events is with 11675.0 events about 15 % higher than the number of observed events with 9951.0 events. This discrepancy needs to be further investigated.

Requirement	Data 18	$\gamma\gamma \to \tau\tau$ 4M	$\gamma\gamma \to \mu\mu$ 7M20	$\gamma\gamma \to \mu\mu$ 20M	$\gamma\gamma \to ee$ 4p5M7	$\gamma\gamma \to ee$ 7M15	$\gamma\gamma \to ee$ 15Mv1	$\gamma\gamma \to$ jets DD	$\gamma\gamma \to$ jets DR	$\gamma\gamma \to$ jets RD	$\gamma\gamma \to$ jets RR	sig/bkg in %
pass GRL	4335070.0	23615.5	89052.9	7554.2	177294.7	135156.7	19274.8	35981.6	7677.2	7677.2	12524.5	4.8
$E_{\mathrm{ZDC}}^{A,C} < 1$ TeV	1435464.0	23615.5	89052.9	7554.2	177294.7	135156.7	19274.8	35981.6	7677.2	7677.2	12524.5	4.8
HLT hi gg L1TAU1	1094198.0	3294.2	11561.0	1154.7	25735.0	52791.1	12072.2	155.7	5.2	5.4	6.4	3.2
$N_e^{\mathrm{baseline}} = 2$	23595.0	89.6	0.1	0.5	955.0	17032.6	7620.5	0.7	0.0	0.0	0.0	0.3
$N_e^{\mathrm{sig}} = 2$	13647.0	15.1	0.0	0.1	6.0	9802.3	5621.3	0.0	0.0	0.0	0.0	0.1
$N_{\mathrm{trk}}(\Delta R > 0.1 \text{ from } \mu) = 0$	13647.0	15.1	0.0	0.0	6.0	9802.3	5621.3	0.0	0.0	0.0	0.0	0.1
$m_{ee} > 11\,\mathrm{GeV}$	9963.0	11.5	0.0	0.0	0.0	6055.6	5618.0	0.0	0.0	0.0	0.0	0.1
$\sum$ charge $= 0$	9951.0	11.4	0.0	0.0	0.0	6052.6	5611.0	0.0	0.0	0.0	0.0	0.1

Table 7.19: Overview of the event counts after the selection requirements for CR-2E-excl applied sequentially. Simulated samples are normalized to $\mathcal{L} = 1.44\ \mathrm{fb}^{-1}$.

8

ESTIMATION OF THE BACKGROUNDS FOR $\gamma\gamma \to \tau\tau$ PRODUCTION

The precise estimation of the background yields and their shapes of the kinematic distributions, which are used in the maximum likelihood fits, is important for a good signal extraction. The main backgrounds to the $\gamma\gamma \to \tau\tau$ signal result from $\gamma\gamma \to ee$ or $\gamma\gamma \to \mu\mu$ production, smaller backgrounds to be investigated are $\gamma\gamma \to q\bar{q}$ production and the photonuclear background. The estimation of the background contributions is discussed in Section 8.1, the comparison of the predictions to data in the five SRs are reported in Section 8.2. The observation of the $\gamma\gamma \to \tau\tau$ production in Pb+Pb collisions is discussed in Section 8.3.

8.1 BACKGROUND ESTIMATION

The estimation of the dominating backgrounds is performed using the simulated MC samples described in Section 4.2. The modeling of $\gamma\gamma \to \mu\mu$ and $\gamma\gamma \to ee$ production in simulation is validated in dedicated control regions, CR-2M-excl and CR-2E-excl- as defined in Section 7.5. The contribution of the $\gamma\gamma \to q\bar{q}$ background process is expected to be minor in all SRs (c.f Section 7.3) and thus, no explicit validation of its modeling from simulation is performed. A non-UPC process, where low-active photonuclear particles are produced, is estimated with a data driven method [60]. The so-called photonuclear background is found to be small as discussed in Appendix A.2 and thus neglected in the analysis presented in this thesis.

8.1.1 *Validation of the $\gamma\gamma \to \mu\mu$ Background Estimate*

The background in the muon based SRs is dominated by the $\gamma\gamma \to \mu\mu$ process. The prediction for the $\gamma\gamma \to \mu\mu$ process is obtained by simulation and needs to be validated with data. The dedicated validation region CR-2M-excl is defined in Section 7.5 to investigate the modeling of this process, both in terms of the total number of events as well as for different kinematic distributions. The event counts for CR-2M-excl are shown in Table 7.18 which was discussed in Section 7.5. The number of expected events was found to be around 8 % higher than the number of observed events while the statistical uncertainty in the data only amounts to around 0.7 %. Systematic uncertainties need to be considered to cover the observed discrepancy. In following studies, when systematic uncertainties are implemented, the photon flux uncertainty and its reweighting procedure (see Table 4.1) could be investigated in detail which might explain the differences. The modeling of several kinematic distributions is checked by comparing the yields to

data in each bin. A correction factor is introduced to scale the prediction of $\gamma\gamma \to \mu\mu$ to data. The correction factor $CF_{\gamma\gamma\to\mu\mu}$ is estimated to be

$$CF_{\gamma\gamma\to\mu\mu} = \frac{N_{\text{data}} - N_{\gamma\gamma\to\tau\tau}}{N_{\gamma\gamma\to\mu\mu}} = 0.9197 \tag{8.1}$$

using the yield for data N_{data} and the yields N_{process} for the respective process $\gamma\gamma \to \tau\tau$ and $\gamma\gamma \to \mu\mu$ in Table 7.18. The events in the $\gamma\gamma \to \mu\mu$ production are scaled with $CF_{\gamma\gamma\to\mu\mu}$ in the following figures for a better comparability of the shape of several kinematic distributions.
The shapes of several kinematic distributions are displayed in Figures 8.1- 8.3, where the transverse momenta, η and ϕ values of the leading and subleading muon are shown in Figure 8.1, angular differences between the two muons in Figure 8.2, and variables characterizing the di-muon system in Figure 8.3. Overall, good agreement of the predictions with the data is observed in most distributions. In the acoplanarity, a clear slope is observed in the data/prediction ratio indicating a mismodeling for the acoplanarity. The uncertainties on the ratio σ_R for each bin i are calculated by

$$\sigma_{R_i} = R_i \frac{\sqrt{N_{\text{data},i}}}{N_{\text{data},i}}$$

with the data/prediction ratio $R_i = N_{\text{data},i}/N_{\text{mc},i}$, and the respective data yield $N_{\text{data},i}$. The hashed bars gives the MC uncertainty on the prediction calculated as the sum of the weights for each contribution squared normalized to the number of expected events in the bin. For bins with high statistical uncertainties and fluctuations, visualized in the ratio panel, a rebinning procedure would be needed to reduce these fluctuations as in ΔR and $\Delta\phi$ in Figure 8.2 for example. Though, within these uncertainties the agreement is reasonable.
In summary, the comparison between the data from 2018 and the estimated background through MC simulation in the $\gamma\gamma \to \mu\mu$ channel shows a good agreement for the shapes of the kinematic distributions. The prediction is systematically higher by 8 % than the measured yields which is corrected by applying the correction factor $CF_{\gamma\gamma\to\mu\mu} = 0.9197$. The background prediction from MC simulation for the $\gamma\gamma \to \mu\mu$ background can be considered as validated.

8.1.2 *Validation of the $\gamma\gamma \to ee$ Background Estimate*

The background of the electron based SRs is dominated by the $\gamma\gamma \to ee$ process. The prediction for the $\gamma\gamma \to ee$ process is obtained by simulation and needs to be validated with data. The dedicated validation region CR-2E-excl is defined in Section 7.5 to investigate the modeling of this process, both in terms of the total number of events as well as for different kinematic distributions. The event counts for CR-2M-excl are shown in Table 7.19 which was discussed in Section 7.5. The number of expected events was found to be around 15 % higher than the number of observed events while the statistical uncertainty in the data only amounts to around 0.7 %. Similar to the $\gamma\gamma \to \mu\mu$ background process, systematic uncertainties need to be considered to estimate the observed discrepancy. Here, the photon flux uncertainty and its reweighting procedure (see Table 4.1) should also be investigated in detail which might explain the differences.

This is, however, not done within this thesis.
The modeling of several kinematic distributions is checked by comparing the yields to data in each bin. A correction factor is introduced to scale the prediction of $\gamma\gamma \to ee$ to data. The correction factor $CF_{\gamma\gamma\to ee}$ is estimated to be

$$CF_{\gamma\gamma\to ee} = \frac{N_{\text{data}} - N_{\gamma\gamma\to\tau\tau}}{N_{\gamma\gamma\to ee}} = 0.8522 \tag{8.2}$$

using the yield for data N_{data} and the yields N_{process} for the respective process $\gamma\gamma \to \tau\tau$ and $\gamma\gamma \to ee$ in Table 7.19. The events in the $\gamma\gamma \to ee$ production are scaled with $CF_{\gamma\gamma\to ee}$ in the following control figures for a better comparability of the shape of several kinematic distributions.
The shapes of several kinematic distributions are displayed in Figures 8.4- 8.6, where the transverse momenta, η and ϕ values of the leading and subleading electrons are shown in Figure 8.4, angular differences between the two electrons in Figure 8.5, and variables characterizing the di-electron system in Figure 8.6. Overall, good agreement of the predictions with the data is observed in most distributions. Again, as for the simulation of the $\gamma\gamma \to \mu\mu$ process, a clear slope is observed for the acoplanarity in the data/prediction ratio indicating a mismodeling for the acoplanarity. Similarly, bins with high statistical uncertainties and fluctuations in the ratio are observed where a rebinning procedure would be needed to reduce these fluctuations e.g. for the pseudorapidity $y(ee)$ and $\Delta R(ee)$ in Figure 8.6. Small discrepancies are found for high $|\eta|$ for the leading and the subleading electron, propagated to $|\Delta\eta(ee)|$. Due to the large uncertainties and the small number of event counts, this difference is negligible. Similar behavior is observed for the p_{T} of the di-electron system $p_{\text{T}}(ee)$ showing large uncertainties. Though, within uncertainties the agreement of all kinematic distributions, except for the acoplanarity, are reasonable.
In summary, the comparison between the data from 2018 and the estimated background through MC simulation in the $\gamma\gamma \to ee$ channel shows a good agreement for the shape of the kinematic distributions. The prediction is systematically higher by 15 % than the measured yields which is corrected for by the application of the correction factor $CF_{\gamma\gamma\to ee} = 0.8522$. The background prediction from MC simulation for the $\gamma\gamma \to ee$ background can be considered as validated.

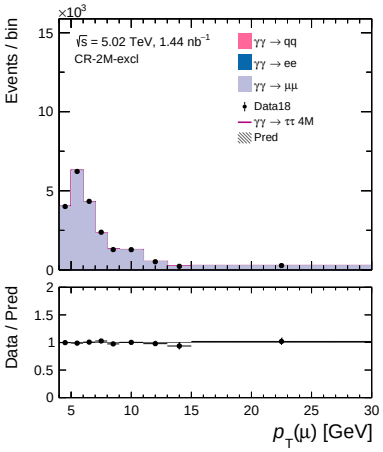

(a) p_{T} of the leading muon

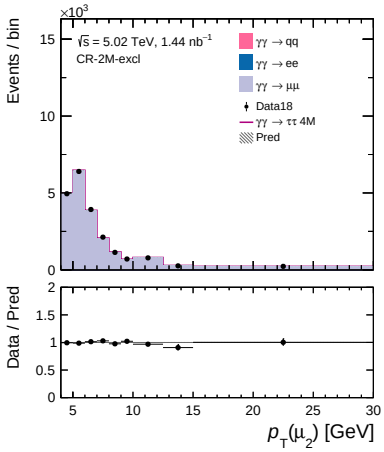

(b) p_{T} of the sub-leading muon

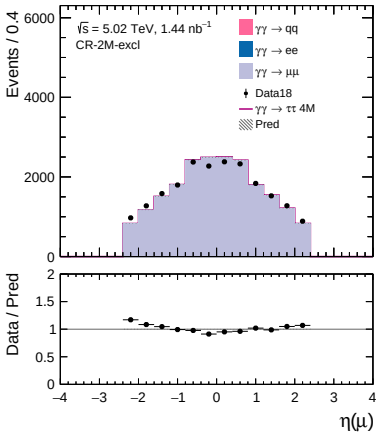

(c) η of the leading muon

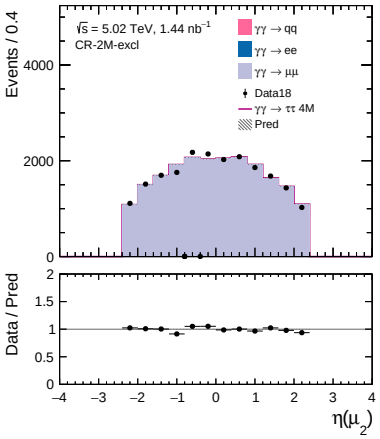

(d) η of the sub-leading muon

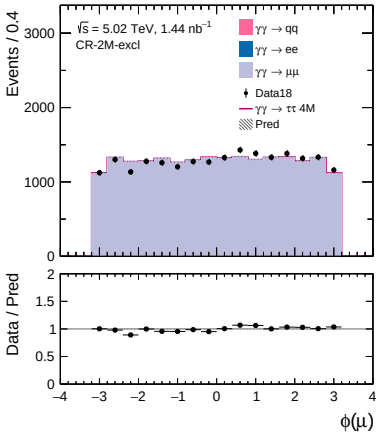

(e) ϕ of the leading muon

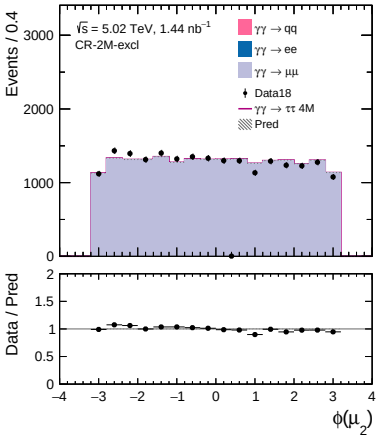

(f) ϕ of the sub-leading muon

Figure 8.1: Kinematic distributions of transverse momentum p_{T} (a)/(b), angle η (c)/(d) and angle ϕ (e)/(f) of the leading (left) and subleading (right) muon in the di-muon CR, CR-2M-excl. The data is shown as black dots, the prediction as stacked histogram from the signal process $\gamma\gamma \to \tau\tau$ (pink solid line) and the background processes $\gamma\gamma \to q\bar{q}$ (pink), $\gamma\gamma \to ee$ (blue) and $\gamma\gamma \to \mu\mu$ (violet). The ratio between the data and the prediction is shown in the lower panel. The applied selection criteria are given in Table 7.17.

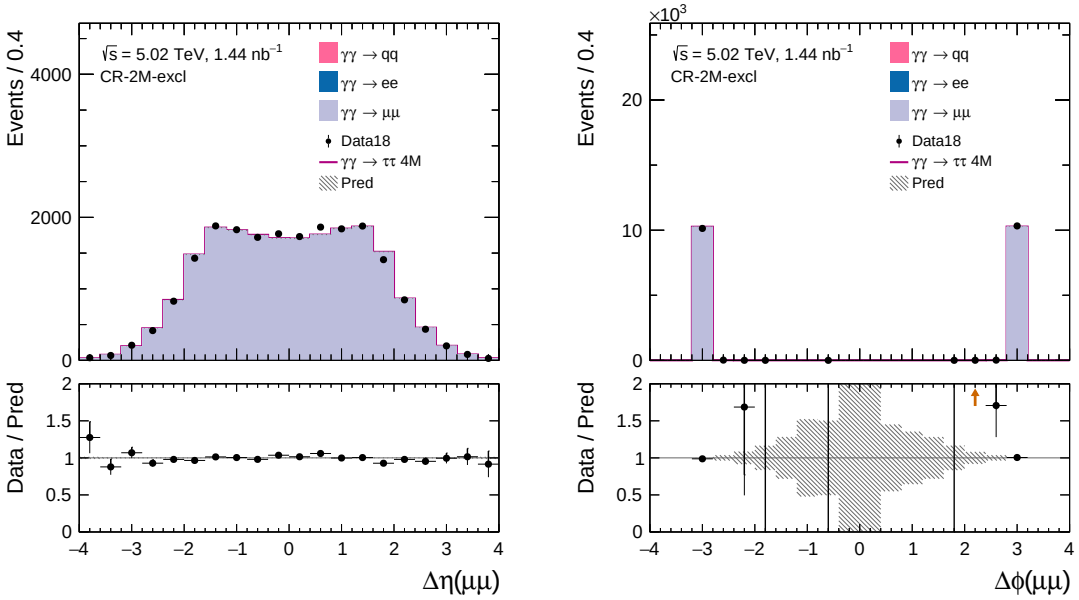

(a) $\Delta\eta$ **(b)** $\Delta\phi$

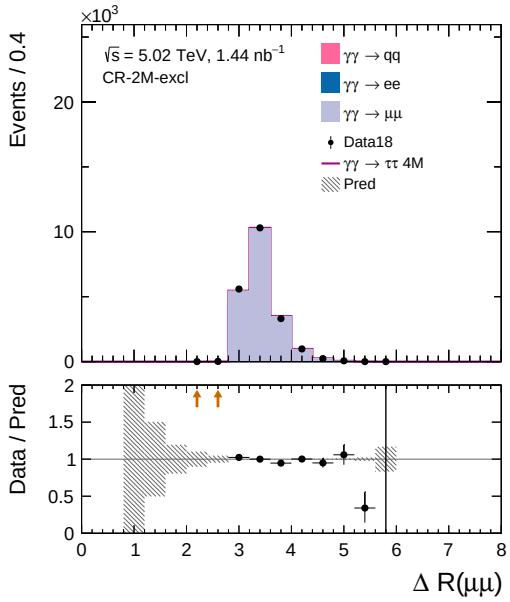

(c) ΔR

Figure 8.2: Kinematic distributions for $\Delta\eta$ (a), $\Delta\phi$ (b) and ΔR (c) of the two muons in the CR-2M-excl. The data is shown as black dots, the prediction as stacked histogram from the signal process $\gamma\gamma \to \tau\tau$ (pink solid line) and the background processes $\gamma\gamma \to q\bar{q}$ (pink), $\gamma\gamma \to ee$ (blue) and $\gamma\gamma \to \mu\mu$ (violet). The ratio between the data and the prediction is shown in the lower panel. The applied selection criteria are given in Table 7.17.

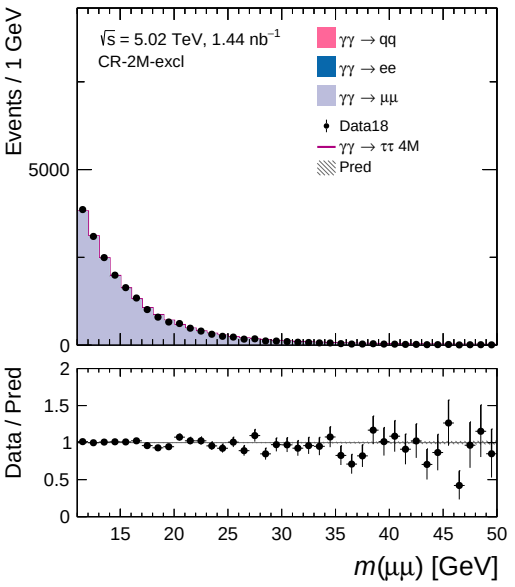

(a) Invariant mass $m_{\mu\mu}$

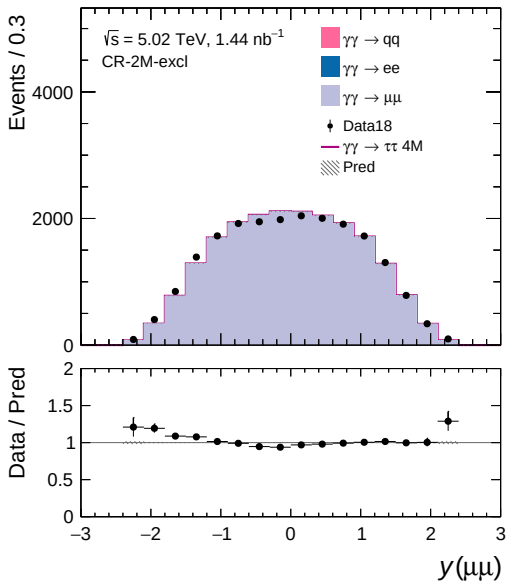

(b) Pseudorapidity $y_{\mu\mu}$

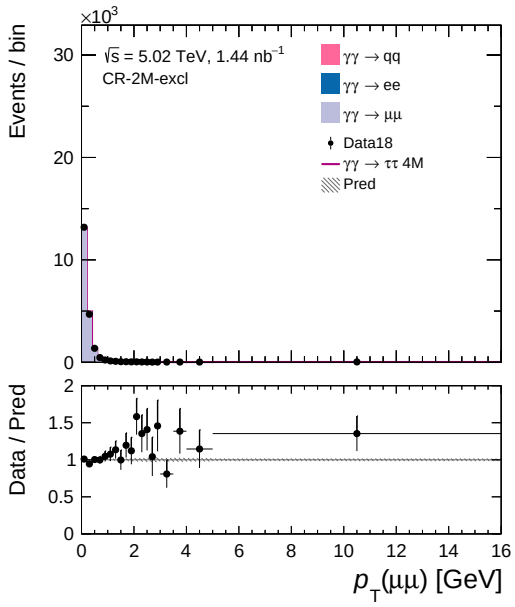

(c) Transverse momentum $p_{\mathrm{T}}(\mu\mu)$

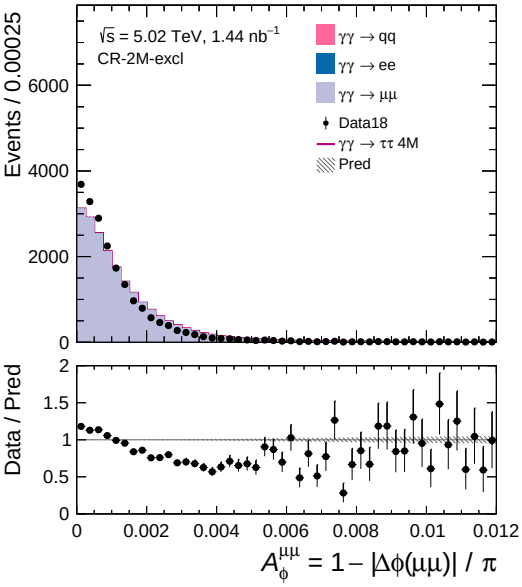

(d) Acoplanarity $A_{\phi}^{\mu\mu}$

Figure 8.3: Kinematic distributions for the invariant mass $m_{\mu\mu}$ (a), the pseudorapidity $y_{\mu\mu}$ (b), the transverse momentum $p_{\mathrm{T}}(\mu\mu)$ (c) and the acoplanarity $A_{\phi}^{\mu\mu}$ (d) of the two muons in the CR-2M-excl. The data is shown as black dots, the prediction as stacked histogram from the signal process $\gamma\gamma \to \tau\tau$ (pink solid line) and the background processes $\gamma\gamma \to q\bar{q}$ (pink), $\gamma\gamma \to ee$ (blue) and $\gamma\gamma \to \mu\mu$ (violet). The ratio between the data and the prediction is shown in the lower panel. The applied selection criteria are given in Table 7.17.

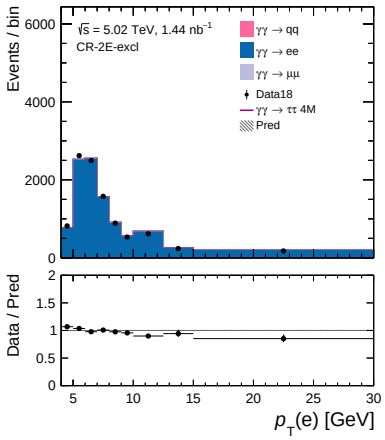

(a) p_{T} of the leading electron

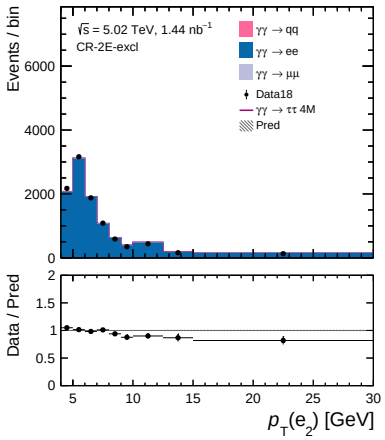

(b) p_{T} of the sub-leading electron

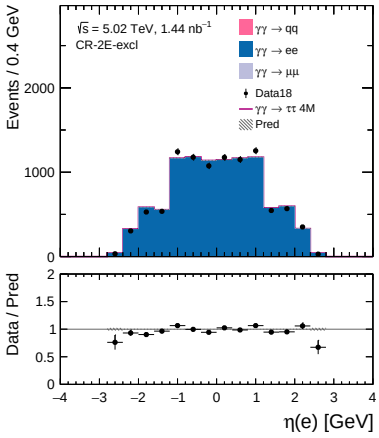

(c) η of the leading electron

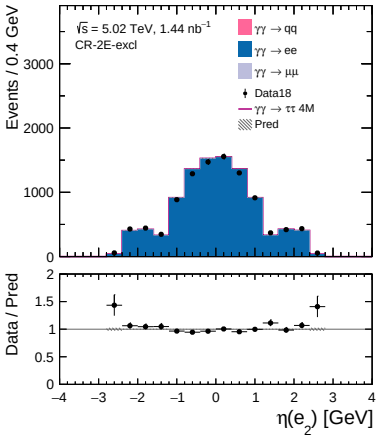

(d) η of the sub-leading electron

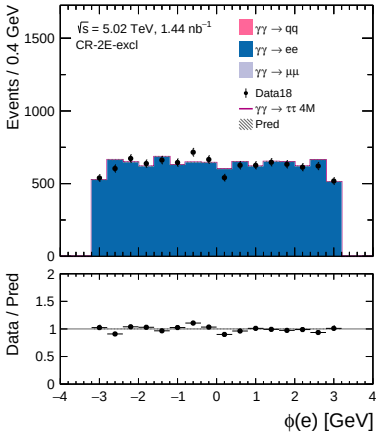

(e) ϕ of the leading electron

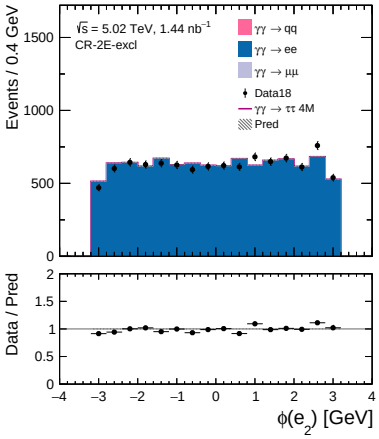

(f) ϕ of the sub-leading electron

Figure 8.4: Kinematic distributions of transverse momentum p_{T} (a)/(b), angle η (c)/(d) and angle ϕ (e)/(f) of the leading (left) and subleading (right) electron in the di-electron CR, CR-2E-excl. The data is shown as black dots, the prediction as stacked histogram from the signal process $\gamma\gamma \to \tau\tau$ (pink solid line) and the background processes $\gamma\gamma \to q\bar{q}$ (pink), $\gamma\gamma \to ee$ (blue) and $\gamma\gamma \to \mu\mu$ (violet). The ratio between the data and the prediction is shown in the lower panel. The applied selection criteria are given in Table 7.17.

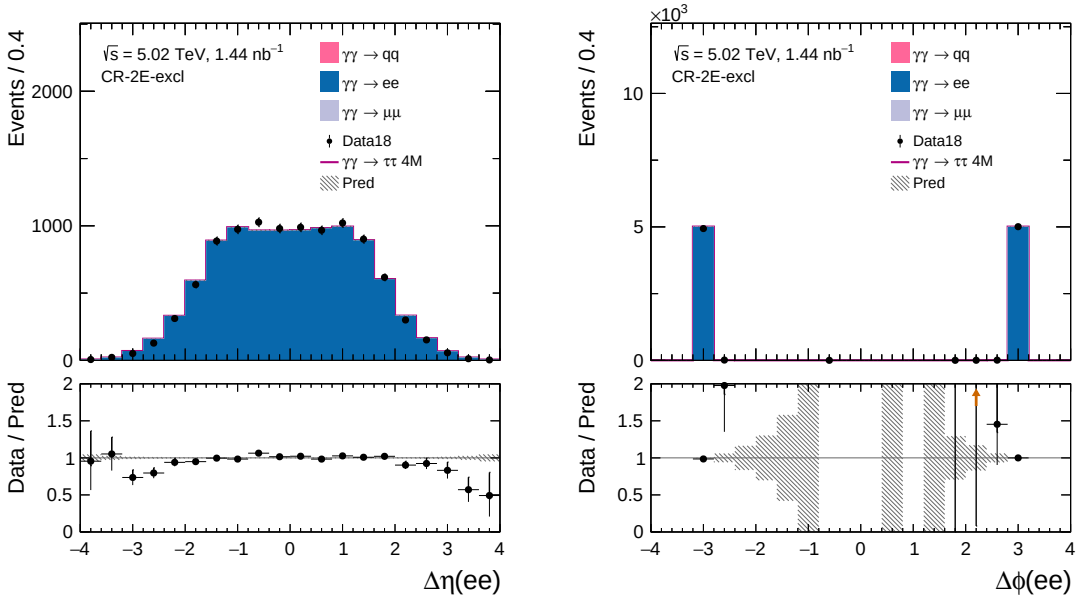

(a) $\Delta\eta$ **(b)** $\Delta\phi$

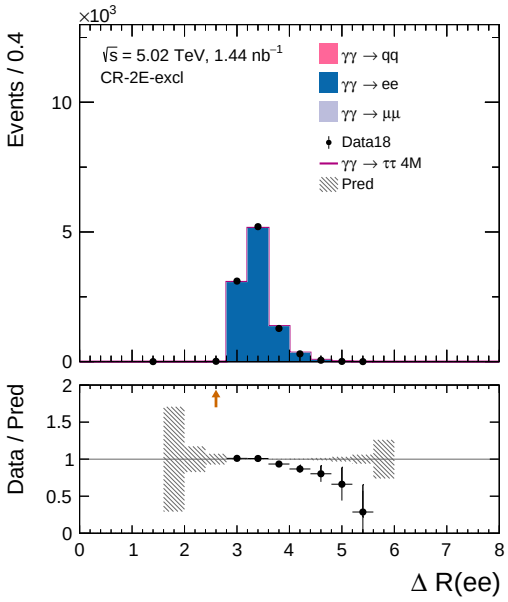

(c) ΔR

Figure 8.5: Kinematic distributions for $\Delta\eta$ (a), $\Delta\phi$ (b) and ΔR (c) of the two electrons in the CR-2E-excl. The data is shown as black dots, the prediction as stacked histogram from the signal process $\gamma\gamma \to \tau\tau$ (pink solid line) and the background processes $\gamma\gamma \to q\bar{q}$ (pink), $\gamma\gamma \to ee$ (blue) and $\gamma\gamma \to \mu\mu$ (violet). The ratio between the data and the prediction is shown in the lower panel. The applied selection criteria are given in Table 7.17.

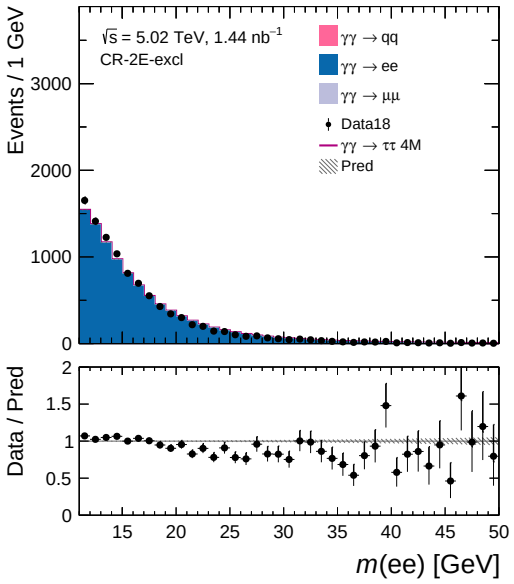

(a) Invariant mass m_{ee}

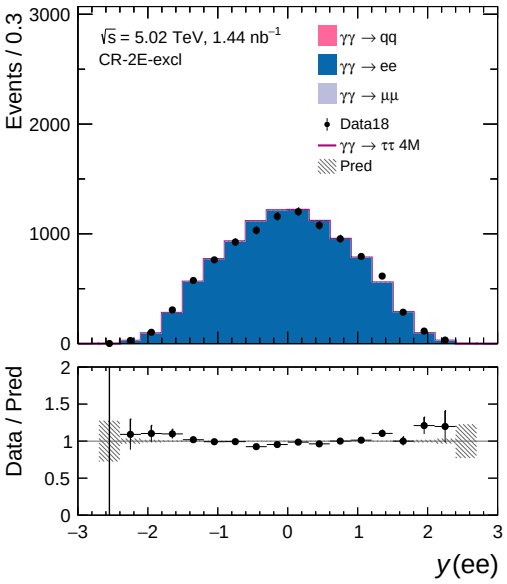

(b) Pseudorapidity y_{ee}

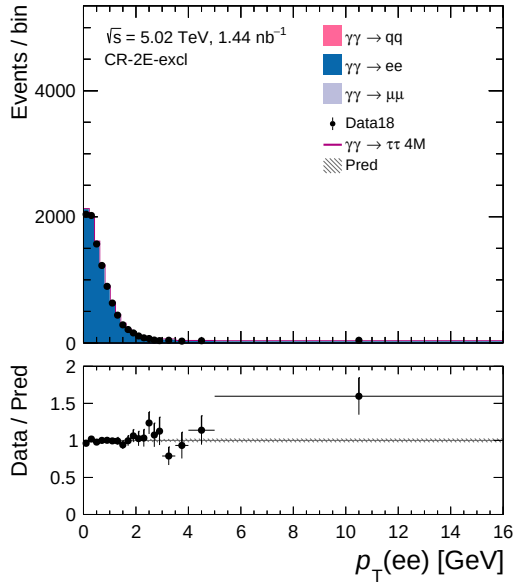

(c) Transverse momentum $p_{\mathrm{T}}(ee)$

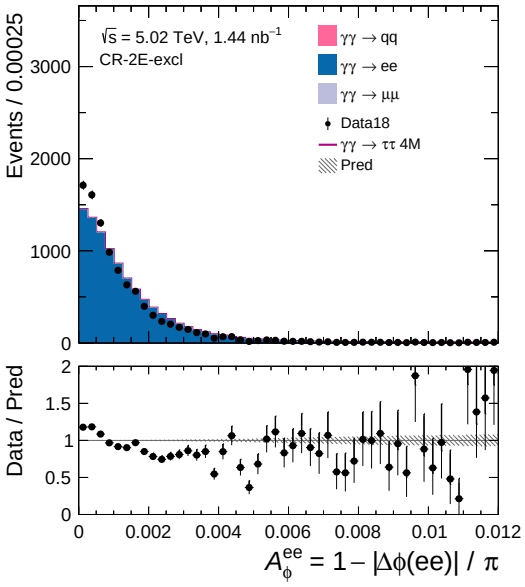

(d) Acoplanarity A_{ϕ}^{ee}

Figure 8.6: Kinematic distributions for the invariant mass m_{ee} (a), the pseudorapidity y_{ee} (b), the transverse momentum $p_{\mathrm{T}}(ee)$ (c) and the acoplanarity A_{ϕ}^{ee} (d) of the two muons in the CR-2E-excl. The data is shown as black dots, the prediction as stacked histogram from the signal process $\gamma\gamma \to \tau\tau$ (pink solid line) and the background processes $\gamma\gamma \to q\bar{q}$ (pink), $\gamma\gamma \to ee$ (blue) and $\gamma\gamma \to \mu\mu$ (violet). The ratio between the data and the prediction is shown in the lower panel. The applied selection criteria are given in Table 7.17.

8.2 COMPARISON OF DATA AND PREDICTION IN THE SIGNAL REGIONS

The background and signal estimations are compared to the measured data in 2018 in the SRs defined in Section 7.3, namely SR-1M1T-excl, SR-1M3T-excl, SR-1E1T-excl, SR-1E3T-excl, SR-1M1E-excl. The production cross section of $\gamma\gamma \to \tau\tau$ is blinded in this analysis, such that the given value is within $\pm 10\,\%$ of the real production cross section. The modeling of the $\gamma\gamma \to \mu\mu$ an $\gamma\gamma \to ee$ background in simulation has been validated in the CR-2M-excl and CR-2E-excl, respectively as discussed in Section 8.1. The correction factors for the $\gamma\gamma \to \mu\mu$ and $\gamma\gamma \to ee$ background estimation introduced in Section 8.1.1 and Section 8.1.2, respectively, are not applied in the following studies of this thesis (unless specified otherwise) due to a negligible effect of $< 1\,\%$ on the total prediction for the muon based SRs. In the electron based SRs, the total prediction of signal and background is affected by around 5- 7 % by the inclusion of the $\gamma\gamma \to ee$ correction factor which is still within the $\pm 10\,\%$ signal blinding range and is therefore not considered in the following (unless specified otherwise). For each SR, different kinematic distributions are considered in the comparison. Details are described in the following for each SR separately. In the following, the label "-excl" is dropped for the SRs for simplicity, unless it is needed for clarification.

SR-1M1T

The comparison of prediction and data for the muon based SR-1M1T is shown in Figure 8.7 for the p_{T} (a)/(b), and the angles η (c)/(d) and ϕ (e)/(f) for the respective muon and track, in Figure 8.8 for the invariant mass $m(\mu, \mathrm{trk})$ (a), the pseudorapidity $y(\mu, \mathrm{trk})$ (b), the $p_{\mathrm{T}}(\mu, \mathrm{trk})$ (c) and the acoplanarity $A_{\phi}^{\mu,\mathrm{trk}}$ of the muon and track system and in Figure 8.9 $\Delta\eta$ (a), $\Delta\phi$ (b) and ΔR (c) between the muon and the track.
The prediction of the total number of event counts is in good agreement with the data as discussed in Section 7.3. The contribution of the fully muonic process $\gamma\gamma \to \mu\mu$ is about 11.3 % such that the impact of its modeling discrepancy of 8 % is low. Overall, the prediction is in good agreement with the data and the shape of the prediction describes well the shape observed in data: The kinematic properties p_{T}, η and ϕ of the muon and the track in Figure 8.7 validate the simulation of the decay products. The data over prediction ratio is one within the the uncertainties for most of the bins. A large signal contribution is seen in the plots.
The kinematics of the muon and track system in Figure 8.8 and the position relative to each other, described by $\Delta\eta$, $\Delta\phi$ and ΔR in Figure 8.9 confirm a good modeling of the decay products. The uncertainty of the ratio and the uncertainty of the prediction (hashed line) shown in the lower panel, is larger for bins with little contribution. There, the modeling is also in agreement with the data within the uncertainties.

SR-1M3T

The comparison of prediction and data for the muon based SR-1M3T is shown in Figure 8.10 for the p_{T} (a)/(b), and the angles η (c)/(d) and ϕ (e)/(f) for the respective muon and the leading track, in Figure 8.11 for the invariant mass $m(\mu, \mathrm{trks})$ (a), the pseudorapidity $y(\mu, \mathrm{trks})$ (b), the $p_{\mathrm{T}}(\mu, \mathrm{trks})$ (c) and the acoplanarity $A_{\phi}^{\mu,\mathrm{trks}}$ of the muon

and tracks system and in Figure 8.12 $\Delta\eta$ (a), $\Delta\phi$ (b) and ΔR (c) between the muon and the tracks.
The prediction for events in SR-1M3T is slightly larger than the observation in data. Thus, the data to prediction ratio, which is used to evaluate the shape of the prediction is expected to be below one on average. SR-1M3T is extremely pure as the main contribution background $\gamma\gamma \to \mu\mu$ is suppressed to a large extent. The statistic is lower than for SR-1M1T. The relative statistical uncertainty for prediction and the data is thus higher. The $\gamma\gamma \to \tau\tau$ production is needed to describe the data here as well as for SR-1M1T.
The prediction is in good agreement with the data and the shape of the prediction describes well the shape observed in data. They agree within statistical uncertainties with a slight undershoot tendency for the data. The same agreement is found for the ratio of data to prediction. If the actual production cross section of $\gamma\gamma \to \tau\tau$ is larger than its blinded value, the agreement between the prediction of signal and background and data would be not given.

SR-1E1T

The comparison of prediction and data for the electron based SR-1E1T is shown in Figure 8.13 for the p_{T} (a)/(b), and the angles η (c)/(d) and ϕ (e)/(f) for the respective electron and track, in Figure 8.14 for the invariant mass $E_{\mathrm{T}}^{\mathrm{miss}}$ (a), the pseudorapidity $y(e, \mathrm{trk})$ (b), the $p_{\mathrm{T}}(e, \mathrm{trk})$ (c) and the acoplanarity $A_{\phi}^{e,\mathrm{trk}}$ of the electron and track system and in Figure 8.15 $\Delta\eta$ (a), $\Delta\phi$ (b) and ΔR (c) between the electron and the track.
The prediction of the signal and the background process describes the shapes observed in data mostly within statistical uncertainties. A larger contribution of the $\gamma\gamma \to ee$ background process is observed in SR-1E1T.
Two peaks in the $\gamma\gamma \to ee$ production are observed in the distribution of $p_{\mathrm{T}}(\mathrm{trk})$ between 0 GeV and 1.0 GeV and between 2.5 GeV and 3.5 GeV in Figure 8.13, as well as in the distribution of $m(e, \mathrm{trk})$ in Figure 8.14 between 3.0 GeV and 5.0 GeV and between 7.0 GeV and 9.0 GeV. This is in agreement with the distribution of $p_{\mathrm{T}}(e, \mathrm{trk})$, where peaks of the $\gamma\gamma \to ee$ contribution occur between 1.0 GeV and 2.0 GeV and 3.0 GeV and 5.0 GeV. The second peak might be a J/ψ resonance. The resonance found in the prediction is also observed in data. The J/ψ meson has a mass of 3096.900(6) MeV and decays in 5.971(32) % [25] cases into an electron positron pair. The signature of the final state of the $\gamma\gamma \to ee$ is the same as for the J/ψ meson. Thus, this particle could be a candidate for the resonance since the energy range of $p_{\mathrm{T}}(\mathrm{trk})$ is in agreement with the J/ψ mass.
A slope of the data and prediction ratio is observed in the distribution $p_{\mathrm{T}}(e)$ in Figure 8.13 and in $p_{\mathrm{T}}(e, \mathrm{trk})$ in Figure 8.14. The prediction tends to be larger than the observed data in for higher p_{T}. For the pseudorapidity shown in Figure 8.14, the shape of the prediction is shifted towards lower values compared to the observed data.

SR-1E3T

The comparison of prediction and data for the electron based SR-1E3T is shown in Figure 8.16 for the p_{T} (a)/(b), and the angles η (c)/(d) and ϕ (e)/(f) for the respective electron and the leading track, in Figure 8.17 for the invariant mass $m(e, \mathrm{trks})$ (a), the pseudorapidity $y(e, \mathrm{trks})$ (b), the $p_{\mathrm{T}}(e, \mathrm{trks})$ (c) and the acoplanarity $A_{\phi}^{e,\mathrm{trks}}$ of the

electron and tracks system and in Figure 8.18 $\Delta\eta$ (a), $\Delta\phi$ (b) and ΔR (c) between the electron and the tracks.
The predictions in this SR overestimate the data significantly. The prediction overshoots the data by almost a factor of two. The data is described well by the $\gamma\gamma \to ee$ background process only. This results into an average data/prediction ratio of 0.5 for the most bins within statistical uncertainties. However, this can not be explained by the 15 % offset in the normalization for the $\gamma\gamma \to ee$ observed in CR-2E. Additionally, in the other electron based SR-1E1T, the agreement between data and prediction is found to be reasonable. Thus, a cross section sensitivity of a_τ as reason can be excluded. An explanation of the low number of observed data in this SR-1E3T is not found by the now and needs to be further investigated.
However, despite the discrepancy between the prediction and the data in terms of the number of events, a slope of the data and prediction ratio is found in the $p_{\mathrm{T}}(\mathrm{trk})$ and $p_{\mathrm{T}}(e, \mathrm{trk})$ distribution shown in Figure 8.16 and Figure 8.17, respectively. A tendency for lower p_{T} values in the prediction compared to data is observed.

SR-1M1E

The comparison of prediction and data for the fully leptonic SR-1M1E is shown in Figure 8.19 for the p_{T} (a)/(b), and the angles η (c)/(d) and ϕ (e)/(f) for the respective muon and electron, in Figure 8.20 for the invariant mass $m(\mu, e)$ (a), the pseudorapidity $y(\mu, e)$ (b), the $p_{\mathrm{T}}(\mu, e)$ (c) and the acoplanarity $A_\phi^{\mu,e}$ of the muon and electron system and in Figure 8.21 $\Delta\eta$ (a), $\Delta\phi$ (b) and ΔR (c) between the muon and the electron.
The SR-1M1E has the lowest statistics among all SRs, but provides very good signal purity. The number of predicted and observed events in each bin is rather low and has thus a high statistical uncertainty. Due to the low background contribution, the signal process $\gamma\gamma \to \tau\tau$ is seen in data. The prediction is in agreement with the data. The ratio of data to prediction agrees within large statistical uncertainties with one.
The signal and background estimation in SR-1M1E is thus sufficiently modeled within the blinded $\gamma\gamma \to \tau\tau$ production cross section and in good agreement with the observed data.

Overall Agreement between Data and Predictions

For all five signal regions, the modeling and signal and background is mostly in good agreement with the data from 2018. This includes on the one hand the cross-section, namely the number of total expected events and on the other hand, the shape of the kinematic distributions. The agreement between data and prediction is observed within the blinding range of the production cross section except for SR-1E3T. There, an overshoot of the prediction by almost 50 % is observed compared to the data. In the electron SR with one track, SR-1E1T, the prediction of signal and background together is slightly higher than the data. For the low statistic SRs, the agreement is within large statistical uncertainties.

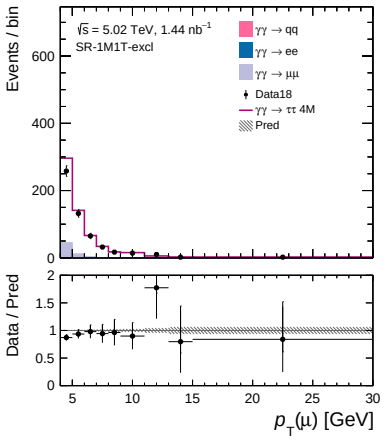

(a) p_{T} of the muon.

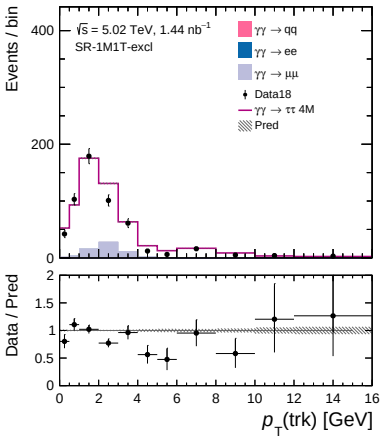

(b) p_{T} of the track.

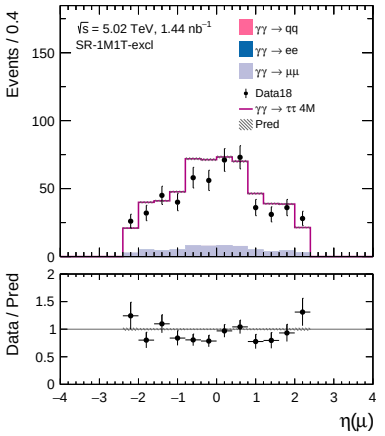

(c) η of the muon.

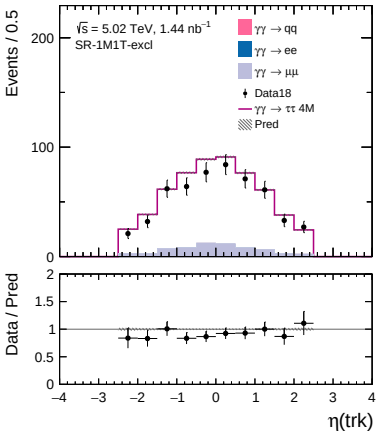

(d) η of the track.

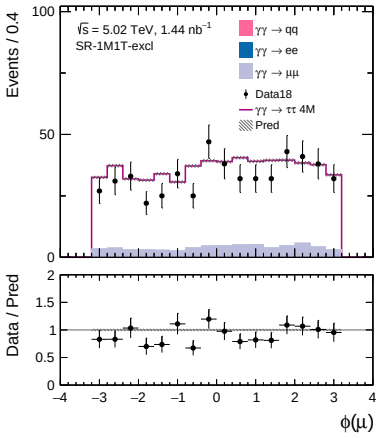

(e) ϕ of the muon.

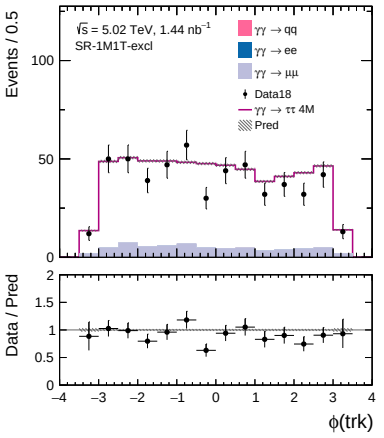

(f) ϕ of the track.

Figure 8.7: Kinematic distributions for the transverse momentum p_{T} of the muon (a) and the track (b), the angle η of the muon (c) and the track (d) and the angle ϕ of the muon (e) and the track (f) in SR-1M1T. The data is shown as black dots, the prediction as stacked histogram from the signal process $\gamma\gamma \to \tau\tau$ (pink solid line) and the background processes $\gamma\gamma \to q\bar{q}$ (pink), $\gamma\gamma \to ee$ (blue) and $\gamma\gamma \to \mu\mu$ (violet). The ratio between the data and the prediction is shown in the lower panel. The applied selection criteria are given in Table 7.1.

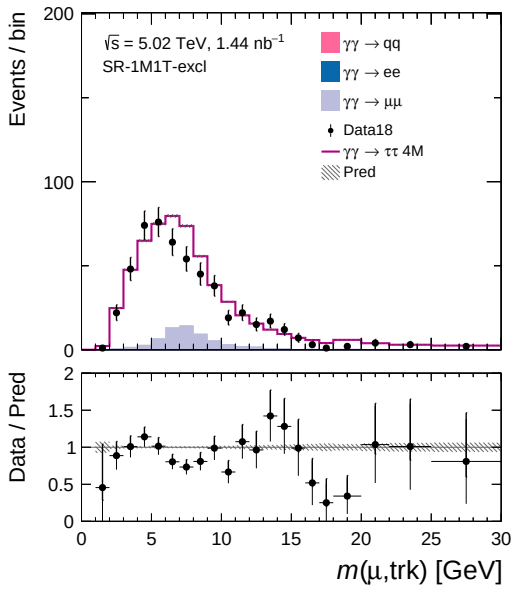

(a) Invariant mass $m(\mu, \mathrm{trk})$.

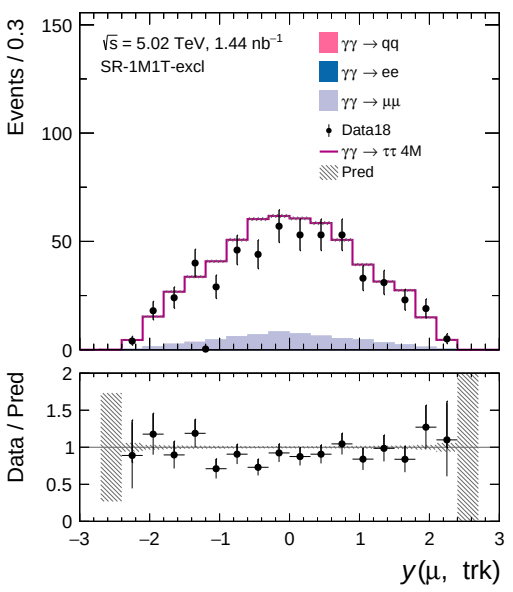

(b) Pseudorapidity $y(\mu, \mathrm{trk})$.

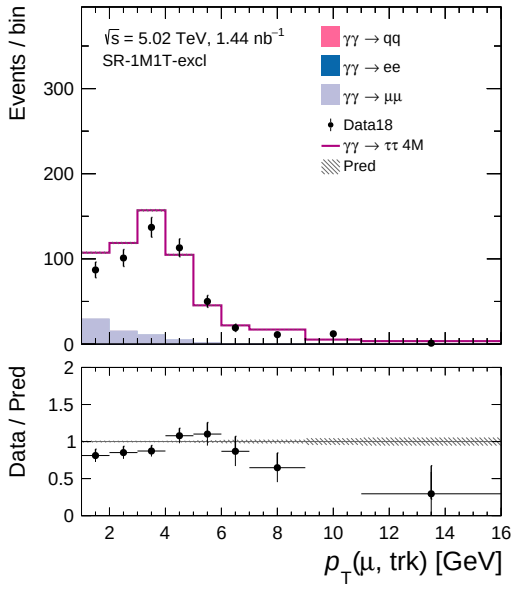

(c) p_{T} of muon and track.

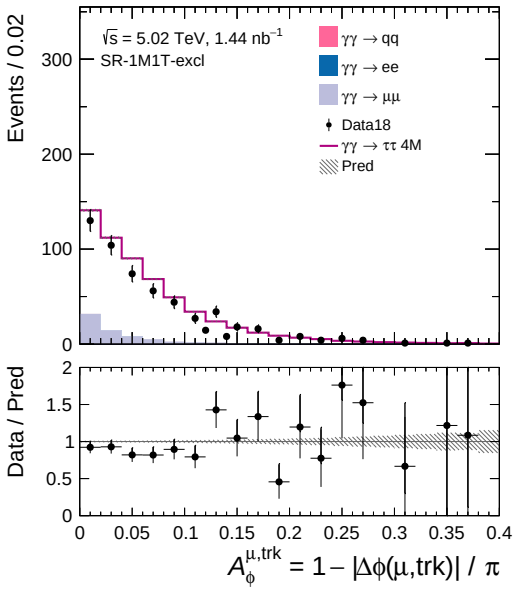

(d) Acoplanarity of muon and track.

Figure 8.8: Kinematic distributions for the invariant mass $m(\mu, \mathrm{trk})$ (a), the pseudorapidity $y(\mu, \mathrm{trk})$ (b), the transverse momentum $p_{\mathrm{T}}(\mu, \mathrm{trk})$ (c) and the acoplanarity $A_{\phi}^{\mu,\mathrm{trk}}$ (d) of the muon and track system in SR-1M1T. The data is shown as black dots, the prediction as stacked histogram from the signal process $\gamma\gamma \to \tau\tau$ (pink solid line) and the background processes $\gamma\gamma \to q\bar{q}$ (pink), $\gamma\gamma \to ee$ (blue) and $\gamma\gamma \to \mu\mu$ (violet). The ratio between the data and the prediction is shown in the lower panel. The applied selection criteria are given in Table 7.1.

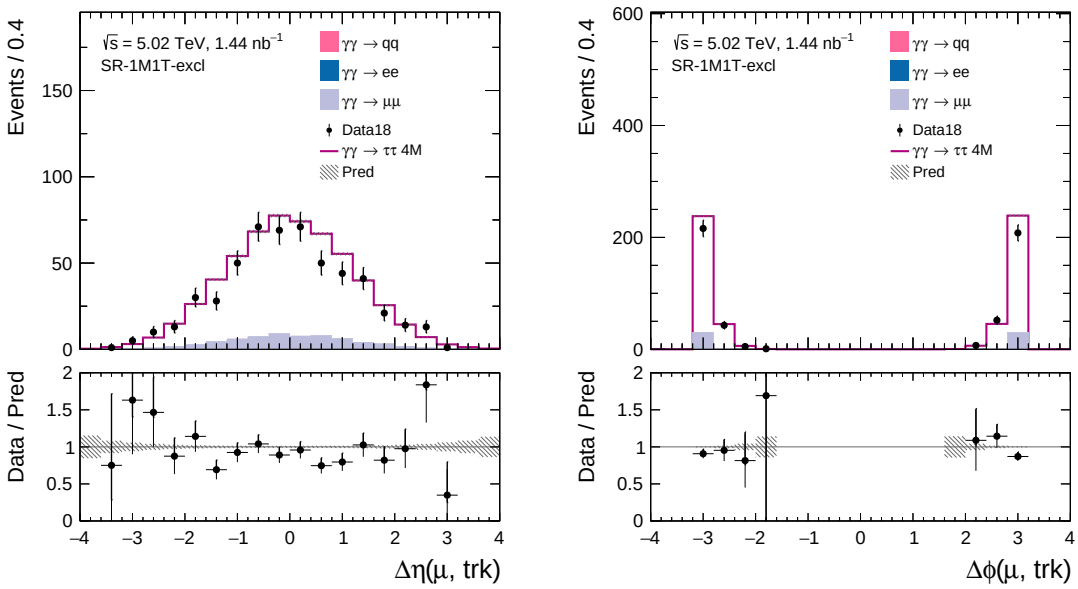

(a) $\Delta\eta$ **(b)** $\Delta\phi$

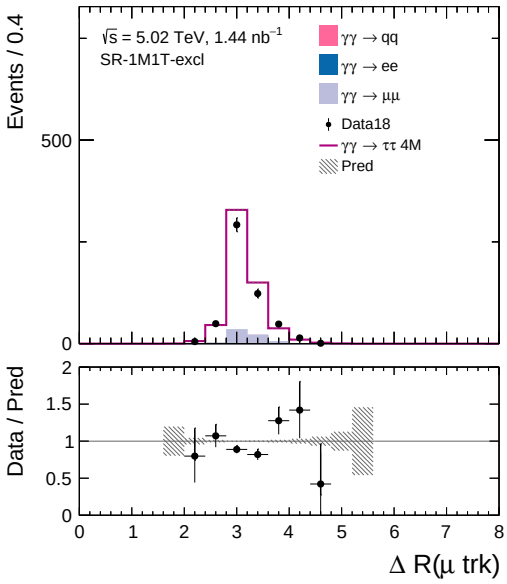

(c) ΔR

Figure 8.9: Kinematic distributions for $\Delta\eta$ (a), $\Delta\phi$ (b) and ΔR (c) of the muon and track system in SR-1M1T. The data is shown as black dots, the prediction as stacked histogram from the signal process $\gamma\gamma \to \tau\tau$ (pink solid line) and the background processes $\gamma\gamma \to q\bar{q}$ (pink), $\gamma\gamma \to ee$ (blue) and $\gamma\gamma \to \mu\mu$ (violet). The ratio between the data and the prediction is shown in the lower panel. The applied selection criteria are given in Table 7.1.

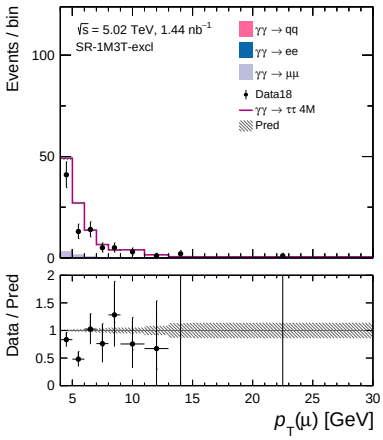

(a) p_{T} of the muon.

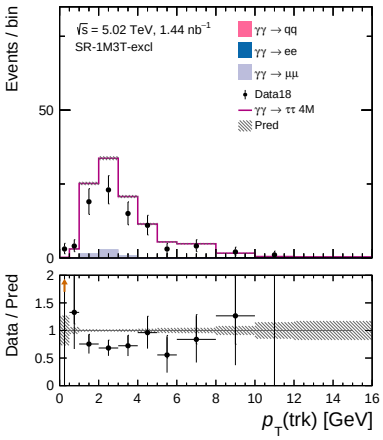

(b) p_{T} of the leading track.

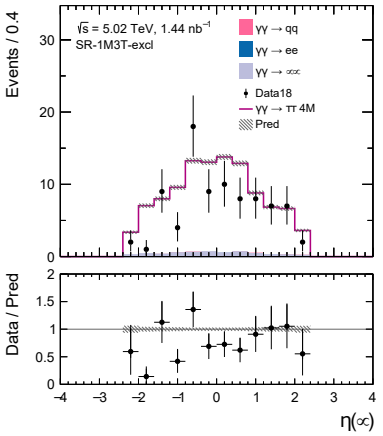

(c) η of the muon.

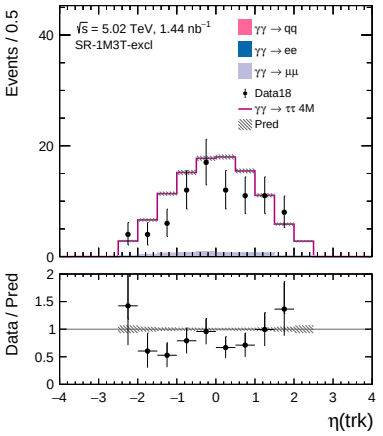

(d) η of the leading track.

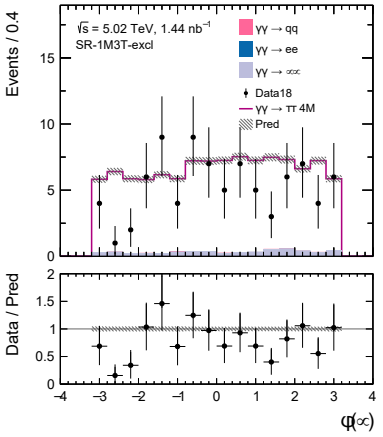

(e) ϕ of the muon.

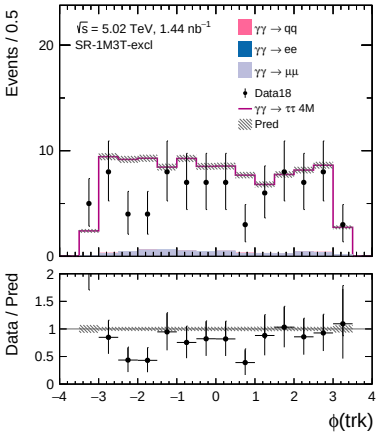

(f) ϕ of the leading track.

Figure 8.10: Kinematic distributions for the transverse momentum p_{T} of the muon (a) and the leading track (b), the angle η of the muon (c) and the leading track (d) and the angle ϕ of the muon (e) and the leading track (f) in in SR-1M3T. The data is shown as black dots, the prediction as stacked histogram from the signal process $\gamma\gamma \to \tau\tau$ (pink solid line) and the background processes $\gamma\gamma \to q\bar{q}$ (pink), $\gamma\gamma \to ee$ (blue) and $\gamma\gamma \to \mu\mu$ (violet). The ratio between the data and the prediction is shown in the lower panel. The applied selection criteria are given in Table 7.1.

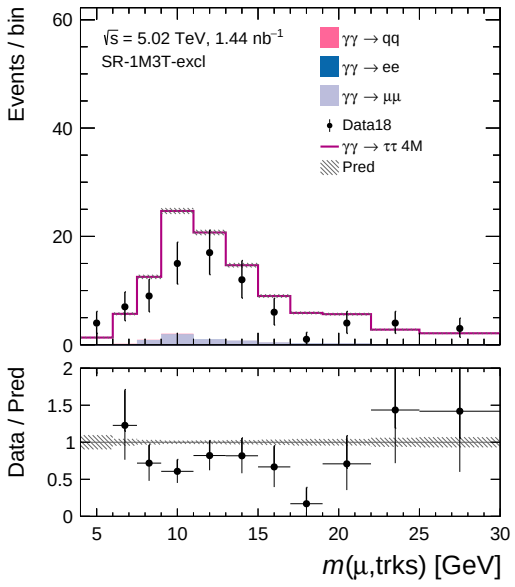

(a) Invariant mass $m(\mu, \text{trks})$.

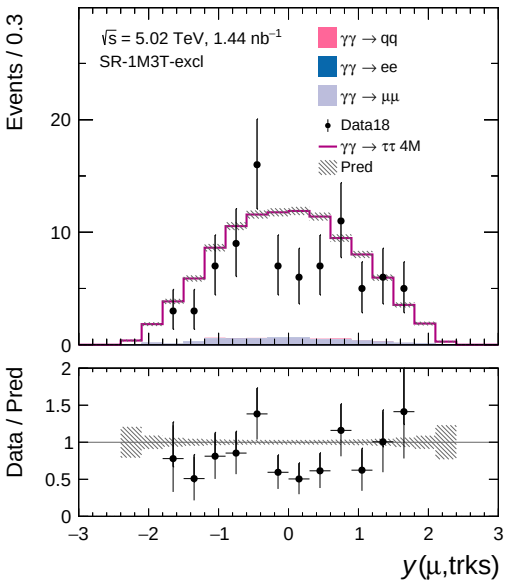

(b) Pseudorapidity $y(\mu, \text{trks})$.

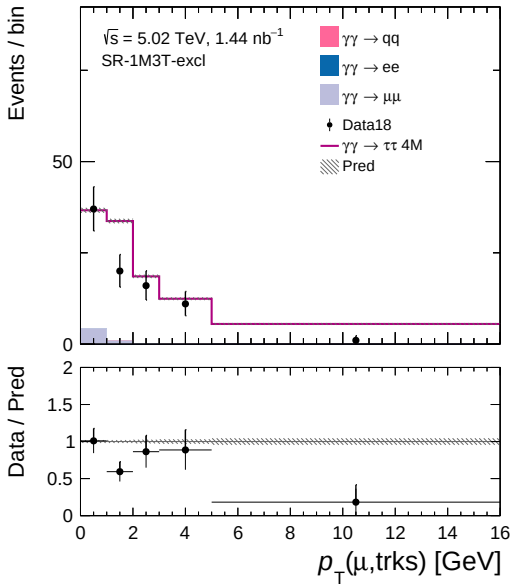

(c) p_{T} of muon and tracks.

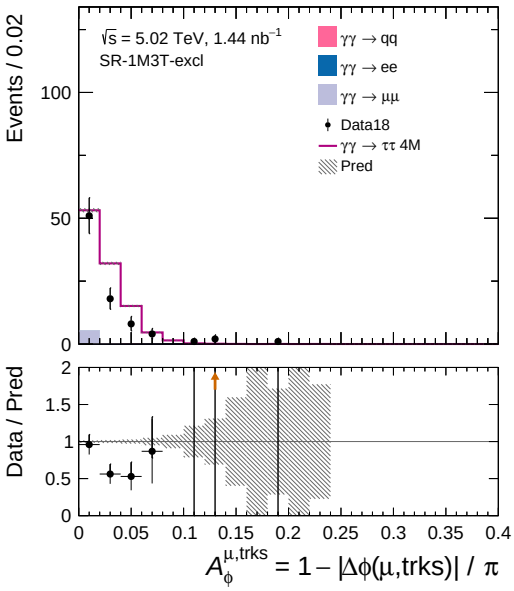

(d) Acoplanarity of muon and tracks.

Figure 8.11: Kinematic distributions for the invariant mass $m(\mu, \text{trks})$ (a), the pseudorapidity $y(\mu, \text{trks})$ (b), the transverse momentum $p_{\mathrm{T}}(\mu, \text{trks})$ (c) and the acoplanarity $A_{\phi}^{\mu,\text{trks}}$ (d) of the muon and tracks system in SR-1M3T. The data is shown as black dots, the prediction as stacked histogram from the signal process $\gamma\gamma \to \tau\tau$ (pink solid line) and the background processes $\gamma\gamma \to q\bar{q}$ (pink), $\gamma\gamma \to ee$ (blue) and $\gamma\gamma \to \mu\mu$ (violet). The ratio between the data and the prediction is shown in the lower panel. The applied selection criteria are given in Table 7.1.

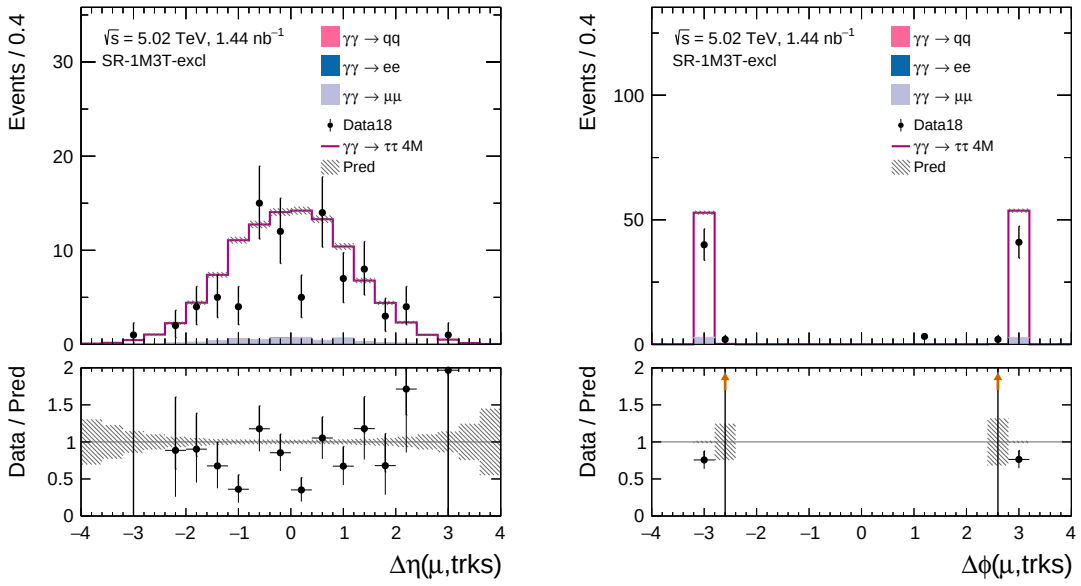

(a) $\Delta\eta$ **(b)** $\Delta\phi$

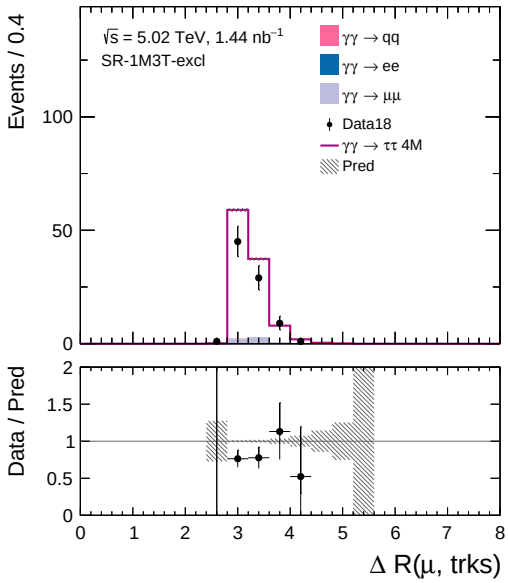

(c) ΔR

Figure 8.12: Kinematic distributions for $\Delta\eta$ (a), $\Delta\phi$ (b) and ΔR (c) of the muon and tracks system in SR-1M3T. The data is shown as black dots, the prediction as stacked histogram from the signal process $\gamma\gamma \to \tau\tau$ (pink solid line) and the background processes $\gamma\gamma \to q\bar{q}$ (pink), $\gamma\gamma \to ee$ (blue) and $\gamma\gamma \to \mu\mu$ (violet). The weighted, fractional and raw yields for each process are displayed in the legend. The ratio between the data and the prediction is shown in the lower panel. The applied selection criteria are shown in the upper left side.

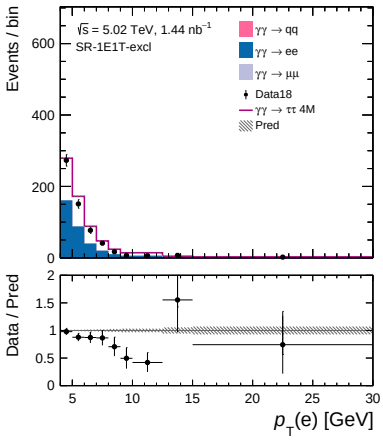

(a) p_{T} of the electron.

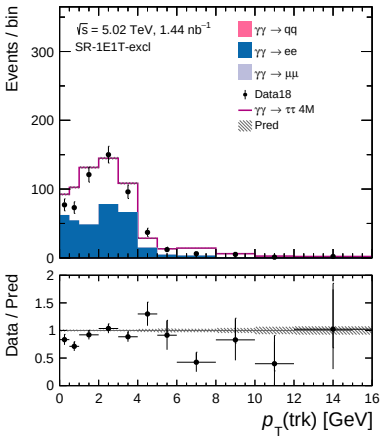

(b) p_{T} of the track.

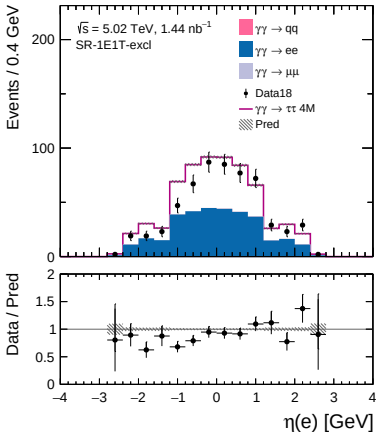

(c) η of the electron.

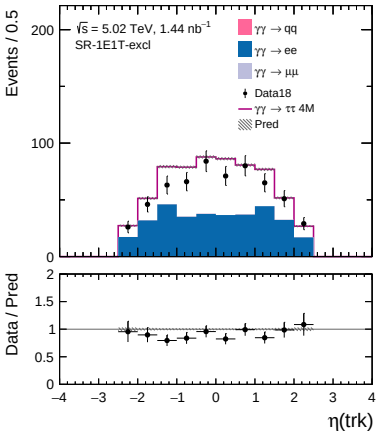

(d) η of the track.

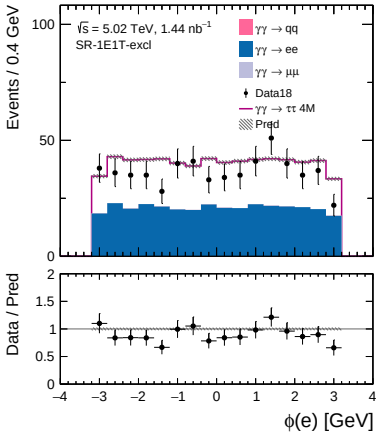

(e) ϕ of the electron.

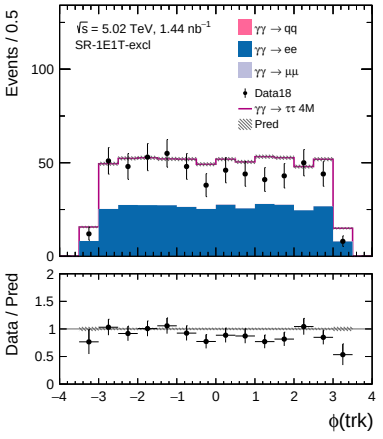

(f) ϕ of the track.

Figure 8.13: Kinematic distributions for the transverse momentum p_{T} of the electron (a) and the track (b), the angle η of the electron (c) and the track (d) and the angle ϕ of the electron (e) and the track (f) in in SR-1E1T. The data is shown as black dots, the prediction as stacked histogram from the signal process $\gamma\gamma \to \tau\tau$ (pink solid line) and the background processes $\gamma\gamma \to q\bar{q}$ (pink), $\gamma\gamma \to ee$ (blue) and $\gamma\gamma \to \mu\mu$ (violet). The ratio between the data and the prediction is shown in the lower panel. The applied selection criteria are given in Table 7.1.

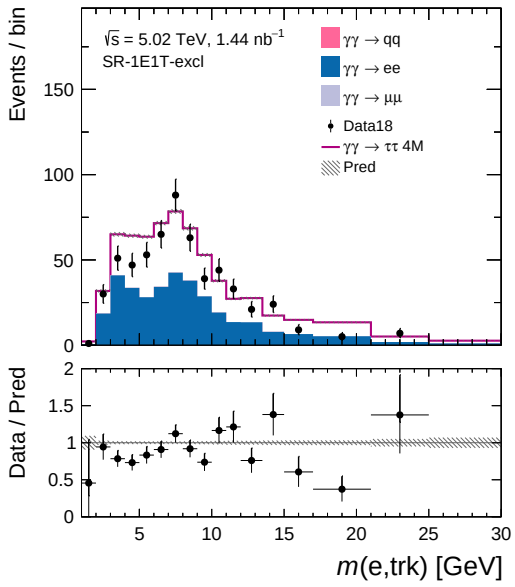

(a) Invariant mass $m(e, \text{trk})$.

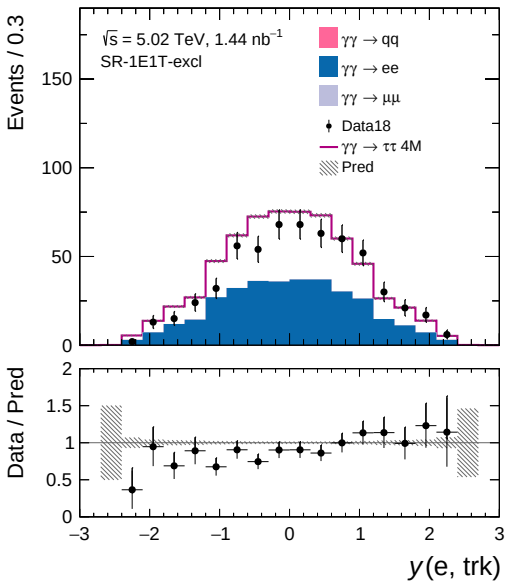

(b) Pseudorapidity $y(e, \text{trk})$.

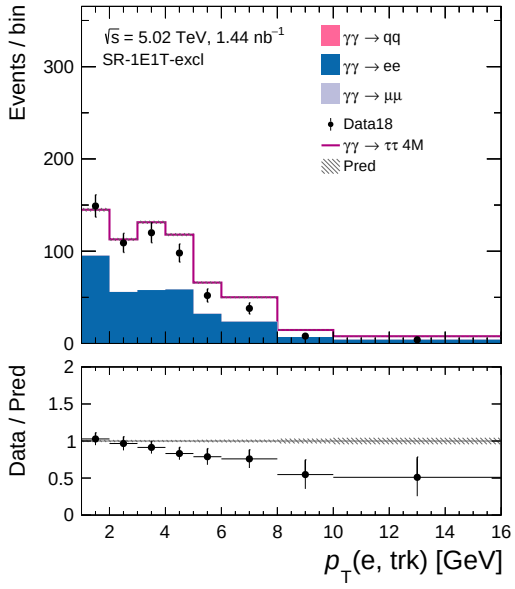

(c) p_{T} of electron and track.

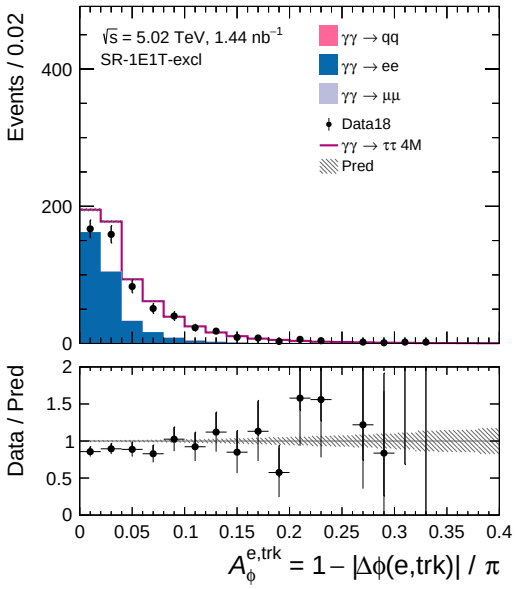

(d) Acoplanarity of electron and track.

Figure 8.14: Kinematic distributions for the invariant mass $E_{\text{T}}^{\text{miss}}$ (a), the pseudorapidity $y(e, \text{trk})$ (b), the transverse momentum $p_{\text{T}}(e, \text{trk})$ (c) and the acoplanarity $A_{\phi}^{e,\text{trk}}$ (d) of the muon and track system in SR-1E1T. The data is shown as black dots, the prediction as stacked histogram from the signal process $\gamma\gamma \to \tau\tau$ (pink solid line) and the background processes $\gamma\gamma \to q\bar{q}$ (pink), $\gamma\gamma \to ee$ (blue) and $\gamma\gamma \to \mu\mu$ (violet). The ratio between the data and the prediction is shown in the lower panel. The applied selection criteria are given in Table 7.1.

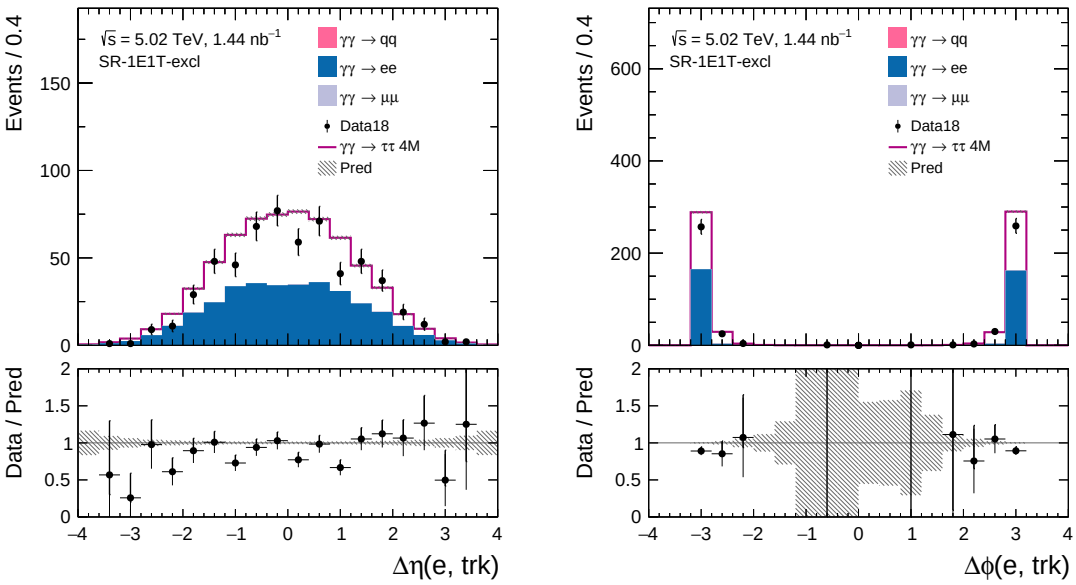

(a) $\Delta\eta$ **(b)** $\Delta\phi$

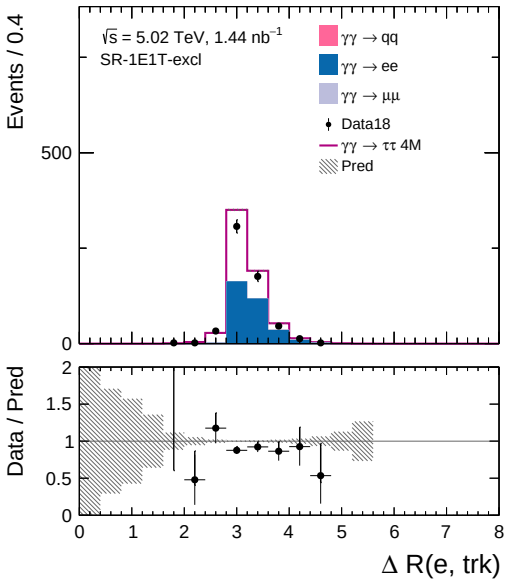

(c) ΔR

Figure 8.15: Kinematic distributions for $\Delta\eta$ (a), $\Delta\phi$ (b) and ΔR (c) of the electron and track system in SR-1E1T. The data is shown as black dots, the prediction as stacked histogram from the signal process $\gamma\gamma \to \tau\tau$ (pink solid line) and the background processes $\gamma\gamma \to q\bar{q}$ (pink), $\gamma\gamma \to ee$ (blue) and $\gamma\gamma \to \mu\mu$ (violet). The ratio between the data and the prediction is shown in the lower panel. The applied selection criteria are given in Table 7.1.

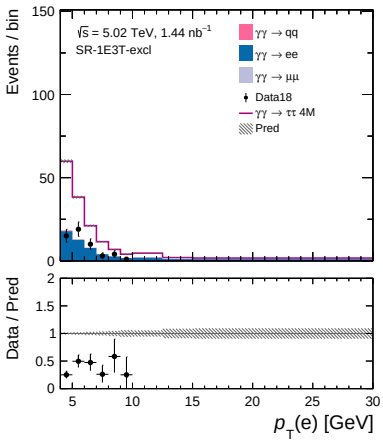

(a) p_T of the electron.

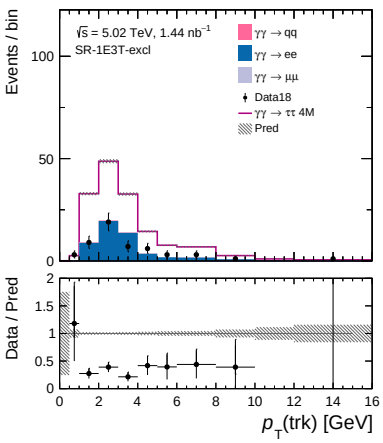

(b) p_T of the tracks.

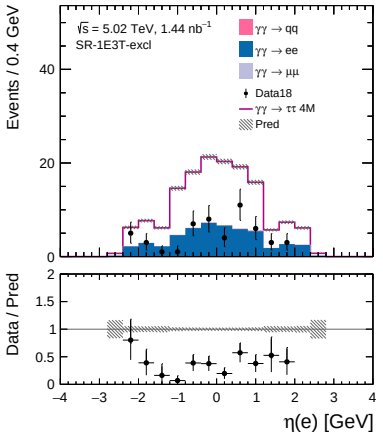

(c) η of the electron.

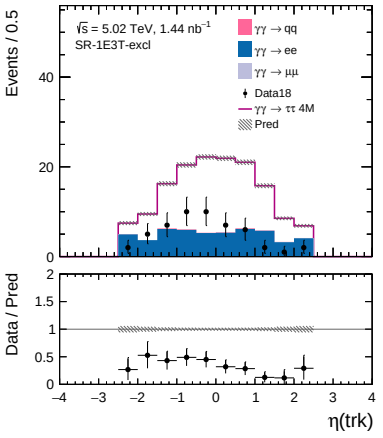

(d) η of the tracks.

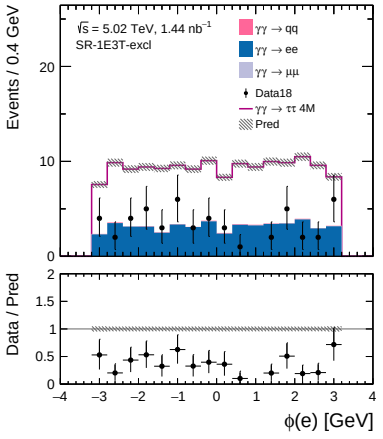

(e) ϕ of the electron.

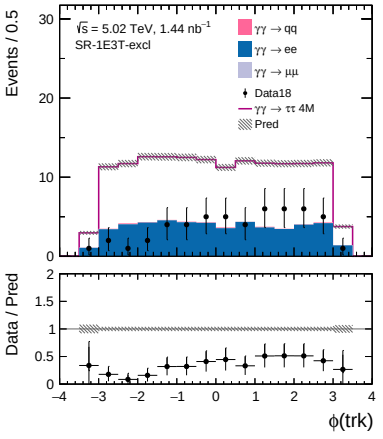

(f) ϕ of the tracks.

Figure 8.16: Kinematic distributions for the transverse momentum p_T of the electron (a) and the leading track (b), the angle η of the electron (c) and the leading track (d) and the angle ϕ of the electron (e) and the leading track (f) in in SR-1E3T. The data is shown as black dots, the prediction as stacked histogram from the signal process $\gamma\gamma \to \tau\tau$ (pink solid line) and the background processes $\gamma\gamma \to q\bar{q}$ (pink), $\gamma\gamma \to ee$ (blue) and $\gamma\gamma \to \mu\mu$ (violet). The ratio between the data and the prediction is shown in the lower panel. The applied selection criteria are given in Table 7.1.

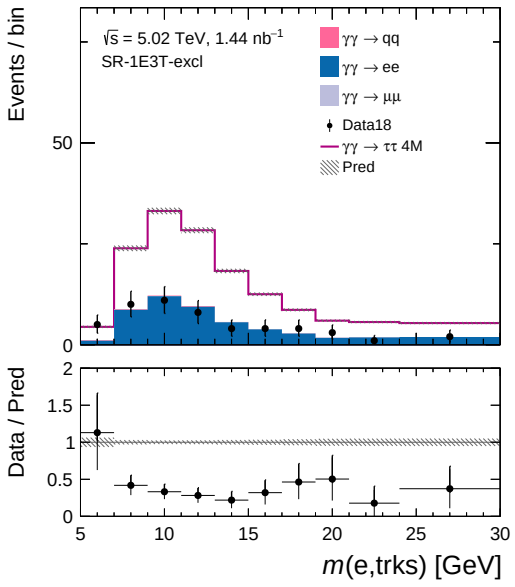

(a) Invariant mass $m(e, \text{trks})$.

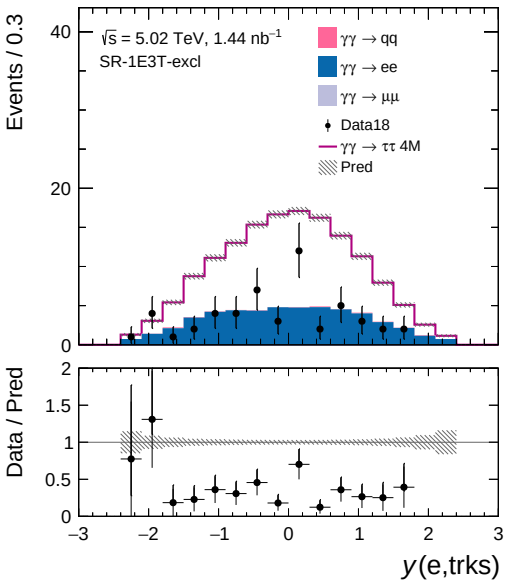

(b) Pseudorapidity $y(e, \text{trks})$.

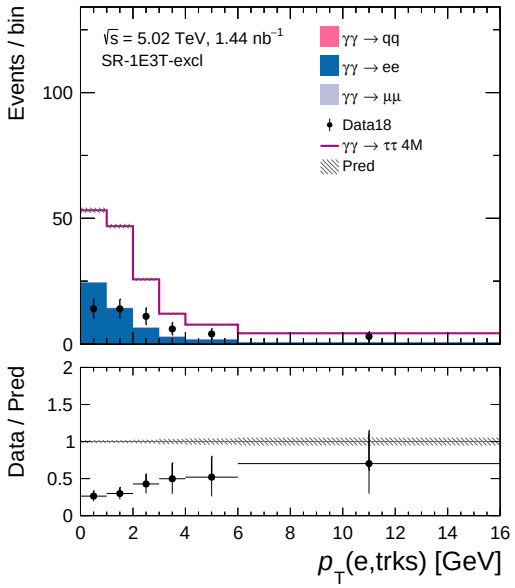

(c) p_{T} of electron and tracks.

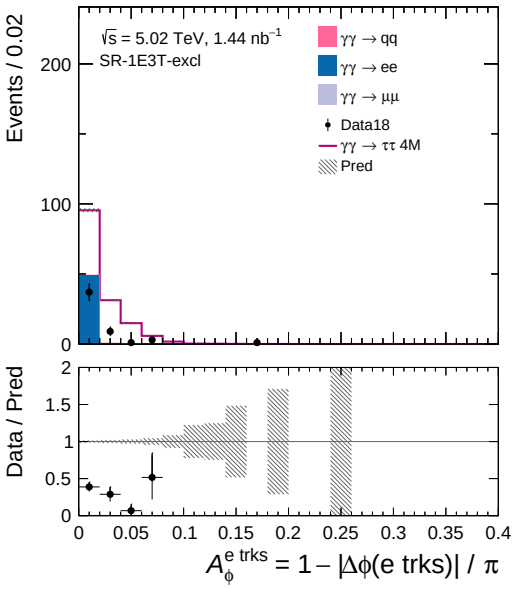

(d) Acoplanarity of electron and tracks.

Figure 8.17: Kinematic distributions for the invariant mass $m(e, \text{trks})$ (a), the pseudorapidity $y(e, \text{trks})$ (b), the transverse momentum $p_{\text{T}}(e, \text{trks})$ (c) and the acoplanarity $A_{\phi}^{e,\text{trks}}$ (d) of the muon and tracks system in SR-1E3T. The data is shown as black dots, the prediction as stacked histogram from the signal process $\gamma\gamma \to \tau\tau$ (pink solid line) and the background processes $\gamma\gamma \to q\bar{q}$ (pink), $\gamma\gamma \to ee$ (blue) and $\gamma\gamma \to \mu\mu$ (violet). The ratio between the data and the prediction is shown in the lower panel. The applied selection criteria are given in Table 7.1.

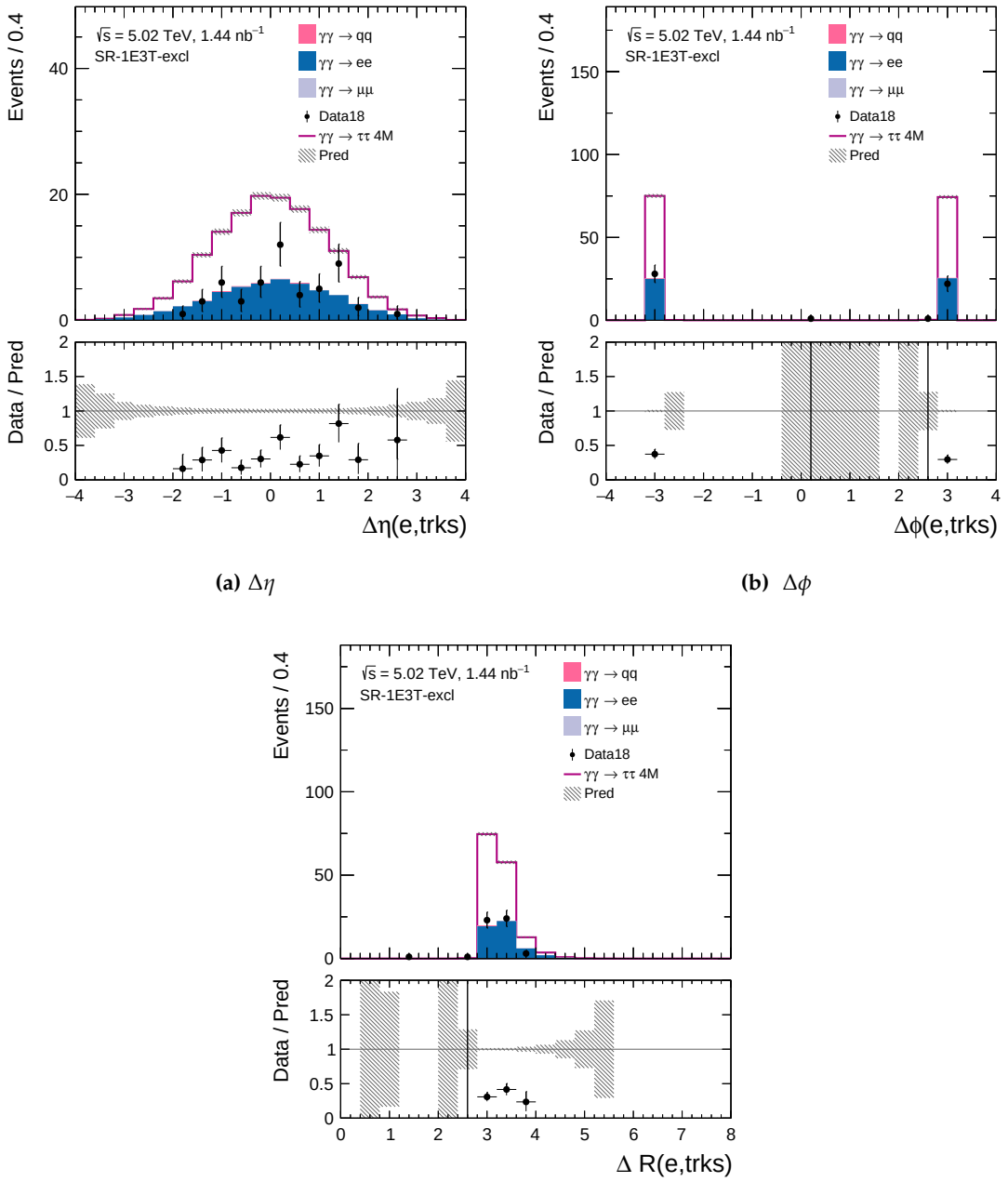

(a) $\Delta\eta$

(b) $\Delta\phi$

(c) ΔR

Figure 8.18: Kinematic distributions for $\Delta\eta$ (a), $\Delta\phi$ (b) and ΔR (c) of the electron and tracks system in SR-1E3T. The data is shown as black dots, the prediction as stacked histogram from the signal process $\gamma\gamma \to \tau\tau$ (pink solid line) and the background processes $\gamma\gamma \to q\bar{q}$ (pink), $\gamma\gamma \to ee$ (blue) and $\gamma\gamma \to \mu\mu$ (violet). The weighted, fractional and raw yields for each process are displayed in the legend. The ratio between the data and the prediction is shown in the lower panel. The applied selection criteria are shown in the upper left side.

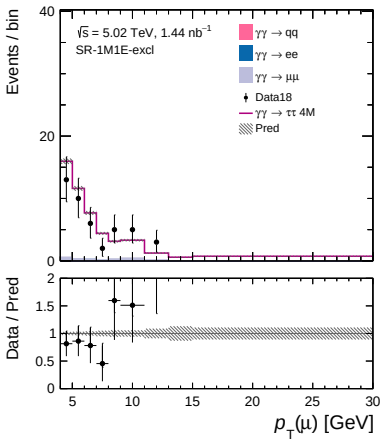

(a) p_{T} of the muon.

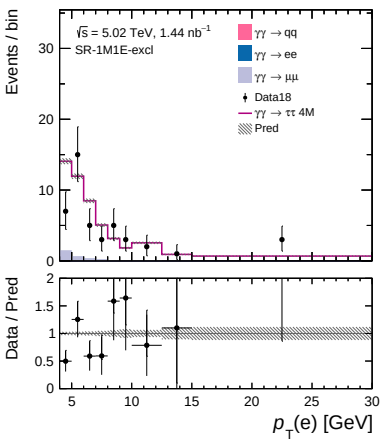

(b) p_{T} of the electron.

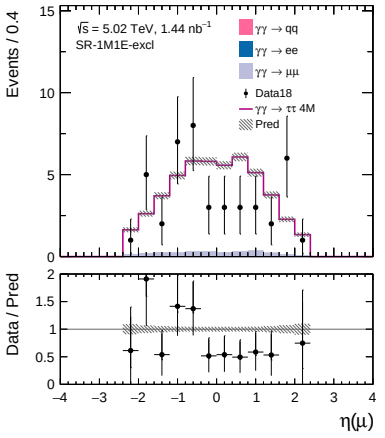

(c) η of the muon.

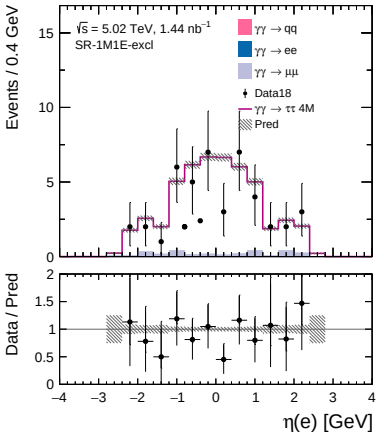

(d) η of the electron.

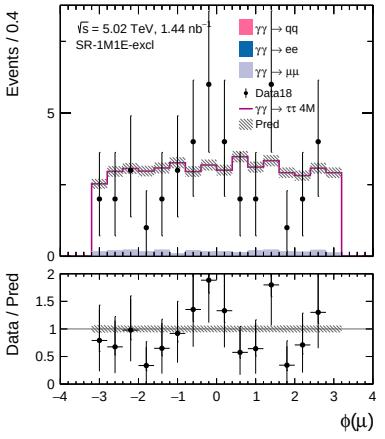

(e) ϕ of the muon.

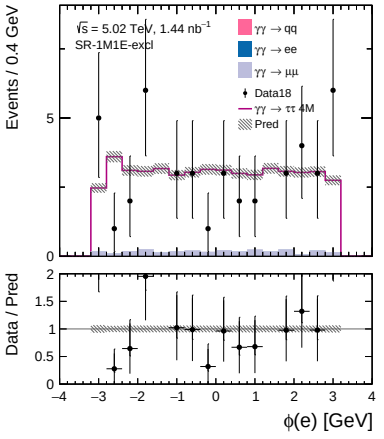

(f) ϕ of the electron.

Figure 8.19: Kinematic distributions for the transverse momentum p_{T} of the muon (a) and the electron (b), the angle η of the muon (c) and the electron (d) and the angle ϕ of the muon (e) and the electron (f) in in SR-1M1E. The data is shown as black dots, the prediction as stacked histogram from the signal process $\gamma\gamma \to \tau\tau$ (pink solid line) and the background processes $\gamma\gamma \to q\bar{q}$ (pink), $\gamma\gamma \to ee$ (blue) and $\gamma\gamma \to \mu\mu$ (violet). The ratio between the data and the prediction is shown in the lower panel. The applied selection criteria are given in Table 7.1.

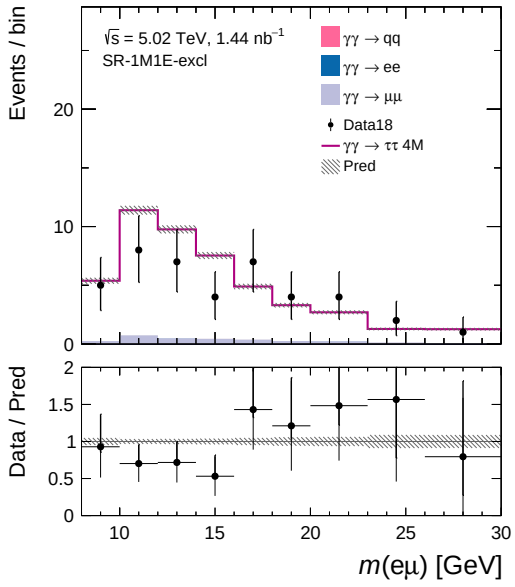

(a) Invariant mass $m(\mu, e)$.

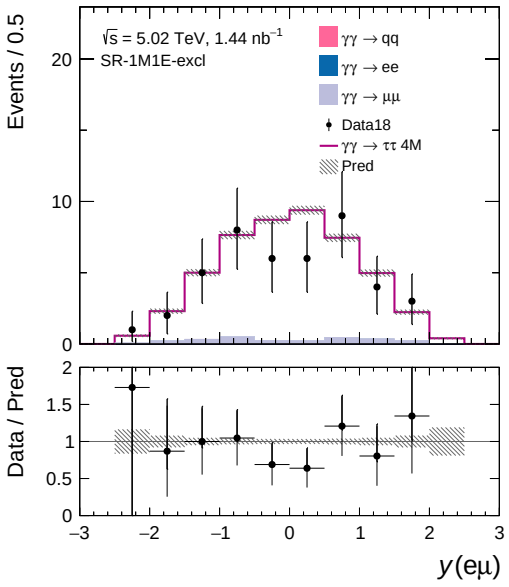

(b) Pseudorapidity $y(\mu, e)$.

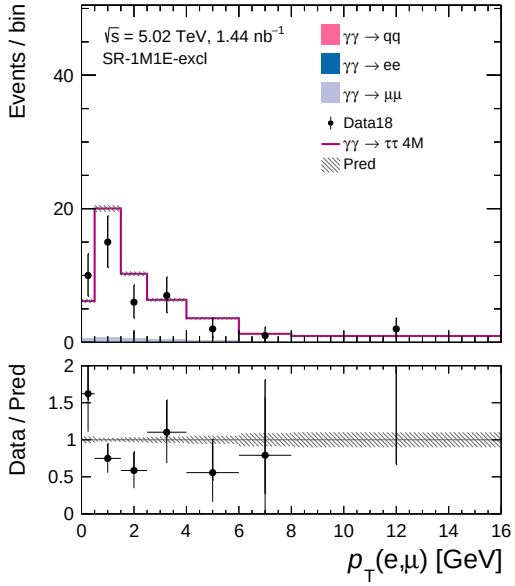

(c) p_{T} of muon and track.

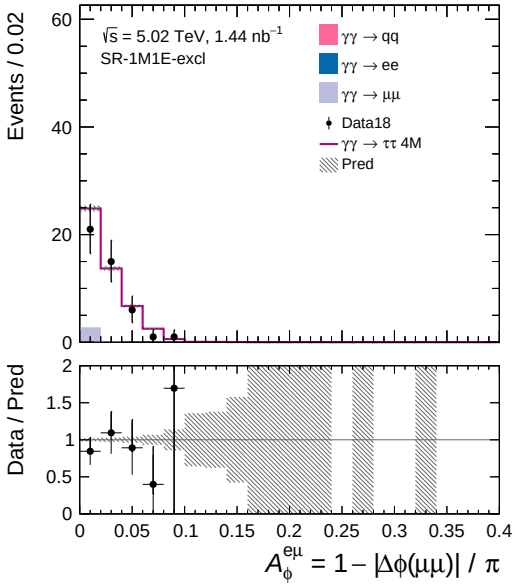

(d) Acoplanarity of muon and track.

Figure 8.20: Kinematic distributions for the invariant mass $m(\mu, e)$ (a), the pseudorapidity $y(\mu, e)$ (b), the transverse momentum $p_{\mathrm{T}}(\mu, e)$ (c) and the acoplanarity $A_{\phi}^{\mu,e}$ (d) of the muon and track system in SR-1M1E. The data is shown as black dots, the prediction as stacked histogram from the signal process $\gamma\gamma \to \tau\tau$ (pink solid line) and the background processes $\gamma\gamma \to q\bar{q}$ (pink), $\gamma\gamma \to ee$ (blue) and $\gamma\gamma \to \mu\mu$ (violet). The ratio between the data and the prediction is shown in the lower panel. The applied selection criteria are given in Table 7.1.

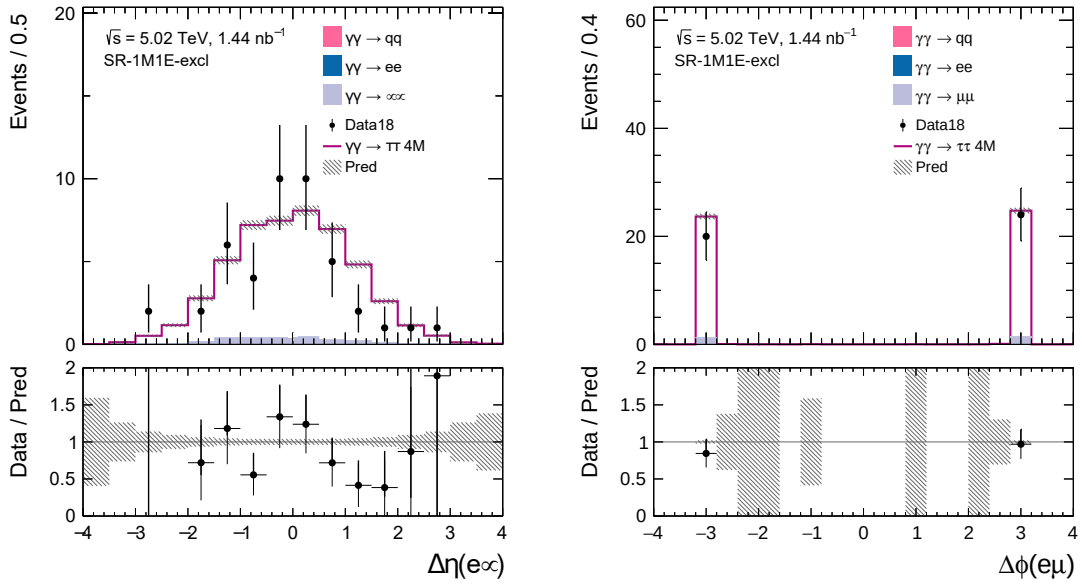

(a) $\Delta\eta$

(b) $\Delta\phi$

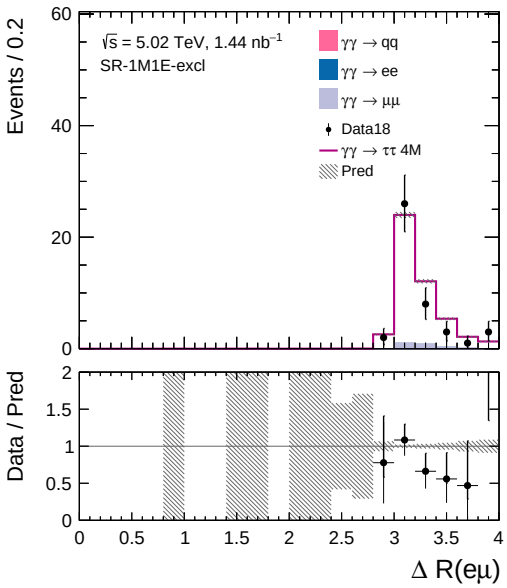

(c) ΔR

Figure 8.21: Kinematic distributions for $\Delta\eta$ (a), $\Delta\phi$ (b) and ΔR (c) of the muon and electron system in SR-1M1E. The data is shown as black dots, the prediction as stacked histogram from the signal process $\gamma\gamma \to \tau\tau$ (pink solid line) and the background processes $\gamma\gamma \to q\bar{q}$ (pink), $\gamma\gamma \to ee$ (blue) and $\gamma\gamma \to \mu\mu$ (violet). The weighted, fractional and raw yields for each process are displayed in the legend. The ratio between the data and the prediction is shown in the lower panel. The applied selection criteria are shown in the upper left side.

8.3 OBSERVATION OF $\gamma\gamma \to \tau\tau$ PRODUCTION

The strength of $\gamma\gamma \to \tau\tau$ signal in Pb+Pb collisions in each SR is estimated by comparing the sum of all contributing background predictions b with data d. The z-value is calculated as

$$z\text{-value} = \frac{d-b}{\sqrt{b}} \tag{8.3}$$

in each SR and is shown in Table 8.1 together with the data yields and the background predictions per SR. In the latter case, the CFs, determined and discussed in Section 8.1.1 and Section 8.1.2, have been applied to the $\gamma\gamma \to \mu\mu$ and $\gamma\gamma \to ee$ backgrounds. The effect is small, but nevertheless considered in this particular case. To factor in the effect of a systematic uncertainties, a z-value with a 10 % systematic uncertainty is defined as

$$z\text{-value}_{\text{sys}} = \frac{d-b}{\sqrt{b + (\zeta \cdot b)^2}}, \tag{8.4}$$

with $\zeta = 0.1$. The values for this are also listed in Table 8.1. A final statement on the signal significance of the $\gamma\gamma \to \tau\tau$ process requires a statistical analysis with full systematics of the measurement, which goes beyond the scope of this thesis. Using the simplified definitions of a significance through the z-value without and with systematics, the $\gamma\gamma \to \tau\tau$ process can be considered as observed if the z-values significantly exceeds approximately 10 (5) without (with) systematic uncertainties.
As shown in Table 8.1, in four of the five SRs, a z-value above of 15 or significantly above is obtained without and with the consideration of systematic uncertainties. In SR-1E3T, no significant $\gamma\gamma \to \tau\tau$ signal is observed.
In four out of five signal regions, the $\gamma\gamma \to \tau\tau$ signal significantly exceeds the threshold for observation based on the simple measure of the z-values, and is thus observed for the first time at the ATLAS experiment in ultraperipheral Pb+Pb collisions.

	SR-1M1T	SR-1M3T	SR-1E1T	SR-1E3T	SR-1M1E
Data d	485.0	78.0	548.0	52.0	42.0
Total Background b	53.3	5.3	273.9	43.8	2.7
Background $\gamma\gamma \to \mu\mu$	53.2	5.0	0.1	0.0	2.7
Background $\gamma\gamma \to ee$	0.0	0.0	273.7	43.1	0.0
Background $\gamma\gamma \to q\bar{q}$	0.1	0.3	0.1	0.7	0.0
z-value	59.2	31.7	16.6	1.2	24.1
z-value$_{\text{sys}}$	47.8	30.8	8.6	1.0	23.6

Table 8.1: Event yields for data and background predictions together with the $\gamma\gamma \to \tau\tau$ production strength for the five SRs.

9 DETERMINATION OF a_τ

The anomalous magnetic moment a_τ of the τ-lepton can be determined using the shape and cross section information of the $\gamma\gamma \to \tau\tau$ process. Negative LL (NLL) fits using the normal and the eNLL function, as described in Section 6.2, are performed to obtain expected estimates for the value of a_τ and its uncertainty.
In this chapter, the constraints of a_τ given by the expected CI and its length are studied using different settings. First, the best expected CI at 68 % CL for a_τ using the signal contribution only is estimated for the five SRs individually. Then, the effect of the background contribution on the expected CI for a_τ is discussed. The impact of different systematic uncertainties is studied. The expected CI can be further constrained by combining the information of a_τ in different SRs. Both fitting methods, eNLL and nNLL, are compared.

9.1 OBSERVABLES SENSITIVE TO a_τ

The $\gamma\tau\tau$ vertex in $\gamma\gamma \to \tau\tau$ production is sensitive to the anomalous magnetic moment a_τ. As shown in Section 2.1 and discussed in detail in Ref. [95], this results in the production cross section of $\gamma\gamma \to \tau\tau$ being highly sensitive to the value of a_τ. Additionally, the shape of kinematic distributions, in other words, the hardness of the spectrum can be systematically affected, meaning e.g. that events in the kinematic distribution are shifted systematically to higher or lower values. The shape information can be used together with the cross section information to extract CIs for a_τ using an eNLL fit. This allows to further constrain the CIs of a_τ compared to a nNLL fit where only the shape information is used.
This section discusses the effect of different predictions for a_τ on the $\gamma\gamma \to \tau\tau$ production cross section. The change of the cross section in the SRs is analyzed under the consideration that the SM signal cross section, assuming $a_\tau = 0$, is blinded within ± 10 %. In the second part of this section, different kinematic distributions are investigated for systematic changes in the shape under the effect of various a_τ values. The observables most impacted by the changes in a_τ are called sensitive to a_τ and are tested later in the fitting procedure of the LL fits.

9.1.1 *Dependence of the Cross Section of $\gamma\gamma \to \tau\tau$ on a_τ*

The partonic cross section for ditau production $\sigma(\gamma\gamma \to \tau\tau)$ depends on the matrix element $\mathcal{M}$ which includes the vertex $\gamma\tau\tau$ (c.f. Equation (2.12)) which is affected by non-zero values of a_τ. Simulated signal events of $\gamma\gamma \to \tau\tau$ production in the SM, assuming $a_\tau = 0$, as well as predictions for a_τ from -0.010 to 0.010 are used to investigate the expected change of the cross section. The simulation procedure for the SM process is described in Section 4.1.1, and for varying a_τ values in Section 4.1.2.
In the SRs, introduced in Section 7.3, the number of selected signal events is a measure

for the production cross section. A larger cross section of the $\gamma\gamma \to \tau\tau$ process leads to an increased expected number of events in the SRs. In Table 9.1, the number of expected signal events for the corresponding a_τ values in the five SRs are shown.

a_τ \ SR	SR-1M1T	SR-1M3T	SR-1E1T	SR-1E3T	SR-1M1E
−0.10	649.3	140.3	440.3	150.2	75.1
−0.06	493.8	103.3	326.2	108.9	49.5
−0.05	471.3	97.9	309.2	102.8	45.6
−0.04	454.7	93.8	296.7	98.2	42.5
−0.03	444.9	91.2	288.9	95.2	40.3
−0.02	441.5	90.2	285.7	93.9	39.1
−0.01	445.0	90.7	287.3	94.3	38.9
0.00	455.5	92.7	293.9	96.4	39.6
0.01	473.1	96.4	305.5	100.3	41.4
0.02	498.0	101.8	322.3	106.0	44.2
0.03	530.7	108.9	344.6	113.6	48.1
0.04	571.3	117.9	372.5	123.2	53.1
0.05	620.1	128.7	406.2	134.9	59.4
0.06	676.6	141.3	445.6	148.5	66.7
0.10	998.5	213.7	671.0	227.1	110.0

Table 9.1: Expected event yields for the five SRs depending on a_τ values between −0.010 to 0.010. The value for $a_\tau = 0$ corresponds to the SM prediction.

The relationship between cross section and number of events is linear. The cross section dependence as function of a_τ is observed to be quadratic and the expected event yields N_{exp} can thus be described with the function

$$N_{\text{exp}}(a_\tau) = A \cdot {a_\tau}^2 + B \cdot a_\tau + C \tag{9.1}$$

where the coefficients A, B and C are defined by a quadratic fit. In fact, $N_{\text{exp}}(a_\tau)$ depends on terms up to the order ${a_\tau}^4$ but the coefficients are negligible small. The minimum of the fit is observed to be in the range of $a_\tau = -0.03$ and $a_\tau = -0.01$. The functional relation between the a_τ values and the number of signal counts is estimated for the five SRs and illustrated in Figure 9.1. The coefficients of the fit are summarized together with the minimum $a_{\tau,\text{min}}$ and χ^2/ndf value in Table 9.2. The parabolic dependence of $N_{\text{exp}}(a_\tau)$ is confirmed by the small values of χ^2/ndf, which is a measure of the goodness of the fit [96].

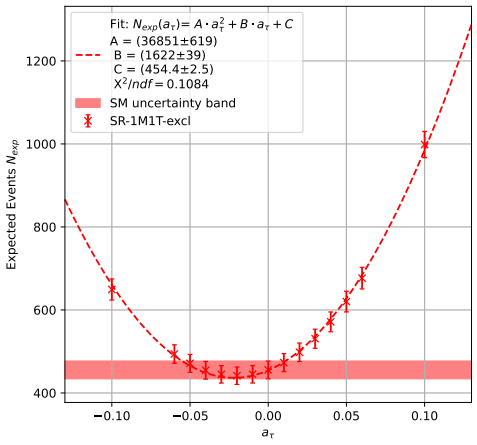

(a) SR-1M1T

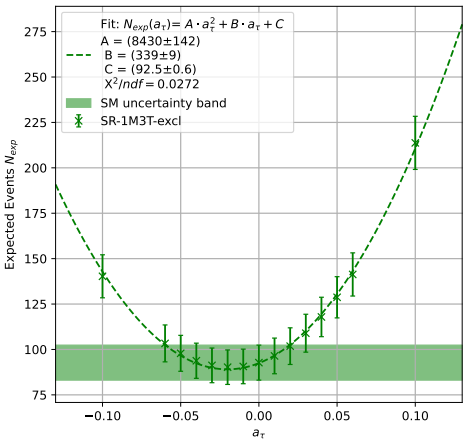

(b) SR-1M3T

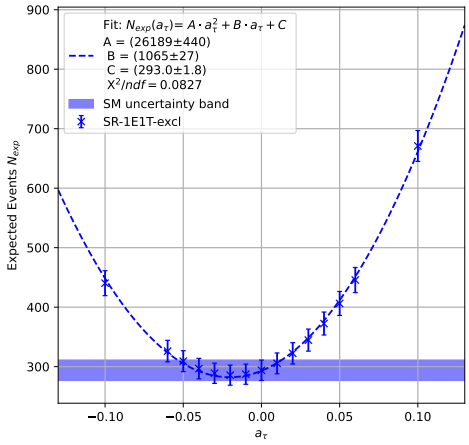

(c) SR-1E1T

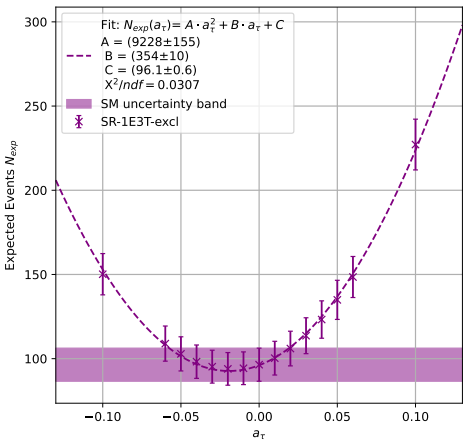

(d) SR-1E3T

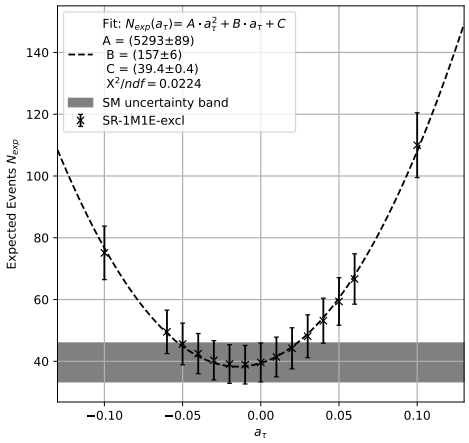

(e) SR-1M1E

Figure 9.1: Expected event yields for the five main SRs SR-1M1T (a), SR-1M3T (b), SR-1E1T (c),SR-1E3T (d) and SR-1M1E (e). The horizontal uncertainty band shows the number of expected events within $\pm 1 - \sigma$ from the SM prediction. The error bars indicate the statistical uncertainty in the predictions. The number of expected events N_{exp} are fitted using a quadratic ansatz. The coefficients A, B and C of the fit function $N_{\text{exp}}(a_\tau) = A{a_\tau}^2 + Ba_\tau + C$ are listed in the legend.

Signal Region	A	B	C	$a_{\tau\text{min}}$	χ^2/ndf
SR-1M1T	36851 ± 619	1622 ± 39	454.4 ± 2.5	-0.022	0.11
SR-1M3T	8430 ± 142	339 ± 9	92.5 ± 0.6	-0.020	0.03
SR-1E1T	26189 ± 440	1065 ± 27	293.0 ± 1.8	-0.020	0.08
SR-1E3T	9228 ± 155	354 ± 10	96.1 ± 0.6	-0.019	0.03
SR-1M1E	5293 ± 89	157 ± 6	39.4 ± 0.4	-0.015	0.02

Table 9.2: Summary of the fit coefficients A, B, C from the fit function $N_{\text{exp}}(a_\tau) = A \cdot {a_\tau}^2 + B \cdot a_\tau + C$, the minimum $a_{\tau,\text{min}}$ and χ^2/ndf for the expected number of events N_{exp} in SR-1M1T, SR-1M3T, SR-1E1T, SR-1E3T and SR-1M1E.

9.1.2 *Sensitive Kinematic Observables*

Similar to the cross section, the shape of kinematic observables can be affected by the anomalous magnetic moment a_τ. The impact of a_τ on the shape of a particular distribution can vary for different kinematic observables.
In the following, the effect of a_τ on the shape predictions is studied for different kinematic observables. For this purpose, the signal prediction for a_τ values from -0.010 to 0.010 are compared to the SM prediction in the five SRs: SR-1M1T, SR-1M3T, SR-1E1T, SR-1E3T and SR-1M1E. Global shifts of the event counts up or down compared to the SM prediction point to an effect of a_τ on the distribution mainly through the cross section dependence. Additional shape dependencies indicate an effect on the kinematic distribution directly.

Figures 9.2, 9.3, 9.4 and 9.5 show the observables most modified in shape by different a_τ values: $p_{\text{T}}(\ell)$, $p_{\text{T}}(\text{trk})$, $p_{\text{T}}(\ell,\text{trk})$ and $m(\ell,\text{trk})$ for all five SRs. The signal predictions for the different a_τ values, $a_\tau = -0.06, -0.02, 0.01, 0.03, 0.06$, are compared to the SM signal prediction ($a_\tau = 0$). The lower panels display the ratio of the BSM signal predictions and the SM signal prediction.
The signal predictions for $a_\tau \neq 0$ differ from the SM prediction ($a_\tau = 0$) in particular at higher values of the $p_{\text{T}}(\ell)$, $p_{\text{T}}(\text{trk})$, $p_{\text{T}}(\ell,\text{trk})$ and $m(\ell,\text{trk})$ distributions. At the highest energy scales, the effect of a_τ on the shape of the distribution alone reaches an enhancement of 2.5 combined with the enhancement through a change of the normalization by 1.5 for $a_\tau = 0.06$. These effects are observed at different scales for $|a_\tau < 0.06|$. The $p_{\text{T}}(\ell)$ distribution overall displays the strongest effects and is therefore a prime candidate to extract the value of a_τ based both on the cross section and the shape, simultaneously.
Beside the transverse momenta and the invariant masses, other observables were tested in the search for sensitive variables. For those, no major change in the shape is observed, and the sensitivity to a_τ is gained through the effect on the cross section only. To give a few examples for less sensitive observables, Figure 9.6 shows the kinematic variables of $\phi(\mu)$, $\eta(\text{trk})$ and the transverse impact parameter significance $|d_0\text{sig}(\mu)| = |d_0/\sigma(d_0)|$ for the muon in SR-1M1T. Figures for further non-sensitive observables in SR-1M1T can be found in Appendix F.

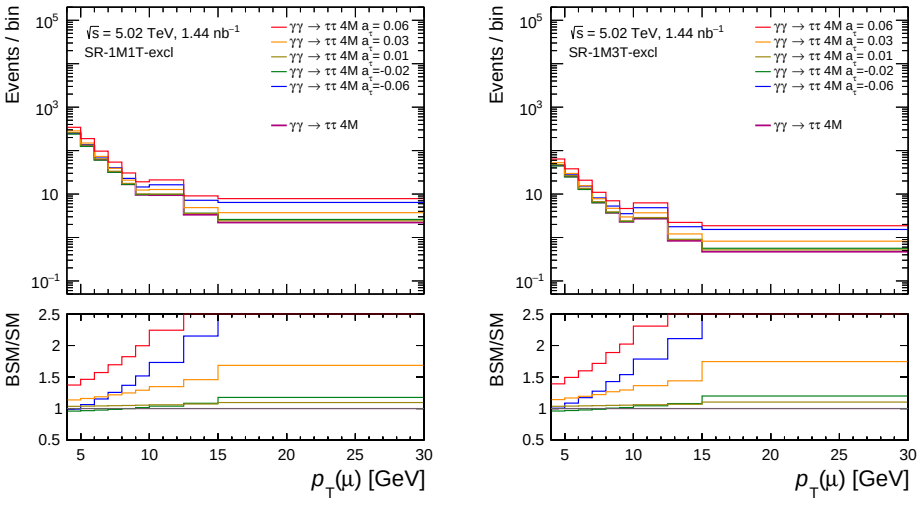

(a)

(b)

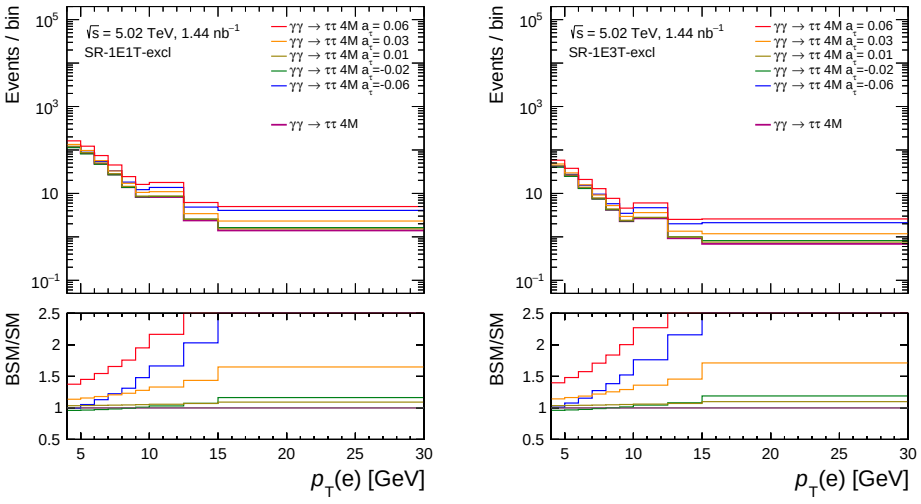

(c)

(d)

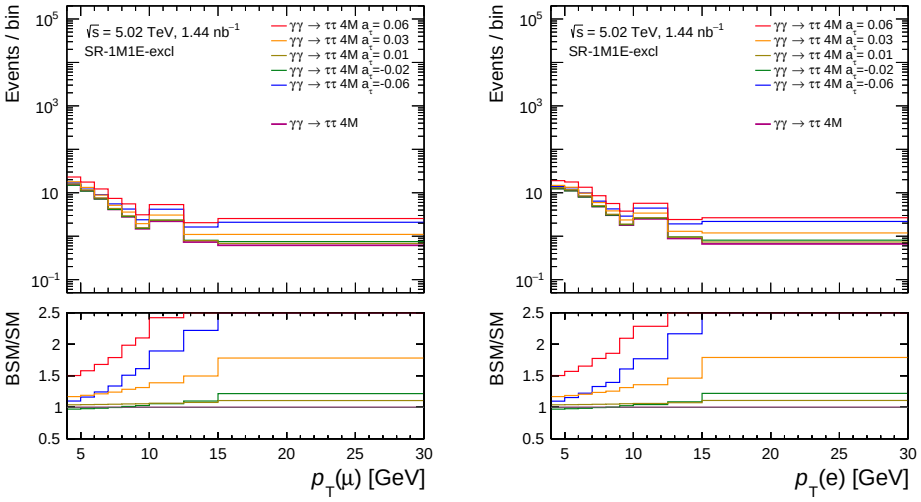

(e)

(f)

Figure 9.2: Lepton p_T distributions in the SRs SR-1M1T (a), SR-1M3T (b), SR-1E1T (c),SR-1E3T (d) for either muon or electron depending on the SR, and in SR-1M1E for the muon (e) and the electron (f). The upper panels show the signal prediction for different a_τ values, the lower panels show the ratios of the predictions with $a_\tau \neq 0$ to the SM prediction ($a_\tau = 0$).

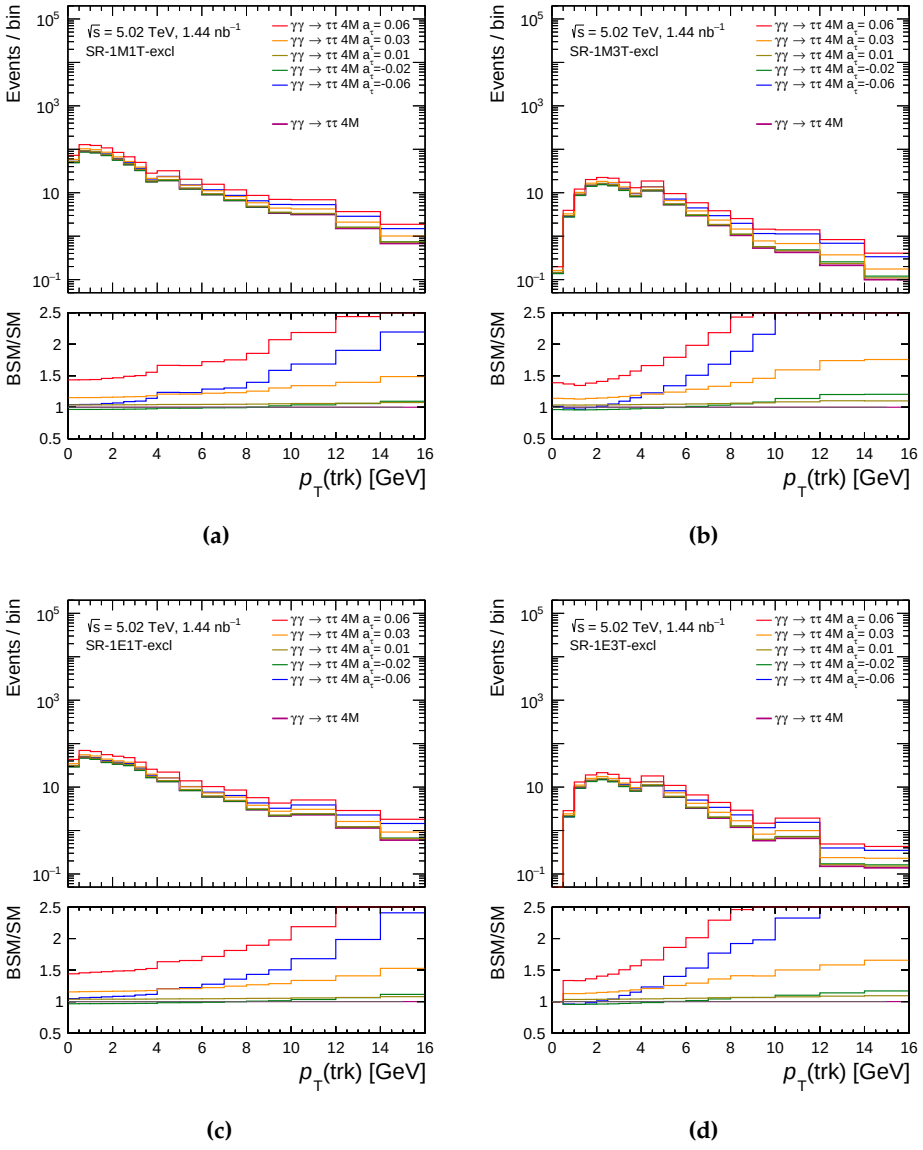

Figure 9.3: Track p_{T} distributions in the signal regions SR-1M1T (a), SR-1M3T (b), SR-1E1T (c), SR-1E3T (d). The upper panels show the signal prediction for different a_τ values, the lower panels show the ratios of the predictions with $a_\tau \neq 0$ to the SM prediction ($a_\tau = 0$).

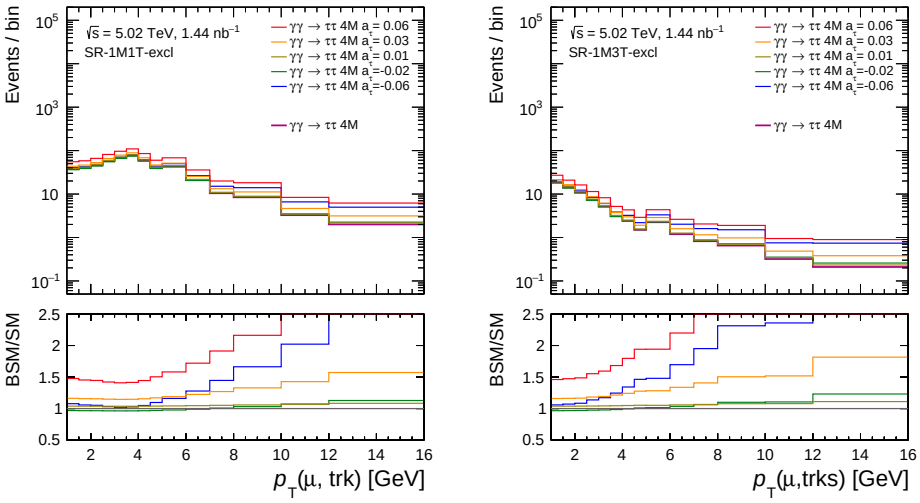

(a) **(b)**

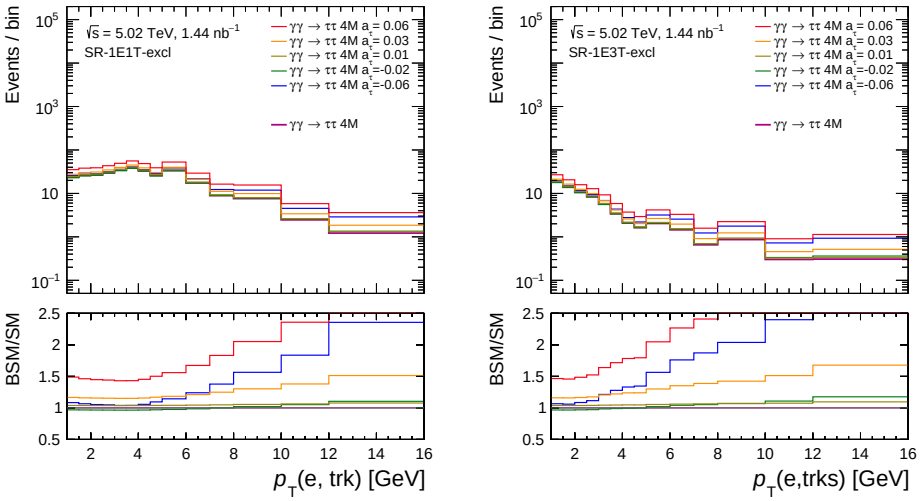

(c) **(d)**

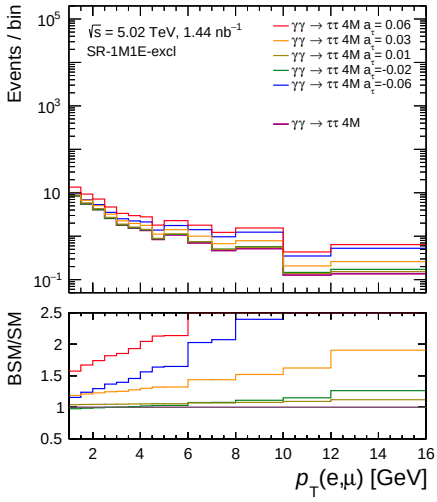

(e)

Figure 9.4: p_T of the lepton and track(s) or the dilepton system distributions in the signal regions SR-1M1T (a), SR-1M3T (b), SR-1E1T (c), SR-1E3T (d) for either muon or electron and track(s), depending on the SR, and SR-1M1E (e) for the muon and the electron. The upper panels show the signal prediction for different a_τ values, the lower panels show the ratios of the predictions with $a_\tau \neq 0$ to the SM prediction ($a_\tau = 0$).

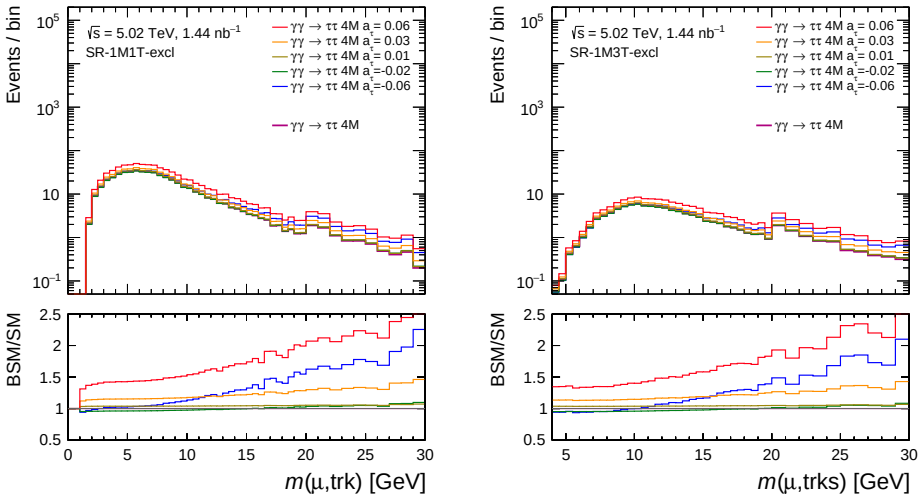

(a)

(b)

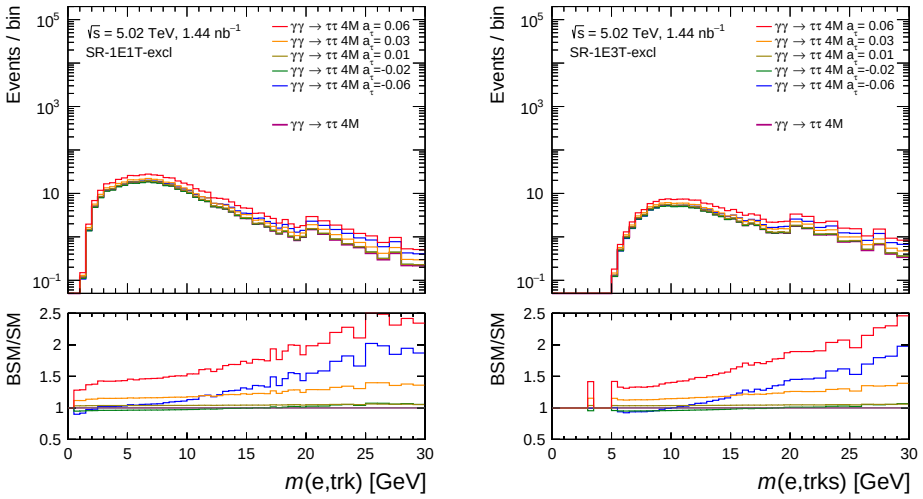

(c)

(d)

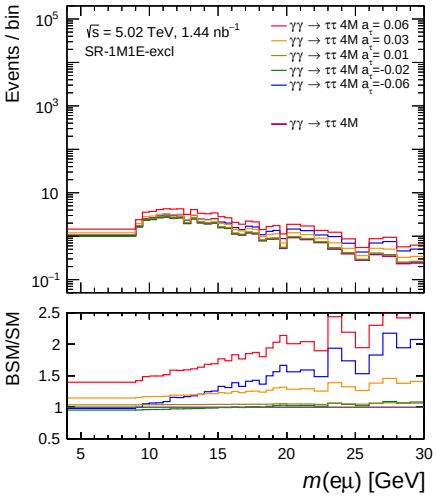

(e)

Figure 9.5: Invariant mass of the lepton and track(s) or the dilepton system distributions in the signal regions SR-1M1T (a), SR-1M3T (b), SR-1E1T (c), SR-1E3T (d) for either muon or electron and track(s), depending on the SR, and SR-1M1E (e) for the muon and the electron. The upper panels show the signal prediction for different a_τ values, the lower panels show the ratios of the predictions with $a_\tau \neq 0$ to the SM prediction ($a_\tau = 0$).

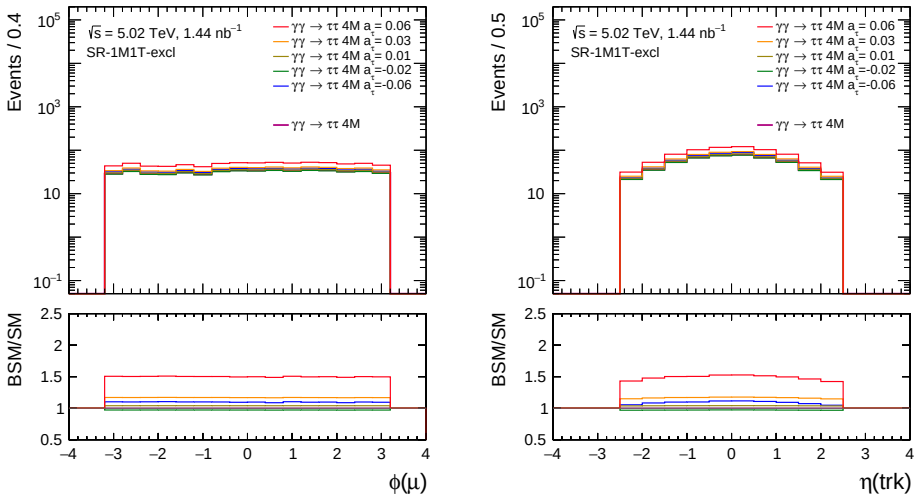

(a) **(b)**

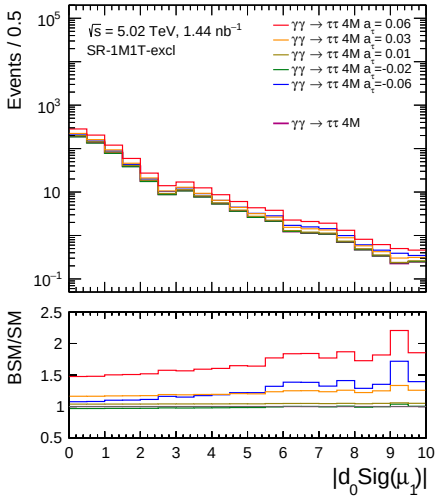

(c)

Figure 9.6: The angle ϕ of the leading muon (a), η of the track (b) and $|d_0\text{sig}(\mu)|$ (c) in SR-1M1T. The upper panels show the signal prediction for different a_τ values, the lower panels show the ratios of the predictions with $a_\tau \neq 0$ to the SM prediction ($a_\tau = 0$).

9.2 PARAMETRIZATION OF THE SIGNAL AS FUNCTION OF a_τ

The dependence of the signal cross section to a_τ, discussed in Section Section 4.1.2, can be investigated per bin of the kinematic distributions. Similar to the overall expected number of events, the expected signal events per bin are found to be quadratic as function of a_τ and can be parametrized using a polynomial of second degree

$$s_i(a_\tau) = A_i {a_\tau}^2 + B_i a_\tau + C_i \tag{9.2}$$

with the coefficients A_i, B_i and C_i. The coefficients per bin i are determined in a quadratic fit to the number of events as function of a_τ per bin i.
Alternatively to the quadratic fit, the dependence can be estimated by linear interpolation

$$s_i(a_\tau) = s_i(a_{\tau,i}) + (a_\tau - a_{\tau,i}) \frac{s_i(a_{\tau,i+1}) - s_i(a_{\tau,i})}{a_{\tau,i+1} - a_{\tau,i}} \tag{9.3}$$

in the interval $[a_{\tau,i}, a_{\tau,i+1}]$ with $a_\tau = [-0.10, -0.06, -0.05, -0.04, -0.03, -0.02, -0.01, 0.00, 0.01, 0.02, 0.03, 0.04, 0.05, 0.06, 0.10]$ which is used in the TRExFitter setup.

9.3 SENSITIVITY FOR THE SIGNAL PROCESS ONLY

The sensitive kinematic observables, found in Section 9.1, can be used to constrain a_τ. A NLL fit is performed as described in Section 6.2.4. In a first consideration, the Gaussian P_{Gaussian} and the Poissonian P_Γ terms, describing systematic and background statistical uncertainties are dropped from the likelihood function as in Equation (6.13). The extended log-likelihood function given in Equation (6.18) is used as first term in the likelihood function, i.e., both shape and cross section information are included in the fit. In order to consider only the signal process in the fit, the function $\nu_i(a_\tau)$ in Equation (6.6) is shorten to $\nu_i(a_\tau) = s_i(a_\tau)$ where the background contribution is neglected by $b_i = 0$.
The SM prediction of the signal process $\gamma\gamma \to \tau\tau$ is used as pseudo data to estimate first expected CIs for a_τ. The prediction of $s_i(a_\tau)$ for $a_\tau \neq 0$ is estimated from a quadratic fit for different values of a_τ between -0.10 to 0.10, for each bin of the kinematic distribution separately - see Section 9.2.
The sensitivity of the different SRs, SR-1M1T, SR-1M3T, SR-1E1T, SR-1E3T and SR-1M1E using different kinematic distributions $p_{\text{T}}(\ell)$, $p_{\text{T}}(\text{trk})$, $p_{\text{T}}(\ell, \text{trk(s)}/\ell')$, $m(\ell, \text{trk(s)}/\ell')$ and N_{Events} is evaluated. The 68 % CI for the best fit value $\hat{a}_\tau$ is determined together with its interval length, where the latter is used as a measure for the sensitivity. A shorter interval length indicates a higher sensitivity to the value of a_τ. The sensitivity estimated under the assumption of no background and related uncertainties, nor systematic uncertainties in the signal predictions highlights an ideal case of 100 % purity in the SRs and negligible uncertainties. This is an experimentally unrealistic case, but interesting here to study the basic sensitivities of the different SRs and kinematic distributions, as well as to serve as a baseline for the later inclusion and discussion of background and uncertainty effects.
The best fit values $\hat{a}_\tau$ from the signal-only fits, its uncertainty intervals I and the interval

lengths l are summarized in Table 9.3. The results are discussed in the following in more detail.

Measurement of a_τ using the Cross Section

The variable N_{Events} measures the sensitivity to a_τ using the cross section information only. The expected extended negative loglikelihood (eNLL) curves for the five SRs and N_{Events} are shown in Figure 9.7. The best a_τ value, denoted as $\hat{a}_\tau$ is determined as the minimum of the eNLL function and marked with a vertical line in the respective color. The usage of pseudo data in the fit results in $\hat{a}_\tau$ values very close to the SM prediction of $a_\tau = 0$.
For a simpler comparability between the SRs, the minimum of the NLL function is shifted to $y = 0$ denoted by ΔNLL. A double minimum structure in the eNLL is observed for all SRs. This is the result of the minimum of the cross section prediction as a function of a_τ being located at small negative values of $a_{\tau,\text{min}} \approx -0.03$. The latter leads to an ambiguity of the BSM cross section predictions for two a_τ values compared to the pseudo data - one as expected at $\hat{a}_\tau$ close to zero, and one at $\hat{a}_\tau < a_{\tau,\text{min}}$- visible as the second minimum in the NLL function. The sensitivity of the SRs is evaluated from the CI length l. The most sensitive SR with the interval length $l = 0.066$ is SR-1M1T, closely followed by SR-1E1T with an interval length $l = 0.067$. The SR-1E3T and SR-1M1E are comparable with interval length of $l = 0.078$ and $l = 0.078$, respectively and SR-1M3T has the lowest sensitivity with $l = 0.081$. The sensitivity for the signal-only fit for N_{Events} is mainly driven by the number of events that are counted in the respective SRs. Higher statistics provides better sensitivity than lower statistics. Another factor is the width of the quadratic curve for the signal production prediction depending on a_τ which is typical for the different phase space regions and kinematics described by each SR. For SR-1M3T, the width in Figure 9.1 is wider than for the other SRs increasing the expected interval lengths.

A first Comparison of the kinematic observables

The sensitivity of a particular kinematic variable changes between the different SRs. Therefore, no explicit pattern is observed but only tendencies for specific SRs can be given. The distribution of the transverse momentum of the leading lepton $p_{\text{T}}(\ell)$ achieves the shortest CIs at 68 % CL in SR-1M1T, SR-1E1T and SR-1M1E while the leading track $p_{\text{T}}(\text{trk})$ provides the overall highest sensitivity in SR-1M3T and SR-1E3T. The kinematic observable $p_{\text{T}}(\ell, \text{trk(s)}/\ell')$ tends to be least sensitive for the SRs expect where $p_{\text{T}}(\text{trk})$ dominates. For the SRs, where the observable $p_{\text{T}}(\ell)$ constraints a_τ best, the distribution $p_{\text{T}}(\text{trk})$ suffers most in sensitivity. As expected, the sensitivity of the N_{Events} variable is surpassed by all kinematic distributions.
Looking exemplary into SR-1E1T, illustrated in Figure 9.8, the eNLL functions for the kinematic observables can be compared. The respective figures for the other SRs can be found in Appendix G.1. The double minimum structure, observed in N_{Events}, is softened when shape information is included into the fit. The ambiguity in the cross section is alleviated or even resolved by the additional shape information and $\hat{a}_\tau$ moves clearly towards the SM value of $a_\tau = 0$, used in the pseudo data. The curves of $p_{\text{T}}(\text{trk})$, $m(e, \text{trk})$ and $p_{\text{T}}(e, \text{trk})$ are almost overlapping in the negative a_τ range, resulting in

Signal Region	Parameter	$\hat{a}_\tau$	Uncertainty interval for $\hat{a}_\tau$	Interval length
SR-1M1T-excl	$p_{\mathrm{T}}(\mu)$	0.00078	$[-0.024, 0.011]$	0.035
	$p_{\mathrm{T}}(\mathrm{trk})$	0.00068	$[-0.038, 0.011]$	0.049
	$p_{\mathrm{T}}(\mu, \mathrm{trk})$	0.00073	$[-0.026, 0.011]$	0.037
	$m(\mu, \mathrm{trk})$	0.00069	$[-0.031, 0.011]$	0.042
	N_{Events}	-0.045	$[-0.055, 0.011]$	0.066
SR-1M3T-excl	$p_{\mathrm{T}}(\mu)$	0.0011	$[-0.045, 0.020]$	0.065
	$p_{\mathrm{T}}(\mathrm{trk})$	0.0011	$[-0.044, 0.020]$	0.064
	$p_{\mathrm{T}}(\mu, \mathrm{trks})$	0.0010	$[-0.047, 0.020]$	0.067
	$m(\mu, \mathrm{trks})$	0.0010	$[-0.045, 0.020]$	0.065
	N_{Events}	-0.041	$[-0.060, 0.020]$	0.080
SR-1E1T-excl	$p_{\mathrm{T}}(e)$	0.00099	$[-0.034, 0.013]$	0.047
	$p_{\mathrm{T}}(\mathrm{trk})$	0.00090	$[-0.043, 0.013]$	0.056
	$p_{\mathrm{T}}(e, \mathrm{trk})$	0.00095	$[-0.040, 0.013]$	0.053
	$m(e, \mathrm{trk})$	0.00087	$[-0.041, 0.013]$	0.054
	N_{Events}	-0.041	$[-0.054, 0.013]$	0.069
SR-1E3T-excl	$p_{\mathrm{T}}(e)$	0.0012	$[-0.044, 0.019]$	0.063
	$p_{\mathrm{T}}(\mathrm{trk})$	0.0012	$[-0.042, 0.019]$	0.061
	$p_{\mathrm{T}}(e, \mathrm{trks})$	0.0011	$[-0.046, 0.019]$	0.065
	$m(e, \mathrm{trks})$	0.0011	$[-0.043, 0.019]$	0.062
	N_{Events}	-0.039	$[-0.058, 0.020]$	0.078
SR-1M1E-excl	$p_{\mathrm{T}}(\mu)$	0.0017	$[-0.045, 0.023]$	0.068
	$p_{\mathrm{T}}(e)$	0.0016	$[-0.046, 0.023]$	0.069
	$p_{\mathrm{T}}(e, \mu)$	0.0015	$[-0.047, 0.023]$	0.070
	$m(\mu, e)$	0.0015	$[-0.046, 0.024]$	0.070
	N_{Events}	-0.031	$[-0.054, 0.024]$	0.078

Table 9.3: Best fit value for a_τ, CI at 68 % CL and the corresponding interval length from eNLL fits for the four kinematic observables $p_{\mathrm{T}}(\ell)$, $p_{\mathrm{T}}(\mathrm{trk})$, $p_{\mathrm{T}}(\ell, \mathrm{trk(s)}/\ell')$ and $m(\ell, \mathrm{trk(s)}/\ell')$ and the cross section observable N_{Events} in the SRs SR-1M1T, SR-1M3T, SR-1E1T, SR-1E3T and SR-1M1E, using the signal prediction, only.

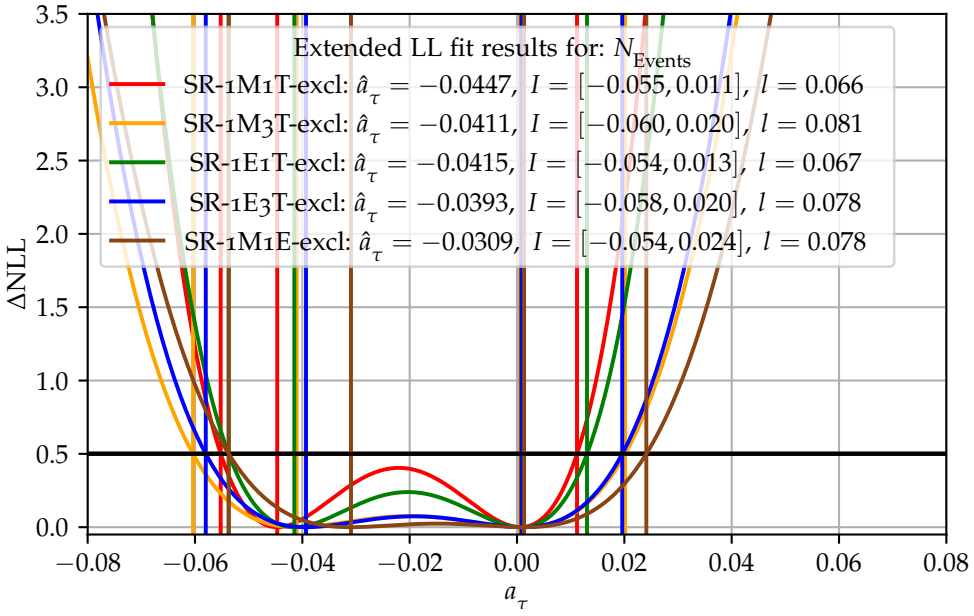

Figure 9.7: Extended NLL fits for the five SRs, SR-1M1T, SR-1M3T, SR-1E1T, SR-1E3T and SR-1M1E based on the cross section variable N_{Events}. The best fit value $\hat{a}_\tau$ is determined as the minimum of the ΔNLL function. The minimum is marked with a vertical line in the respective color. The 68 % CI I is determined by the intersection points of the ΔNLL function with a line at 0.5 marked by a horizontal line. The interval length is given in the legend.

similar interval lengths l and sensitivity to a_τ. The $p_{\text{T}}(e)$ distribution performs best from eNLL fits in SR-1E1T.

A First Comparison of the Signal Regions

The SRs can be compared easiest on the basis of the same kinematic distribution, e.g. $p_{\text{T}}(\ell)$. The eNLL functions of the overall very well performing $p_{\text{T}}(\ell)$ observable are shown in Figure 9.9, comparing the different SRs. The muon-based SR-1M1T constraints a_τ at 68 % CL best, with an expected interval length of $l = 0.0347$. The second best SR is the electron based SR-1E1T. In both SRs, SR-1M1T and SR-1E1T, the relatively large numbers of expected events (see the discussion above for the sensitivity of N_{Events}) boost the sensitivity in these regions compared to other SRs, while the $p_{\text{T}}(\ell)$ shape improves the sensitivity by about 30 % compared to the N_{Events} variable. The observations from the comparison of the relation of the SRs in N_{Events} are also visible in the kinematic distributions, but the shape information improves all SRs to a similar extent. For the other kinematic observables, similar patterns are observed (c.f. Table 9.3).
Overall, the lepton-based SRs with one tracks, SR-1M1T and SR-1E1T, show the highest sensitivity, followed by the three-track-based SR-1E3T and SR-1M3T. The SR based on one muon and one electron, SR-1M1E, has the smallest sensitivity when only the signal prediction is considered in the NLL fit.

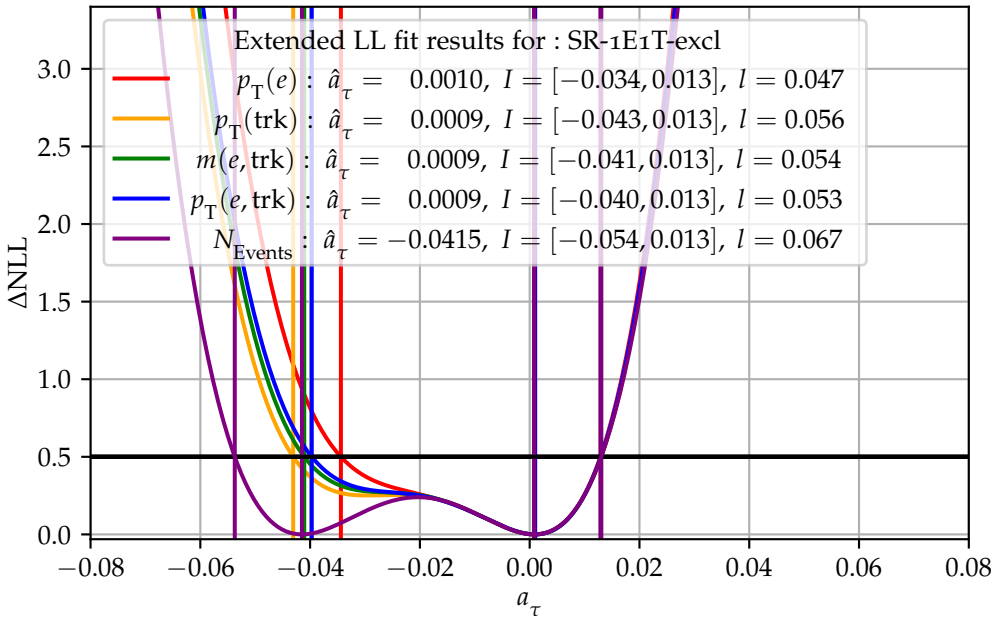

Figure 9.8: Extended NLL fits for the five observables $p_T(\ell)$, $p_T(\text{trk})$, $p_T(\ell, \text{trk(s)}/\ell')$, $m(\ell, \text{trk(s)}/\ell')$ and N_{Events} in SR-1E1T. The best fit value $\hat{a}_\tau$ is determined as the minimum of the ΔNLL function. The minimum is marked with a vertical line in the respective color. The 68 % CI I is determined by the intersection points of the ΔNLL function with a line at 0.5 marked by a horizontal line. The interval length is given in the legend.

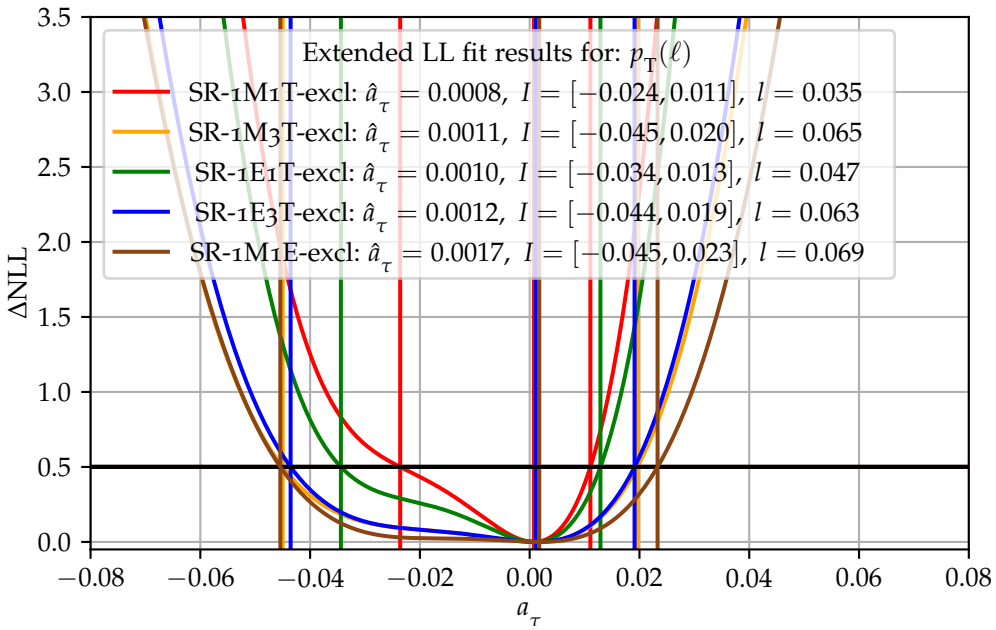

Figure 9.9: Extended NLL fits for the five SRs, SR-1M1T, SR-1M3T, SR-1E1T, SR-1E3T and SR-1M1E, for $p_T(\ell)$. The best fit value $\hat{a}_\tau$ is determined as the minimum of the ΔNLL function. The minimum is marked with a vertical line in the respective color. The 68 % CI I is determined by the intersection points of the ΔNLL function with a line at 0.5 marked by a horizontal line. The interval length is given in the legend.

9.4 SENSITIVITY WHEN INCLUDING BACKGROUND PROCESSES

In reality, the SRs are contaminated by background contributions. The relevant background processes of the SR-1M1T, SR-1M3T, SR-1E1T, SR-1E3T and SR-1M1E are $\gamma\gamma \to \mu\mu$, $\gamma\gamma \to ee$ and $\gamma\gamma \to q\bar{q}$ production. These background processes do not contain a $\gamma\tau\tau$ vertex and are therefore not sensitive to a_τ. A larger background contribution in the SRs thus leads to a loss of the sensitivity to a_τ.
The signal purity of the five SRs are presented together with the observed data and the expected signal and background yields in Table 9.4. The production cross section of the $\gamma\gamma \to \tau\tau$ process is blinded within $\pm 10\,\%$. The prediction is compared to data in Section 7.3 and the correction factors on the background processes $\gamma\gamma \to \mu\mu$ and $\gamma\gamma \to \tau\tau$ introduced in Section 8.1 are not applied in the following.
SR-1M3T and SR-1M1E are the cleanest SRs with a purity $> 90\,\%$. SR-1M1T has the highest statistics with a high purity of about 89 %. Both electron based SRs suffer in terms of purity, with SR-1E1T displaying the worst purity of all SRs with only 65 %, though still at least with the benefit of reasonably large statistics.
The effect of the expected background in the SRs on the CIs at 68 % CL for a_τ is investigated using eNLL fits, where both signal and background predictions are considered. The background yields are included in each bin for the expected number of events, i.e. $f_i(a_\tau) = s_i(a_\tau) + b_i$, as well as in the definition of the pseudo data.
The results of the fits are shown in Table 9.5 for the five SRs as well as the same variables as tested in Section 9.3. The results are compared in Table 9.6 to the CIs obtained with the signal-only fit configuration of Section 9.3, summarized in Table 9.3. The absolute and the percentage enhancement of the CI at 68 % CL from eNLL fits with the inclusion of the background prediction are shown there.

	SR 1M1T	SR 1M3T	SR 1E1T	SR 1E3T	SR 1M1E
Data d	485.0	78.0	548.0	52.0	42.0
Exp. Signal s	455.5	92.7	293.9	96.4	39.6
Exp. Background b	57.9	5.7	321.4	51.3	2.9
Signal purity in [%]	88.7	94.2	47.8	65.3	93.2

Table 9.4: Data, expected signal and background yields together with the signal purity of the SR-1M1T, SR-1M3T, SR-1E1T, SR-1E3T and SR-1M1E. The expected background yields b sum the contributions of the $\gamma\gamma \to \mu\mu$, $\gamma\gamma \to ee$ and $\gamma\gamma \to q\bar{q}$ backgrounds.

The increase of the CI length l for the signal and background eNLL fit is, as expected, an effect of the impurity caused by the background contributions in the SRs. For the cleanest two SRs SR-1M3T and SR-1M1E with only 5.8 % and 6.8 % background events, respectively, the increase of the interval length is the lowest. Except for the kinematic distribution of $m(\mu, \text{trks})$ in SR-1M3T, the interval length l is extended by less than 4 % in these two SRs. The most background-contaminated SR-1E1T with only 47.8 % signal events has an increase of the interval length within 12.28 % to 23.34 % depending on the kinematic distribution. The overall best performing SR, SR-1M1T, shows an intermediate increase of the interval lengths when the background prediction is included. The cross section observable N_{Events} is almost not affected by the contamination of the

Signal Region	Parameter	$\hat{a}_\tau$	Uncertainty interval for $\hat{a}_\tau$	Interval length
SR-1M1T	$p_{\mathrm{T}}(\mu)$	0.00087	$[-0.028, 0.012]$	0.039
	$p_{\mathrm{T}}(\mathrm{trk})$	0.00069	$[-0.044, 0.012]$	0.056
	$p_{\mathrm{T}}(\mu, \mathrm{trk})$	0.00077	$[-0.033, 0.012]$	0.044
	$m(\mu, \mathrm{trk})$	0.00070	$[-0.039, 0.012]$	0.050
	N_{Events}	-0.045	$[-0.056, 0.012]$	0.068
SR-1M3T	$p_{\mathrm{T}}(\mu)$	0.0012	$[-0.046, 0.020]$	0.066
	$p_{\mathrm{T}}(\mathrm{trk})$	0.0013	$[-0.046, 0.020]$	0.066
	$p_{\mathrm{T}}(\mu, \mathrm{trks})$	0.0012	$[-0.048, 0.020]$	0.068
	$m(\mu, \mathrm{trks})$	0.00081	$[-0.051, 0.021]$	0.072
	N_{Events}	-0.041	$[-0.061, 0.021]$	0.081
SR-1E1T	$p_{\mathrm{T}}(e)$	0.0011	$[-0.041, 0.017]$	0.058
	$p_{\mathrm{T}}(\mathrm{trk})$	0.00098	$[-0.047, 0.016]$	0.063
	$p_{\mathrm{T}}(e, \mathrm{trk})$	0.00086	$[-0.048, 0.017]$	0.065
	$m(e, \mathrm{trk})$	0.00089	$[-0.047, 0.017]$	0.064
	N_{Events}	-0.041	$[-0.058, 0.017]$	0.075
SR-1E3T	$p_{\mathrm{T}}(e)$	0.0010	$[-0.049, 0.022]$	0.072
	$p_{\mathrm{T}}(\mathrm{trk})$	0.0011	$[-0.047, 0.022]$	0.069
	$p_{\mathrm{T}}(e, \mathrm{trks})$	0.0013	$[-0.049, 0.022]$	0.071
	$m(e, \mathrm{trks})$	0.00088	$[-0.051, 0.023]$	0.074
	N_{Events}	-0.039	$[-0.061, 0.023]$	0.084
SR-1M1E	$p_{\mathrm{T}}(\mu)$	0.0017	$[-0.047, 0.024]$	0.071
	$p_{\mathrm{T}}(e)$	0.0016	$[-0.046, 0.024]$	0.070
	$p_{\mathrm{T}}(e, \mu)$	0.0016	$[-0.049, 0.024]$	0.073
	$m(\mu, e)$	0.0013	$[-0.050, 0.025]$	0.075
	N_{Events}	-0.031	$[-0.054, 0.025]$	0.079

Table 9.5: Best fit value for a_τ, CI at 68 % CL and the corresponding interval length from from eNLL fits for the four kinematic observables $p_{\mathrm{T}}(\ell)$, $p_{\mathrm{T}}(\mathrm{trk})$, $p_{\mathrm{T}}(\ell, \mathrm{trk(s)}/\ell')$ and $m(\ell, \mathrm{trk(s)}/\ell')$ and the cross section observable N_{Events} in the SRs, SR-1M1T, SR-1M3T, SR-1E1T, SR-1E3T and SR-1M1E using the signal and background prediction.

SR \ Obs.	$p_T(\ell)$		$p_T(\text{trk})$		$p_T(\ell, \text{trk(s)}/\ell)$		$m(\ell, \text{trk(s)}/\ell)$		N_{Events}	
	Δl	$\Delta l/l$ [%]	Δl	$\Delta l/l$ [%]	Δl	$\Delta l/l$ [%]	Δl	$\Delta l/l$ [%]	Δl	$\Delta l/l$ [%]
SR-1M1T	0.0043	12.4	0.0066	13.3	0.0071	19.0	0.0086	20.6	0.0011	1.7
SR-1M3T	0.0009	1.4	0.0018	2.8	0.0014	2.1	0.0067	10.4	0.0009	1.1
SR-1E1T	0.0103	21.8	0.0072	12.8	0.0123	23.3	0.0109	20.2	0.0082	12.3
SR-1E3T	0.0090	14.4	0.0076	12.5	0.0059	9.1	0.0121	19.6	0.0063	8.1
SR-1M1E	0.0021	3.1	0.0008	1.2	0.0026	1.4	0.005	3.7	0.0011	1.4

Table 9.6: Increase of the CIs at 68 % CL for the eNLL fit using signal and background predictions compared to the signal only fit. The absolute difference $\Delta l = l_{\text{sigbkg}} - l_{\text{sigonly}}$ of the interval lengths l and the increase $\Delta l / L_{\text{sigonly}}$ in % are listed for the four kinematic observables $p_T(\ell)$, $p_T(\text{trk})$, $p_T(\ell, \text{trk(s)}/\ell')$ and $m(\ell, \text{trk(s)}/\ell')$ and the cross section observable N_{Events} in the SRs SR-1M1T, SR-1M3T, SR-1E1T, SR-1E3T and SR-1M1E.

background, while for the kinematic distributions of $p_T(\mu, \text{trk})$ and $m(\mu, \text{trk})$ an increase of the interval length of about 20 % is observed. The increase of the interval length for $p_T(\mu)$ and $p_T(\text{trk})$ is only approximately 13 %. The high statistics in this SR suppresses the effect of the background contribution in N_{Events} while the shape of the kinematic distributions $p_T(\ell)$, $p_T(\text{trk})$, $p_T(\ell, \text{trk(s)}/\ell')$ and $m(\ell, \text{trk(s)}/\ell')$ are affected to a larger extent. In SR-1E3T, $m(e, \text{trks})$ is also affected by an increase of the CI by about 20 % while the other kinematic distributions are less affected with < 15 %.
The change of the shape of the likelihood function when including the background in the fit is exemplary shown for $p_T(\ell)$, $m(\ell, \text{trk(s)}/\ell')$ and N_{Events} in SR-1M1T in Figure 9.10. Further figures can be found in Appendix G.2. The widening of the eNLL function in a_τ for $p_T(\ell)$ and $m(\ell, \text{trk(s)}/\ell')$ for the signal and background when including the background in the fit, is clearly visible, while the shape of the curve for N_{Events} remains nearly constant (with only a very small widening effect). Inspite of the stronger increase of the CIs for the kinematic variables, the CIs obtained from fits to these are still smaller than the ones for N_{Events}. So, there is still a gain in using the shape dependence in addition to just the cross section dependence.
Overall, the background events that contribute the SRs affect the sensitivity of the shape of kinematic distributions to a_τ to a larger extend than the cross section - under the assumption of a full knowledge of background effects. For SRs with a high expected background yield, the effect of the decrease in sensitivity to the cross section alone is non-negligible. The observed behavior of increase of the interval lengths is thus expected and can be understood.

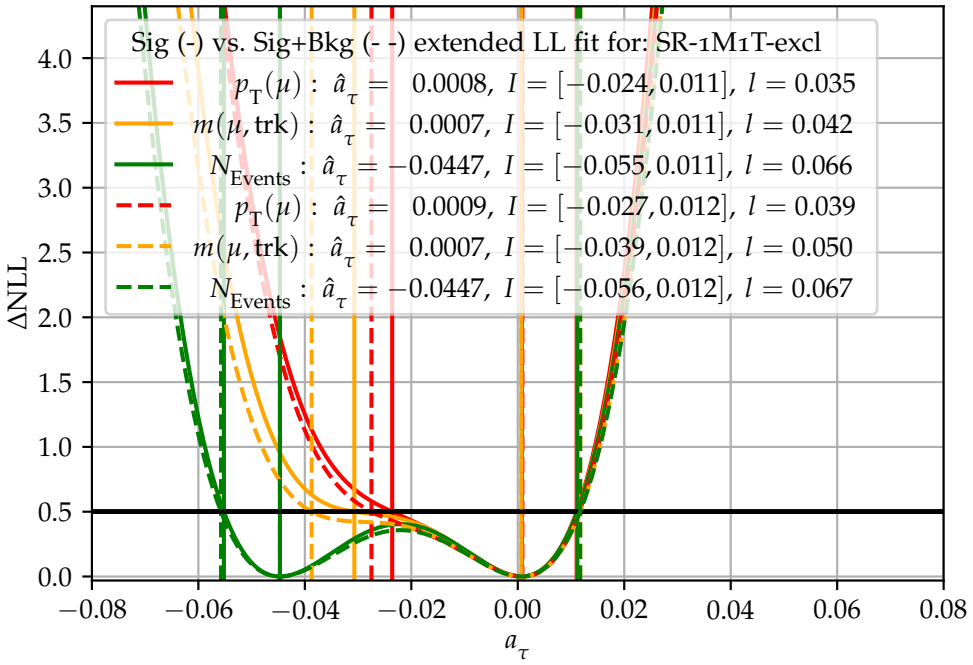

Figure 9.10: Comparison of eNLL fit functions in SR-1M1T for the kinematic distribution $p_T(\mu)$, $m(\mu, \text{trk})$ and the cross section observable N_{Events} for the signal-only (solid lines) and signal+background (dashed lines) fits. The best fit value $\hat{a}_\tau$ is determined as the minimum of the ΔNLL function. The minimum is marked with a vertical line in the respective color. The 68 % CI I is determined by the intersection points of the ΔNLL function with a line at 0.5 marked by a horizontal line. The interval length is given in the legend.

9.5 COMPARISON OF NORMAL AND EXTENDED NEGATIVE LOG-LIKELIHOOD FITS

The two types of LL fits introduced in Chapter 6: extended and normal. They use different information from the distribution of an observable to calculate the constraints on a_τ. In both fit functions, the shape information is processed, while the sensitivity of a_τ to the cross section is only taken into account in an eNLL fit function.
In the following, the sensitivity to measure a_τ is compared for the method of the nNLL and the eNLL fits. The cross section observable N_{Events} that does not contain any shape information is therefore left out of the comparison. It is expected for the eNLL function to constrain a_τ better than for the nNLL since the cross section information is additionally used. The difference of the constraints on a_τ is estimated for the kinematic observables $p_T(\ell)$, $p_T(\text{trk})$, $p_T(\ell, \text{trk(s)}/\ell')$ and $m(\ell, \text{trk(s)}/\ell')$ in SR-1M1T, SR-1M3T, SR-1E1T, SR-1E3T and SR-1M1E.
The nNLL fit is performed with the same setup as discussed for the eNLL fit in Section 9.4. The best fit values $\hat{a}_\tau$, the respective CIs I and interval lengths are given in Table 9.7 for the nNLL fits. A direct comparison of the interval lengths to the values from corresponding eNLL fits (compared Table 9.5 for the results) is given in Table 9.8.

Signal Region	Parameter	$\hat{a}_\tau$	Uncertainty interval for $\hat{a}_\tau$	Interval length
SR-1M1T	$p_{\mathrm{T}}(\mu)$	0.0024	$[-0.029, 0.034]$	0.063
	$p_{\mathrm{T}}(\mathrm{trk})$	0.0024	$[-0.045, 0.049]$	0.094
	$p_{\mathrm{T}}(\mu, \mathrm{trk})$	0.0023	$[-0.035, 0.039]$	0.073
	$m(\mu, \mathrm{trk})$	0.0045	$[-0.040, 0.049]$	0.089
SR-1M3T	$p_{\mathrm{T}}(\mu)$	0.0034	$[-0.047, 0.054]$	0.101
	$p_{\mathrm{T}}(\mathrm{trk})$	0.0031	$[-0.047, 0.054]$	0.101
	$p_{\mathrm{T}}(\mu, \mathrm{trks})$	0.0031	$[-0.052, 0.058]$	0.110
	$m(\mu, \mathrm{trks})$	0.0047	$[-0.055, 0.064]$	0.119
SR-1E1T	$p_{\mathrm{T}}(e)$	-0.0014	$[-0.039, 0.037]$	0.076
	$p_{\mathrm{T}}(\mathrm{trk})$	-0.0041	$[-0.047, 0.037]$	0.084
	$m(e, \mathrm{trk})$	-0.00096	$[-0.049, 0.046]$	0.095
	$p_{\mathrm{T}}(e, \mathrm{trk})$	-0.0011	$[-0.050, 0.048]$	0.098
SR-1E3T	$p_{\mathrm{T}}(e)$	0.0045	$[-0.054, 0.063]$	0.117
	$p_{\mathrm{T}}(\mathrm{trk})$	0.0010	$[-0.048, 0.050]$	0.098
	$p_{\mathrm{T}}(e, \mathrm{trks})$	-0.000011	$[-0.052, 0.051]$	0.103
	$m(e, \mathrm{trks})$	0.0027	$[-0.055, 0.061]$	0.116
SR-1M1E	$p_{\mathrm{T}}(\mu)$	0.0043	$[-0.060, 0.069]$	0.129
	$p_{\mathrm{T}}(e)$	0.0030	$[-0.059, 0.065]$	0.124
	$p_{\mathrm{T}}(\mu, e)$	0.0040	$[-0.067, 0.075]$	0.141
	$m(\mu, e)$	0.0052	$[-0.068, 0.079]$	0.147

Table 9.7: Best fit value for a_τ, CI at 68 % CL and the corresponding interval length from nNLL fit for the four kinematic observables $p_{\mathrm{T}}(\ell)$, $p_{\mathrm{T}}(\mathrm{trk})$, $p_{\mathrm{T}}(\ell, \mathrm{trk(s)}/\ell')$ and $m(\ell, \mathrm{trk(s)}/\ell')$ in the SRs SR-1M1T, SR-1M3T, SR-1E1T, SR-1E3T and SR-1M1E using the signal and background prediction as input of the fit.

Obs. / SR	$p_T(\ell)$			$p_T(\text{trk})$			$p_T(\ell, \text{trk(s)})$			$m(\ell, \text{trk(s)})$		
	E	N	Δl[%]	E	N	Δl[%]	E	N	Δl[%]	E	N	Δl[%]
SR-1M1T	0.039	0.063	37.7	0.056	0.094	40.4	0.044	0.074	39.7	0.050	0.074	31.5
SR-1M3T	0.066	0.101	35.3	0.066	0.101	34.9	0.068	0.110	37.6	0.071	0.119	40.1
SR-1E1T	0.058	0.076	24.1	0.063	0.084	25.0	0.064	0.095	32.4	0.065	0.098	33.3
SR-1E3T	0.072	0.117	38.6	0.069	0.098	30.4	0.071	0.103	31.5	0.074	0.116	36.1
SR-1M1E	0.071	0.129	45.0	0.070	0.124	43.2	0.073	0.142	48.5	0.075	0.147	49.0

Table 9.8: Comparison of 68 % CI lengths l for the eNLL (E) and nNLL (N) fits in for the observables $p_T(\ell)$, $p_T(\text{trk})$, $p_T(\ell, \text{trk(s)}/\ell')$ and $m(\ell, \text{trk(s)}/\ell')$ in the SRs SR-1M1T, SR-1M3T, SR-1E1T, SR-1E3T and SR-1M1E using the signal and background prediction as inputs to the fits. Δl is gives the improvement for the eNLL compared to the nNLL fit.

As shown in Table 9.8, the interval lengths increase for the nNLL fits compared to the eNLL fits as a result of the removal of the cross section contribution to determining a_τ. The interval length increases for most kinematic observables in most SRs by over 60 % for the nNLL fit. Thus, the cross section sensitivity to a_τ which is included in the eNLL helps to constrain a_τ.
The distribution of $p_T(\ell)$ and the SR-1M1T show the highest expected sensitivity in the nNLL fit which is in agreement with the eNLL results. Similarly, the SR with the least sensitivity is for both methods SR-1M1E. For the SRs and kinematic observables with an intermediate sensitivity, the sensitivity obtained with the nNLL fit is enlarged compared to the nELL fit, but the same tendency is observed.
The shape of the LL functions is compared in the kinematic distribution of $p_T(\text{trk})$ in Figure 9.11 exemplary for SR-1E1T. The nNLL function is almost symmetric around the best a_τ value $\hat{a}_\tau = -0.0041$. In contrast, for the eNLL function, a faint double minimum structure is found. The SM minimum is observed near the SM prediction at $a_\tau = 0$, while the second, weaker minimum is located in a negative a_τ range between -0.04 and -0.03.
The first minimum at $a_\tau = 0$ is driven by the shape sensitivity to a_τ which is included to both fits. The sensitivity of the cross section on a_τ, considered in the eNLL fit, results in the second weaker minimum at $a_\tau \approx= -0.033$ (compare to the discussion in Table 9.3 of the NLL form for fits of N_{Events}). The combination of a shape fit and a cross section fit leads to the asymmetric NLL form, observed for the eNLL fit.
The investigations described above lead to the conclusion that the information of the cross section sensitivity to a_τ is valuable information in the LL function and therefore an effective, necessary way to constrain the best fit value $\hat{a}_\tau$ further. The gain in constraining a_τ by through eNLL fits instead of nNLL fits is over 25 % in all kinematic distributions and SRs. As a consequence, only the eNLL fits are used in the following studies about the impact of systematic uncertainties. Normal NLL fits are not considered further.

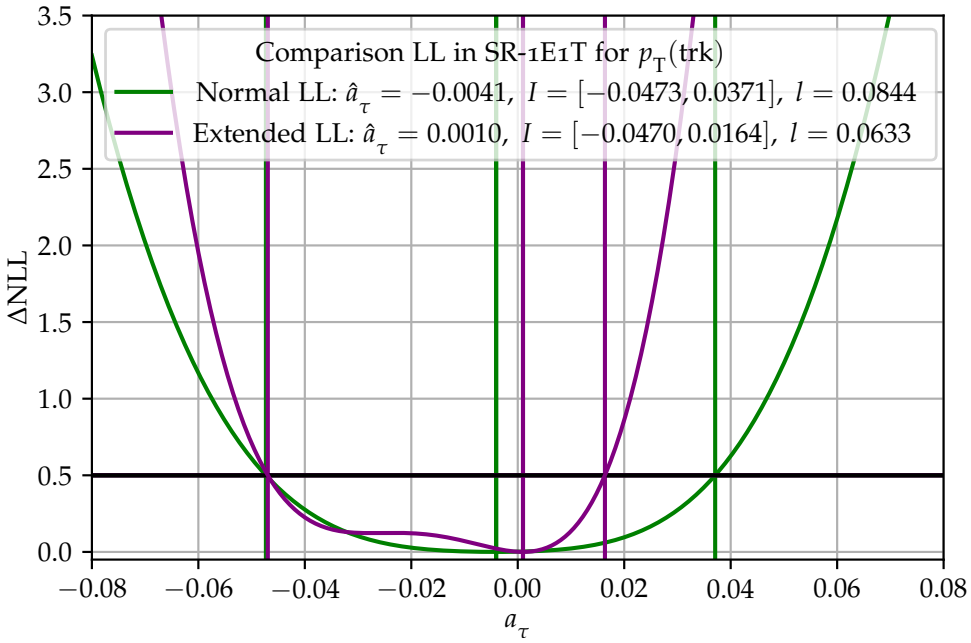

Figure 9.11: Comparison of the normal (green) and extended (purple) LL fit functions in SR-1E1T for the kinematic distribution p_T(trk). The best fit value $\hat{a}_\tau$ is determined as the minimum of the ΔNLL function. The minimum is marked with a vertical line in the respective color. The 68 % CI I is determined by the intersection points of the ΔNLL function with a line at 0.5 marked by a horizontal line. The interval length is given in the legend.

9.6 SENSITIVITY INCLUDING SYSTEMATIC UNCERTAINTIES

For the determination of a_τ and its constraints, different aspects need to be considered. So far, the expected background contribution and statistical effects were included. Another very important aspect that needs to be discussed, are systematic uncertainties.
The estimation of the signal and background prediction through simulation but also data-driven background estimates are associated with a variety of systematic uncertainties. These include for example trigger efficiencies as well as track, topocluster or lepton reconstruction, identification, calibration and isolation efficiencies. Theoretical uncertainties from the modeling of both signal and background processes include the choice of the MC generator, or in particular for the $\gamma\gamma \to \tau\tau$ analysis, the modeling of the photon flux as important uncertainty sources. Experimentally, another contributing factor is the integrated luminosity uncertainty.
To test the impact of systematic uncertainties on the estimation of CIs, a simple approach is employed which assumes very basic overall uncertainties that are rough estimates of the expected combined uncertainty. For this purpose, the relevant uncertainties from various sources are summarized into a global uncertainty of 5 % on both, signal and background separately. The impact of these arbitrary chosen systematics on the CI for a_τ are evaluated.
For the inclusion of systematic uncertainties in the eNLL fit, a tool called TRExFitter [88] is used. Similar to the self-written `Python`-based software used in this thesis so

far, TRExFitter performs an eNLL fit based on the description in Chapter 6. To proof the consistency of the two frameworks, a validation is performed. Afterwards, global systematic uncertainties are included in the fit and the effect is studied.

9.6.1 *Validation of the TRExFitter Results*

To validate the CIs obtained with the TRExFitter, the results of an eNLL fit using signal and background predictions as input are compared to the results obtained with the `Python`-based software which the previous results are based upon. TRExFitter uses a linear interpolation method, while for the `Python`-based the quadratic terms are considered. The CIs at 68 % CL for a_τ obtained with TRExFitter are given in Table 9.9 and can be compared to the previous results in Table 9.5. The last column in Table 9.9 shows the percentage difference of the interval length l from the TRExFitter software compared to the interval length l obtained with the `Python`-based software.
The observed differences between the two softwares are small, with the maximum percentage difference of $|\Delta l| = 3.2\,\%$. On average, the difference is $|\Delta l| = 1.7\,\%$. These differences are though small, still too large to come from numerical instabilities in the calculation of the eNLL function or the calculation of the the CI. Thus, another factor in the calculation must be different in order to explain the interval length differences.
In order to access predictions for all a_τ values in a fit, an interpolation method, also called *morphing* is used in both setups. The interpolation between the BSM predictions for $a_\tau = -0.10, -0.06, -0.05, \ldots 0.05, 0.06, 0.10$ is performed to obtain the predictions for intermediate a_τ values. In Section 9.1, it was shown that the dependence of the cross section on a_τ in each bin i is quadratic in a_τ. Hence, the most adequate and precise morphing option therefore is to interpolate quadratically. This ansatz is implemented and used in the `Python`-based software.
For the TRExFitter fitter setup, different `Template Interpolation Options` can be chosen by the user: *linear*, *smoothlinear* and *squareroot*[1]. TRExFitter does not provide a quadratic morphing option.
An illustration of the quadratic vs. the linear morphing method is given in Figure 9.12 for SR-1M1T and the N_{Events} variable. For the linear interpolation, only the two neighboring points are included, while for the quadratic fits, all provided a_τ values are included simultaneously in the function $N_{\text{exp}}(a_\tau) = A{a_\tau}^2 + Ba_\tau + C$ with the fit coefficients A, B, C. The comparison of the linear and the quadratic morphing shows a good agreement in the lower $|a_\tau|$ range, while small discrepancies are found for the range $|a_\tau| > 0.06$. The discrepancies are thus inherently linked to the sampling steps in a_τ for the BSM predictions. The smaller the differences between a_τ values for which predictions are provided, the better is the agreement with the more accurate quadratic interpolation. In this analysis, the expected range for the best-fit a_τ value is within $|a_\tau| < 0.06$, and the BSM predictions at $|a_\tau| = 0.10$ are included mainly to ensure a proper behavior of boundary cases. Therefore, the small discrepancies between the two morphing approaches, in particular for $|a_\tau| > 0.06$, are considered to be acceptable.
In Table 9.10, the three morphing options are investigated and compared to the quadratic

1 These three interpolation options are provided in the TRExFitter setup. For all three options, an interpolation between neighbored input points for the morphing is performed. *Linear* interpolates between the inputs with a linear ansatz, *smoothlinear* approximates it by aj integral of the hyperbolic tangent and *squareroot* approximates is by $\sqrt{x^2 + \epsilon}$.

Signal Region	Parameter	$\hat{a}_\tau$	Uncertainty interval for $\hat{a}_\tau$	Interval length l	Δl [%]
SR-1M1T	$p_{\mathrm{T}}(\mu)$	−0.000001	[−0.028, 0.012]	0.040	3.2
	$p_{\mathrm{T}}(\mathrm{trk})$	−0.000001	[−0.042, 0.012]	0.055	−2.9
	$p_{\mathrm{T}}(\mu, \mathrm{trk})$	−0.000000	[−0.034, 0.012]	0.046	2.4
	$m(\mu, \mathrm{trk})$	0.000000	[−0.038, 0.012]	0.050	−0.2
	N_{Events}	−0.000001	[−0.053, 0.012]	0.065	−3.2
SR-1M3T	$p_{\mathrm{T}}(\mu)$	−0.000000	[−0.043, 0.021]	0.065	−1.4
	$p_{\mathrm{T}}(\mathrm{trk})$	0.000000	[−0.044, 0.021]	0.065	−1.4
	$p_{\mathrm{T}}(\mu, \mathrm{trk})$	0.000000	[−0.046, 0.023]	0.069	1.6
	$m(\mu, \mathrm{trk})$	0.000000	[−0.049, 0.022]	0.071	−0.8
	N_{Events}	−0.000000	[−0.059, 0.022]	0.081	−0.4
SR-1E1T	$p_{\mathrm{T}}(e)$	−0.000001	[−0.039, 0.017]	0.056	−2.9
	$p_{\mathrm{T}}(\mathrm{trk})$	0.000000	[−0.045, 0.017]	0.062	−2.8
	$p_{\mathrm{T}}(e, \mathrm{trk})$	−0.000000	[−0.046, 0.018]	0.064	−1.3
	$m(e, \mathrm{trk})$	−0.000000	[−0.045, 0.018]	0.063	−3.5
	N_{Events}	−0.000001	[−0.056, 0.018]	0.074	−1.6
SR-1E3T	$p_{\mathrm{T}}(e)$	−0.000000	[−0.047, 0.024]	0.071	−1.3
	$p_{\mathrm{T}}(\mathrm{trk})$	−0.000000	[−0.044, 0.023]	0.067	−1.8
	$p_{\mathrm{T}}(e, \mathrm{trk})$	−0.000001	[−0.047, 0.025]	0.071	0.8
	$m(e, \mathrm{trk})$	0.000000	[−0.049, 0.024]	0.073	−0.8
	N_{Events}	−0.000000	[−0.060, 0.024]	0.084	−0.1
SR-1M1E	$p_{\mathrm{T}}(\mu)$	−0.000001	[−0.045, 0.025]	0.070	−1.6
	$p_{\mathrm{T}}(e)$	−0.000000	[−0.044, 0.025]	0.069	−1.9
	$p_{\mathrm{T}}(\mu, e)$	−0.000001	[−0.047, 0.028]	0.075	2.4
	$m(\mu, e)$	0.000000	[−0.048, 0.026]	0.074	−1.1
	N_{Events}	−0.000000	[−0.052, 0.026]	0.078	−0.9

Table 9.9: Best fit value for a_τ, CI at 68 % CL and the corresponding interval length from eNLL fits for the four kinematic observables $p_{\mathrm{T}}(\ell)$, $p_{\mathrm{T}}(\mathrm{trk})$, $p_{\mathrm{T}}(\ell, \mathrm{trk(s)}/\ell')$ and $m(\ell, \mathrm{trk(s)}/\ell')$ in the SRs SR-1M1T, SR-1M3T, SR-1E1T, SR-1E3T and SR-1M1E using the signal and background prediction as input. Δl is the difference of the interval length l from the fit using the Python-based and the TRExFitter software.

morphing from the Python-based software, exemplary for SR-1M1T. The best agreement is found for the linear morphing option in TRExFitter, while the *smoothlinear* and *squareroot* are not properly working or have higher discrepancies. The discrepancies of the expected CI lengths between the quadratic, in the Python-based and the linear interpolation method, in TRExFitter are between 0.2 % and 3.3 %. For the smoothlinear in all kinematic observables, and the squareroot option in the $p_{\mathrm{T}}(\mu, \mathrm{trk})$ and $m(\mu, \mathrm{trk})$ distribution, the fit is broken such that a CI length of 0.0010 returned. These lengths can not be physically interpreted and show a discrepancy of over 95 % compared to the interval lengths obtained with the quadratic interpolation in the Python-based and the linear option in TRExFitter software.
To conclude, due to the different morphing methods used in the Python-based and TRExFitter software, a small discrepancy between the obtained CIs at 68 % CL for signal plus background fits is observed. Taking this into consideration, both softwares are found to be compatible and TRExFitter can be used for further investigations.

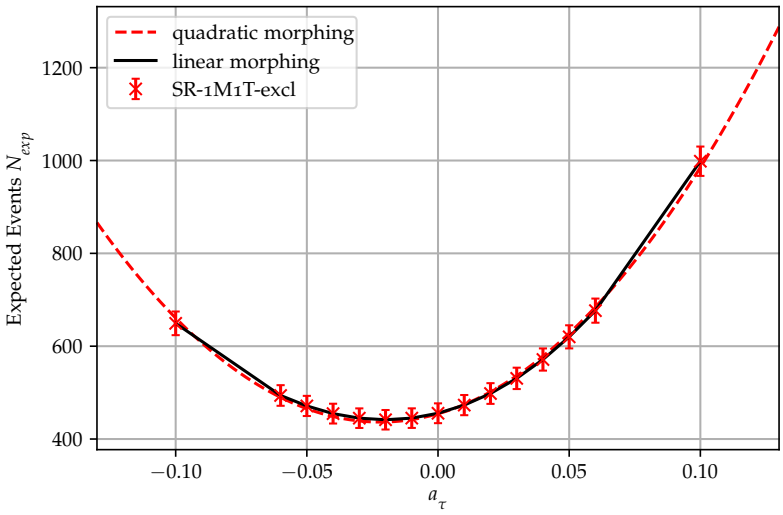

Figure 9.12: Differences of linear and quadratic morphing for SR-1M1T and the N_{Events} variable. For the linear morphing (black lines), the data points of the number of expected events are connected with a linear ansatz $N_{\mathrm{exp}}(a_\tau) = Aa_\tau + B$ between two a_τ predictions. In the method of the quadratic morphing (red dashed line), the fit function $N_{\mathrm{exp}}(a_\tau) = Aa_\tau{}^2 + Ba_\tau + C$ is used.

9.6.2 *Inclusion of Statistical Uncertainties on the Background Prediction*

The effect of limited MC statistics for the background estimation, which is based on simulated event samples, on the determination of a_τ is investigated in the following. The Gamma term in the likelihood function in Equation (6.13) describes this effect. The uncertainty of the MC prediction is accounted for in each bin, denoted as γ-factors, which are considered nuisance parameters (NPs) in the fit, and thus impact the CI lengths of the best-fit values $\hat{a}_\tau$.

Parameter	Python-based	*Linear*	Δl [%]	*Smoothlinear*	Δl [%]	*Squareroot*	Δl [%]
$p_{\mathrm{T}}(\mu)$	0.039	0.040	3.3	0.0010	−97.4	0.041	6.2
$p_{\mathrm{T}}(\mathrm{trk})$	0.056	0.055	−2.9	0.0010	−98.2	0.052	−8.0
$p_{\mathrm{T}}(\mu, \mathrm{trk})$	0.044	0.046	2.5	0.0010	−97.8	0.0010	−97.5
$m(\mu, \mathrm{trk})$	0.050	0.050	−0.2	0.0010	−98.0	0.0010	−98.0
N_{Events}	0.068	0.065	−3.1	0.0010	−98.5	0.063	−6.7

Table 9.10: Comparison of the CI length l at 68 % CL from an eNLL fit with the Python-based, and the TRExFitter software with the morphing options *linear*, *smoothlinear* and *squareroot* in $p_{\mathrm{T}}(\mu)$, $p_{\mathrm{T}}(\mathrm{trk})$, $p_{\mathrm{T}}(\mu, \mathrm{trk})$, $m(\mu, \mathrm{trk})$ and N_{Events} in SR-1M1T. The percentage difference of the results Δl with respect to the Python-based software is calculated for the three morphing options. The fit results using the *linear* morphing are best in agreement to the previously calculated CIs.

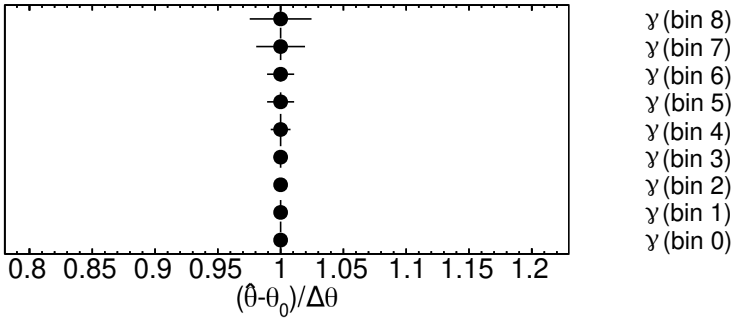

Figure 9.13: Visualization of the γ-factors in every bin calculated for the $p_{\mathrm{T}}(\mu)$ distribution in SR-1M1T indicate potential pulls (non-existent for a fit with pseudo data), the black error bars potential constraints calculated by $\hat{\theta} - \theta_0 / \Delta\theta$ for each NP θ.

The γ-factors are determined for the kinematic distributions in the five SRs and the CI lengths at 68 % CL for the best-fit values $\hat{a}_\tau$ is calculated. The quadratic sum of the statistical uncertainties is used and both SM signal and SM background are considered as "background" here in the fit for a_τ. Table 9.11 gives an overview of the obtained interval lengths for the two cases: excluding the effect of γ-factors (l_{StatOnly}) and including the effect of γ-factors ($l_{\gamma\text{-factors}}$). The difference of both interval lengths Δl is calculated and the relative increase to with respect to l_{StatOnly} is shown in the last column. The increase of the interval length, caused by the γ-factors is ≤ 0.06 % for all kinematic distributions in all SRs. The impact of the γ-factors is a minor effect, and a testimony that adequate statistics were produced for the signal and background MC simulation.
The behavior of the γ-factors in the fit of the $p_{\mathrm{T}}(\mu)$ distribution in SR-1M1T (c.f. Figure 8.7 (a)) is shown in Figure 9.13 and Figure 9.14. The $p_{\mathrm{T}}(\mu)$ distribution uses 9 bins with the following bin boundaries: 4, 5, 6, 7, 8, 9, 10, 12.5, 15, 30 in GeV, which are numbered from 0 (lowest p_{T}) to 8 (highest p_{T}) by TRExFitter. The largest statistical uncertainties are expected for the highest p_{T} bins where the impact of a_τ on the prediction is strongest.
The statistical uncertainty of the background MC is reflected in the size of the γ-factors. For bins with large numbers of events (low $p_{\mathrm{T}}(\mu)$), the γ-factors are small, only for the

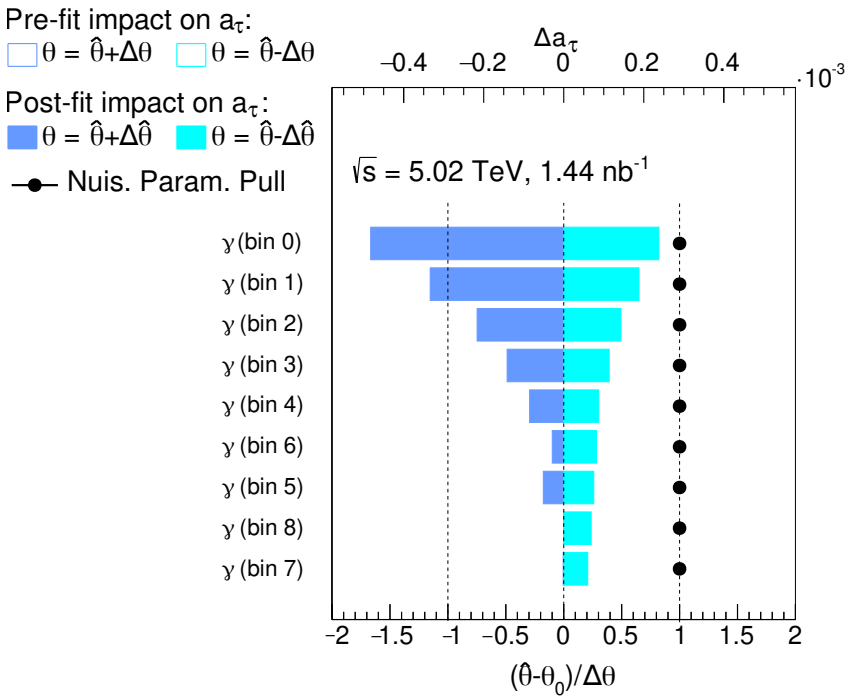

Figure 9.14: Ranking of NPs (here γ-factors) regarding their post-fit impact on the fit of a_τ based on the $p_T(\mu)$ distribution in SR-1M1T. Blue solid bars show the post-fit impact on a_τ, the blue empty bars show the pre-fit impact on a_τ for the different NPs - quantified by Δa_τ in the upper x-axis. The black dots indicate the pulls, black error bars the constraints on the different NPs θ - quantified by $\hat{\theta} - \theta_0/\Delta\theta$ in the lower x-axis. In a fit with pseudo data as performed here, no pulls are possible; γ-factors are located at one, other NPs at zero.

Signal Region	Parameter	l_{StatOnly}	$l_{\gamma\text{-factors}}$	Δl	Δl in %
SR-1M1T	$p_{\text{T}}(\mu)$	0.040329	0.040348	0.000019	0.05
	$p_{\text{T}}(\text{trk})$	0.054460	0.054476	0.000017	0.03
	$p_{\text{T}}(\mu, \text{trk})$	0.045504	0.045524	0.000020	0.04
	$m(\mu, \text{trk})$	0.050340	0.050360	0.000020	0.04
	N_{Events}	0.065378	0.065388	0.000010	0.02
SR-1M3T	$p_{\text{T}}(\mu)$	0.064556	0.064579	0.000023	0.04
	$p_{\text{T}}(\text{trk})$	0.064933	0.064956	0.000023	0.04
	$p_{\text{T}}(\mu, \text{trk})$	0.069500	0.069527	0.000026	0.04
	$m(\mu, \text{trk})$	0.070765	0.070787	0.000022	0.03
	N_{Events}	0.081067	0.081084	0.000017	0.02
SR-1E1T	$p_{\text{T}}(e)$	0.055999	0.056032	0.000034	0.06
	$p_{\text{T}}(\text{trk})$	0.061616	0.061641	0.000024	0.04
	$p_{\text{T}}(e, \text{trk})$	0.063504	0.063539	0.000035	0.05
	$m(e, \text{trk})$	0.062798	0.062828	0.000030	0.05
	N_{Events}	0.073841	0.073869	0.000028	0.04
SR-1E3T	$p_{\text{T}}(e)$	0.070797	0.070838	0.000041	0.06
	$p_{\text{T}}(\text{trk})$	0.067300	0.067329	0.000028	0.04
	$p_{\text{T}}(e, \text{trk})$	0.071168	0.071198	0.000030	0.04
	$m(e, \text{trk})$	0.073257	0.073289	0.000032	0.04
	N_{Events}	0.083760	0.083786	0.000026	0.03
SR-1M1E	$p_{\text{T}}(\mu)$	0.069734	0.069761	0.000027	0.04
	$p_{\text{T}}(e)$	0.068885	0.068910	0.000024	0.03
	$p_{\text{T}}(\mu, e)$	0.074781	0.074810	0.000029	0.04
	$m(\mu, e)$	0.074162	0.074185	0.000023	0.03
	N_{Events}	0.078163	0.078184	0.000021	0.03

Table 9.11: The interval lengths of the CI at 68 % CL from eNLL fits w/ and w/o γ-factors for the four kinematic observables $p_{\text{T}}(\ell)$, $p_{\text{T}}(\text{trk})$, $p_{\text{T}}(\ell, \text{trk(s)}/\ell')$ and $m(\ell, \text{trk(s)}/\ell')$ in the SRs SR-1M1T, SR-1M3T, SR-1E1T, SR-1E3T and SR-1M1E using TRExFitter and the signal and background prediction. The absolute and the relative difference Δl of $l_{\gamma\text{-factors}}$ and l_{StatOnly} is given with respect to l_{StatOnly}.

highest-p_T bins in the distribution a visible uncertainty is displayed in Figure 9.13.
The NP ranking in Figure 9.14 displays in addition the impact of each NP on a_τ. The pre- and post-fit impacts are determined as described in Section 6.3, the order is defined by the size of the post-fit impact, with the NP with largest impact at the top, and successively lower impacts underneath. In the fit of the $p_T(\mu)$ distribution in SR-1M1T, the γ-factors with the highest post-fit impacts are the ones at the lowest p_T values, where a variation has the largest impact on the overall number of events and thus the cross section dependence for a_τ. Higher p_T bins become relevant for the shape dependence for a_τ, and in these cases even higher p_T bins can have a high impact than lower ones - visible in the inversion of the impact for bins 5 and 6, as well as 7 and 8.
The pre- and the post-fit uncertainties are observed to be the same for the γ-factors.
Due to the limited statistics in the modeling of the SM signal and background MC predictions, γ-factors need to be included in the fit. In this analysis the effect on the fit, however is relatively small - an indication that the number of modeled background events is sufficiently large for this analysis.

9.6.3 *Inclusion of a Global Normalization Uncertainty*

For a first approximation of the impact of various systematic uncertainties that are correlated among the simulated processes $\gamma\gamma \to \tau\tau$, $\gamma\gamma \to \mu\mu$, $\gamma\gamma \to ee$ and $\gamma\gamma \to q\bar{q}$, a global systematic uncertainty is introduced. For the combination of the systematic uncertainties coming from the lepton trigger, as well as lepton and track reconstruction and identification efficiencies, modeling of the processes and the integrated luminosity, a global 5 % systematic uncertainty, individually on the signal and the background prediction is considered a reasonable first approximation. The largest uncertainty contribution from the photon flux modeling which reaches up to approximately 25 % in the highest p_T bins can be - in a simultaneous fit with the CR-2M or CR-2E - strongly constrained, and is therefore not considered in the following considerations.
The background systematic of 5 % is only applied to the background prediction while the signal systematic is applied onto SM and BSM signal predictions, i.e. for the a_τ values $a_\tau = -0.10, -0.06, -0.05, \ldots 0.05, 0.06, 0.10$. The two global uncertainties are treated as not correlated. Additionally, the γ-factors are considered.

The impact of the systematic uncertainties can be studied by calculating the CI lengths at 68 % CL. This is compared to the CI lengths obtained from fits, considering statistical uncertainties only. The results are summarized in Table 9.12. The inclusion of systematic uncertainties increases the CI length as expected.
The last two columns show the absolute and the relative differences Δl to the eNLL fit using γ-factors only. As expected, the inclusion of the systematic uncertainties increases the determined CIs. The relative difference, shows that the SRs and the observables are differently sensitive to the global systematic uncertainty. The observable N_{Events} is most sensitive to the uncorrelated 5 % systematic uncertainties on signal and background prediction, where the effect varies between 2.4 % and 13.8 %. The kinematic observables $p_T(\ell)$, $p_T(\text{trk})$, $p_T(\ell, \text{trk(s)}/\ell')$ and $m(\ell, \text{trk(s)}/\ell')$ are approximately similarly affected within each SR, between 7.7 % and 12.5 % for SR-1M1T, between 1.5 % and 2.8 % for SR-1M3T, SR-1E3T and SR-1M1E and between 7.0 % and 7.7 % for SR-1E1T. The SRs based on one track exhibit an increase in the interval lengths of around 7-13 % with

small variations among the variables, while the other SRs only display increases in the interval lengths of approximately 1.5-3 %.
Overall, the inclusion of 5 % global uncertainties in the signal and background predictions demonstrates the handling of systematic uncertainties in TRExFitter, and gives an idea of the impact on a_τ. Depending on the SR, they translate to an increase in the CIs on a_τ at 68 % CL between 2 % to maximally about 15 %. In reality, the various systematic sources would need to be considered separately and determined from variations of the respective efficiencies, momenta, modeling parameters, etc., but that exceeds the scope of this thesis.

9.7 CHOICE OF OBSERVABLE IN SR-1M1E

The studies on the search for sensitive observables as well as the comparisons of extracted CIs at 68 % CL (Sections 9.2 -9.6) have shown that the lepton p_T distribution is a highly sensitive observable to extract a_τ. In the SRs based on a muon and track(s), the muon p_T, and in the SRs based on an electron and track(s), the electron p_T is used. In the fully leptonic SR-1M1E, the choice of the lepton p_T variable is not directly apparent, since the muon p_T, the electron p_T or a combination of both would all be reasonable choices. Several possibilities are therefore tested in the following:

- muon p_T: $p_\mathrm{T}(\mu)$
- electron p_T: $p_\mathrm{T}(e)$
- maximum p_T of muon or electron per event: $\max(p_\mathrm{T}(\mu), p_\mathrm{T}(e))$
- mean p_T of muon and electron as $(p_\mathrm{T}(\mu) + p_\mathrm{T}(e))/2$ per event: $p_\mathrm{T}(\ell_\mathrm{mean})$
- combination of muon p_T and electron p_T per bin: $p_\mathrm{T}(\ell)$

where in the last option, the muon p_T and electron p_T events counts are added in every event and each entry is scaled by 0.5. The kinematic distributions of $p_\mathrm{T}(\mu)$ and $p_\mathrm{T}(e)$ are shown in Figure 8.19 and of the muon and electron p_T combinations in Figure 9.15. The prediction is in good agreement with the data for the tested muon and electron p_T combinations.

The expected CIs at 68 % CL and interval lengths are determined using the same TRExFitter setup as described in Section 9.6.3. This includes statistical uncertainties, γ-factors and an approximate systematic uncertainty of 5 %, and uses signal plus background predictions as input in the fit. The results are summarized in Table 9.13 and are illustrated in Figure 9.16.

Signal Region	Parameter	Uncertainty interval for $\hat{a}_\tau$	Interval length l	Δl	Δl [%]
SR-1M1T	$p_{\mathrm{T}}(\mu)$	$[-0.0297, 0.0156]$	0.045	0.005	12.5
	$p_{\mathrm{T}}(\mathrm{trk})$	$[-0.0424, 0.0163]$	0.059	0.004	7.7
	$p_{\mathrm{T}}(\mu, \mathrm{trk})$	$[-0.0341, 0.0160]$	0.050	0.004	9.9
	$m(\mu, \mathrm{trk})$	$[-0.0383, 0.0163]$	0.055	0.004	8.5
	N_{Events}	$[-0.0580, 0.0165]$	0.074	0.009	13.8
SR-1M3T	$p_{\mathrm{T}}(\mu)$	$[-0.0436, 0.0226]$	0.066	0.002	2.5
	$p_{\mathrm{T}}(\mathrm{trk})$	$[-0.0440, 0.0226]$	0.067	0.002	2.6
	$p_{\mathrm{T}}(\mu, \mathrm{trk})$	$[-0.0467, 0.0244]$	0.071	0.002	2.3
	$m(\mu, \mathrm{trk})$	$[-0.0492, 0.0235]$	0.073	0.002	2.7
	N_{Events}	$[-0.0610, 0.0234]$	0.084	0.003	4.1
SR-1E1T	$p_{\mathrm{T}}(e)$	$[-0.0389, 0.0210]$	0.060	0.004	7.0
	$p_{\mathrm{T}}(\mathrm{trk})$	$[-0.0451, 0.0209]$	0.066	0.004	7.1
	$p_{\mathrm{T}}(e, \mathrm{trk})$	$[-0.0466, 0.0218]$	0.068	0.005	7.7
	$m(e, \mathrm{trk})$	$[-0.0457, 0.0218]$	0.068	0.005	7.5
	N_{Events}	$[-0.0607, 0.0226]$	0.083	0.009	12.7
SR-1E3T	$p_{\mathrm{T}}(e)$	$[-0.0477, 0.0252]$	0.073	0.002	2.8
	$p_{\mathrm{T}}(\mathrm{trk})$	$[-0.0445, 0.0245]$	0.069	0.002	2.5
	$p_{\mathrm{T}}(e, \mathrm{trk})$	$[-0.0471, 0.0257]$	0.073	0.002	2.2
	$m(e, \mathrm{trk})$	$[-0.0497, 0.0256]$	0.075	0.002	2.7
	N_{Events}	$[-0.0613, 0.0256]$	0.087	0.003	3.8
SR-1M1E	$p_{\mathrm{T}}(\mu)$	$[-0.0449, 0.0261]$	0.071	0.001	1.9
	$p_{\mathrm{T}}(e)$	$[-0.0443, 0.0258]$	0.070	0.001	1.7
	$p_{\mathrm{T}}(\mu, e)$	$[-0.0472, 0.0287]$	0.076	0.001	1.5
	$m(\mu, e)$	$[-0.0485, 0.0271]$	0.076	0.001	1.9
	N_{Events}	$[-0.0532, 0.0269]$	0.080	0.002	2.4

Table 9.12: Best fit value for a_τ, CI at 68 % CL and the corresponding interval length from eNLL fits for the four kinematic observables $p_{\mathrm{T}}(\ell)$, $p_{\mathrm{T}}(\mathrm{trk})$, $p_{\mathrm{T}}(\ell, \mathrm{trk(s)}/\ell')$ and $m(\ell, \mathrm{trk(s)}/\ell')$ in the SRs SR-1M1T, SR-1M3T, SR-1E1T, SR-1E3T and SR-1M1E using the signal and background prediction as input and a global 5 % systematic uncertainty applied individually. Δl is the difference of the interval length l from the fit using the γ-factors and γ-factors and the global systematic uncertainty.

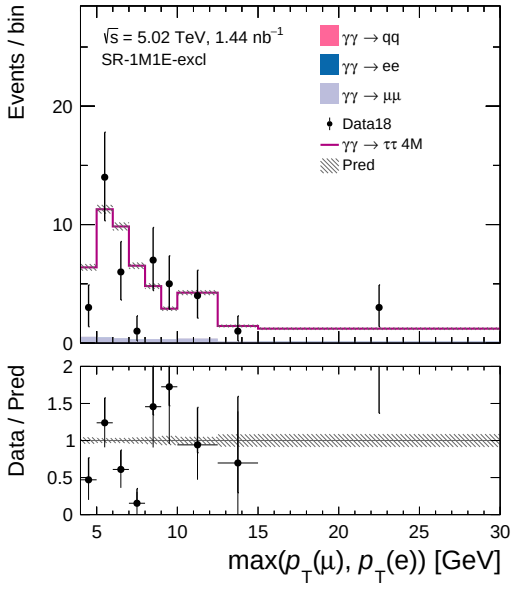

(a) $\max(p_{\mathrm{T}}(\mu), p_{\mathrm{T}}(e))$

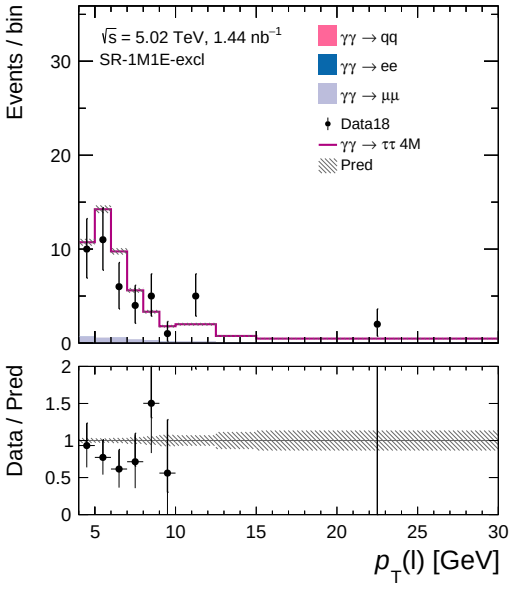

(b) $p_{\mathrm{T}}(\ell_{\mathrm{mean}})$

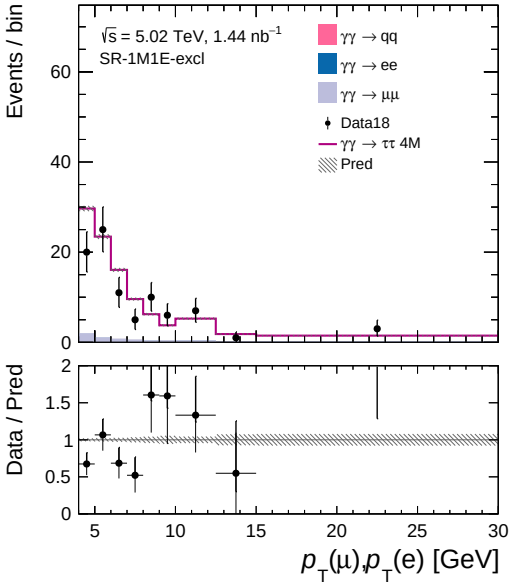

(c) $p_{\mathrm{T}}(\ell)$

Figure 9.15: Kinematic distributions for the transverse momentum p_{T} of the muon and electron combined: (a) $\max(p_{\mathrm{T}}(\mu), p_{\mathrm{T}}(e))$, (b) $p_{\mathrm{T}}(\ell_{\mathrm{mean}})$ and (c) $p_{\mathrm{T}}(\ell)$ in SR-1M1E. The data is shown as black dots, the prediction as stacked histogram from the signal process $\gamma\gamma \to \tau\tau$ (pink solid line) and the background processes $\gamma\gamma \to q\bar{q}$ (pink), $\gamma\gamma \to ee$ (blue) and $\gamma\gamma \to \mu\mu$ (violet). The weighted, fractional and raw yields for each process are displayed in the legend. The ratio between the data and the prediction is shown in the lower panel. The applied selection criteria are shown in the upper left side.

Type of lepton p_T	Uncertainty interval for $\hat{a}_\tau$	Interval length
$p_T(\mu)$	$[-0.045, 0.026]$	0.071
$p_T(e)$	$[-0.044, 0.026]$	0.070
$p_T(\ell)$	$[-0.044, 0.026]$	0.070
$\max(p_T(\mu), p_T(e))$	$[-0.042, 0.026]$	0.068
$p_T(\ell_{\text{mean}})$	$[-0.042, 0.026]$	0.068

Table 9.13: Comparison of the expected CIs and interval lengths for a_τ at 68 % CL for potential lepton p_T choices in SR-1M1E.

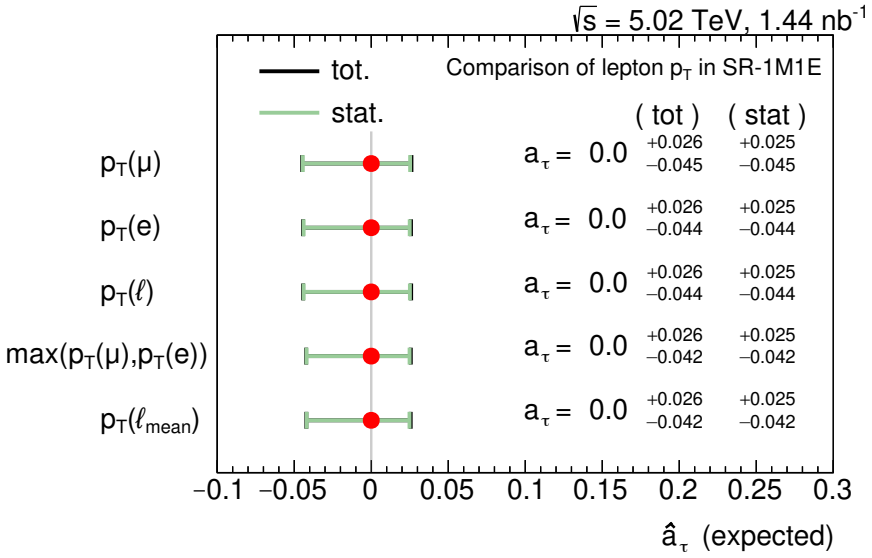

Figure 9.16: Comparison of expected CIs at 68 % CL for a_τ for potential lepton p_T choices in SR-1M1E.

The most sensitive lepton p_T options are the mean lepton p_T and the maximum p_T of muon and electron with an interval length of 0.068 each. In comparison to the muon p_T, this corresponds to an improvement of about 4.2 %. The single muon p_T is actually least sensitive with an interval length 0.071. In the following, the mean p_T of muon and electron $p_T(\ell_{\text{mean}})$ is used as default choice for the lepton p_T distribution in the SR-1M1E.

9.8 COMBINATION OF SIGNAL REGIONS

The five SRs in this analysis have been defined to be exclusive with respect to each other, i.e., no event is selected in more than one SR. On this basis, the five SRs can be combined in the fit, defining a joint likelihood function. The exclusivity of the SRs prevents statistical overlap and double counting of events. Two versions for the combination are tested: A combination of the three muon-based SRs (1M1T, 1M3T and 1M1E) only and combination of all five SRs (1M1T, 1M3T, 1E1T, 1E3T and 1M1E).

For the electron-based SRs, the electron trigger is not yet well understood. Thus the potential improvement compared to the muon-based SRs only is studied. The combined likelihood function Equation (6.14) in either case becomes

$$L(a_\tau) = L_{1\mathrm{M}1\mathrm{T}}(a_\tau) \cdot L_{1\mathrm{M}3\mathrm{T}}(a_\tau) \cdot L_{1\mathrm{M}1\mathrm{E}}(a_\tau)$$

and

$$L(a_\tau) = L_{1\mathrm{M}1\mathrm{T}}(a_\tau) \cdot L_{1\mathrm{M}3\mathrm{T}}(a_\tau) \cdot L_{1\mathrm{E}1\mathrm{T}}(a_\tau) \cdot L_{1\mathrm{E}3\mathrm{T}}(a_\tau) \cdot L_{1\mathrm{M}1\mathrm{E}}(a_\tau)$$

with the corresponding likelihood functions in each SR L_{SR}, respectively. The CIs at 68 % for the best-fit value $\hat{a}_\tau$ are estimated for the kinematic observables $p_{\mathrm{T}}(\ell)$, $p_{\mathrm{T}}(\mathrm{trk})$, $p_{\mathrm{T}}(\ell, \mathrm{trk(s)}/\ell')$, $m(\ell, \mathrm{trk(s)}/\ell')$ as well as N_{Events} using the TRExFitter setup and the same configurations as in Section 9.7.

The results of the combination of the SRs in this analysis are listed in Table 9.14, with the results from the muon-based SRs only on the left, and the results including the electron-based SRs on the right. The improvements from using the electron-base SRs in addition is shown in the last column of this table. Figure 9.17 shows the extracted a_τ values of the combination for all SRs, with the contributions from each SR displayed separately. The combinations have been performed using the kinematic variables, $p_{\mathrm{T}}(\ell)$, $p_{\mathrm{T}}(\mathrm{trk})$, $p_{\mathrm{T}}(\ell, \mathrm{trk(s)}/\ell')$, $m(\ell, \mathrm{trk(s)}/\ell')$, as well as N_{Events}, using all SRs where the respective variable are applicable. In SR-1M1E, the $p_{\mathrm{T}}(\mathrm{trk})$ is not defined and for this particular combination, the SR-1M1E is therefore left out. In case of the combination, based on the lepton p_{T} distributions, the mean lepton $p_{\mathrm{T}}(\ell_{\mathrm{mean}})$, as discussed in Section 9.7, is used for SR-1M1E.

The improvements including the electron-based SRs in the combination are between 7 % and 13 %, depending on the distribution. In comparison to the most sensitive individual SR: SR-1M1T, the improvement from the combination of the five SRs is between 12 % and 24 %, depending again on the kinematic distribution.

The best performance, i.e. the smallest confidence interval lengths are observed for the lepton p_{T} distributions as fitted observable, both without and with inclusion of the electron-based SRs. The final results of this analysis are therefore based on the combination of the five SRs.

	Only muon-based SR		All SRs		Improvement
Parameter	CI at 68 % CL for $\hat{a}_\tau$	Interval length	CI at 68 % CL for $\hat{a}_\tau$	Interval length	in [%]
$p_{\mathrm{T}}(\ell)$	$[-0.026, 0.016]$	0.040	$[-0.024, 0.014]$	0.038	6.9
$p_{\mathrm{T}}(\mathrm{trk})$	$[-0.035, 0.015]$	0.050	$[-0.030, 0.015]$	0.044	12.6
$p_{\mathrm{T}}(\ell, \mathrm{trk(s)})$	$[-0.030, 0.015]$	0.045	$[-0.027, 0.014]$	0.041	8.0
$m(\ell, \mathrm{trk(s)})$	$[-0.032, 0.015]$	0.048	$[-0.029, 0.015]$	0.043	9.1
N_{Events}	$[-0.051, 0.015]$	0.066	$[-0.050, 0.015]$	0.065	2.0

Table 9.14: Expected CIs and interval lengths for a_τ at 68 % CL for the combination of SRs in an eNLL fit using TRExFitter, including either the muon-based SRs only, or also the electron-based SRs in addition. The last column indicates the improvement when fitting with five SRs (electron-based included) vs three SRs (muon-based only).

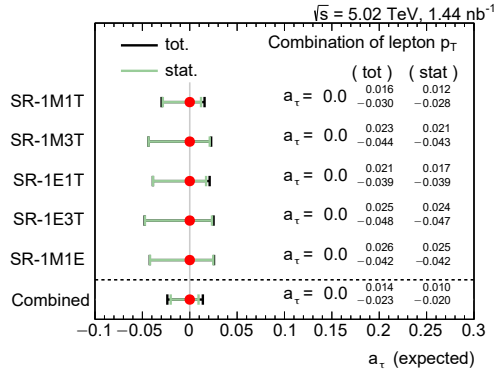

(a) $p_{\mathrm{T}}(\ell)$

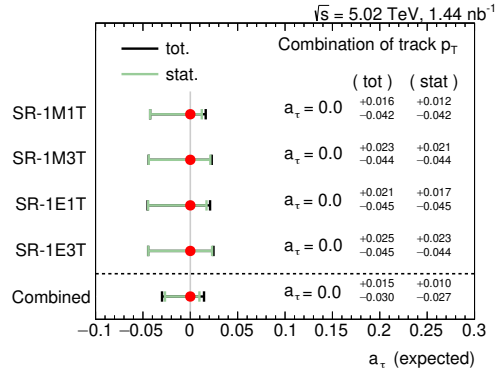

(b) p_{T} (trk)

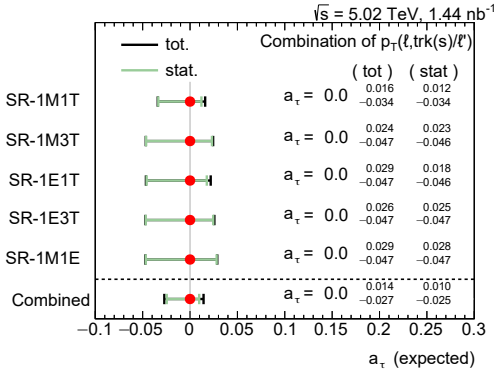

(c) $p_{\mathrm{T}}(\ell, \mathrm{trk(s)}/\ell')$

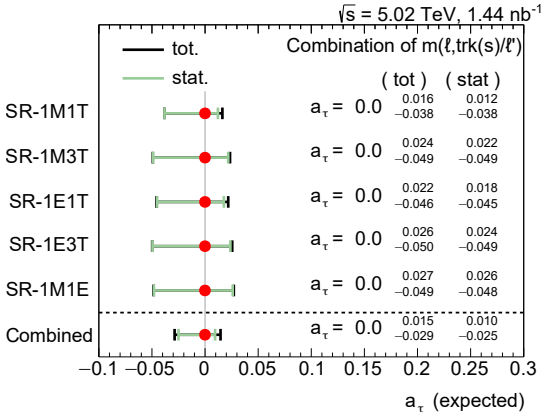

(d) $m(\ell, \mathrm{trk(s)}/\ell')$

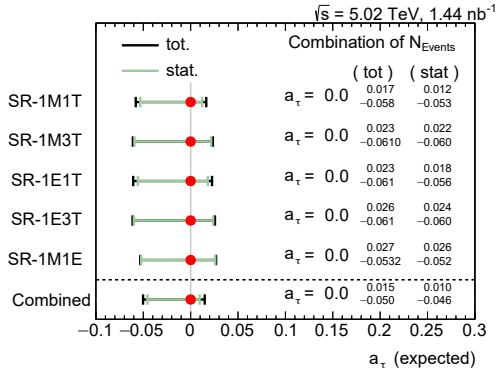

(e) N_{Events}

Figure 9.17: Summary figures of the combination results comparing the fits with the five SRs included for the kinematic distributions for $p_{\mathrm{T}}(\ell)$, $p_{\mathrm{T}}(\mathrm{trk})$, $p_{\mathrm{T}}(\ell, \mathrm{trk(s)})$, $m(\ell, \mathrm{trk(s)})$ and the cross section variable N_{Events}. The CIs are shown and listed for the statistical only and the total fit uncertainties including the γ-factors and the approximate global systematic uncertainties.

9.9 COMPARISON WITH OTHER MEASUREMENTS

Experimental constraints on a_τ have been determined previously by measurements at lepton colliders. Typically, the obtained confidence intervals in these cases are determined at 95 % CL. For comparison with these results, the CIs obtained in this analysis need to be determined at 95 % CL.
The CIs for a_τ at 95 % CL in thesis are estimated from a scan of the likelihood function determined by TRExFitter. The procedure is illustrated in Figure 9.18. Using 100 linearly interpolated points for the calculation of the shape of the likelihood, the CIs at 95 % CL can be read out as the intersections of the likelihood with a horizontal line at 1.92 above the minimum of the likelihood (compare to Section Section 6.2.4 for the choice of the line's position). The results are summarized in Table 9.15. The eNLL fits are performed using the same configuration as in section 9.8, i.e. including γ-factors and approximate global systematic uncertainties, and are determined for the combination of the applicable SRs (four in the case of p_{T} (track), five otherwise). The kinematic distributions $p_{\mathrm{T}}(\ell)$, $p_{\mathrm{T}}(\mathrm{trk})$, $p_{\mathrm{T}}(\ell, \mathrm{trk(s)}/\ell')$ and $m(\ell, \mathrm{trk(s)}/\ell')$ and the cross section variable N_{Events} are compared.
The most sensitive kinematic observables is $p_{\mathrm{T}}(\ell)$ followed by $m(\ell,\mathrm{trk}/\ell')$ and $p_{\mathrm{T}}(\mathrm{trk})$. The cross section variable N_{Events} provides the weakest constraints, in line with the observations at at 68 % CL, discussed in the previous sections.
The expected CIs on a_τ at 95 % CL are compared to the measurements obtained by the experiments OPAL, L3 and DELPHI at LEP. OPAL and L3 [29, 30] studied the τ-lepton production via electron scattering

$$e^+e^- \to e^+e^-\tau^+\tau^+$$

and DELPHI [8] used the

$$Z \to \tau\tau\gamma$$

process. Recently, the CMS collaboration published first preliminary limits on a_τ, analogous to this analysis, using one SR for the process

$$\mathrm{Pb} + \mathrm{Pb} \to \mathrm{Pb}(\gamma\gamma \to \tau\tau)\mathrm{Pb}.$$

from ultraperipheral heavy ion collisions of the LHC run from 2015 [97]. The ditau production $\gamma\gamma \to \tau\tau$ is observed in These results are not included in the comparison here due the short-term scale.
The comparison to measurements from OPAL, L3 and DELPHI is displayed in Figure Figure 9.19. The expected CIs on a_τ determined in this analysis are of a similar size as the currently best measurement by DELPHI, for all kinematic variables. The sensitivity obtained with N_{Events} alone is worse by 34 % than the results by DELPHI, the sensitivity obtained using $p_{\mathrm{T}}(\ell)$ as kinematic variables is about 10 % better than the DELPHI measurement.
The studies discussed in this thesis thus demonstrate that the measurement of $\gamma\gamma \to \tau\tau$ production in Pb+Pb collisions at the LHC has the potential to provide the world's best measurement of the anomalous magnetic moment of the tau lepton. The expected sensitivities are close to or slightly better than those by DELPHI - the currently best measurement - and the first measurement of the $\gamma\gamma \to \tau\tau$ process with the ATLAS

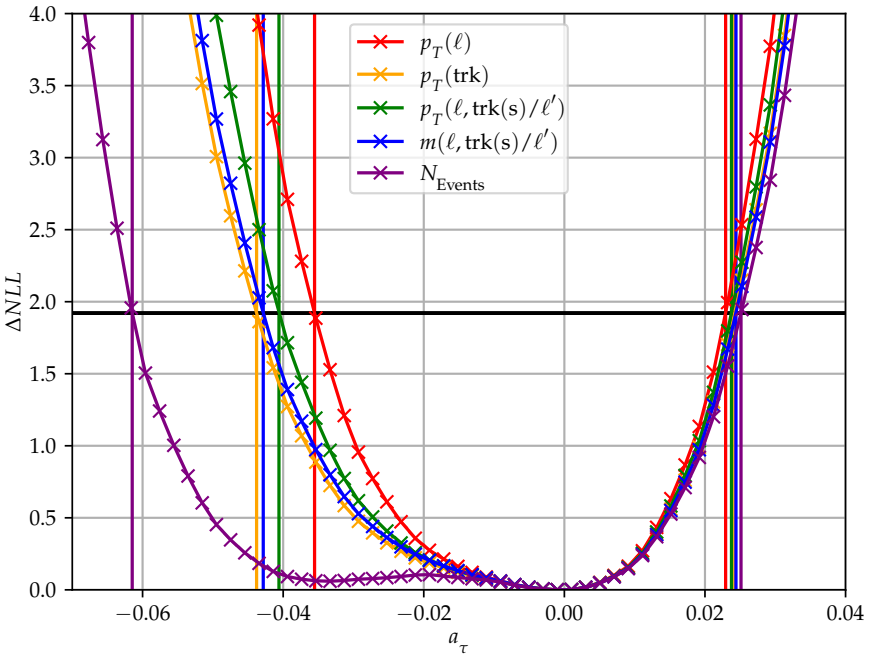

Figure 9.18: Procedure to determine the expected CI at 95 % CL for the combination of the all five SRs in the kinematic observables $p_{\mathrm{T}}(\ell)$, $p_{\mathrm{T}}(\mathrm{trk})$, $p_{\mathrm{T}}(\ell,\mathrm{trk}/\ell')$, $m(\ell,\mathrm{trk}/\ell')$ and N_{Events}.

detector certainly paves the way for further measurements with larger data sets to come in the future.

9.10 OUTLOOK TOWARDS MORE DATA

A conceptionally simple way to improve the measurement, but experimentally not free of charge is the addition of more data.
Currently, one additional data set from 2015 is available, corresponding to an integrated luminosity of $\mathcal{L} = 0.49\,\mathrm{nb}^{-1}$, and could be added relatively quickly and easy to the presently used 2018 data set. This would increase the data set by about 34 %. The more costly option is to record additional Pb+Pb data. In the context of the next run of the LHC (also labeled as Run 3), Pb+Pb data taking periods are currently scheduled for the end of three of the four years of Run 3 with a target integrated luminosity of $\mathcal{L} = 6.0\,\mathrm{nb}^{-1}$ [99]. This increase of the data set by a factor slightly above 3 compared to the combined 2015+2018 data set would reduce statistical uncertainties significantly (by a factor of around 1.7). Both mentioned possibilities go beyond the scope of this thesis, but demonstrate that more is to come in future and the methodology discussed in this thesis can certainly be expanded upon.

Parameter	CI at 95 % CL	Interval length
OPAL 1998	$[-0.065, 0.068]$	0.133
L3 1998	$[-0.058, 0.052]$	0.11
DELPHI 2004	$[-0.013, 0.052]$	0.065
$p_{\mathrm{T}}(\ell)$	$[-0.036, 0.023]$	0.059
$p_{\mathrm{T}}(\mathrm{trk})$	$[-0.044, 0.024]$	0.068
$p_{\mathrm{T}}(\ell, \mathrm{trk(s)})$	$[-0.041, 0.024]$	0.064
$m(\ell, \mathrm{trk(s)})$	$[-0.043, 0.024]$	0.067
N_{Events}	$[-0.062, 0.025]$	0.087

Table 9.15: Measured CIs for a_τ at 95 % by OPAL [30], L3 [29] and DELPHI [8] experiments at the LEP collider [98] and expected CIs for a_τ at 95 % for combined extended NLL fits of the SRs (four in case of p_{T} (trk), five for the others) for $p_{\mathrm{T}}(\ell)$, $p_{\mathrm{T}}(\mathrm{trk})$, $p_{\mathrm{T}}(\ell, \mathrm{trk(s)}$, $m(\ell, \mathrm{trk(s)})$ and N_{Events} as fitted observables in this thesis.

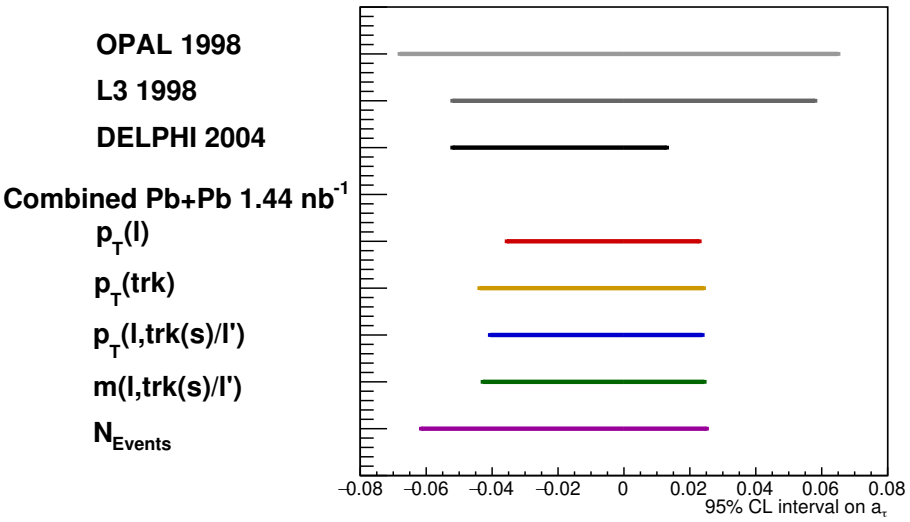

Figure 9.19: Expected confidence intervals for a_τ at 95 % CL for different kinematic and cross section based variables, combining the associated SRs, in comparison with the existing measurements from OPAL [30], L3 [29] and DELPHI [8] experiments at the LEP collider [98].

10 CONCLUSION

The anomalous magnetic moment of the τ-lepton a_τ is an important property to probe the Standard Model (SM) of particle physics. While the anomalous magnetic moments of the electron and muon are among the most precisely measured quantities in the SM, the precision of the measurement of a_τ is severely limited by the short lifetime of the τ-lepton.
The process $\gamma\gamma \to \tau\tau$, which can be measured in ultra-peripheral Pb+Pb collisions at the LHC, is sensitive to the value of a_τ and can thus be used to constrain a_τ. The measurement is performed based on Pb+Pb collisions at a center-of-mass energy of $\sqrt{s} = 5.02\,\text{TeV}$ recorded in 2018 with the ATLAS detector. The data set corresponds to an integrated luminosity of $\mathcal{L} = 1.44\,\text{nb}^{-1}$.
The τ-leptons of the final state of $\gamma\gamma \to \tau\tau$ production decay either leptonically, i.e. to one electron or one muon and neutrinos in the final state, or hadronically to pions or kaons and one neutrino. The τ-lepton can be reconstructed in the ATLAS detector mainly through its decay products of electrons, muons, and charged particle tracks.

In this thesis, the signal selection is defined to cover the semileptonic final states $\tau_{\text{lep}}\tau_{\text{had}}$ with one muon or electron plus one track (1M1T/1E1T), one muon or electron plus three tracks (1M3T/1E3T), and the fully leptonic final state $\tau_\mu\tau_e$ with one muon plus one electron (1M1E). The one and three track selections target the hadronic decays of τ-leptons involving one or three charged pions or kaons. The selections, denoted as signal regions (SRs), are based on the definition of tightly selected *signal* leptons, looser selected *baseline* leptons and tracks with very low transverse momenta p_{T} going down to 100 MeV. The SRs employ kinematic requirements, using the transverse momenta of the lepton-track(s) or lepton-lepton system $p_{\text{T}}(\ell, \text{trk(s)}/\ell')$, the invariant mass of the track system $m(\text{trks})$ or the acoplanarity $A_\phi^{\ell,\text{trk(s)}}$ of the leptons and tracks, respectively. The acoplanarity is a measure for the azimuthal distance $\Delta\phi$ between lepton and track(s) or lepton and lepton. The requirements to suppress backgrounds from other processes were optimized in the context of this thesis.
Processes, such as di-muon $\gamma\gamma \to \mu\mu$ production, di-electron $\gamma\gamma \to ee$ production and low p_{T}-jet production leave similar signatures as the $\gamma\gamma \to \tau\tau$ process in the ATLAS detector and contribute in this analysis as backgrounds. The signal and the background contributions are estimated through MC simulations using the Starlight 2.0 generator interfaced to Pythia 8.245. In this analysis, the cross section of the signal process $\gamma\gamma \to \tau\tau$ is kept unknown to the analyzers, i.e. it is blinded within a range of $\pm 10\,\%$ of the correct value.
The simulation of the background processes: $\gamma\gamma \to \mu\mu$ and $\gamma\gamma \to ee$ is validated in two control regions enriched with the respective processes. Except for a global offset which can easily be corrected for, the modeling is found to be in good agreement with the data in the control regions.
The predictions of signal and background are compared to data in the five SRs and

found to be in very good agreement for the muon-based and in reasonable agreement for electron-based SRs with the data. The $\gamma\gamma \to \tau\tau$ signal exceeds the background in four of the five SRs significantly. The presence of the $\gamma\gamma \to \tau\tau$ signal in the data is clearly observed.

The anomalous magnetic moment of the τ-lepton can be constrained from the data using maximum likelihood fits of the observed event counts and the observed distributions for various observables. In this analysis, only pseudo data corresponding to the expected number of events are used as input to the fit procedure.

The production cross section of $\gamma\gamma \to \tau\tau$ can be parametrized using a polynomial of second degree as a function of a_τ. The shape of kinematic observables, especially for $p_{\mathrm{T}}(\ell)$, $p_{\mathrm{T}}(\mathrm{trk})$, $p_{\mathrm{T}}(\ell, \mathrm{trk(s)}/\ell')$ and $m(\ell, \mathrm{trk(s)}/\ell')$, is affected by a_τ in all five SRs. Expected confidence intervals (CIs) at 68 % confidence level (CL) and CIs at 95 % CL are extracted with maximum likelihood fits. Various effects that impact the obtained CIs for a_τ were studied to understand the behavior of the likelihood fit and quantify the approximate size of the different effects. Fits were performed using the signal predictions only, including statistical uncertainties arising from the limited size of simulated samples and testing the impact of global systematic uncertainties on signal and background yields. The effect of the statistical uncertainties is very small while the sensitivity to a_τ is affected by global systematic uncertainties. The performance of individual different kinematic observables as input to the fit are compared and found to differ in sensitivity to a_τ, with the best sensitivity to a_τ is obtained for the $p_{\mathrm{T}}(\ell)$ distribution. The different SRs can be used individually as input to the fit, are compared and then combined. They cover different phase space regions of $\gamma\gamma \to \tau\tau$ production, are contaminated differently by background processes and have different statistics which lead to different expected CIs. The SR 1M1T with high statistics and good purity shows the best performance.

The constraints on a_τ can be maximized through the choice of the fitted input distributions as well as the choice or combination of the different SRs. The kinematic distributions $p_{\mathrm{T}}(\ell)$ and $p_{\mathrm{T}}(\ell, \mathrm{trk(s)}/\ell')$ are most sensitive and the combination of all five SRs results in an improvement of 10 % compared to the best single SR 1M1T. Using the lepton p_{T} distribution in each SR and combining the five SRs, the expectation for the CI for a_τ at 95 % CL is:

$$-0.036 < a_\tau < 0.023$$

with an interval length of $l = 0.059$. This includes approximate global systematic uncertainties on both, signal and background predictions, separately. Comparing to the currently best measurement of

$$-0.052 < a_\tau < 0.013$$

at 95 % CL [8] by the DELPHI collaboration, this analysis provides an improvement of about 10 % in the confidence interval length. This clearly demonstrates the potential of the measurement of $\gamma\gamma \to \tau\tau$ production at the LHC for the determination of a_τ.

A

ADDITIONAL MINOR BACKGROUND CONTRIBUTIONS

Several background processes, leaving the same signature as the signal production, $\gamma\gamma \to \tau\tau$, need to be considered in the analysis. The main background contributions come from the dimuon $\gamma\gamma \to \mu\mu$, the dielectron $\gamma\gamma \to ee$ and the diquark $\gamma\gamma \to q\bar{q}$ production. Minor background contributions, such as the $\gamma\gamma \to \mu\mu + \gamma$ and the photonuclear production are studied and found to be negligible for this thesis.

A.1 BACKGROUND PROCESS $\gamma\gamma \to \mu\mu + \gamma$

In the dimuon production process $\gamma\gamma \to \mu\mu + \gamma$, an additional photon is emitted which comes from the hard interaction. The $\gamma\gamma \to \mu\mu + \gamma$ processes is estimated in MC simulation using MadGraph5_aMC@NLO. The signatures of the photon can mimic the decay of a τ-lepton, as discussed in Section 4.2. In $\gamma\gamma \to \mu\mu$ samples, produced with Starlight 2.0 and interfaced to Pythia 8, also $\gamma\gamma \to \mu\mu + \gamma$ events with are included where the photon results from FSR. Thus, if the MadGraph5_aMC@NLO $\gamma\gamma \to \mu\mu + \gamma$ sample is to be used, an overlap with the standard Starlight sample needs to be avoided. For that, the *pass_mg5_sl_overlapremoval* variable flags the events accordingly.
The muon based SRs, SR-1M1T, SR-1M3T and SR-1M1E are affected most by the dimuon background. The effect of the $\gamma\gamma \to \mu\mu + \gamma$ sample on the event yields is studied. The event counts, based on the requirements from Table 7.8, are shown in Table A.1 for SR-1M1T, in Table A.2 for SR-1M3T and Table A.3 for SR-1M1E.
The background yields and the signal significances from Table 7.7 are compared to the ones obtained with the $\gamma\gamma \to \mu\mu + \gamma$ sample for each SR. The results are summarized in Table A.4. Despite the slightly higher background contribution in $\gamma\gamma \to \mu\mu$, when including the $\gamma\gamma \to \mu\mu + \gamma$ sample, the signal significance is not affected. Thus, the description of the $\gamma\gamma \to \mu\mu + \gamma$ process is sufficiently modeled with the Starlight $\gamma\gamma \to \mu\mu$ sample for the studies within this thesis.

Requirement	Data 18	$\gamma\gamma \to \tau\tau$ 4M	$\gamma\gamma \to \mu\mu$ 7M20	$\gamma\gamma \to \mu\mu$ 20M	$\gamma\gamma \to \mu\mu\gamma$ MGPy8	$\gamma\gamma \to ee$ 4p5M7	$\gamma\gamma \to ee$ 7M15	$\gamma\gamma \to ee$ 15Mv1	$\gamma\gamma \to$ jets DD	$\gamma\gamma \to$ jets DR	$\gamma\gamma \to$ jets RD	$\gamma\gamma \to$ jets RR	sig/$\sqrt{\text{sig+bkg}}$
pass GRL	4335070.0	23615.5	88094.6	7380.6	1687.6	177294.7	135156.7	19274.8	35981.6	7677.2	7677.2	12524.5	32.9
$E_{\text{ZDC}}^{A,C} < 1$ TeV	1435464.0	23615.5	88094.6	7380.6	1687.6	177294.7	135156.7	19274.8	35981.6	7677.2	7677.2	12524.5	32.9
HLT mu4 trigger	60313.0	1214.5	48272.4	6013.9	838.3	0.0	0.1	0.3	36.0	5.7	6.1	9.5	5.1
$N_\mu^{\text{baseline}} = 1$	13806.0	1113.8	5754.6	1226.8	522.8	0.0	0.1	0.2	34.1	5.5	5.8	9.1	12.0
$N_\mu^{\text{sig}} = 1$	10641.0	906.1	4537.2	1143.7	444.8	0.0	0.1	0.2	21.8	3.3	3.6	5.7	10.8
$N_e^{\text{sig}} = 0$	10575.0	874.2	4535.8	1143.3	439.2	0.0	0.0	0.0	21.6	3.2	3.6	5.7	10.4
$N_{\text{trk}}(\Delta R > 0.1 \text{ from } \mu) = 1$	1790.0	569.7	614.8	24.6	332.6	0.0	0.0	0.0	0.5	0.0	0.0	0.0	14.5
Veto unmatched clusters	1320.0	560.9	610.3	24.2	154.6	0.0	0.0	0.0	0.3	0.0	0.0	0.0	15.3
$\sum$ charge = 0	1304.0	553.8	608.5	23.3	152.9	0.0	0.0	0.0	0.2	0.0	0.0	0.0	15.1
$p_{\text{T}}^{(\mu,\text{trk})} > 1$ GeV	688.0	518.4	101.2	7.1	152.6	0.0	0.0	0.0	0.2	0.0	0.0	0.0	18.6
$p_{\text{T}}^{(\mu,\text{trk},\gamma)} > 1$ GeV	577.0	496.0	60.4	3.8	55.3	0.0	0.0	0.0	0.2	0.0	0.0	0.0	20.0
$p_{\text{T}}^{(\mu,\text{trk,cluster})} > 1$ GeV	501.0	457.3	37.5	2.6	25.8	0.0	0.0	0.0	0.1	0.0	0.0	0.0	20.0
$A_\phi^{\mu,\text{trk}} < 0.4$	485.0	455.5	36.7	2.1	25.5	0.0	0.0	0.0	0.1	0.0	0.0	0.0	20.0

Table A.1: Overview of the event counts after the selection requirements for SR-1M1T-excl applied sequentially. Simulated samples, including the $\gamma\gamma \to \mu\mu + \gamma$ sample, are normalized to $\mathcal{L} = 1.44$ fb^{-1}.

Requirement	Data 18	$\gamma\gamma \to \tau\tau$ 4M	$\gamma\gamma \to \mu\mu$ 7M20	$\gamma\gamma \to \mu\mu$ 20M	$\gamma\gamma \to \mu\mu\gamma$ MGPy8	$\gamma\gamma \to ee$ 4p5M7	$\gamma\gamma \to ee$ 7M15	$\gamma\gamma \to ee$ 15Mv1	$\gamma\gamma \to$ jets DD	$\gamma\gamma \to$ jets DR	$\gamma\gamma \to$ jets RD	$\gamma\gamma \to$ jets RR	sig/$\sqrt{\text{sig+bkg}}$
pass GRL	4335070.0	23615.5	88094.6	7380.6	1687.6	177294.7	135156.7	19274.8	35981.6	7677.2	7677.2	12524.5	32.9
$E_{\text{ZDC}}^{A,C} < 1$ TeV	1435464.0	23615.5	88094.6	7380.6	1687.6	177294.7	135156.7	19274.8	35981.6	7677.2	7677.2	12524.5	32.9
HLT mu4 trigger	60313.0	1214.5	48272.4	6013.9	838.3	0.0	0.1	0.3	36.0	5.7	6.1	9.5	5.1
$N_\mu^{\text{baseline}} = 1$	13806.0	1113.8	5754.6	1226.8	522.8	0.0	0.1	0.2	34.1	5.5	5.8	9.1	12.0
$N_\mu^{\text{sig}} = 1$	10641.0	906.1	4537.2	1143.7	444.8	0.0	0.1	0.2	21.8	3.3	3.6	5.7	10.8
$N_e^{\text{sig}} = 0$	10575.0	874.2	4535.8	1143.3	439.2	0.0	0.0	0.0	21.6	3.2	3.6	5.7	10.4
$N_{\text{trk}}(\Delta R > 0.1 \text{ from } \mu) = 3$	310.0	95.8	3.8	0.3	9.6	0.0	0.0	0.0	1.8	0.1	0.1	0.2	9.1
Veto unmatched clusters	135.0	94.7	3.8	0.3	9.4	0.0	0.0	0.0	1.5	0.1	0.1	0.1	9.0
$\sum$ charge = 0	121.0	93.4	3.8	0.2	8.9	0.0	0.0	0.0	1.2	0.0	0.1	0.0	9.0
$m_{\text{trks}} < 1.7$ GeV	78.0	92.8	3.0	0.2	3.8	0.0	0.0	0.0	0.4	0.0	0.0	0.0	9.3
$A_\phi^{\mu,\text{trks}} < 0.4$	78.0	92.7	3.0	0.2	3.8	0.0	0.0	0.0	0.3	0.0	0.0	0.0	9.3

Table A.2: Overview of the event counts after the selection requirements for SR-1M13-excl applied sequentially. Simulated samples, including the $\gamma\gamma \to \mu\mu + \gamma$ sample, are normalized to $\mathcal{L} = 1.44$ fb^{-1}.

Requirement	Data 18	$\gamma\gamma \to \tau\tau$ 4M	$\gamma\gamma \to \mu\mu$ 7M20	$\gamma\gamma \to \mu\mu$ 20M	$\gamma\gamma \to \mu\mu\gamma$ MGPy8	$\gamma\gamma \to ee$ 4p5M7	$\gamma\gamma \to ee$ 7M15	$\gamma\gamma \to ee$ 15Mv1	$\gamma\gamma \to$ jets DD	$\gamma\gamma \to$ jets DR	$\gamma\gamma \to$ jets RD	$\gamma\gamma \to$ jets RR	sig/$\sqrt{\text{sig+bkg}}$
pass GRL	4335070.0	23615.5	88094.6	7380.6	1687.6	177294.7	135156.7	19274.8	35981.6	7677.2	7677.2	12524.5	32.9
$E_{\text{ZDC}}^{A,C} < 1$ TeV	1435464.0	23615.5	88094.6	7380.6	1687.6	177294.7	135156.7	19274.8	35981.6	7677.2	7677.2	12524.5	32.9
HLT mu4 trigger HLT hi gg L1TAU1	1153927.0	4283.1	52699.7	6138.7	1166.5	25735.0	52791.2	12072.4	191.5	10.9	11.4	15.9	10.9
$N_\mu^{\text{sig}} = 1$	19581.0	1043.3	13021.0	1897.0	737.0	0.0	0.1	0.3	22.7	3.4	3.8	5.9	8.1
$N_e^{\text{sig}} = 1$	75.0	40.9	2.4	1.4	7.8	0.0	0.0	0.2	0.1	0.0	0.0	0.0	5.6
N_{trk} ($\Delta R > 0.1$ from μ/e) $= 0$	45.0	39.7	1.9	1.0	1.1	0.0	0.0	0.0	0.0	0.0	0.0	0.0	6.0
$\sum$ charge = 0	42.0	39.6	1.8	0.9	0.4	0.0	0.0	0.0	0.0	0.0	0.0	0.0	6.1

Table A.3: Overview of the event counts after the selection requirements for SR-1M1E-excl applied sequentially. Simulated samples, including the $\gamma\gamma \to \mu\mu + \gamma$ sample, are normalized to $\mathcal{L} = 1.44$ fb^{-1}.

	SR-1M1T		SR-1M3T		SR-1M1E	
$\gamma\gamma \to \mu\mu + \gamma$	w/o	w	w/o	w	w/o	w
Background $\gamma\gamma \to \mu\mu$	57.8	64.3	5.4	7.0	2.9	3.1
$s/\sqrt{s+b}$	20.1	20.1	9.3	9.3	6.1	6.1

Table A.4: Comparison of the $\gamma\gamma \to \mu\mu$ background yields and the signal significance $s/\sqrt{s+b}$ for the muon based SRs with and without the $\gamma\gamma \to \mu\mu + \gamma$ sample.

A.2 PHOTONUCLEAR BACKGROUND

The photonuclear process $\gamma A \to \gamma AX$ is estimated using STARLIGHT 2.0, DPMJETIII and a data-driven method. The MC-based estimate shows no contribution to the five SRs defined in Section 7.3. The effect of the data-driven estimate is shown below.
The non-exclusive background, which is dominated by photonuclear events, can be extracted using events with a large number of unmatched clusters in data from 2018 [100]. The modeling of the non-exclusive background shows a good agreement as seen in Figure A.1 for the p_T of system of the muon and the track, when the cluster veto usually applied for the SR-1M1T is dropped.
The p_T distribution for the muon is shown for SR-1M1T after background suppression in Figure A.2. The precise requirements can be found in Ref. [100]. The contribution of the non-exclusive background, is with 19 expected events, is rather small compared to the 348 expected $\gamma\gamma \to \tau\tau$ and the 39 expected $\gamma\gamma \to \mu\mu$ events. Based on this study, it has been decided, not to implement the photonuclear background in the studies of this thesis. The selection criteria, however, are optimized to also suppress the photonuclear background.

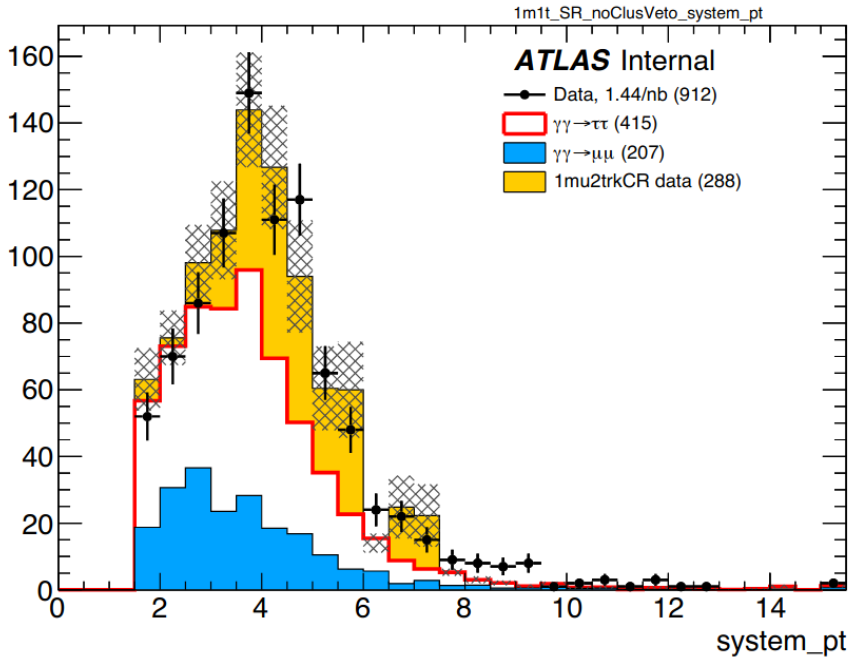

Figure A.1: Modeling of a non-exclusive background describing the photonuclear process $\gamma A \to \gamma A X$ in $p_{\mathrm{T}}(\mu, \mathrm{trk})$ before background suppression. Taken from Ref. [100].

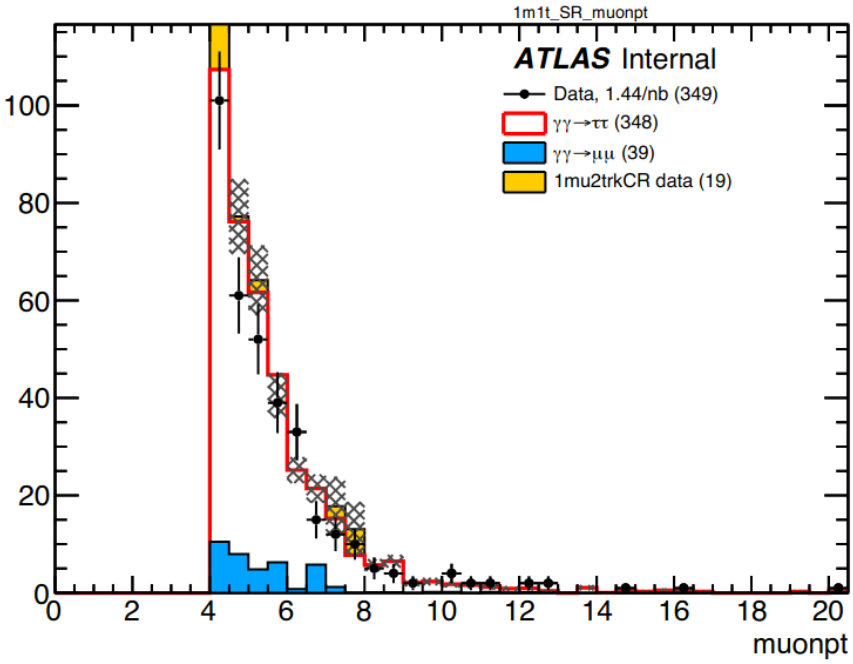

Figure A.2: Kinematic distribution for $p_{\mathrm{T}}(\mu)$ in SR-1M1T showing the $\gamma\gamma \to \mu\mu$ background (blue), the signal (red solid line) and the non-exclusive background (red) prediction stacked and compared to the measured data in black dots. The statistical uncertainty on the prediction is denoted by the hashed are. Taken from Ref. [100].

B

RECONSTRUCTION EFFICIENCY OF τ-LEPTONS

The reconstruction efficiency for τ-leptons in ATLAS that decay hadronically with one or three prongs τ_{had} is determined in Ref. [101]. The obtained reconstruction efficiencies are shown in Figure B.1 where the efficiency depends on the true p_{T} of the respective τ-lepton. The efficiency is estimated for τ-leptons with $p_{\text{T}} > 20\,\text{GeV}$ and $p_{\text{T}} < 500\,\text{GeV}$. In the reconstruction procedure, τ-lepton reconstruction is seeded by jets with $p_{\text{T}} > 10\,\text{GeV}$ and $|\eta| < 2.5$. Tracks are associated to the τ_{had} candidate within a cone of $\Delta R < 0.2$. The τ-leptons in this analysis, have a typical transverse energy of $p_{\text{T}} < 10\,\text{GeV}$, such that the standard τ_{had} reconstruction in ATLAS in Ref. [101] cannot be relied on for this analysis.
Instead, the hadronic τ-leptons τ_{had} are identified by reconstructed tracks, either by one track for a one prong decay, or by three tracks for the three prong decay. The efficiency of the track reconstruction is determined in Ref. [60] for charged pions and shown in Figure B.2. It varies from about 55 % to 83 % for tracks with $p_{\text{T}} > 20\,\text{GeV}$ to 500 GeV, where the reconstruction efficiency is largest for central tracks and reduces significantly for forward tracks.
Decaying leptonically, the τ-leptons are identified by the reconstruction of lighter leptons, namely muons or electrons. The reconstruction efficiency of electrons is determined in Ref. [80] and for muons in Ref. [60] and shown in Figure 5.2 and Figure 5.1 and are further discussed in Chapter 5.

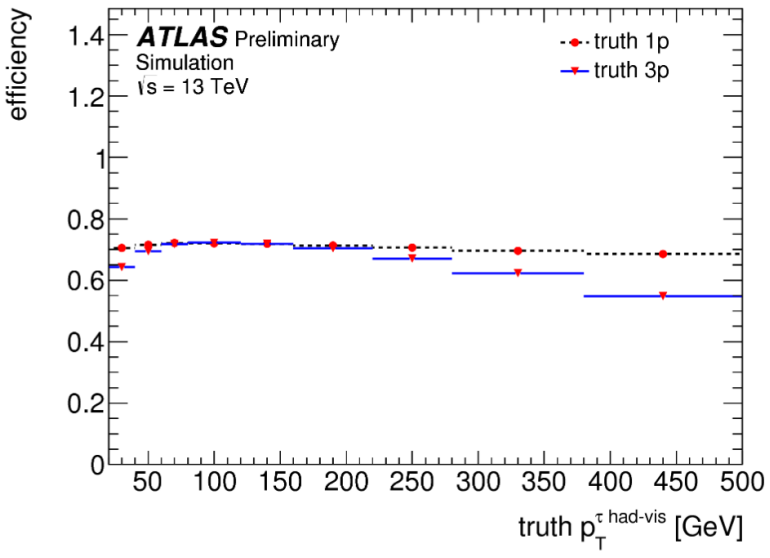

Figure B.1: ATLAS reconstruction efficiency for τ_{had} with one or three prongs as a function of the $p_{\text{T}}(\tau_{\text{had}})$ taken from Ref. [101].

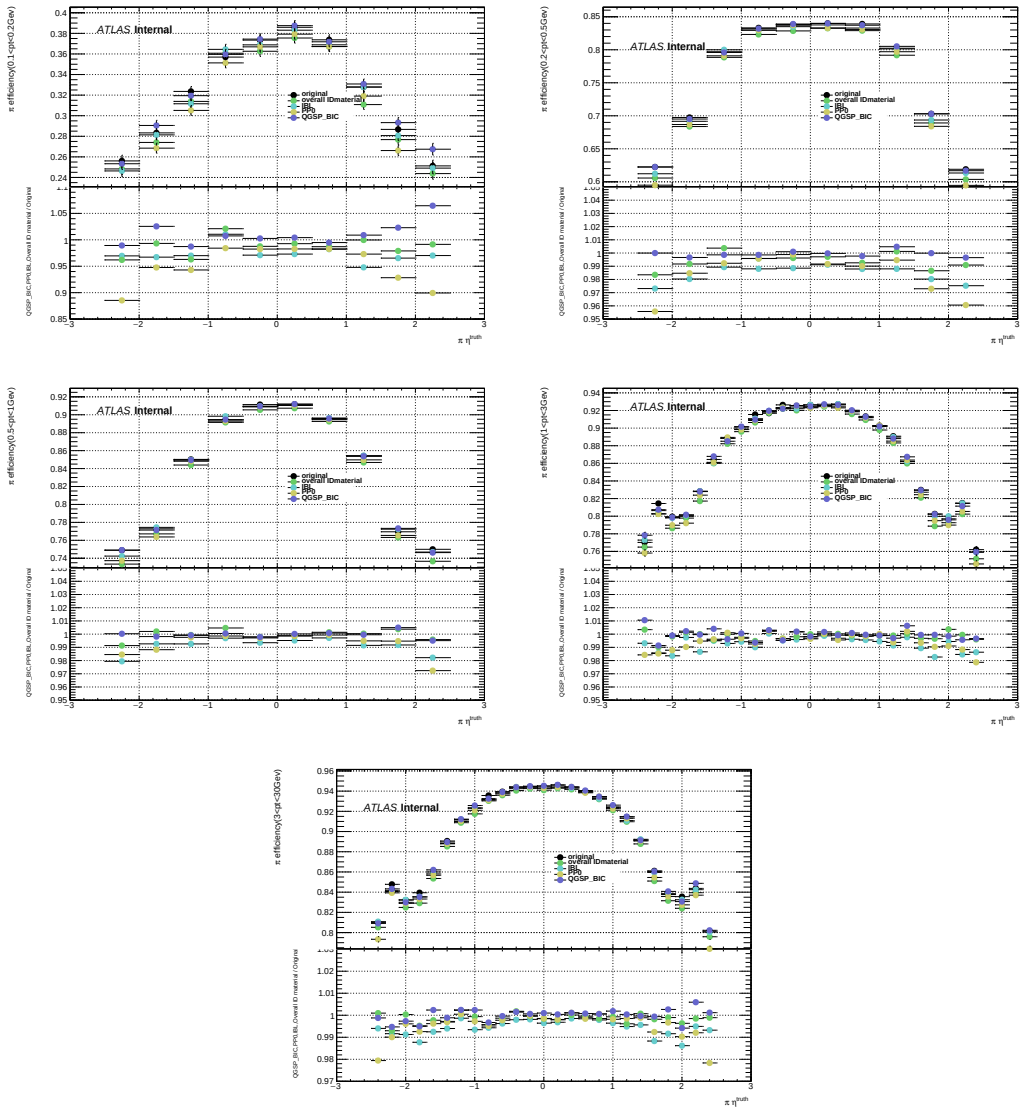

Figure B.2: Track reconstruction efficiency for charged pions as a function of truth pion pseudo-rapidity in several pion transverse momentum regions: $0.1 - 0.2$ GeV, $0.2 - 0.5$ GeV, $0.5 - 1$ GeV, $1 - 3$ GeVand $3 - 30$ GeV. The nominal MC simulation setup (black points) is compared with alternative settings that include alternative Geant4 geometry with +5 % Overall ID material (green), with +10 % IBL material (light blue), with +25 % PPo material (gold), or alternative Geant4 physics model QGSP (dark blue). Taken from Ref. [60].

C

EFFECT OF SCALE FACTORS ON EVENT YIELDS

To correct simulated events for differences in the trigger and reconstruction efficiencies compared to data, specially determined scale factors (SFs) are used. A SF is the ratio $SF = \epsilon_{\text{data}}/\epsilon_{\text{MC}}$, scaling the MC efficiency ϵ_{MC} to the value in data ϵ_{data}. The effect of the SFs on the event yields are estimated.
The object selection in Ref. [60], which differs slightly from the object selection in Table 5.1, is used, while the signal selection in Table 7.8 is applied. The event yields are estimated without (w/o) and with (w/) additional SF applied. The SFs for

- Muon reconstruction and identification: *muon_recoid_sfo* and *muon_recoid_sf1*
- Electron reconstruction and identification: *electron_recoid_sfo* and *electron_recoid_sf1*
- Trigger efficiency L1: *L1MU4_sf*
- Trigger efficiency HLT: *HLT_mu4_sf*
- Trigger efficiency FgapAC3: 0.991
- Topocluster for unmatched topocluster cut: 0.975

are considered.
The event yields for data, signal and background predictions are presented in Table C.1 together with the figure of merits: s/b, $s/\sqrt{b}$, $s/\sqrt{s+b}$ and $s/\sqrt{s+b+(\zeta s)^2+(\zeta b)^2}$ with a conservative uncertainty assumption of $\zeta = 10\,\%$ to quantify the size of and the sensitivity to the signal. The values are taken from Table C.2 and Table C.3 showing the events yields for each sample without and with SFs applied, respectively.
The SFs affect the combined signal and background estimation by around 5 %. The signal purity is changed by a maximum of 0.4 % in SR-1M3T and less in the other SRs. The figure of merits are also barely affected by the SFs. In this thesis, SFs have been neglected as they became available only at the very end of the thesis. This comparison demonstrates however that the effect is rather small and the results shown in this thesis are not significantly impacted by the omission of the SFs.

	SR-1M1T		SR-1M3T		SR-1E1T		SR-1E3T		SR-1M1E	
SF (w/o)/(w/)	w/o	w/	w/o	w/	w/o	w/	w/o	w/	w/o	w/
Data d	532.0	532.0	85.0	85.0	581.0	581.0	52.0	52.0	44.0	44.0
Expected Events $s+b$	581.2	548.4	106.8	100.6	646.4	629.7	149.9	145.4	48.7	47.1
Signal s	514.7	485.5	101	95.2	311.4	301.2	98.7	95.9	45.8	44.2
Total Background b	66.5	62.9	5.8	5.4	335	328.5	51.2	49.5	2.9	2.9
Background $\gamma\gamma \to \mu\mu$	66.4	62.8	5.5	5.1	0.1	0.1	0.0	0.0	2.9	2.9
Background $\gamma\gamma \to ee$	0.0	0.0	0.0	0.0	334.9	328.3	50.5	48.8	0.0	0.0
Background $\gamma\gamma \to q\bar{q}$	0.1	0.1	0.3	0.3	0.0	0.1	0.7	0.7	0.0	0.0
Signal purity in [%]	88.6	88.5	94.6	94.6	48.2	47.8	65.8	66.0	94.0	93.8
s/b	7.7	7.7	17.4	17.6	0.9	0.9	1.9	1.9	15.8	15.2
$s/\sqrt{b}$	63.1	61.2	41.9	41.0	17.0	16.6	13.8	13.6	26.9	26.0
$s/\sqrt{s+b}$	21.3	20.7	9.8	9.5	12.2	12.0	8.1	8.0	6.6	6.4
$s/\sqrt{s+b+(\zeta s)^2+(\zeta b)^2}$	20.4	19.8	9.3	9.0	11.7	11.4	7.7	7.6	6.3	6.1

Table C.1: Comparison of event yields for data, signal and background predictions, obtained with and without SFs, together with the signal purity and the figure of merits: s/b, $s/\sqrt{b}$, $s/\sqrt{s+b}$ and $s/\sqrt{s+b+(\zeta s)^2+(\zeta b)^2}$ with a conservative uncertainty assumption of $\zeta = 10\,\%$ for the SR-*excl*.

Requirement	Data 18	$\gamma\gamma \to \tau\tau$ 4M	$\gamma\gamma \to \mu\mu$ 7M20	$\gamma\gamma \to \mu\mu$ 20M	$\gamma\gamma \to ee$ 4p5M7	$\gamma\gamma \to ee$ 7M15	$\gamma\gamma \to ee$ 15Mv1	$\gamma\gamma \to$ jets DD	$\gamma\gamma \to$ jets DR	$\gamma\gamma \to$ jets RD	$\gamma\gamma \to$ jets RR	sig/$\sqrt{\text{sig+bkg}}$
SR-1M1T	532.0	514.7	62.0	4.4	0.0	0.0	0.0	0.1	0.0	0.0	0.0	21.3
SR-1M3T	85.0	101.0	5.1	0.4	0.0	0.0	0.0	0.3	0.0	0.0	0.0	9.8
SR-1E1T	581.0	311.4	0.1	0.0	3.7	246.3	84.9	0.1	0.0	0.0	0.0	12.2
SR-1E3T	52.0	98.7	0.0	0.0	0.1	32.5	17.9	0.7	0.0	0.0	0.0	8.1
SR-1M1E	44.0	45.8	1.9	1.0	0.0	0.0	0.0	0.0	0.0	0.0	0.0	6.6

Table C.2: Overview of the event counts after all selection requirements are applied for SR-1M1T, SR-1M3T, SR-1E1T, SR-1E3T and SR-1M1E, obtained without SFs. Simulated samples are normalized to $\mathcal{L} = 1.44\,\text{fb}^{-1}$.

Requirement	Data 18	$\gamma\gamma \to \tau\tau$ 4M	$\gamma\gamma \to \mu\mu$ 7M20	$\gamma\gamma \to \mu\mu$ 20M	$\gamma\gamma \to ee$ 4p5M7	$\gamma\gamma \to ee$ 7M15	$\gamma\gamma \to ee$ 15Mv1	$\gamma\gamma \to$ jets DD	$\gamma\gamma \to$ jets DR	$\gamma\gamma \to$ jets RD	$\gamma\gamma \to$ jets RR	sig/$\sqrt{\text{sig+bkg}}$
SR-1M1T	532.0	485.5	58.6	4.2	0.0	0.0	0.0	0.1	0.0	0.0	0.0	20.7
SR-1M3T	85.0	95.2	4.8	0.3	0.0	0.0	0.0	0.3	0.0	0.0	0.0	9.5
SR-1E1T	581.0	301.2	0.1	0.0	4.1	242.8	81.4	0.1	0.0	0.0	0.0	12.0
SR-1E3T	52.0	95.9	0.0	0.0	0.1	31.6	17.1	0.7	0.0	0.0	0.0	8.0
SR-1M1E	44.0	44.2	1.9	1.0	0.0	0.0	0.0	0.0	0.0	0.0	0.0	6.4

Table C.3: Overview of the event counts after all selection requirements are applied for SR-1M1T, SR-1M3T, SR-1E1T, SR-1E3T and SR-1M1E, obtained with SFs. Simulated samples are normalized to $\mathcal{L} = 1.44\,\text{fb}^{-1}$.

D

CUTFLOW TABLES FOR THE OPTIMIZATION OF SIGNAL REGIONS

Additional cutflow tables for the optimization throught the inclusion of baseline leptons are listed. The cutflow tables without baseline muon requirement for the muon based SRs (Table D.1, Table D.2) and the cutflow tables with the baseline electron requirement for the electron based SRs (Table D.3, Table D.4) are given in this appendix.

Requirement	Data 18	$\gamma\gamma \to \tau\tau$ 4M	$\gamma\gamma \to \mu\mu$ 7M20	$\gamma\gamma \to \mu\mu$ 20M	$\gamma\gamma \to ee$ 4p5M7	$\gamma\gamma \to ee$ 7M15	$\gamma\gamma \to ee$ 15Mv1	$\gamma\gamma \to$ jets DD	$\gamma\gamma \to$ jets DR	$\gamma\gamma \to$ jets RD	$\gamma\gamma \to$ jets RR	sig/$\sqrt{\text{sig+bkg}}$
pass GRL	4335070.0	23615.5	88094.6	7380.6	177294.7	135156.7	19274.8	35981.6	7677.2	7677.2	12524.5	32.9
$E_{\text{ZDC}}^{A,C} < 1$ TeV	1435464.0	23615.5	88094.6	7380.6	177294.7	135156.7	19274.8	35981.6	7677.2	7677.2	12524.5	32.9
HLT mu4 trigger	60313.0	1214.5	48272.4	6013.9	0.0	0.1	0.3	36.0	5.7	6.1	9.5	5.2
$N_{\mu}^{\text{sig}} = 1$	19407.0	968.9	12418.7	1846.0	0.0	0.1	0.3	22.7	3.3	3.8	5.9	7.8
$N_{e}^{\text{sig}} = 0$	19337.0	936.1	12416.6	1844.6	0.0	0.0	0.0	22.6	3.3	3.7	5.9	7.6
$N_{\text{trk}}(\Delta R > 0.1 \text{ from } \mu) = 1$	10096.0	627.3	8391.5	714.4	0.0	0.0	0.0	0.5	0.0	0.0	0.0	6.4
Veto unmatched clusters	9283.0	618.0	8341.0	706.3	0.0	0.0	0.0	0.3	0.0	0.0	0.0	6.3
$\sum$ charge = 0	9267.0	610.9	8339.0	705.4	0.0	0.0	0.0	0.2	0.0	0.0	0.0	6.2
$p_{\text{T}}^{(\mu,\text{trk})} > 1$ GeV	1212.0	565.9	460.3	77.1	0.0	0.0	0.0	0.2	0.0	0.0	0.0	17.0
$p_{\text{T}}^{(\mu,\text{trk},\gamma)} > 1$ GeV	1029.0	543.4	392.0	69.7	0.0	0.0	0.0	0.2	0.0	0.0	0.0	17.1
$p_{\text{T}}^{(\mu,\text{trk,cluster})} > 1$ GeV	877.0	500.1	320.9	63.1	0.0	0.0	0.0	0.1	0.0	0.0	0.0	16.8
$A_{\phi}^{\mu,\text{trk}} < 0.4$	860.0	498.3	320.1	62.6	0.0	0.0	0.0	0.1	0.0	0.0	0.0	16.8

Table D.1: Overview of the event counts after the selection requirements for SR-1M1T-excl are applied sequentially, using the definition of baseline muons as veto. Simulated samples are normalized to $\mathcal{L} = 1.44$ fb^{-1}.

Requirement	Data 18	$\gamma\gamma \to \tau\tau$ 4M	$\gamma\gamma \to \mu\mu$ 7M20	$\gamma\gamma \to \mu\mu$ 20M	$\gamma\gamma \to ee$ 4p5M7	$\gamma\gamma \to ee$ 7M15	$\gamma\gamma \to ee$ 15Mv1	$\gamma\gamma \to$ jets DD	$\gamma\gamma \to$ jets DR	$\gamma\gamma \to$ jets RD	$\gamma\gamma \to$ jets RR	sig/$\sqrt{\text{sig+bkg}}$
pass GRL	4335070.0	23615.5	88094.6	7380.6	177294.7	135156.7	19274.8	35981.6	7677.2	7677.2	12524.5	32.9
$E_{\text{ZDC}}^{A,C} < 1$ TeV	1435464.0	23615.5	88094.6	7380.6	177294.7	135156.7	19274.8	35981.6	7677.2	7677.2	12524.5	32.9
HLT mu4 trigger	60313.0	1214.5	48272.4	6013.9	0.0	0.1	0.3	36.0	5.7	6.1	9.5	5.2
$N_{\mu}^{\text{sig}} = 1$	19407.0	968.9	12418.7	1846.0	0.0	0.1	0.3	22.7	3.3	3.8	5.9	7.8
$N_{e}^{\text{sig}} = 0$	19337.0	936.1	12416.6	1844.6	0.0	0.0	0.0	22.6	3.3	3.7	5.9	7.6
$N_{\text{trk}}(\Delta R > 0.1 \text{ from } \mu) = 3$	401.0	98.3	11.0	1.3	0.0	0.0	0.0	1.9	0.1	0.1	0.2	9.2
Veto unmatched clusters	207.0	97.1	11.0	1.3	0.0	0.0	0.0	1.6	0.1	0.1	0.1	9.2
$\sum$ charge = 0	191.0	95.8	10.9	1.3	0.0	0.0	0.0	1.2	0.0	0.1	0.0	9.2
$m_{\text{trks}} < 1.7$ GeV	89.0	95.0	8.3	0.8	0.0	0.0	0.0	0.4	0.0	0.0	0.0	9.3
$A_{\phi}^{\mu,\text{trks}} < 0.4$	89.0	95.0	8.3	0.8	0.0	0.0	0.0	0.3	0.0	0.0	0.0	9.3

Table D.2: Overview of the event counts after the selection requirements for SR-1M3T-excl are applied sequentially, using the definition of baseline muons as veto. Simulated samples are normalized to $\mathcal{L} = 1.44$ fb^{-1}.

Requirement	Data 18	$\gamma\gamma \to \tau\tau$ 4M	$\gamma\gamma \to \mu\mu$ 7M20	$\gamma\gamma \to \mu\mu$ 20M	$\gamma\gamma \to ee$ 4p5M7	$\gamma\gamma \to ee$ 7M15	$\gamma\gamma \to ee$ 15Mv1	$\gamma\gamma \to$ jets DD	$\gamma\gamma \to$ jets DR	$\gamma\gamma \to$ jets RD	$\gamma\gamma \to$ jets RR	sig/$\sqrt{\text{sig+bkg}}$
pass GRL	4335070.0	23615.5	88094.6	7380.6	177294.7	135156.7	19274.8	35981.6	7677.2	7677.2	12524.5	32.9
$E_{\text{ZDC}}^{A,C} < 1$ TeV	1435464.0	23615.5	88094.6	7380.6	177294.7	135156.7	19274.8	35981.6	7677.2	7677.2	12524.5	32.9
HLT hi gg L1TAU1	1094198.0	3294.2	11228.2	1064.3	25735.0	52791.1	12072.2	155.7	5.2	5.4	6.4	10.1
$N_e^{\text{sig}} = 1$	26007.0	589.0	1.9	1.9	321.6	16873.4	4656.3	0.8	0.0	0.1	0.0	3.9
$N_\mu^{\text{sig}} = 0$	25972.0	557.1	0.3	0.1	321.6	16873.4	4656.2	0.8	0.0	0.1	0.0	3.7
$N_e^{\text{baseline}} = 1$	18985.0	517.6	0.3	0.1	238.7	11612.2	2778.4	0.8	0.0	0.1	0.0	4.2
$N_{\text{trk}}(\Delta R > 0.1 \text{ from } e) = 1$	11177.0	396.8	0.2	0.1	202.5	8572.0	1707.4	0.2	0.0	0.0	0.0	3.8
Cluster veto	10630.0	390.3	0.2	0.1	202.3	8503.1	1663.3	0.1	0.0	0.0	0.0	3.8
$\sum$ charge = 0	10579.0	389.0	0.2	0.1	202.1	8473.1	1649.5	0.1	0.0	0.0	0.0	3.8
$p_{\text{T}}^{(e,\text{trk})} > 1$ GeV	7566.0	363.8	0.1	0.1	174.4	6044.8	1260.1	0.1	0.0	0.0	0.0	4.1
$p_{\text{T}}^{(e,\text{trk},\gamma)} > 1$ GeV	6105.0	346.0	0.1	0.1	153.8	4689.0	1047.0	0.1	0.0	0.0	0.0	4.4
$p_{\text{T}}^{(e,\text{trk,cluster})} > 1$ GeV	5050.0	316.4	0.1	0.1	126.6	3817.8	851.7	0.1	0.0	0.0	0.0	4.4
$A_\phi^{e,\text{trk}} > 0.012$	469.0	276.4	0.1	0.0	3.0	183.7	60.3	0.1	0.0	0.0	0.0	12.1

Table D.3: Overview of the event counts after the selection requirements for SR-1E1T-excl are applied sequentially, using the definition of baseline electrons as veto. Simulated samples are normalized to $\mathcal{L} = 1.44$ fb^{-1}.

Requirement	Data 18	$\gamma\gamma \to \tau\tau$ 4M	$\gamma\gamma \to \mu\mu$ 7M20	$\gamma\gamma \to \mu\mu$ 20M	$\gamma\gamma \to ee$ 4p5M7	$\gamma\gamma \to ee$ 7M15	$\gamma\gamma \to ee$ 15Mv1	$\gamma\gamma \to$ jets DD	$\gamma\gamma \to$ jets DR	$\gamma\gamma \to$ jets RD	$\gamma\gamma \to$ jets RR	sig/$\sqrt{\text{sig+bkg}}$
pass GRL	4335070.0	23615.5	88094.6	7380.6	177294.7	135156.7	19274.8	35981.6	7677.2	7677.2	12524.5	32.9
$E_{\text{ZDC}}^{A,C} < 1$ TeV	1435464.0	23615.5	88094.6	7380.6	177294.7	135156.7	19274.8	35981.6	7677.2	7677.2	12524.5	32.9
HLT hi upc L12TAU1	192906.0	10652.2	47378.8	3546.3	95296.6	88813.9	14651.0	19309.4	4031.1	4030.8	6143.0	19.7
$N_e^{\text{sig}} = 1$	23133.0	792.5	2.8	2.8	534.2	20455.3	4866.7	51.8	7.7	7.5	12.2	4.8
$N_\mu^{\text{sig}} = 0$	23130.0	753.8	0.5	0.2	534.2	20455.3	4866.5	51.6	7.7	7.5	12.2	4.6
$N_e^{\text{baseline}} = 1$	14959.0	697.7	0.5	0.2	430.5	14630.7	2819.3	46.3	7.3	7.1	11.5	5.1
$N_{\text{trk}}(\Delta R > 0.1 \text{ from } e) = 3$	209.0	94.7	0.0	0.0	0.3	53.0	20.3	4.4	0.3	0.3	0.4	7.2
Cluster veto	130.0	93.5	0.0	0.0	0.3	52.8	19.9	3.6	0.2	0.2	0.2	7.2
$\sum$ charge = 0	116.0	91.9	0.0	0.0	0.3	50.9	18.6	2.3	0.1	0.1	0.1	7.2
$m_{\text{trks}} < 1.7$ GeV	49.0	89.5	0.0	0.0	0.3	47.8	16.3	0.7	0.0	0.0	0.0	7.2
$m_{\text{trks}} > 0.5$ GeV	36.0	89.1	0.0	0.0	0.1	25.1	8.3	0.7	0.0	0.0	0.0	8.0

Table D.4: Overview of the event counts after the selection requirements for SR-1E3T-excl are applied sequentially, using the definition of baseline electrons as veto. Simulated samples are normalized to $\mathcal{L} = 1.44$ fb^{-1}.

E

BINNING OF THE KINEMATIC OBSERVABLES USED FOR THE FIT

The binning used for the fit for the relevant and sensitive kinematic observables is listed below. The binning should be chosen such that all bins are filled and the shape of the distribution is visible. Non-equidistant bins are chosen to fulfill these criteria. The edges of the bins in GeV are summarized in Table E.1 for the p_{T} of the leptons and the tracks, in Table E.2 for the p_{T} of the lepton-track(s)/lepton-lepton system $p_{\mathrm{T}}(\ell, \mathrm{trk(s)}/\ell')$ and in Table E.3 for the invariant masses $m(\ell, \mathrm{trk(s)}/\ell')$ of the lepton-track(s)/lepton-lepton system.

SR	Variable	Binning [GeV]
All SR with a muon	$p_{\mathrm{T}}(\mu)$	$[4, 5, 6, 7, 8, 9, 10, 12.5, 15, 30]$
All SR with an electron	$p_{\mathrm{T}}(e)$	$[4, 5, 6, 7, 8, 9, 10, 12.5, 15, 30]$
All SR with > 0 tracks	$p_{\mathrm{T}}(\mathrm{trk})$	$[0, 0.5, 1, 1.5, 2, 2.5, 3, 3.5, 4, 5,$ $6, 7, 8, 9, 10, 12, 14, 16]$
SR-1M1E	$\max(p_{\mathrm{T}}(\mu), p_{\mathrm{T}}(e))$	$[4, 5, 6, 7, 8, 9, 10, 12.5, 15, 30]$
SR-1M1E	$p_{\mathrm{T}}(\ell_{\mathrm{mean}})$	$[4, 5, 6, 7, 8, 9, 10, 12.5, 15, 30]$
SR-1M1E	$p_{\mathrm{T}}(\ell)$	$[4, 5, 6, 7, 8, 9, 10, 12.5, 15, 30]$

Table E.1: Binning used for the kinematic distribution $p_{\mathrm{T}}(\ell)$ and $p_{\mathrm{T}}(\mathrm{trk})$ in the respective SRs. The bin edges are given in GeV.

SR	Variable	Binning [GeV]
SR-1M1T	$p_{\mathrm{T}}(\mu, \mathrm{trk})$	$[1, 1.5, 2, 2.5, 3, 3.5, 4, 4.5, 5, 6,$ $7, 8, 10, 12, 16]$
SR-1M3T	$p_{\mathrm{T}}(\mu, \mathrm{trks})$	$[1, 1.5, 2, 2.5, 3, 3.5, 4, 4.5, 5, 6,$ $7, 8, 10, 12, 16]$
SR-1E1T	$p_{\mathrm{T}}(e, \mathrm{trk})$	$[1, 1.5, 2, 2.5, 3, 3.5, 4, 4.5, 5, 6,$ $7, 8, 10, 12, 16]$
SR-1E3T	$p_{\mathrm{T}}(e, \mathrm{trks})$	$[1, 1.5, 2, 2.5, 3, 3.5, 4, 4.5, 5, 6,$ $7, 8, 10, 12, 16]$
SR-1M1E	$p_{\mathrm{T}}(\mu, e)$	$[1, 1.5, 2, 2.5, 3, 3.5, 4, 4.5, 5, 6,$ $7, 8, 10, 12, 16]$

Table E.2: Binning used for the kinematic distribution $p_{\mathrm{T}}(\ell, \mathrm{trk(s)}/\ell')$ in the respective SR. The bin edges are given in GeV.

SR	Variable	Binning [GeV]
SR-1M1T	$m(\mu, \text{trk})$	[0, 0.5, 1, 1.5, 2, 2.5, 3, 3.5, 4, 4.5, 5, 5.5, 6, 6.5, 7, 7.5, 8, 8.5, 9, 9.5, 10, 10.5, 11, 11.5, 12, 12.5, 13, 13.5, 14, 14.5, 15, 15.5, 16, 16.5, 17, 17.5, 18, 18.5, 19, 19.5, 20, 21, 22, 23, 24, 25, 26, 27, 28, 29, 30]
SR-1M3T	$m(\mu, \text{trks})$	[0, 0.5, 1, 1.5, 2, 2.5, 3, 3.5, 4, 4.5, 5, 5.5, 6, 6.5, 7, 7.5, 8, 8.5, 9, 9.5, 10, 10.5, 11, 11.5, 12, 12.5, 13, 13.5, 14, 14.5, 15, 15.5, 16, 16.5, 17, 17.5, 18, 18.5, 19, 19.5, 20, 21, 22, 23, 24, 25, 26, 27, 28, 29, 30]
SR-1E1T	$m(e, \text{trk})$	[0, 0.5, 1., 1.5, 2, 2.5, 3, 3.5, 4, 4.5, 5, 5.5, 6, 6.5, 7, 7.5, 8, 8.5, 9, 9.5, 10, 10.5, 11, 11.5, 12, 12.5, 13, 13.5, 14, 14.5, 15, 15.5, 16, 16.5, 17, 17.5, 18, 18.5, 19, 19.5, 20, 21, 22, 23, 24, 25, 26, 27, 28, 29, 30]
SR-1E3T	$m(e, \text{trks})$	[0, 0.5, 1, 1.5, 2, 2.5, 3, 3.5, 4, 4.5, 5, 5.5, 6, 6.5, 7, 7.5, 8, 8.5, 9, 9.5, 10, 10.5, 11, 11.5, 12, 12.5, 13, 13.5, 14, 14.5, 15, 15.5, 16, 16.5, 17, 17.5, 18, 18.5, 19, 19.5, 20, 21, 22, 23, 24, 25, 26, 27, 28, 29, 30]
SR-1M1E	$m(\mu, e)$	[4, 9, 9.5, 10, 10.5, 11, 11.5, 12, 12.5, 13, 13.5, 14, 14.5, 15, 15.5, 16, 16.5, 17, 17.5, 18, 18.5, 19, 19.5, 20, 21, 22, 23, 24, 25, 26, 27, 28, 29, 30]

Table E.3: Binning used for the kinematic distribution $m(\ell, \text{trk(s)}/\ell')$ in the respective SR. The bin edges are given in GeV. Note: For a fit with data, the binning should be chosen not as fine as listed in this table. Table E.4 makes an appropriate suggestion.

SR	Variable	Binning [GeV]
SR-1M1T	$m(\mu, \text{trk})$	[0, 1, 2, 3, 4, 5, 6, 7, 8, 9, 10, 11, 12, 13, 14, 15, 16, 17, 18, 20, 22, 25, 30]
SR-1M3T	$m(\mu, \text{trks})$	[4, 6, 7.5, 9, 11, 13, 15, 17, 19, 22, 25, 30]
SR-1E1T	$m(e, \text{trk})$	[1, 2, 3, 4, 5, 6, 7, 8, 9, 10, 11, 12, 13.5, 15, 17, 21, 25, 30]
SR-1E3T	$m(e, \text{trks})$	[5, 7, 9, 11, 13, 15, 17, 19, 21, 24, 30]
SR-1M1E	$m(\mu, e)$	[8, 10, 12, 14, 16, 18, 20, 23, 26, 30]

Table E.4: Binning used for the kinematic distribution $m(\ell, \text{trk(s)}/\ell')$ in the respective SR. The bin edges are given in GeV.

F

OBSERVABLES NON-SENSITIVE TO a_τ

The observables sensitive to a_τ are discussed in Section 9.1. Here, a list of kinematic observables that are tested and found to be less sensitive are listed and exemplary shown for SR-1M1T-excl in Figure F.1 - Figure F.4:

- d_0 significance of the lepton $|d_0/\sigma(\ell)|$ or track $|d_0\sigma(\text{trk})|$ (Figure F.1)
- Angle ϕ and pseudorapidity η of leptons or tracks (Figure F.2)
- Angular distances $\Delta\phi$, $\Delta\eta$ and ΔR between lepton and tracks or lepton and lepton (Figure F.3)
- The acoplanarity $A_\phi^{\ell,\text{trk(s)}}$, and $\cos(\vartheta^*(\ell,\text{trk}))$ (Figure F.4)
- Rapidity y of lepton and track system (Figure F.4)

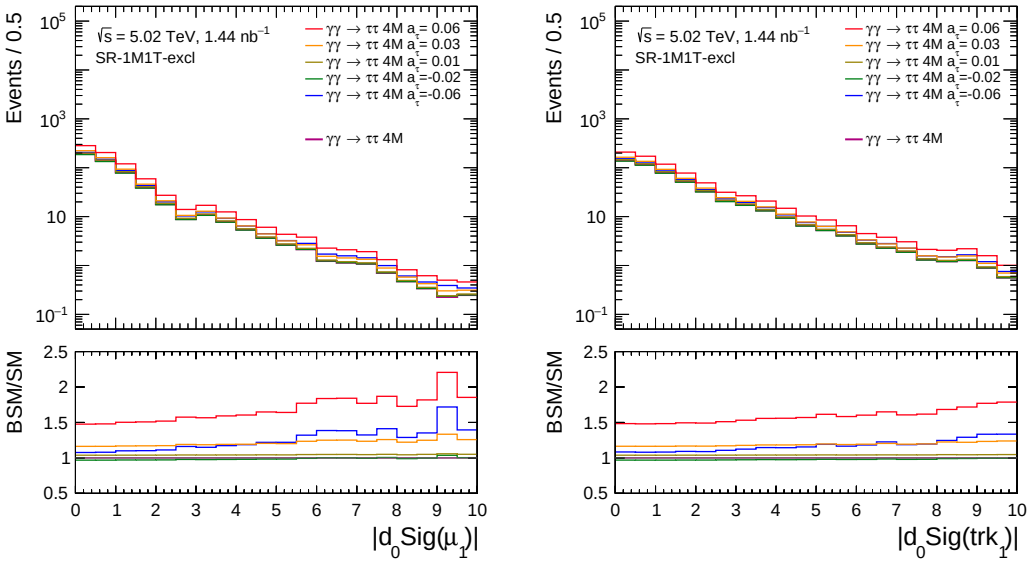

(a) **(b)**

Figure F.1: The d_0 significances $|d_0 Sig(\mu)|$ (a), $|d_0\text{sig(trk)}|$ (b) in SR-1M1T-excl. The upper panels show the shape of the signal prediction for different a_τ values, the lower panels show the ratios of the predictions with $a_\tau \neq 0$ to the SM prediction ($a_\tau = 0$).

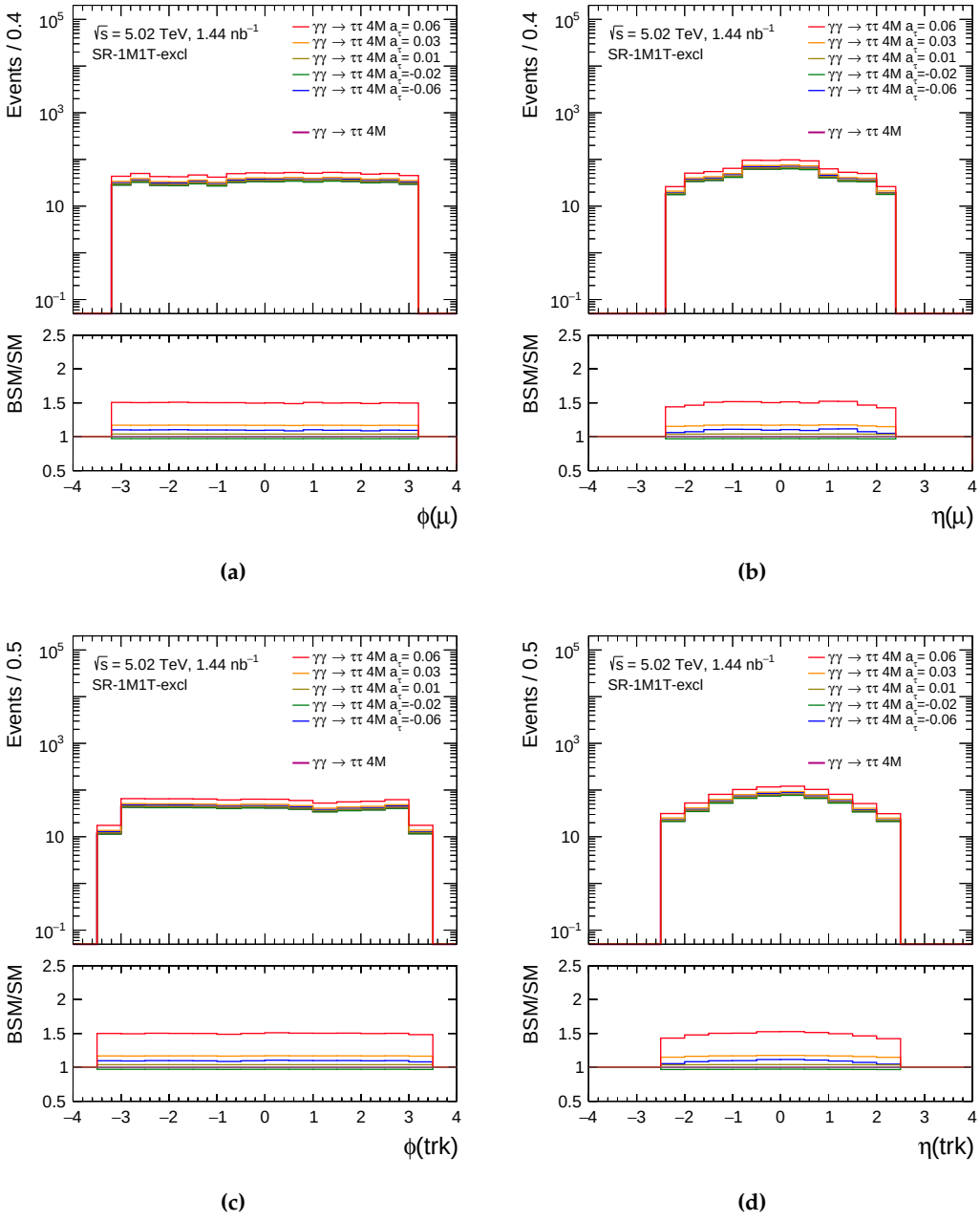

Figure F.2: The angle ϕ of the leading muon (a), η of the leading muon (b), ϕ of the track (c) and η of the track (d) in SR-1M1T-excl. The upper panels show the shape of the signal prediction for different a_τ values, the lower panels show the ratios of the predictions with $a_\tau \neq 0$ to the SM prediction ($a_\tau = 0$).

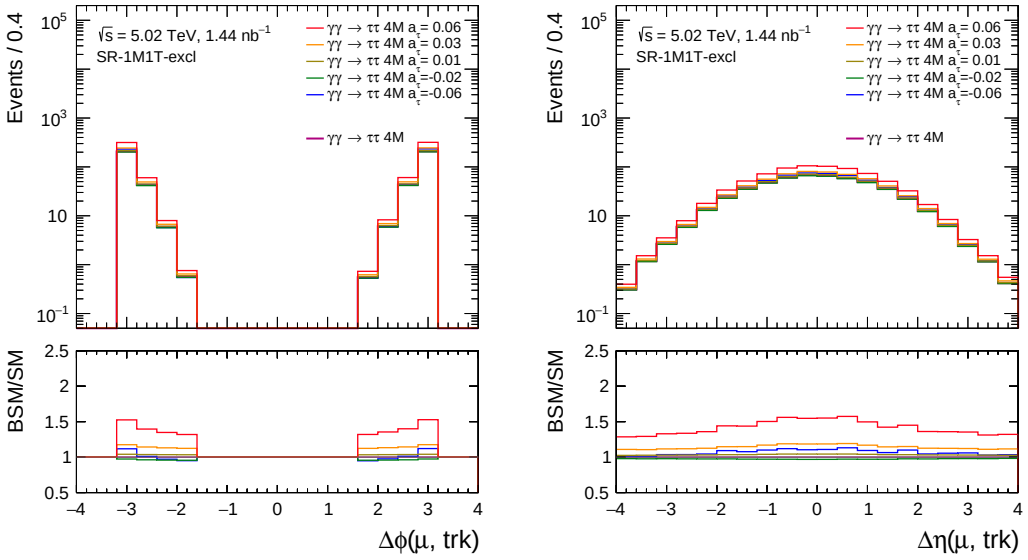

(a) **(b)**

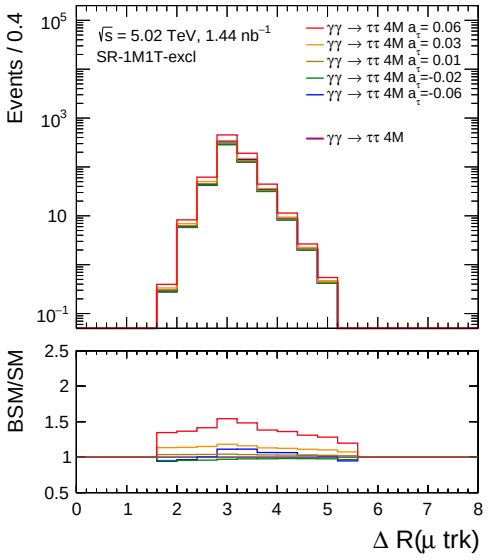

(c)

Figure F.3: The angular distance $\Delta\phi$ (a), $\Delta\eta$ (b) and ΔR (c) between the leading muon and the track in SR-1M1T-excl. The upper panels show the shape of the signal prediction for different a_τ values, the lower panels show the ratios of the predictions with $a_\tau \neq 0$ to the SM prediction ($a_\tau = 0$).

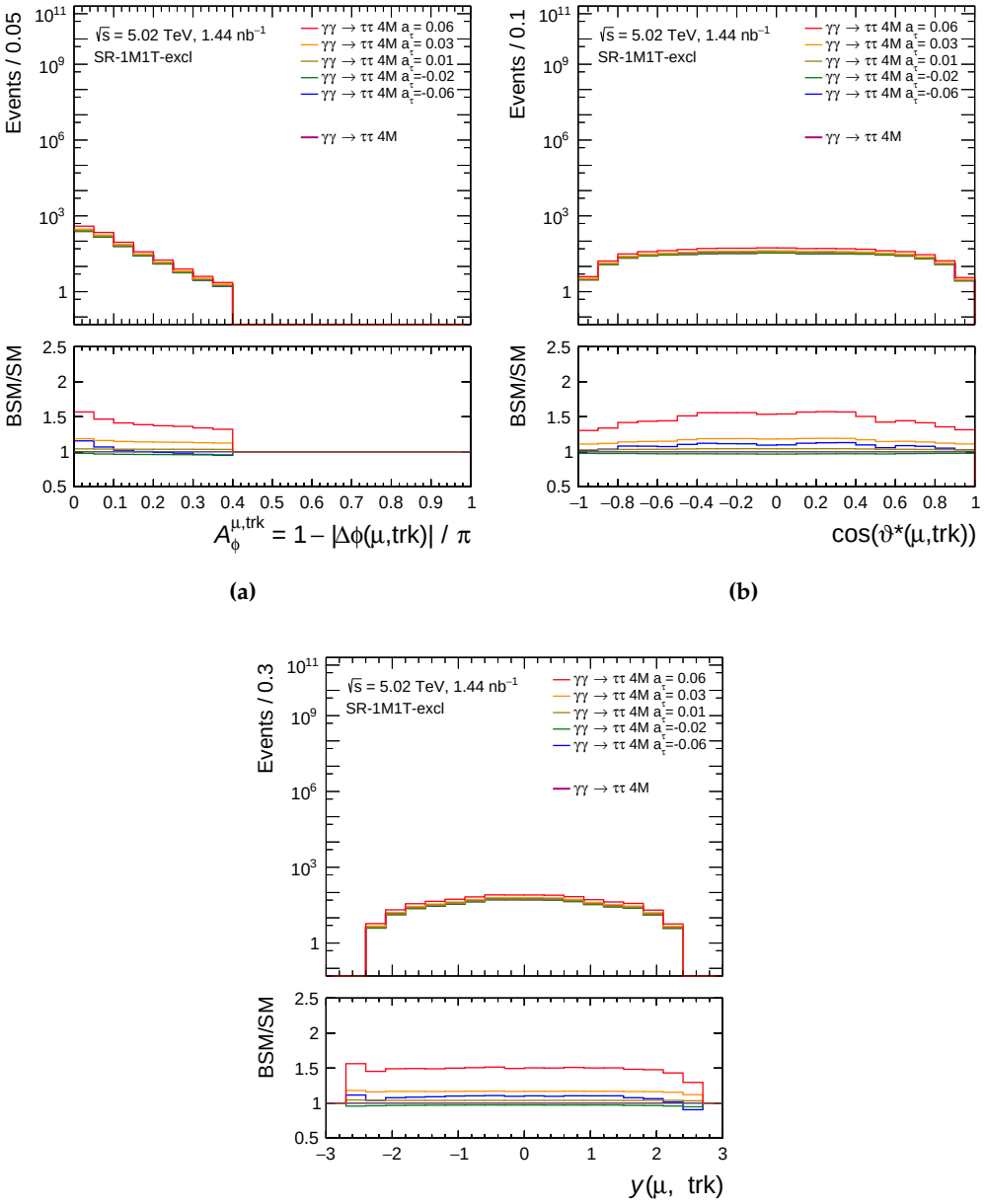

Figure F.4: The acoplanarity $A_\phi^{\mu,\text{trk}}$ (a), the angle $\cos(\vartheta^*(\mu,\text{trk}))$ (b) and the rapidity $y(\mu,\text{trk})$ (c) in SR-1M1T-excl. The upper panels show the shape of the signal prediction for different a_τ values, the lower panels show the ratios of the predictions with $a_\tau \neq 0$ to the SM prediction ($a_\tau = 0$).

G

SUPPLEMENTARY MATERIAL FOR DETERMINATION OF a_τ

Supplementary material for the eNLL and nNLL fits, discussed in Chapter 9, is given. Figures, comparing the expected sensitivity to a_τ for the kinematic distributions $p_T(\ell)$, $p_T(\text{trk})$, $p_T(\ell, \text{trk(s)}/\ell')$, $m(\ell, \text{trk(s)}/\ell')$ and N_{Events} in the SR-1M1T, SR-1M3T, SR-1E1T, SR-1E3T and SR-1M1E are shown for different fit inputs:

- only the signal prediction as input (Appendix G.1
- signal and background prediction as input compared to the signal only prediction Appendix G.2
- comparison of the eNLL and nNLL functions with the signal and background prediction as input Appendix G.3

G.1 SENSITIVITY FOR THE SIGNAL PROCESS ONLY

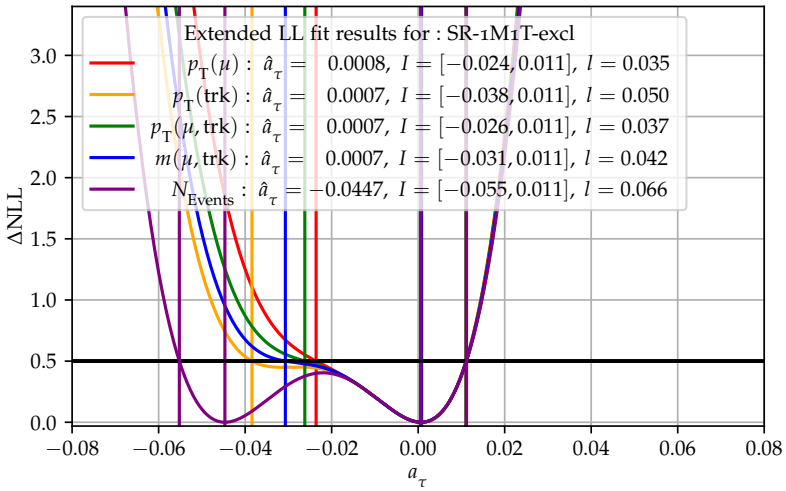

Figure G.1: Extended NLL fits for the five observables $p_T(\ell)$, $p_T(\text{trk})$, $p_T(\ell, \text{trk(s)}/\ell')$, $m(\ell, \text{trk(s)}/\ell')$ and N_{Events} in SR-1M1T. The best fit value $\hat{a}_\tau$ is determined as the minimum of the ΔNLL function. The minimum is marked with a vertical line in the respective color. The 68 % confidence interval I is determined by the intersection points of the ΔNLL function with a line at 0.5 marked by a horizontal line. The interval length is given in the legend.

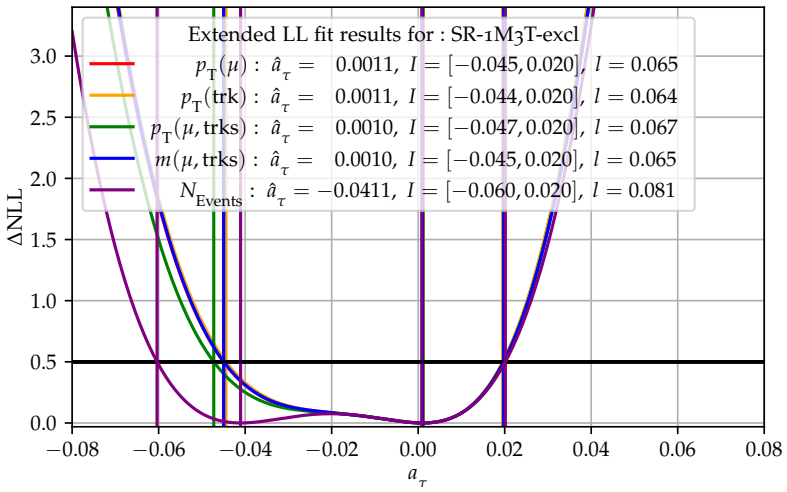

Figure G.2: Extended NLL fits for the five observables $p_T(\ell)$, $p_T(\text{trk})$, $p_T(\ell, \text{trk(s)}/\ell')$, $m(\ell, \text{trk(s)}/\ell')$ and N_{Events} in SR-1M3T. The best fit value $\hat{a}_\tau$ is determined as the minimum of the ΔNLL function. The minimum is marked with a vertical line in the respective color. The 68 % confidence interval I is determined by the intersection points of the ΔNLL function with a line at 0.5 marked by a horizontal line. The interval length is given in the legend.

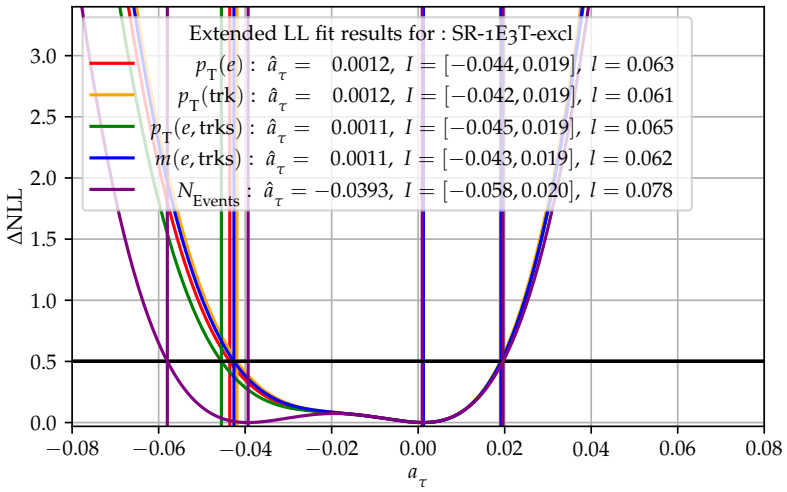

Figure G.3: Extended NLL fits for the five observables $p_T(\ell)$, $p_T(\text{trk})$, $p_T(\ell, \text{trk(s)}/\ell')$, $m(\ell, \text{trk(s)}/\ell')$ and N_{Events} in SR-1E3T. The best fit value $\hat{a}_\tau$ is determined as the minimum of the ΔNLL function. The minimum is marked with a vertical line in the respective color. The 68 % confidence interval I is determined by the intersection points of the ΔNLL function with a line at 0.5 marked by a horizontal line. The interval length is given in the legend.

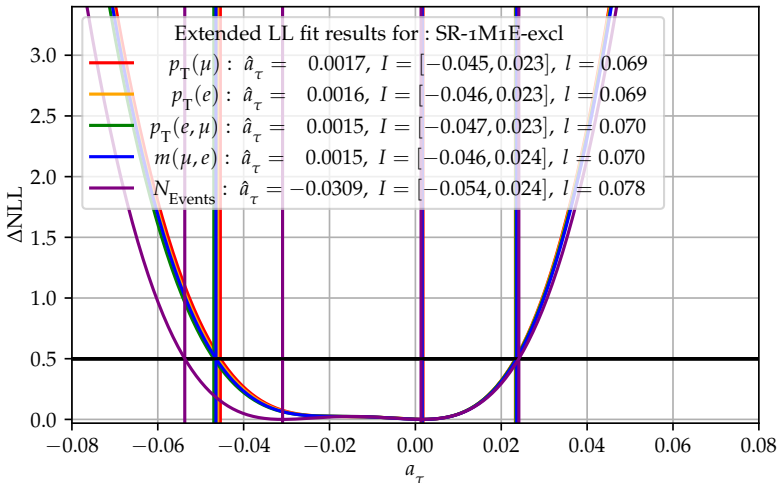

Figure G.4: Extended NLL fits for the five observables $p_T(\ell)$, $p_T(\text{trk})$, $p_T(\ell, \text{trk(s)}/\ell')$, $m(\ell, \text{trk(s)}/\ell')$ and N_{Events} in SR-1M1E. The best fit value $\hat{a}_\tau$ is determined as the minimum of the ΔNLL function. The minimum is marked with a vertical line in the respective color. The 68 % confidence interval I is determined by the intersection points of the ΔNLL function with a line at 0.5 marked by a horizontal line. The interval length is given in the legend.

G.2 SIGNAL ONLY VS. SIGNAL + BACKGROUND PREDICTION

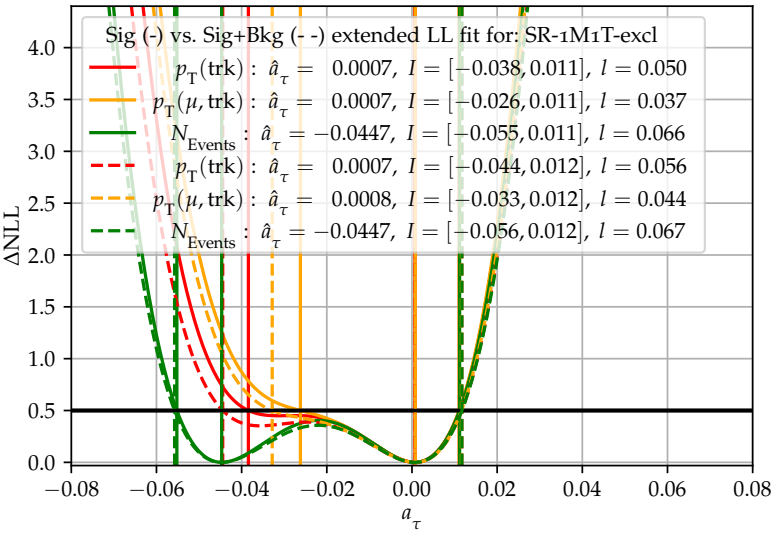

Figure G.5: Comparison of eNLL fit functions in SR-1M1T for the kinematic distribution $p_T(\text{trk})$, $p_T(\mu, \text{trk})$ and the cross section observable N_{Events} for the signal-only (solid lines) and signal+background (dashed lines) fits. The best fit value $\hat{a}_\tau$ is determined as the minimum of the ΔNLL function. The minimum is marked with a vertical line in the respective color. The 68 % confidence interval I is determined by the intersection points of the ΔNLL function with a line at 0.5 marked by a horizontal line. The interval length is given in the legend.

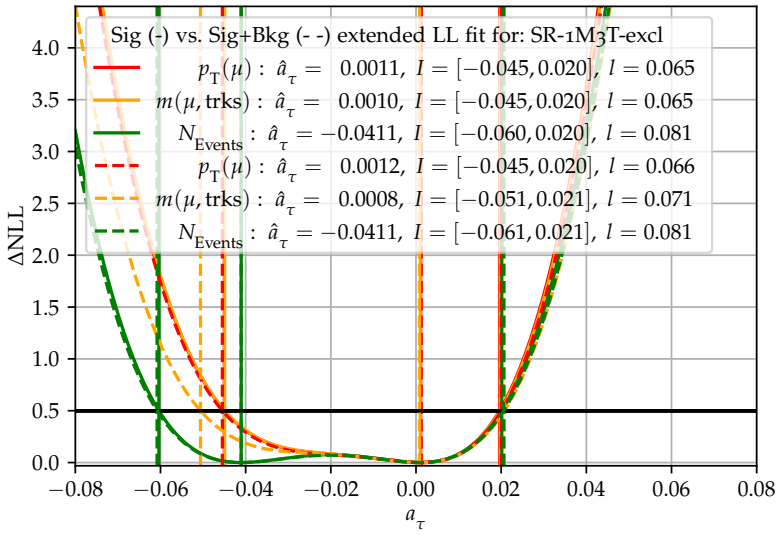

Figure G.6: Comparison of eNLL fit functions in SR-1M3T for the kinematic distribution $p_T(\mu)$, $m(\mu, \text{trks})$ and the cross section observable N_{Events} for the signal-only (solid lines) and signal+background (dashed lines) fits. The best fit value $\hat{a}_\tau$ is determined as the minimum of the ΔNLL function. The minimum is marked with a vertical line in the respective color. The 68 % confidence interval I is determined by the intersection points of the ΔNLL function with a line at 0.5 marked by a horizontal line. The interval length is given in the legend.

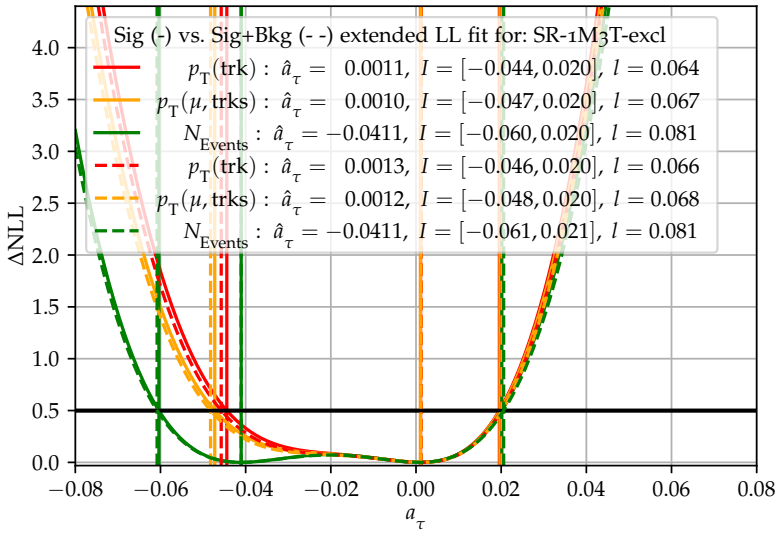

Figure G.7: Comparison of eNLL fit functions in SR-1M3T for the kinematic distribution $p_T(\text{trk})$, $p_T(\mu, \text{trks})$ and the cross section observable N_{Events} for the signal-only (solid lines) and signal+background (dashed lines) fits. The best fit value $\hat{a}_\tau$ is determined as the minimum of the ΔNLL function. The minimum is marked with a vertical line in the respective color. The 68 % confidence interval I is determined by the intersection points of the ΔNLL function with a line at 0.5 marked by a horizontal line. The interval length is given in the legend.

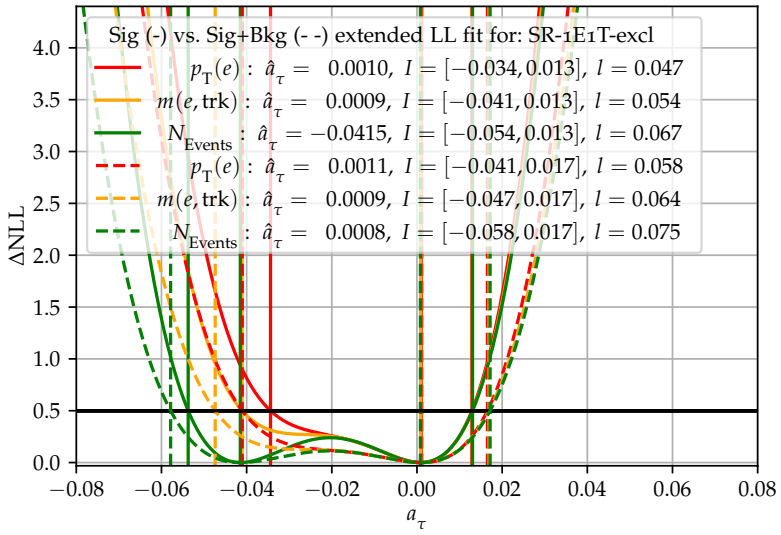

Figure G.8: Comparison of eNLL fit functions in SR-1E1T for the kinematic distribution $p_T(e)$, $m(e, \mathrm{trk})$ and the cross section observable N_{Events} for the signal-only (solid lines) and signal+background (dashed lines) fits. The best fit value $\hat{a}_\tau$ is determined as the minimum of the ΔNLL function. The minimum is marked with a vertical line in the respective color. The 68 % confidence interval I is determined by the intersection points of the ΔNLL function with a line at 0.5 marked by a horizontal line. The interval length is given in the legend.

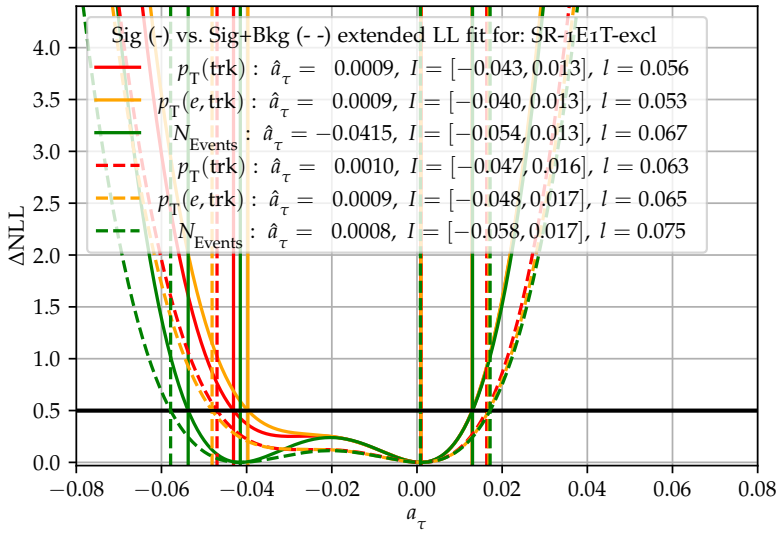

Figure G.9: Comparison of eNLL fit functions in SR-1E1T for the kinematic distribution $p_T(\mathrm{trk})$, $p_T(e, \mathrm{trk})$ and the cross section observable N_{Events} for the signal-only (solid lines) and signal+background (dashed lines) fits. The best fit value $\hat{a}_\tau$ is determined as the minimum of the ΔNLL function. The minimum is marked with a vertical line in the respective color. The 68 % confidence interval I is determined by the intersection points of the ΔNLL function with a line at 0.5 marked by a horizontal line. The interval length is given in the legend.

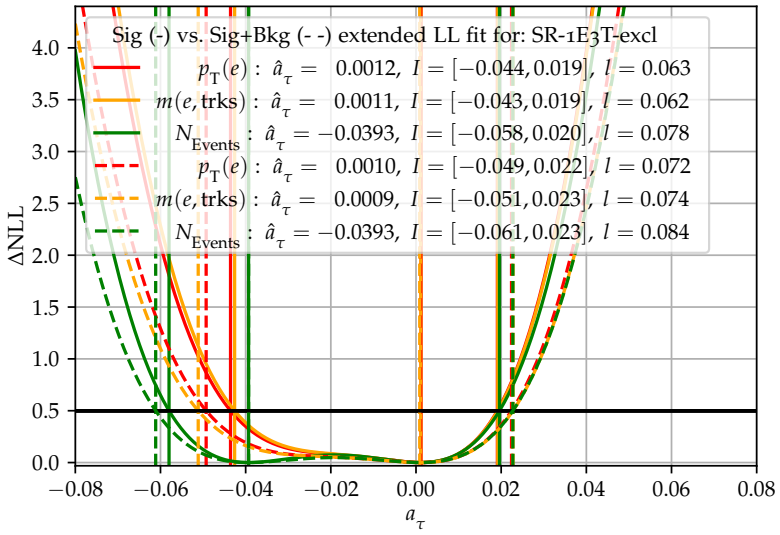

Figure G.10: Comparison of eNLL fit functions in SR-1E3T for the kinematic distribution p_T, $m(e, \text{trks})$ and the cross section observable N_{Events} for the signal-only (solid lines) and signal+background (dashed lines) fits. The best fit value $\hat{a}_\tau$ is determined as the minimum of the ΔNLL function. The minimum is marked with a vertical line in the respective color. The 68 % confidence interval I is determined by the intersection points of the ΔNLL function with a line at 0.5 marked by a horizontal line. The interval length is given in the legend.

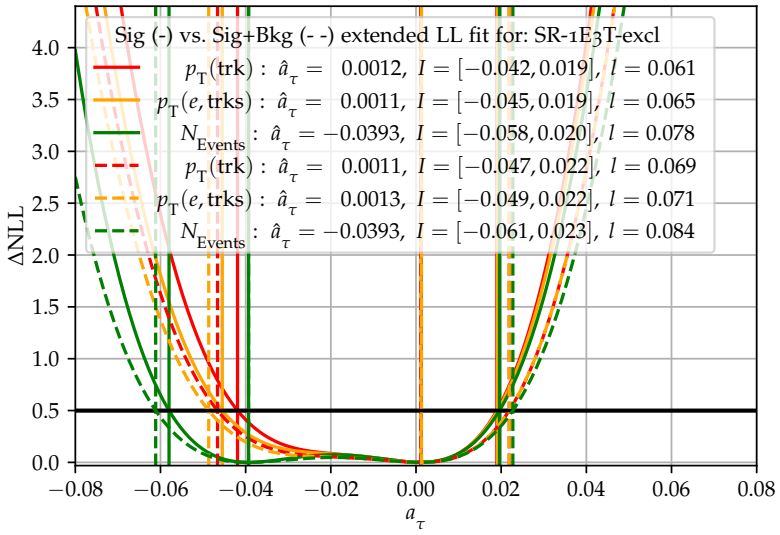

Figure G.11: Comparison of eNLL fit functions in SR-1E3T for the kinematic distribution $p_T(\text{trk})$, $p_T(e, \text{trks})$ and the cross section observable N_{Events} for the signal-only (solid lines) and signal+background (dashed lines) fits. The best fit value $\hat{a}_\tau$ is determined as the minimum of the ΔNLL function. The minimum is marked with a vertical line in the respective color. The 68 % confidence interval I is determined by the intersection points of the ΔNLL function with a line at 0.5 marked by a horizontal line. The interval length is given in the legend.

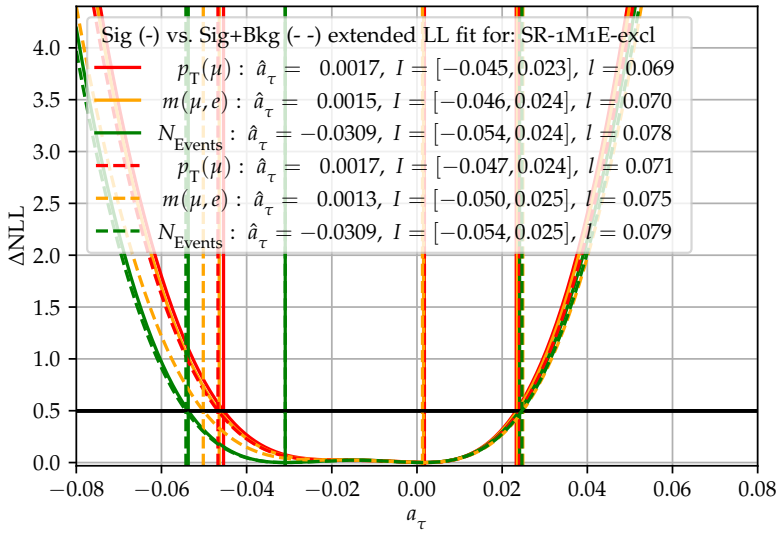

Figure G.12: Comparison of eNLL fit functions in SR-1M1T for the kinematic distribution $p_T(\mu)$, $m(\mu, e)$ and the cross section observable N_{Events} for the signal-only (solid lines) and signal+background (dashed lines) fits. The best fit value $\hat{a}_\tau$ is determined as the minimum of the ΔNLL function. The minimum is marked with a vertical line in the respective color. The 68 % confidence interval I is determined by the intersection points of the ΔNLL function with a line at 0.5 marked by a horizontal line. The interval length is given in the legend.

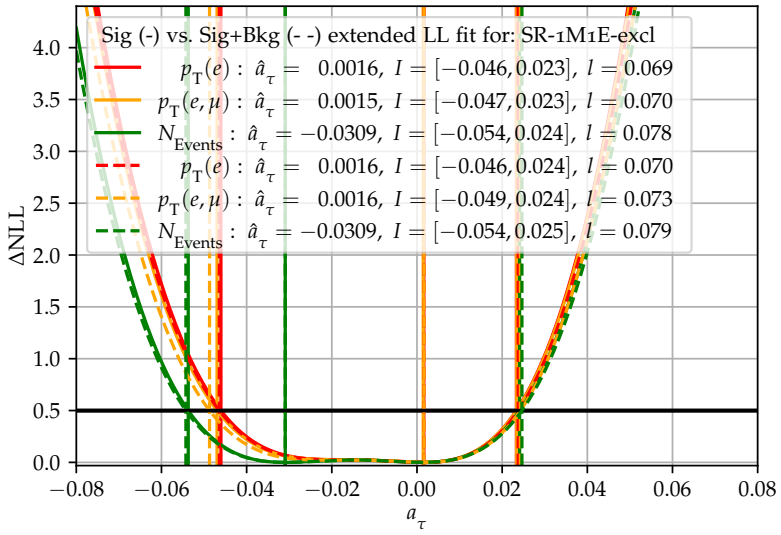

Figure G.13: Comparison of eNLL fit functions in SR-1M1E for the kinematic distribution $p_T(e)$, $p_T(\mu, e)$ and the cross section observable N_{Events} for the signal-only (solid lines) and signal+background (dashed lines) fits. The best fit value $\hat{a}_\tau$ is determined as the minimum of the ΔNLL function. The minimum is marked with a vertical line in the respective color. The 68 % confidence interval I is determined by the intersection points of the ΔNLL function with a line at 0.5 marked by a horizontal line. The interval length is given in the legend.

G.3 COMPARISON OF EXTENDED AND NORMAL LOGLIKELIHOOD FUNCTION

The comparison of the normal (green) and extended (purple) LL fit functions in for the kinematic distributions $p_{\mathrm{T}}(\ell)$, $p_{\mathrm{T}}(\mathrm{trk})$, $p_{\mathrm{T}}(\ell, \mathrm{trk(s)}/\ell')$ and $m(\ell, \mathrm{trk(s)}/\ell')$ in SR-1M1T, SR-1M3T, SR-1E1T, SR-1E3T and SR-1M1E are shown in Figures G.14-G.18, respectively. The best fit value $\hat{a}_\tau$ is there determined as the minimum of the ΔNLL function. The minimum is marked with a vertical line in the respective color. The 68 % CI I is determined by the intersection points of the ΔNLL function with a line at 0.5 marked by a horizontal line. The interval length is given in each legend.

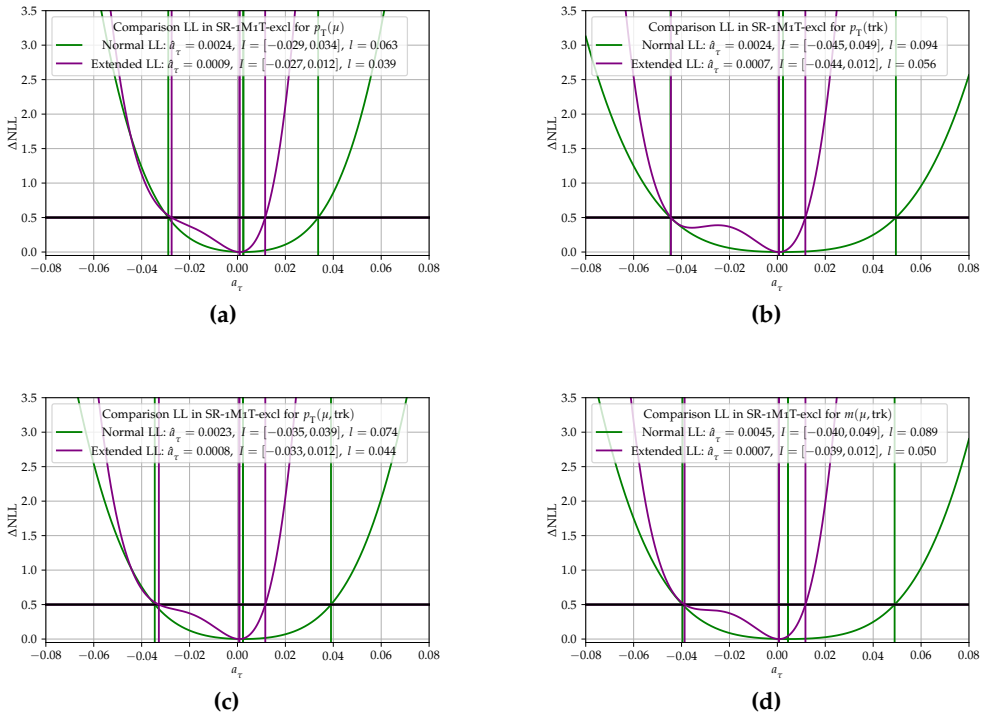

(a) **(b)** **(c)** **(d)**

Figure G.14

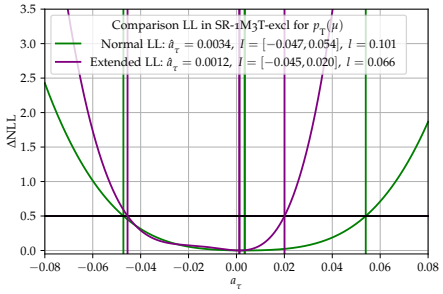

(a)

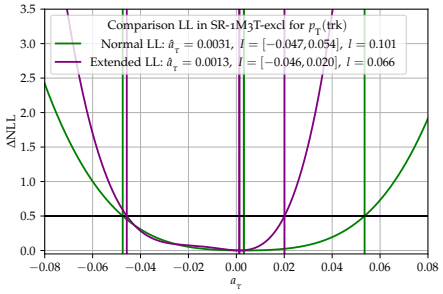

(b)

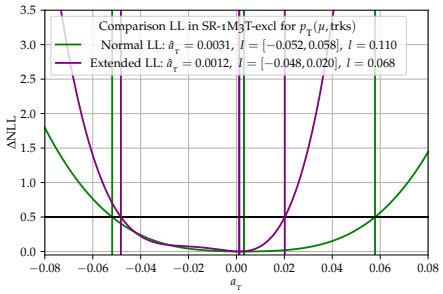

(c)

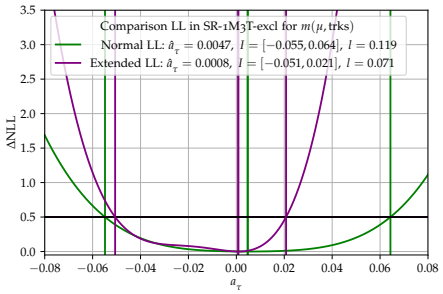

(d)

Figure G.15

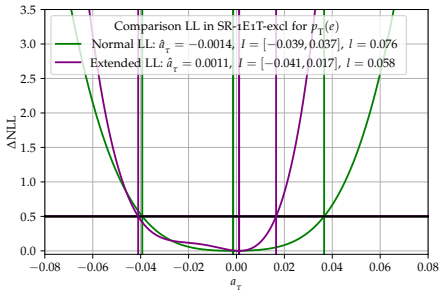

(a)

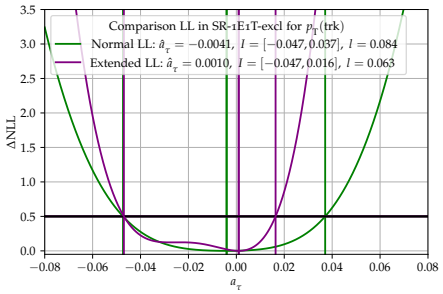

(b)

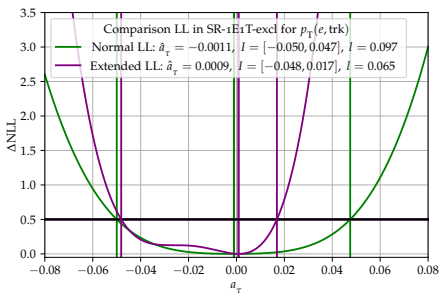

(c)

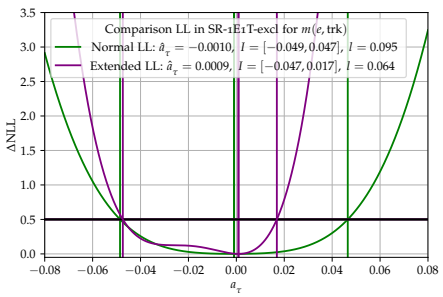

(d)

Figure G.16

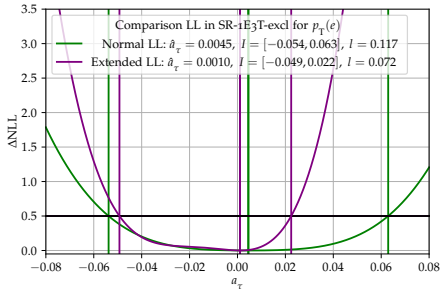

(a)

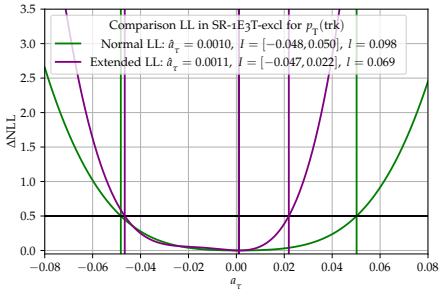

(b)

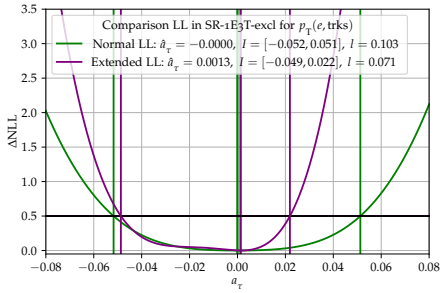

(c)

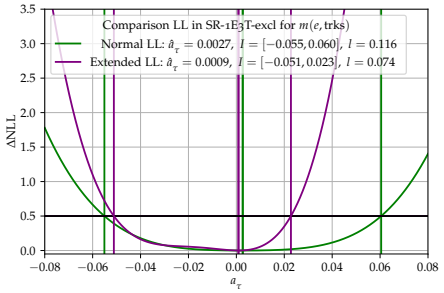

(d)

Figure G.17

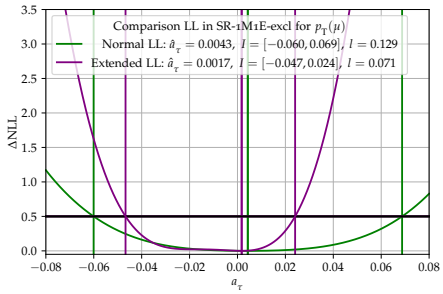

(a)

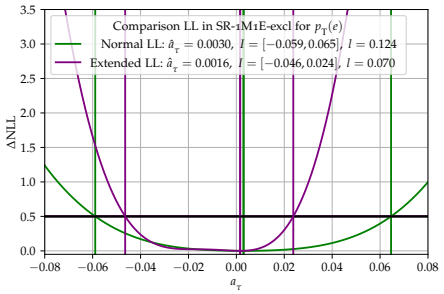

(b)

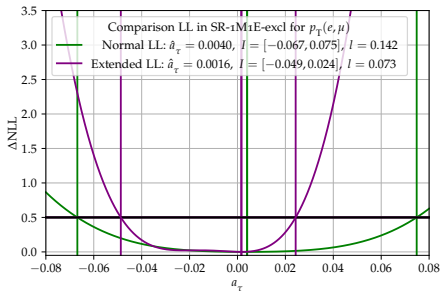

(c)

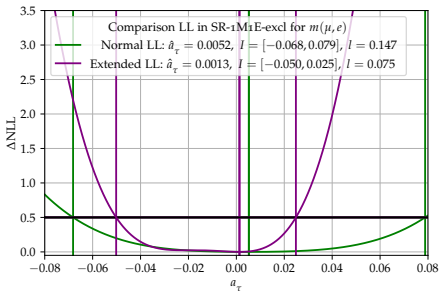

(d)

Figure G.18

BIBLIOGRAPHY

[1] ATLAS Collaboration, *Observation of a new particle in the search for the Standard Model Higgs boson with the ATLAS detector at the LHC*, Phys. Lett. B **716** (2012) 1 (cit. on pp. 1, 4).

[2] CMS Collaboration, *Observation of a new boson at a mass of 125GeVwith the CMS experiment at the LHC*, Phys. Lett. B **716** (2012) 30 (cit. on p. 1).

[3] S. P. Martin and J. D. Wells, *Muon Anomalous Magnetic Dipole Moment in Supersymmetric Theories*, Phys. Rev. **D64** (2001) 035003, arXiv: hep-ph/0103067 [hep-ph] (cit. on pp. 1, 6).

[4] D. Hanneke, S. Fogwell, and G. Gabrielse, *New Measurement of the Electron Magnetic Moment and the Fine Structure Constant*, Phys. Rev. Lett. **100** (12 2008) 120801, arXiv: 0801.1134 [physics.atom-ph] (cit. on pp. 1, 7).

[5] A. Keshavarzi, K. S. Khaw, and T. Yoshioka, *Muon g-2: A review*, Nuclear Physics B **975** (2022) 115675, arXiv: 2106.06723 [hep-ex] (cit. on p. 1).

[6] M. Passera, *Precise mass-dependent QED contributions to leptonic g-2 at order α^2 and α^3*, Phys. Rev. **D75** (2007) 013002, arXiv: hep-ph/0606174 [hep-ph] (cit. on pp. 1, 19).

[7] S. Eidelman and M. Passera, *Theory of the tau lepton anomalous magnetic moment*, Mod. Phys. Lett. **A22** (2007) 159, arXiv: hep-ph/0701260 [hep-ph] (cit. on pp. 1, 5–7, 19).

[8] DELPHI Collaboration, *Study of tau-pair production in photon-photon collisions at LEP and limits on the anomalous electromagnetic moments of the tau lepton*, Eur. Phys. J. C **35** (2004) 159, arXiv: hep-ex/0406010 (cit. on pp. 1, 7, 135, 137, 140).

[9] F. Cornet and J. I. Illana, *Tau pair production via photon-photon collisions at LEP*, Phys. Rev. **D53** (1996) 1181, arXiv: hep-ph/9503466 [hep-ph] (cit. on p. 1).

[10] B. R. Martin and G. Shaw, *Particle physics*, John Wiley & Sons, 2017 (cit. on p. 3).

[11] O. Brüning, H. Burkhardt, and S. Myers, *The Standard Model and beyond*, Progress in Particle and Nuclear Physics **67** (2012) 705 (cit. on p. 3).

[12] T. Nakano and K. Nishijima, *Charge Independence for V-particles*, Prog. Theor. Phys. **10** (1953) 581 (cit. on p. 4).

[13] M. Gell-Mann, *The interpretation of the new particles as displaced charge multiplets*, Il Nuovo Cimento **4** (1956) 848 (cit. on p. 4).

[14] S. Tomonaga, *On a Relativistically Invariant Formulation of the Quantum Theory of Wave Fields**, Progress of Theoretical Physics **1** (1946) 27 (cit. on p. 4).

[15] R. P. Feynman, *Relativistic cutoff for quantum electrodynamics*, Phys. Rev. **74** (1948) 1430 (cit. on p. 4).

[16] J. Schwinger, *On Quantum-Electrodynamics and the Magnetic Moment of the Electron*, Phys. Rev. **73** (4 1948) 416 (cit. on pp. 4–6).

[17] S. L. Glashow, *Partial-symmetries of weak interactions*, Nucl. Phys. **22** (1961) 579 (cit. on p. 4).

[18] A. Salam and J. Ward, *Electromagnetic and weak interactions*, Phys. Lett. **13** (1964) 168 (cit. on p. 4).

[19] S. Weinberg, *A Model of Leptons*, Phys. Rev. Lett. **19** (1967) 1264 (cit. on p. 4).

[20] H. Fritzsch, M. Gell-Mann, and H. Leutwyler, *Advantages of the color octet gluon picture*, Phys, Lett, B **47** (1973) 365 (cit. on p. 4).

[21] D. J. Gross and F. Wilczek, *Ultraviolet Behavior of Non-Abelian Gauge Theories*, Phys. Rev. Lett. **30** (1973) 1343 (cit. on p. 4).

[22] H. D. Politzer, *Reliable Perturbative Results for Strong Interactions?* Phys. Rev. Lett. **30** (1973) 1346 (cit. on p. 4).

[23] F. Englert and R. Brout, *Broken Symmetry and the Mass of Gauge Vector Mesons*, Phys. Rev. Lett. **13** (1964) 321 (cit. on p. 4).

[24] P. W. Higgs, *Broken Symmetries and the Masses of Gauge Bosons*, Phys. Rev. Lett. **13** (1964) 508 (cit. on p. 4).

[25] Particle Data Group, *Review of Particle Physics*, Phys. Rev. D **98** (2018) 030001 (cit. on pp. 4, 83).

[26] F. Halzen and A. D. Martin, *Quark & Leptons: An introductory course in modern particle physics*, John Wiley & Sons, 2008 (cit. on p. 4).

[27] Muon $g-2$ Collaboration, *Measurement of the Positive Muon Anomalous Magnetic Moment to 0.46 ppm*, Phys. Rev. Lett. **126** (14 2021) 141801 (cit. on p. 7).

[28] T. Aoyama et al., *The anomalous magnetic moment of the muon in the Standard Model*, Physics Reports **887** (2020) 1 (cit. on p. 7).

[29] L3 Collaboration, *Measurement of the anomalous magnetic and electric dipole moments of the tau lepton*, Phys. Lett. **B434** (1998) 169 (cit. on pp. 7, 135, 137).

[30] OPAL Collaboration, *An Upper limit on the anomalous magnetic moment of the tau lepton*, Phys. Lett. **B431** (1998) 188, arXiv: hep-ex/9803020 [hep-ex] (cit. on pp. 7, 135, 137).

[31] J. Jowett, *Colliding Heavy Ions in the LHC*, (2018) TUXGBD2. 6 p (cit. on pp. 8, 13).

[32] ATLAS Collaboration, *Exclusive dimuon production in ultraperipheral Pb+Pb collisions at* $\sqrt{s_{NN}} = 5.02$ *TeV with ATLAS*, (2020), arXiv: 2011.12211 [hep-ex] (cit. on p. 8).

[33] M. Dyndał, M. Kłusek-Gawenda, A. Szczurek, and M. Schott, *Anomalous electromagnetic moments of τ lepton in $\gamma\gamma \to \tau^+\tau^-$ reaction in Pb+Pb collisions at the LHC*, Physics Letters B **809** (2020) 135682 (cit. on p. 9).

[34] M. Kłusek-Gawenda, P. Lebiedowicz, O. Nachtmann, and A. Szczurek, *From the $\gamma\gamma \to p\overline{p}$ reaction to the production of $p\overline{p}$ pairs in ultraperipheral ultrarelativistic heavy-ion collisions at the LHC*, Phys. Rev. D **96** (9 2017) 094029 (cit. on p. 9).

[35] P. Zyla et al., *Review of Particle Physics*, PTEP **2020** (2020) 083C01 (cit. on p. 10).

[36] *About CERN*, (2012), URL: http://cds.cern.ch/record/1997225 (cit. on p. 11).

[37] O. Brüning, H. Burkhardt, and S. Myers, *The Large Hadron Collider*, Progress in Particle and Nuclear Physics **67** (2012) 705 (cit. on p. 11).

[38] ATLAS Collaboration, *The ATLAS Experiment at the CERN Large Hadron Collider*, JINST **3** (2008) S08003. 437 p (cit. on pp. 11, 14).

[39] L. Evans and P. Bryant (Eds.), *LHC Machine*, JINST **3** (2008) S08001 (cit. on p. 11).

[40] J. Jowett et al., *The 2018 heavy-ion run of the LHC*, (2019) WEYYPLM2. 4 p (cit. on pp. 11, 13).

[41] *Experiments*, (2012), URL: http://cds.cern.ch/record/1997374 (cit. on p. 12).

[42] E. Mobs, *The CERN accelerator complex - August 2018. Complexe des accélérateurs du CERN - Août 2018*, (2018), URL: http://cds.cern.ch/record/2636343, General Photo (cit. on p. 12).

[43] ATLAS Collaboration, *ATLAS Twiki*, URL: https://twiki.cern.ch/twiki/bin/viewauth/Atlas/LuminosityForPhysics#2018_5_02_TeV_lead_lead_prelimin, (accessed 10 Mar, 2022) (cit. on p. 13).

[44] ATLAS Collaboration, *ATLAS public Twiki*, URL: https://twiki.cern.ch/twiki/bin/view/AtlasPublic/LuminosityPublicResultsRun2, (accessed 17 Jan, 2022) (cit. on p. 13).

[45] ATLAS Collaboration, URL: https://atlas.cern/discover/detector, (accessed February 1, 2022) (cit. on p. 14).

[46] M. Schott and M. Dunford, *Review of single vector boson production in pp collisions at $\sqrt{s} = 7$ TeV*, Eur. Phys. J. **C74** (2014) 2916, arXiv: 1405.1160 [hep-ex] (cit. on p. 15).

[47] ATLAS Collaboration, *The ATLAS Experiment at the CERN Large Hadron Collider*, JINST **3** (2008) S08003 (cit. on pp. 16, 18).

[48] P. Puzo, *ATLAS calorimetry*, Nuclear Instruments and Methods in Physics Research **494** (2002) 340 (cit. on p. 17).

[49] V. S. Kaushik, *Electromagnetic Showers And Shower Detectors*, Internal Documents, University of Texas at Arlington (2002) (cit. on p. 17).

[50] ATLAS Collaboration, *Exclusive dimuon production in ultraperipheral Pb+Pb collisions at $\sqrt{s_{\mathrm{NN}}} = 5.02$ TeV with ATLAS*, Phys. Rev. C **104** (2021) 024906, arXiv: 2011.12211 [hep-ex] (cit. on pp. 18, 25).

[51] ATLAS Collaboration, *Operation of the ATLAS trigger system in Run 2*, Journal of Instrumentation **15** (2020) P10004 (cit. on pp. 18, 41).

[52] *Trigger menu in 2018*, CERN, 2019, URL: https://cds.cern.ch/record/2693402 (cit. on pp. 18, 41).

[53] S. R. Klein, J. Nystrand, J. Seger, Y. Gorbunov, and J. Butterworth, *STARlight: A Monte Carlo simulation program for ultra-peripheral collisions of relativistic ions*, Comput. Phys. Commun. **212** (2017) 258, arXiv: 1607.03838 [hep-ph] (cit. on p. 20).

[54] T. Sjöstrand et al., *An introduction to* PYTHIA *8.2*, Comput. Phys. Commun. **191** (2015) 159, arXiv: 1410.3012 [hep-ph] (cit. on p. 20).

[55] T. Sjöstrand, S. Mrenna, and P. Skands, PYTHIA *6.4 physics and manual*, J. High Energy Phys. **05** (2006) 026, arXiv: hep-ph/0603175 (cit. on p. 20).

[56] N. Davidson, T. Przedzinski, and Z. Was, *PHOTOS Interface in C++: Technical and physics documentation*, Comput. Phys. Commun. **199** (2016) 86, arXiv: 1011.0937 [hep-ph] (cit. on p. 20).

[57] E. Barberio, B. van Eijk, and Z. Was, PHOTOS - *a universal Monte Carlo for QED radiative corrections in decays*, Comput. Phys. Commun. **66** (1991) 115 (cit. on p. 20).

[58] E. Barberio and Z. Was, PHOTOS - *a universal Monte Carlo for QED radiative corrections: version 2.0*, Comput. Phys. Commun. **79** (1994) 291 (cit. on p. 20).

[59] L. A. Harland-Lang, V. A. Khoze, and M. G. Ryskin, *Exclusive LHC physics with heavy ions: SuperChic 3*, Eur. Phys. J. C **79** (2019) 39, arXiv: 1810.06567 [hep-ph] (cit. on p. 20).

[60] M. Akbiyik et al., *Search for anomalous magnetic moment of τ lepton in ultra-peripheral Pb+Pb collisions with ATLAS*, Geneva, 2021, URL: https://cds.cern.ch/record/2798409 (cit. on pp. 20–23, 25, 28, 29, 31, 42, 49, 67, 69, 73, 145–147).

[61] M. Dyndal, M. Klusek-Gawenda, M. Schott, and A. Szczurek, *Anomalous electromagnetic moments of τ lepton in $\gamma\gamma \to \tau^+\tau^-$ reaction in Pb+Pb collisions at the LHC*, Phys. Lett. B **809** (2020) 135682, arXiv: 2002.05503 [hep-ph] (cit. on p. 20).

[62] J. Alwall et al., *The automated computation of tree-level and next-to-leading order differential cross sections, and their matching to parton shower simulations*, J. High Energy Phys. **07** (2014) 79, arXiv: 1405.0301 [hep-ph] (cit. on p. 21).

[63] T. Walsh and P. Zerwas, *Two-photon processes in the parton model*, Physics Letters B **44** (1973) 195 (cit. on p. 22).

[64] S. R. Klein and P. Steinberg, *Photonuclear and Two-Photon Interactions at High-Energy Nuclear Colliders*, Annual Review of Nuclear and Particle Science **70** (2020) 323, arXiv: 2005.01872 [hep-ex] (cit. on p. 23).

[65] S. Roesler, R. Engel, and J. Ranft, *The Monte Carlo event generator DPMJET-III*, (2000), arXiv: hep-ph/0012252 (cit. on p. 23).

[66] *EGamma recommendations for release 21*, URL: https://twiki.cern.ch/twiki/bin/viewauth/AtlasProtected/EGammaRecommendationsR21, (accessed 5 Jan, 2022) (cit. on p. 27).

[67] *HeavyIonUPCWG*, URL: https://twiki.cern.ch/twiki/bin/view/AtlasProtected/HeavyIonUPCWG, (accessed 5 Jan, 2022) (cit. on pp. 27, 29).

[68] *Photon efficiencies for Run2*, URL: https://twiki.cern.ch/twiki/bin/view/AtlasProtected/PhotonEfficiencyRun2, (accessed 5 Jan, 2022) (cit. on p. 27).

[69] *MCPAnalysisGuidelinesMC16*, URL: https://twiki.cern.ch/twiki/bin/view/AtlasProtected/MCPAnalysisGuidelinesMC16, (accessed 5 Jan, 2022) (cit. on p. 27).

[70] *InDetTrackingPerformanceGuidelines*, URL: https://twiki.cern.ch/twiki/bin/view/AtlasProtected/InDetTrackingPerformanceGuidelines, (accessed 5 Jan, 2022) (cit. on p. 27).

[71] ATLAS Collaboration, *Performance of the ATLAS track reconstruction algorithms in dense environments in LHC Run 2*, Eur. Phys. J. C **77** (2017) 673, arXiv: 1704.07983 [hep-ex] (cit. on p. 27).

[72] R. Frühwirth, *Application of Kalman filtering to track and vertex fitting*, Nucl. Instrum. Methods Phys. Res. A **262** (1987) 444 (cit. on p. 27).

[73] *Tracking CP Recommendations for Early 2018 Analyses*, URL: https://twiki.cern.ch/twiki/bin/view/AtlasProtected/TrackingCPRecsEarly2018#Track_Selection, (accessed 5 Jan, 2022) (cit. on p. 28).

[74] A. Wharton, W. Yao, and R. Jansky, *ATLAS Inner Detector Track Quality Cuts for Run 2*, CERN, 2014, URL: https://cds.cern.ch/record/1752536 (cit. on p. 28).

[75] ATLAS Collaboration, *Topological cell clustering in the ATLAS calorimeters and its performance in LHC Run 1*, Eur. Phys. J. C **77** (2017) 490, arXiv: 1603.02934 [hep-ex] (cit. on p. 28).

[76] W. Lampl et al., *Calorimeter Clustering Algorithms: Description and Performance*, CERN, 2008, URL: https://cds.cern.ch/record/1099735 (cit. on p. 28).

[77] ATLAS Collaboration, *Electron reconstruction and identification in the ATLAS experiment using the 2015 and 2016 LHC proton–proton collision data at $\sqrt{s} = 13$ TeV*, Eur. Phys. J. C **79** (2019) 639, arXiv: 1902.04655 [physics.ins-det] (cit. on pp. 28, 29).

[78] ATLAS Collaboration, *Improved electron reconstruction in ATLAS using the Gaussian Sum Filter-based model for bremsstrahlung*, ATLAS-CONF-2012-047, 2012, URL: https://cds.cern.ch/record/1449796 (cit. on p. 29).

[79] C. Anastopoulos et al., *Electron identification and efficiency measurements in 2017 data*, CERN, 2019, URL: https://cds.cern.ch/record/2652163 (cit. on p. 29).

[80] I. Grabowska-Bold et al., *Measurement of light-by-light scattering with 2.2 nb^{-1} of Pb+Pb data in the ATLAS detector - Supporting Note*, CERN, 2019, URL: https://cds.cern.ch/record/2703499 (cit. on pp. 30, 32, 145).

[81] ATLAS Collaboration, *Muon reconstruction performance of the ATLAS detector in proton–proton collision data at $\sqrt{s} = 13$ TeV*, Eur. Phys. J. C **76** (2016) 292, arXiv: 1603.05598 [hep-ex] (cit. on p. 30).

[82] M. K. Bugge et al., *Muon Selection and Identification Working Points*, CERN, 2019, URL: https://cds.cern.ch/record/2665711 (cit. on p. 31).

[83] ATLAS Collaboration, *Measurement of the photon identification efficiencies with the ATLAS detector using LHC Run 2 data collected in 2015 and 2016*, The European Physical Journal C **79** (2019) (cit. on p. 31).

[84] A. C. Olivieri and G. M. Escandar, *Chapter 6 - Analytical Figures of Merit*, Elsevier (2014) 93 (cit. on p. 33).

[85] G. Cowan, *Statistical data analysis*, Oxford university press, 1998 (cit. on pp. 34, 37).

[86] K. Cranmer, G. Lewis, L. Moneta, A. Shibata, and W. Verkerke, *HistFactory: A tool for creating statistical models for use with RooFit and RooStats*, CERN-OPEN-2012-016, URL: https://cds.cern.ch/record/1456844 (cit. on pp. 34, 35, 38).

[87] R. Barlow and C. Beeston, *Fitting using finite Monte Carlo samples*, Comput. Phys. Commun. 77 (1993) 219 (cit. on p. 35).

[88] *TRExFitter documentation*, URL: https://trexfitter-docs.web.cern.ch, (accessed on 18 Aug, 2021) (cit. on pp. 38, 40, 121).

[89] L. Moneta et al., *The RooStats Project*, 2011, arXiv: 1009.1003 [physics.data-an] (cit. on p. 38).

[90] W. Verkerke and D. Kirkby, *The RooFit toolkit for data modeling*, 2003, arXiv: physics/0306116 [physics.data-an] (cit. on p. 38).

[91] F. James and M. Roos, *Minuit - a system for function minimization and analysis of the parameter errors and correlations*, Computer Physics Communications **10** (1975) 343 (cit. on p. 38).

[92] ATLAS Collaboration, *Identification and energy calibration of hadronically decaying τ leptons with the ATLAS experiment in pp collisions at $\sqrt{s} = 8$ TeV*, The European Physical Journal C **75** (2015) (cit. on p. 41).

[93] J. Kremer, *ATLAS tau g minus 2 analysis*, (accessed 10 Feb, 2022), URL: https://its.cern.ch/jira/browse/ATR-24396 (cit. on p. 41).

[94] M. Dyndal, *Analysis Update*, (2022), URL: https://indico.cern.ch/event/1112164/contributions/4676034/attachments/2371495/4050236/mdyndal_2022-01-12_taug-2.pdf (cit. on p. 62).

[95] M. D. Mariola Klusek-Gawenda Antoni Szczurek and M. Schott, *The sensitivity to BSM in di-taon production at the LHC*, 2021, arXiv: 2107.13274 [hep-ph] (cit. on p. 101).

[96] R. L. Plackett, *Karl Pearson and the chi-squared test*, International statistical review/revue internationale de statistique (1983) 59 (cit. on p. 102).

[97] *Observation of tau lepton pair production in ultraperipheral nucleus-nucleus collisions*, CERN, 2022, URL: https://cds.cern.ch/record/2803742 (cit. on p. 135).

[98] CERN, *LEP design report: Vol.2. The LEP Main Ring*, CERN-LEP-84-01, 1984, URL: https://cds.cern.ch/record/102083 (cit. on p. 137).

[99] B. A. Petersen and C. Schwick, *Experiment Requests and constrains for run 3*, URL: https://indico.cern.ch/event/751857/contributions/3259413/attachments/1781638/3257666/ExperimentsInRun3_proceedings.pdf, (accessed February 14, 2022) (cit. on p. 136).

[100] M. Dyndal, *Analysis Update*, (2021), URL: https://indico.cern.ch/event/994065/contributions/4179745/attachments/2191778/3704544/mdyndal_2021-02-10_taug-2.pdf (cit. on pp. 143, 144).

[101] C. Galloni, *Hadronic Tau reconstruction and identification performance in ATLAS and CMS*, tech. rep., CERN, 2018, URL: http://cds.cern.ch/record/2644381 (cit. on p. 145).

ACKNOWLEDGMENTS

Mit Abschluss dieser Arbeit möchte ich mich bei denjenigen bedanken, die mich unterstützt haben:
Bei Markus, dass er mir ein so spannendes Thema angeboten hat, mich so intensitiv betreut hat und immer die richtigen kritischen Fragen gestellt hat.
Bei Valerie, für die richtig, richtig gute Betreuung, die lehrreichen und lustigen Meetings, die hilfreichen Tipps und Tricks und die Unterstützung zu jeder Zeit.
Bei der ganzen Arbeitsgruppe, für die entspannte Atmosphäre, die Plaudereien zwischendurch und ihrer Offenheit. Besonders möchte ich Katharina, Benjamin, David, Dirk, und Fabian erwähnen, die immer ansprechbar waren, wenn ich irgendwelche Fragen und Probleme zur Physik, zum Computing oder einfach so hatte.
Bei meinem Analyse Team, für die unkomplizierte Aufnahme in das Team, die gute Zusammenarbeit bis hin zur Veröffentlichung der Ergebnisse.
Bei Alex, Andreas und Dennis für die gute Gesellschaft, die gemütlichen Abende und die aufmunternden Worte, und natürlich bei Justin, der immer für einen Lacher gut war.
Bei Anna, Jenny und Julie. So wurde das Mittagessen am Mittwoch immer zu einem Höhepunkt.
Bei Ali, Soso, Wiebke, Konsti, Marlo und Robin, die immer für mich da sind.
Bei meinen Eltern und meinem Bruder, für ihre Unterstützung in jeder Hinsicht.
Und bei allen anderen, die ich vergessen habe zu erwähnen.

Erklärung gem. der geltenden Prüfungsordnung:

Hiermit versichere ich, dass

1. ich die eingereichte Masterarbeit bzw. bei einer Gruppenarbeit meinen Anteil entsprechend gekennzeichneten Anteil der Arbeit selbständig verfasst habe,
2. ich keine anderen als die angegebenen Quellen und Hilfsmittel benutzt und alle wörtlich oder sinngemäß aus anderen Werken übernommenen Inhalte als solche kenntlich gemacht habe und
3. die eingereichte Masterarbeit weder vollständig noch in wesentlichen Teilen Gegenstand eines anderen Prüfungsverfahrens war oder ist.

_____ _____

Ort, Datum Unterschrift

Auszug Prüfungsordnung M.Sc.
Vom 19. August 2005 (Amtliche Bekanntmachungen Jg. 36, Nr. 46, S. 269–293) in der Fassung vom 25. September 2020 (Amtliche Bekanntmachungen Jg. 51, Nr. 66, S. 328–337)

§20 (8) Bei der Einreichung hat der/die Studierende schriftlich zu versichern, dass

1. er/sie die eingereichte Masterarbeit beziehungsweise bei einer Gruppenarbeit seinen/ihren entsprechend gekennzeichneten Anteil der Arbeit selbständig verfasst hat,
2. er/sie keine anderen als die angegebenen Quellen und Hilfsmittel benutzt und alle wörtlich oder sinngemäß aus anderen Werken übernommenen Inhalte als solche kenntlich gemacht hat und
3. die eingereichte Masterarbeit weder vollständig noch in wesentlichen Teilen Gegenstand eines anderen Prüfungsverfahrens war oder ist.